Cardiff
Catalysis Institute

Sefydliad Catalysis
Caerdydd

Gold catalysts for the low-temperature water-gas shift reaction

Thesis submitted in accordance with the requirement of Cardiff University for the degree of Doctor of Philosophy

James Henry Carter

January 2016

Student ID Number:	0824753

Summary of Thesis:

The stability of gold catalysts in the low-temperature water-gas shift (WGS) reaction was investigated. The deactivation mechanism of the benchmark catalyst, 2 wt% Au/$CeZrO_4$ was probed using microscopy and spectroscopy. After exposure to reaction conditions, particle agglomeration and morphological changes were observed. These were thought to contribute to the deactivation of the catalyst. Improvements to the stability of the benchmark catalyst were attempted by modification of the supported metal and the support.

A series of 2 wt% Au, AuPd and Pd / $CeZrO_4$ catalysts were prepared by deposition precipitation and screened for their WGS activity and stability. It was shown that the addition of Pd resulted in a significant decrease in the catalytic activity. There was no change in catalyst stability. Several characterisation methods showed that there was a particle size effect that explained the catalytic activity.

A series of Mo-doped $CeZrO_4$ supports were prepared and characterised. After the addition of 2 wt% Au, the catalysts were screened for their WGS activity. Mo appeared to poison the catalysts and the stability remained unchanged.

The role of the support was examined by comparing $CeZrO_4$ to $Ce_{0.5}Ti_{0.5}O_x$ and $Ce_{0.5}Al_{0.5}O_x$. $Ce_{0.5}Ti_{0.5}O_x$ was the subject of further work after it was shown that Au/$Ce_{0.5}Ti_{0.5}O_x$ was as active as and more stable than Au/$CeZrO_4$. A series of 2 wt% Au/$Ce_aTi_{1-a}O_x$ (where a= 0, 0.1, 0.2, 0.5, 0.8, 0.9 and 1) were screened for their WGS activity and stability. Au/$Ce_{0.2}Ti_{0.8}O_x$ was more active and more stable than Au/$CeZrO_4$. Characterisation revealed that the most active and stable catalysts featured a high surface area, small crystallite size, high reducibility and high concentration of oxygen defect sites. These properties were concluded to facilitate highly dispersed gold while providing strongly anchored nanoparticles that resulted in an active and stable catalyst.

Acknowledgements

I would like to firstly thank my supervisors Stanislaw Golunski and Graham Hutchings for giving the opportunity to study for a PhD and for their supervision throughout my course. I would also like to express my sincere gratitude to my post-docs Simon Freakley and Ewa Nowicka for their day-to-day supervision and guidance, which was invaluable.

In addition to the immediate research team mentioned above, many other people contributed to this project along the way, including Dave Willock, Dave Morgan, Stuart Taylor, Dave Sellick, Dave Watson, Christopher Kiely, Sam Pattisson, Sultan Althahban and Parag Shah. I am grateful to all of these people for their expertise.

I would also like to thank the outstanding team of technical staff that support the research throughout the catalysis institute, in particular Steve Morris, Alun Davies, Lee Wescombe, Chris Morgan and Greg Shaw.

I have greatly enjoyed my time as a PhD student and a large part of that is due to the colourful spectrum of characters with whom I have been lucky enough to work. I won't name people as the idea of forgetting someone is too traumatic but I'm sure these people know who they are.

I would like to thank my family who have supported me every step of the way throughout my studies in Cardiff. Finally, I would like to thank Beth for putting up with me.

Abstract

The stability of gold catalysts in the low-temperature water-gas shift reaction (WGS) was investigated. Using state-of-the-art electron microscopy and x-ray photoelectron spectroscopy, the deactivation mechanism of 2wt% Au/$CeZrO_4$ was probed. After exposure to reaction conditions, particle agglomeration and morphological changes were observed.

Two strategies were developed to improve the stability of an Au/$CeZrO_4$ catalyst: Modification of the supported metal and modification of the support. The former strategy involved the addition of Pd the catalyst, while the latter consisted of the use of sub-surface Mo dopants and the substitution of Zr for Ti or Al.

A series of 2wt% Au, AuPd and Pd supported on $CeZrO_4$ catalysts were prepared by deposition precipitation (DP) and screened for their WGS activity and stability. It was shown that the addition of Pd resulted in a significant decrease in the catalytic activity. There was no change in catalyst stability. Several characterisation methods showed that there was a particle size effect that explained the catalytic activity.

A series of Mo-doped $CeZrO_4$ supports were prepared and characterised using several characterisation methods. After the addition of 2wt% Au, the catalysts were screened for their WGS activity. It was shown that Mo poisoned the catalysts and there was no improvement to the catalyst stability.

The role of the support was examined by preparing $Ce_{0.5}Ti_{0.5}O_X$ and $Ce_{0.5}Al_{0.5}O_X$ by a sol-gel methodology. After the deposition of Au by DP the catalysts were tested for WGS activity and stability and compared with an equivalent 2wt %Au/$CeZrO_4$ catalyst. The 2 wt% Au/ $Ce_{0.5}Ti_{0.5}O_X$ was the most stable catalyst and was as active as 2 wt%Au/$CeZrO_4$. $Ce_{0.5}Ti_{0.5}O_x$ was the subject of further work to establish the effect of the Ce:Ti ratio. Gold catalysts prepared by DP on $Ce_aTi_{1-a}O_X$ (where a = 0, 0.1, 0.2, 0.5, 0.8, 0.9 or 1) were screened for WGS activity and stability before being characterised. Au/$Ce_{0.2}Ti_{0.8}O_X$ exhibited the same stability as Au/$Ce_{0.5}Ti_{0.5}O_X$ but achieved an even higher conversion. Characterisation showed that Au/$Ce_{0.2}Ti_{0.8}O_X$ had similar chemical properties to the Au/$Ce_{0.5}Ti_{0.5}O_X$ and an even higher surface area. The combination of defect sites, a high surface area, and a small crystallite size were concluded to be the key properties for an active WGS catalyst support.

Contents

Glossary of terms

Term	Definition
ADF	Annular Dark Field
BE	Binding energy (eV)
BET	Brunauer-Emmett-Teller
BF	Bright Field
CCD	Charge Coupled Device
CEM	Controlled Evaporaotr Mixer
CO-DRIFTS	Carbon monoxide - Diffuse Reflectance InfraRed Fourier Transform Spectroscopy
DF	Dark Field
DFT	Density Functional Theory
DP	Deposition-precipitation
DTA	Differential Thermal Analysis
EDX	Energy Dispersive X-ray spectroscopy
ETEM	Environmental Transmission Electron Microscopy
EXAFS	Extended X-ray Absorption Fine Structure spectroscopy
FAD	Formic Acid Decomposition
FT	Fourier Transform
FTIR	Fourier Transform InfraRed spectrscopy
FWHM	Full Width Half Maximum
GC	Gas Chromatography
HAADF	High-Angle Annular Dark Field
ICDD	International Centre for Diffraction Data
IR	InfraRed
MC	Mechano-Chemically
MCT	Mercuray Cadmium Telluride
MFC	Mass Flow Controller
MP-AES	Microwave Plasma-Atomic Emission Spectroscopy
PC	Personal Computer
PEMFC	Proton Exchange Membrane Fuel Cell
PZC	Point of Zero Charge
SEM	Scanning Electron Microscopy
STEM	Scanning Transmission Electron Microscopy
STM	Scanning Tunnelling Microscopy
TCD	Thermal Conductivity Detector
TEM	Transmission Electron Microscopy
TGA	Thermal Gravimetric Analysis
TPO	Temperature Programmed Oxidation
TPR	Temperature Programmed Reduction
WGS	Water-Gas Shift
XANES	X-ray Absorption Near Edge Spectroscopy
XPS	X-ray Photo-electon Spectroscopy
XRD	X-Ray Diffraction

Chapter 1

Introduction

1.1. Catalysis in context

1.1.1. Catalysis in society

Human beings first took advantage of catalysis in the production of alcohol from sugars using yeast many thousands of years ago, but only in the last few hundred years has catalysis emerged as a scientific field in its own right. Although Jöns Jacob Berzelius is credited with defining the term “catalysis” in 1835, it was as early as 1552 that the first reference to catalysis was made when Valerious Cordus used sulphuric acid to catalyse the conversion of alcohol to ether.[1-3] Catalysts are as ubiquitous as chemistry itself, existing all over the world and throughout the universe on some of the largest and smallest scales imaginable: Carbon, nitrogen and oxygen catalyse the fusion of protons to make helium in certain stars on an astronomical scale[4] while microscopic enzymes catalyse countless biological processes in all living organisms. Today, catalysts power countless industrial processes that are integral to society and it is estimated that 85-90% of the products of the chemical industry are made using catalysis.[5] A catalyst is a material that increases the rate of a reaction but is not consumed in the reaction. It affects the kinetics of a reaction but not the thermodynamics. Heterogeneous catalysts are almost always solids and can be formed from many of the elements in the periodic table. Often the active phase of a heterogeneous catalyst is dispersed on a catalyst support, such as a metal oxide. This type of catalyst, known as a supported metal catalyst, typically consists of finely dispersed metals. When divided into nanoparticulate form, their properties are dramatically different from the bulk material and this principle is exploited in heterogeneous catalysis.

1.1.2. Catalysis by gold

One of the landmark discoveries in heterogeneous catalysis was that gold, when finely divided, is a remarkably active material. First predicted by Hutchings[6] to be the most active catalyst for the hydrochlorination of acetylene based on the standard electrode potential, gold's high activity was subsequently reported for low-temperature CO oxidation by Haruta.[7]

Catalysis by gold has become an increasingly important field of catalysis in recent years. Since the seminal work of Haruta and Hutchings it has been demonstrated that nanoparticulate gold can catalyse the oxidation of numerous molecules, such as carbon monoxide, saturated hydrocarbons,[8] benzyl alcohol[9] and glycerol.[10] Hutchings and Hashmi published a review in 2006 that described the extensive research carried out on gold catalysts for homogeneous and heterogeneous processses.[11] Since then, the field has continued to grow and even review articles are being published on gold catalysts for specific sets of reactions such as organic reactions,[12] CO oxidation[13] and the water-gas shift (WGS) reaction.[14] Recently a gold catalyst was commercialised in the production of the vinyl chloride monomer for the production of polyvinyl chloride, cementing the precious metal's significance to both academia and industry.[15] These developments have been made alongside the optimisation and discovery of new synthesis methods and gold catalyst systems. Furthermore, gold has been combined with numerous metals to create novel nano-alloy catalysts such as Au-Pd,[9] Au-Cu,[16] Au-Pt,[17] Au-Ag[18] and Au-Re,[19] demonstrating its versatility. Overall, gold catalysis is a significant field of research in heterogeneous catalysis and research in this area has led to the discovery of some of the most active catalysts known for certain reactions.

1.1.3. Catalysis by ceria

Cerium oxide, CeO_2, and the many formulations of mixed metal oxides that contain cerium have emerged as one of the most important materials in catalysis. Ce-based oxides are of major significance to researchers and industry, notably in their application to automotive catalysis.[20, 21] There are many properties of Ce-based oxides that make them attractive catalytic materials to work with although the redox properties of the materials are undoubtedly one of the main reasons for their

popularity. The origin of these properties lies in the fact that cerium can easily cycle between the +3 and +4 oxidation states and thus can be used as an oxygen storage material as well as participate in reactions. This is in contrast to an 'innocent' support such as SiO_2, which does not exhibit analogous redox properties. These redox properties can be enhanced by introducing a second metal to form a mixed metal oxide. The addition of zirconia to ceria for example, results in an enhancement of the oxygen storage capacity and the number of defect sites in the material, the latter of which facilitate the activation of water and serve as nucleation sites for supported metals.[20, 22] This in part explains its triumph in three-way catalysts in the form of the mixed metal oxide ceria-zirconia.[23] Many other metals have been added to ceria that have generated novel, valuable materials. These include Ti,[24] Pr,[25] Hf,[25] Mg[20] and many more.

1.2. The water-gas shift reaction: past, present and future

The water-gas shift (WGS) reaction is a chemical reaction between water and carbon monoxide that produces hydrogen and carbon dioxide, shown below:

$$CO_{(g)} + H_2O_{(g)} \rightleftharpoons CO_{2(g)} + H_{2(g)}$$

As a source of H_2, the WGS reaction has historically been utilised in ammonia synthesis[26] and methanol synthesis and continues to be used today.[27] It is also of industrial significance because it can be used to adjust the proportion of CO/H_2 in reforming reactions, which produce H_2-rich gases (also containing CO, H_2O, N_2 and CO_2) from hydrocarbons.[28] The reformate must be passed from the reformer to a shift reactor and then to a catalytic preferential oxidation reactor to reduce the CO content to less than 100 ppm, and in some cases down to a few ppm.[29] As a moderately exothermic reaction (ΔH^o_{298}= −41.1 kJ mol^{-1}) the highest conversions can be achieved at low temepratures. Industrial catalysts are based on copper-zinc-aluminium oxide systems (low-temperature WGS) and iron-chromium oxide systems (high-temperature WGS).

1.2.1. The water-gas shift reaction for the hydrogen economy

The WGS reaction has seen a renewed interest in recent years in the context of the emerging H_2 economy, specifically for gas purification in proton-exchange membrane fuel cells (PEMFCs). PEMFCs are a new generation of fuel cells that can operate at low temperatures (below 150 ^{o}C) and pressures (atmospheric), the applications of which include transport, stationary and portable power generation.[30] Therefore the WGS reaction could be a vital reaction step in the production of future power sources. PEMFCs use H_2 to conduct protons and generate electricity. They are extremely sensitive to CO; Pt electrodes can tolerate only a few ppm of CO exposure so it is vital that the gas streams are ultra-pure. H_2 that is generated from syngas contains CO and therefore must be removed. The WGS reaction has been recognised as an ideal reaction to minimise CO impurities as it generates one mole of H_2 for every mole of CO that is removed. However, the current WGS catalysts are not appropriate for this application; the most stable catalysts based on Cu/ZnO are not intrinsically active enough and require pre-reduction steps. Further, they are pyrophoric when activated so pose a safety concern, especially in the context of applications in transport. The most active catalysts are based on supported precious metals that are not stable enough for commercial application.

1.2.2. The benchmark catalyst: Gold supported on ceria-zirconia

One of the strongest candidates for a catalyst to be utilised in fuel cell technology is gold supported on ceria-zirconia, $Au/CeZrO_4$. In this section, a detailed description of this catalyst, including the proposed active site and deactivation mechanism will be presented and the limitations of the current system will be described.

$Au/CeZrO_4$ was first developed by Johnson Matthey and Queen's University, Belfast.[31] As part of a collaborative project with Johnson Matthey, a number of precious metals supported on a selection of reducible supports were screened, as shown in Figure 1.1. $Au/CeZrO_4$ was identified as the most active catalyst compared to Au/CeO_2, Au/TiO_2 and Pt/CeO_2, especially at low temperatures. Au/CeO_2 achieved 50% conversion at 350^{o}C whereas the $Au/CeZrO_4$ catalyst achieved the same conversion at 140^{o}C. The dramatic decrease in the light-off temperature associated with the mixed metal oxide

support was reported to be due to the stabilisation of oxygen vacancies by zirconium, which was thought to be crucial for high activity. This explanation is consistent with other reports that show the enhancement in activity in $CeZrO_4$ based catalysts.[32] However, the importance of Ce vacancies was also reported; it was shown using DFT calculations that the binding of a gold cluster was strongest in a cation vacancy on a CeO_2 support.[31]

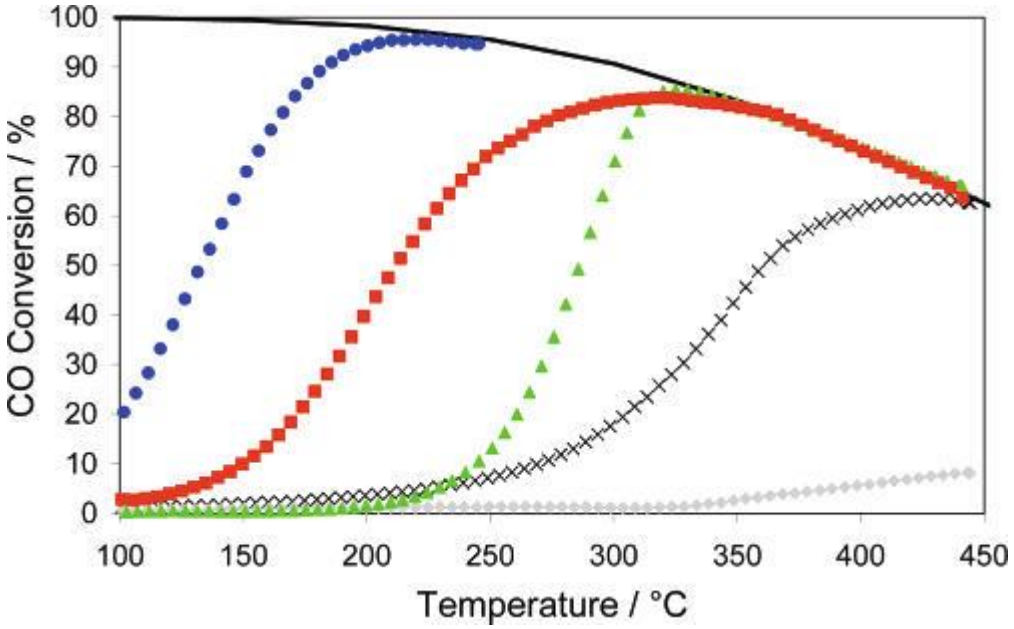

Figure 1.1 Catalytic activity under WGS conditions (2.0% CO, 2.5% CO_2, 7.5% H_2O, and 8.1% H_2 in N_2) for 2% Au/$CeZrO_4$ (●), 0.2% Au/$CeZrO_4$ (■), 2% Au/CeO_2 (×), 2% Au/TiO_2 (♦), and 2% Pt/CeO_2 (▲). Reprinted with permission from Tibiletti *et al.* Journal of Physical Chemistry B, 2005, 109. Copyright 2005 American Chemical Society.

The metal loading was optimised to 2 wt% using the catalyst preparation method of deposition precipitation, which was also more effective than preparing the catalyst using other methods, most likely because this method gives a narrow particle size distribution of metal particles a few nanometres in diameter.[33] The role of the supported metal and the support itself are well understood in the gold-catalysed WGS reaction: CO adsorbs onto the edge of an Au nanoparticle while water is activated by oxygen defect sites on the support close to a metal nanoparticle, where OH groups are formed on the surface.[31, 34, 35] CO_{ads} and OH_{ads} then react to form a reaction intermediate, which finally decomposes into CO_2 and H_2. The active site therefore, is thought to be at the metal-support interface[31] although the active phase of the catalyst is less clear. Gold exists in multiple oxidation states on supported catalysts[36]

which change under reaction conditions and so identification of the active phase can be challenging. Initially, it was found that positively charged Au exists on the catalyst, but this rapidly reduces to metallic Au under reaction conditions.[31] Recently it was proposed that $Au^{\delta+}$ species were not involved in the reaction due to their instability under reaction conditions. Instead it was thought that the active sites are formed during the reaction as the gold nanoparticles are locked into the support.[37]

As stated above, the support facilitates the activation of water although it has also been shown to provide nucleation sites for gold nanoparticles.[34, 36, 38-41] The role of oxygen vacancies in adsorbing water has also been investigated in the context of the WGS reaction. Ribeiro and co-workers compared Au/TiO_2 and Au/Al_2O_3 for WGS activity and found that the superior activity of the Au/TiO_2 catalyst was due to the support's ability to activate water and provide high concentrations of hydroxyl species.[42]

Despite the high activity of the $Au/CeZrO_4$ system, rapid deactivation has been reported for this system which prohibits commercial application. Furthermore, there are conflicting reports of the most significant process that cause deactivation, which hinders efforts to design stable catalyst systems. Goguet *et al.* published a model for the deactivation mechanism using a combination of *in situ* XPS, *in situ* CO-DRIFTS and DFT calculations.[35] It was proposed that under reaction conditions, specifically in the presence of high concentrations of water, the gold nanoparticles de-wetted from the support and changed from hemi-spherical to spherical, as shown in Figure 1.2. This significantly reduced the metal-support interface – the proposed active site in this system. However, this process has not been directly observed experimentally.

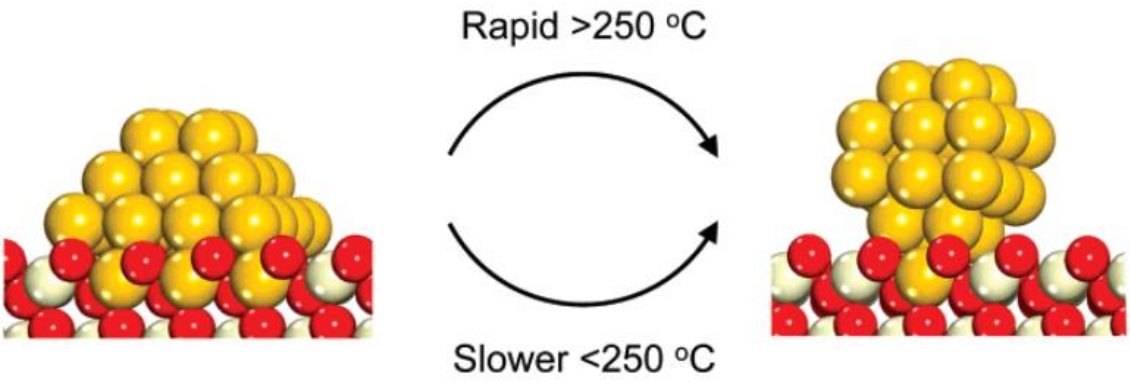

Figure 1.2 Schematic of the proposed deactivation mechanism showing the de-wetting of Au on CeZrO4 under reaction conditions. Reprinted with permission from Gouget *et al.* Journal of Physical Chemistry C, 2007, 111.Copyright 2007 American Chemical Society.

In situ EXAFS was used by Tibiletti *et al.* to disregard particle agglomeration on $Au/CeZrO_4$ as a relevant deactivation process[31] although this has been reported as being the cause of deactivation in Au supported on Pr-doped CeO_2[43] and on Au/CeO_2.[44] Karpenko *et al.* identified the mono-dentate carbonate formation as the primary cause of deactivation in Au/CeO_2 catalysts[45] and later showed that changes in the oxidation state of Ce and Au were also significant.[46] However, it is thought that $CeZrO_4$ supports are not as susceptible to carbonate formation as CeO_2.[35] In fact comparisons between Au/CeO_2 and $CeZrO_4$ must be made with caution. It has been shown that the reaction mechanism is highly sensitive to the catalyst preparation and formulation[34] and the same sensitivity could apply to the deactivation mechanism.

The sensitivity of similar systems has been demonstrated by investigation of different facets of CeO_2. It was shown that for CO oxidation, CeO_2 nanowires and nanorods were the most active morphology compared to nanoparticles. This high activity was attributed to an abundance of exposed surface reactive (100) and (110) planes.[47] It was also shown using environmental transmission electron microscopy (ETEM) that when gold was supported on CeO_2 nanorods, the resultant catalyst was highly stable under redox cycles and resistant to sintering up to 300 ^{o}C.[48] However, water was not included in the gas feed, which has been shown to be crucial to the deactivation rate.[35] In addition, the particle size of the support plays an important role in determining the redox properties of the catalyst as well as the number of defect sites.[49]

While no microscopic studies have been reported on the $Au/CeZrO_4$ system, fresh and used Au/CeO_2 catalysts were analysed by HAADF STEM after exposure to a mixture of CO and H_2O at 290 ^{o}C.[50] Evidence of particle agglomeration was found as well as a change in morphology in the Au nanoparticles. Furthermore, the specific facet of the support that the gold was attached to was shown to heavily influence the stability under water-gas shift conditions. While this work highlighted the importance of sintering in these systems, the catalytic testing was carried out at high temperatures and the gas composition did not include CO_2 or H_2, both of which have been shown to be important in the deactivation mechanism.[35, 44] Several publications on $Au/CeZrO_4$ have been reported although a detailed microscopic investigation remains to be carried out, despite it being one of the most powerful tools available to characterise these systems. The discordance in the literature is most likely due to the wide range of

preparation methods and reaction conditions studied. In addition, it highlights the important role of the support in determining the stability of the catalyst.

1.3. Supported precious metal catalysts for the low-temperature water-gas shift reaction

In this section, the recent publications on developing precious metal catalysts, in particular gold, for the low-temperature WGS reaction are discussed. In addition, recent breakthroughs in the fundamental chemistry associated with the mechanism and design of catalysts for the WGS reaction are described.

1.3.1. Monometallic systems

Nanoparticulate metals, when supported on a high surface area support, have been shown to be highly active for low-temperature WGS. Gold was first identified as a remarkably active WGS catalyst by Andreeva *et al.* who reported the high activity of Au/α-Fe_2O_3 in 1996.[51] Platinum was also shown to be highly active for WGS when supported on metal oxides, although the highest activity of Pt catalysts was observed at higher temperatures than an equivalent gold catalyst.[36] A comparative study of gold and platinum catalysts on zirconia and ceria-zirconia conducted by Trovarelli and co-workers also showed that at lower temperatures gold is more active than platinum, making it an appealing element to explore.[52]

Research into gold-based WGS catalysts has been intensive and several literature reviews have been published,[34, 53] most recently by Tao and Ma.[14] In this review, the importance of the support identity was discussed. Specifically, it was observed that non-reducible supports such as SiO_2 and Al_2O_3 are not suitable catalyst supports whereas TiO_2, CeO_2 and Fe_2O_3 generally produce more active WGS catalysts. His reducibility is thought to facilitate the activation of water and drive the reaction. Numerous examples of gold catalysts that have been published and include Au/CeO_2-Ga_2O_3,[54] Au/CeO_2-Fe_2O_3, [55] Au/CeO_2-SnO_2,[55] Au/CeO_2-MnO_2,[55] Au/CeO_2-TiO_2[56] and Au/CeO_2-Al_2O_3.[57] The latter study, conducted by Rodriguez and co-workers was a surface science study and therefore the activity is not comparable with studies carried out on conventional reactors. However, the study showed that the addition of Al_2O_3

stabilised Ce^{3+} on the surface of the catalyst which was conducive to high WGS activity. The former studies investigated the effect of an adding a second metal to Ce to form a mixed metal oxide support. Similarly, in these studies an abundance of Ce^{3+} was correlated with higher WGS activity. This was observed for CeO_2-Fe_2O_3 and CeO_2-MnO_2.[55] Vecchietti *et al.* reported that Au/CeO_2 was more active than Au/CeO_2-Ga_2O_3 in the WGS reaction, but did not explain the origin of this observation. The variable conditions and catalyst preparation techniques have prevented conclusive comparisons being made between many of these catalysts. However, it has been widely reported that a reducible support is desirable as this facilitates the activation of water. Indeed, the most active catalysts are often supported on CeO_2-based oxides.

In addition to Au, many other transition metals have been screened for their WGS activity when dispersed on Ce-based oxides. These studies are summarised in Table 1.2. Pd has been the subject of many investigations, notably by Gorte and co-workers.[58, 59] More recently, Fornasiero and co-workers showed that Pd@CeO_2/Al_2O_3 was also active for the WGS reaction, reporting rates that were similar to Pd/CeO_2. The CeO_2 shell protected the Pd from agglomeration and the porous structure allowed the transport of reactant gases. However, the over-reduction of the thin CeO_2 shell quickly deactivated the catalyst.[60]

Rh/CeO_2 was investigated for WGS activity by Gorte and co-workers and it was shown that the activity was similar to that of Pd and Pt. Furthermore, the equivalent catalysts on Al_2O_3 were two orders of magnitude less active.[41] Cu/CeO_2 was also reported to be active for WGS, although pre-reduction was required for high activity.[61] Nickel was recently reported to be active, when prepared by urea-co-precipitation-gelation method, although the activity displayed was at a higher temperature than an equivalent Cu catalyst (250-300 ^{o}C). Ru/SiO_2/CeO_2 was investigated by Shinde *et al.*[62] and was shown to be active for the reaction, although the intrinsic activity was much lower than for an equivalent Au catalyst.

Overall, many transition metals have been dispersed on CeO_2 and Ce-based oxides. NO reports have emerged that show a catalyst more active than Au. However, comparison of different catalysts with Au catalysts in the WGS reaction is problematic based on the current literature as the gas compositions and reaction conditions vary significantly.

For example, Hardacre and co-workers reported the activity of $Au/CeZrO_4$ under a mixture of 2%CO, 2%CO_2, 7.5% H_2O and 8.1% H_2[63] whereas Gorte and co-workers[58] used 25 Torr of CO and H_2O to screen Pd/CeO_2. Therefore comparison of the activation energy between such studies is not instructive.

Table 1.2. Summary of literature data for various monometallic WGS catalysts with Ce-based oxides as supports.

Catalyst	Temperature (^oC)	Gas composition	Conversion (%)	Comments	Reference
$Au/CeZrO_4$	150-270	2% CO, 2% CO_2, 7.5% H_2O, 8.1% H_2	95% at 200 ^oC	High active and unstable	1
Au/CeO_2	250	10% CO, 22% H_2O, 6% CO_2, 43% H_2 + N_2	90	Catalyst prepared by DP. Unstable.	2
Pt/CeO_2	300	1.6% CO, 52.4% H_2O, 41.9% H_2 + N_2	90	Catalyst pre-reduced	3
Pd/CeO_2	200	25 Torr of CO and H_2O	-	Addition of Fe to surface increased activity	4
Rh/CeO_2	300	20 Torr CO, 15 Torr H_2O	<1	Rh exhibited similar activity to Pt and Pd	5
Cu/CeO_2	400	6.5% CO, H_2O,7.1% CO_2, 0.7% CH_4, 42% H_2, 28% + N_2.	73	Catalyst was pre-reduced	6
$Ni/LaO_x/CeO_2$	400	2 % CO, 10.7% H_2O, 40% H_2 + He	>95	No catalyst activation required	7
$Ru/SiO_2/CeO_2$	280	1.3% CO and 35% H_2O	99	Highly selective	8

1.3.2. Bimetallic systems

The earliest example of bimetallic gold catalysts for the WGS reaction was by Venugopal *et al.* [64] The authors examined Au-M/Fe_2O_3 catalysts where M= Ag, Bi, Co, Cu, Mn, Ni, Pb, Ru, Sn, or Tl. The catalysts were calcined at 400 ^oC and many of the bimetallic catalysts tested were reported to be more active than the unmodified gold catalyst. Although comparisons are difficult to make between research groups, it is

likely that the high calcination temperatures used would mean that an uncalcined catalyst would be more active than the bimetallic ones calcined at 400 ^{o}C. This is because the particle size of gold would be expected to be much larger than an uncalcined catalyst. Tsang and co-workers prepared Au-Pd/CeO_2 and Au-Pt/CeO_2 by co-precipitation and also calcined the catalysts at 400 ^{o}C.[65] They reported the particle size of the monometallic gold to be 22 nm. In the bimetallic catalysts, particularly Au-Pt/CeO_2, the particle size was smaller and a greater activity was reported. These data do not compare the bimetallic catalysts to the most active monometallic gold catalysts and so are not of great significance. The aforementioned paper by Tsang and co-workers is the only experimental report on AuPd catalysts for the WGS reaction.[65] Due to the catalyst preparation method, it is not comparable to the Au/$CeZrO_4$ catalysts prepared by deposition-precipitation and the question of whether the AuPd bimetallic system is effective at catalysing the WGS reaction remains unanswered.

1.3.3. Fundamental studies on the low-temperature water-gas shift reaction

As well as rigorous screening of various formulations of precious metal/metal oxide systems, there has been a drive to understand the fundamental science of the WGS reaction, including the active sites and reaction mechanisms on precious metal catalysts.

As mentioned earlier, Tao and Ma recently summarised the new advances in gold catalysed water-gas shift, including the nature of the active site. [14] Early spectroscopic work conducted by Tabakova and co-workers observed that metallic Au in contact with defective ceria was the active site in an Au/CeO_2 system and that a formate intermediate is present in the reaction.[66] However, Flytzani-Stephanopoulos and co-workers reported that strongly associated non-metallic Au is in fact the active site for WGS.[36] Subsequent studies on Au/$CeGdO_2$,[67, 68] Au/CeO_X/TiO_2,[82] Au/TiO_2,[69] and Au/Al_2O_3[70] proposed that metallic Au was the active component.

The metal-support interface has been widely accepted as the active site on the catalyst.[14, 35] The importance of the metal-support interface has been demonstrated by Rodriguez and co-workers by doping CeO_X and TiO_X onto model Au (111) surfaces.[39] It

was shown that the reaction occurred at the interface between the dispersed metal oxide and the bulk Au surface.

The dynamic structure and properties of gold under WGS conditions makes it very challenging to identify the active site. Furthermore, common catalyst preparation methods such as deposition-precipitation result in a heterogeneous distribution of metal species with different intrinsic activities, thus separating the catalytically active sites from the spectator species is very challenging. The very recent work of Flytzani-Stephanopoulos and co-workers attempted to address this issue using NaCN leaching studies and novel preparation routes to supported gold catalysts. They concluded that single atoms of ionic gold were the active sites.[71] In addition, it has been shown that reducible supports are not essential for an active catalyst.[71, 72] It has been demonstrated on TiO_2,[71] zeolites[73] and mesoporous SiO_2[73] that the active site consists of atomically dispersed $Au(OH)_X$ or $Au\text{-}O(OH)_X\text{-}M$ (where M=Na or K). On zeolites and MCM-41, alkali metal dopants were used to facilitate OH groups at the surface rather than defective Ce-based oxides. It was found that the intrinsic activity of the catalysts was the same as gold supported on CeO_2. The significance of this work is that it goes against the accepted dogma that a reducible support, often based on a formulation of cerium oxide, is required to produce an active WGS catalyst and that the active sites are gold nanoparticles. Furthermore, it clarifies the role of the support: to anchor gold and to create OH groups on the surface. This can demonstrably be achieved without a reducible support and means that a wider range of materials can be investigated as supports for gold. The same active site was found for alkali-promoted Pt catalysts on carbon nanotubes.[74]

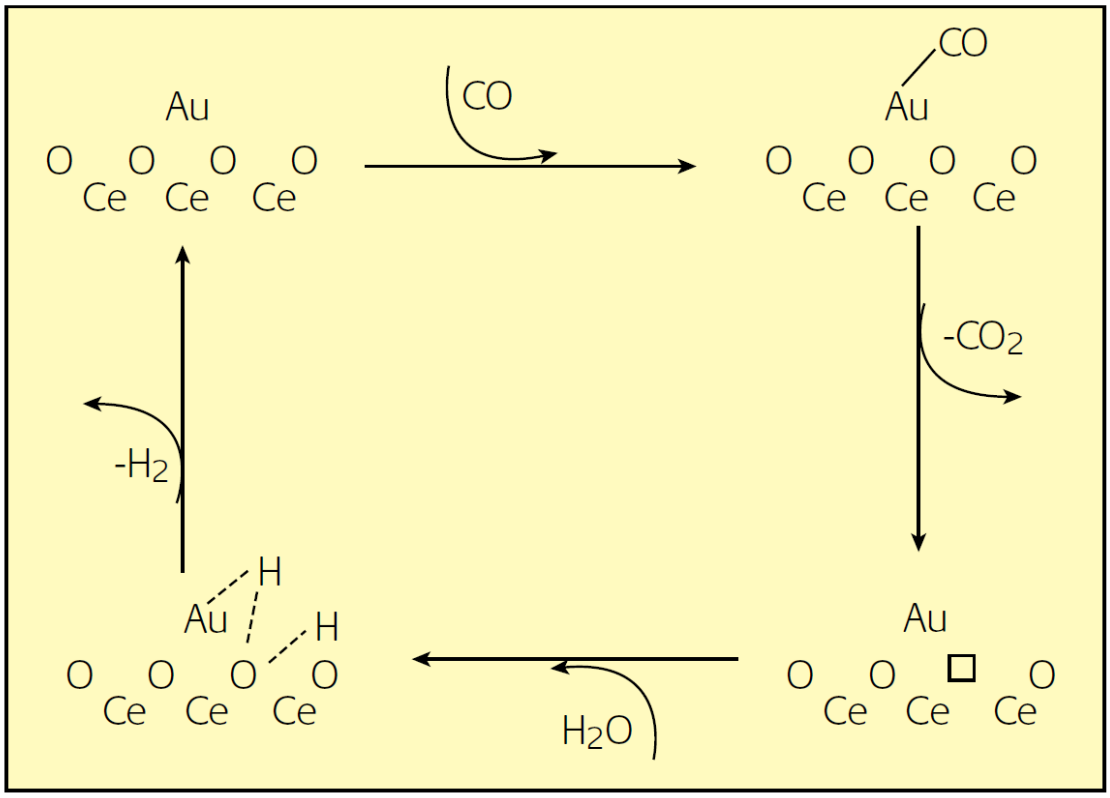

Figure 1.3 A reaction pathway of the redox mechanism. Reproduced with permission of Springer from D. Andreeva, Gold Bull., 2002, 35, 82.

A full understanding of the reaction mechanism of the low-temperature WGS reaction, including the active site, is necessary to optimise the design of catalysts. However, like the active site, the reaction mechanism of the WGS reaction is still hotly debated. Broadly speaking, there are two mechanisms that have been proposed: the redox mechanism and the associative mechanism. The redox or regenerative mechanism involves the oxidation of CO by O on the surface of the catalyst to form CO_2. The support is then re-oxidised by H_2O and forms H_2 as a result.[14, 53, 75 76] The reaction pathway is illustrated in Figure 1.3 using Au/CeO_2 as an example.[76] This reaction pathway is generally thought to occur at higher temperatures.[14, 76, 77] However, the temperature range that is relevant to this investigation is below 220 ^{o}C. The main criticism of this pathway is that is does not take into consideration the reaction intermediates, which are more important at lower temperatures due to their longer lifetime on the surface.

The associative mechanism by contrast, includes the reaction intermediates in the reaction scheme, although the identity of the intermediate is still debated. There are two candidate intermediates: the formate and the carboxyl intermediate. There are

also reports that a carbonate species is an important intermediate.[34] Burch reviewed the literature on the mechanistic studies and reported that there is evidence for both the formate and carboxyl intermediates.[34] It was also noted that the mechanism is likely dependent on the experimental conditions used in the study. Spectroscopic evidence has been reported for the formate species under realistic WGS conditions over Au/CeO_2.[77-80] However, spectroscopically observed formate species have been shown to be insignificant mechanistically.[81] Meunier and co-workers measured the rate of CO_2 formation and the rate of formate decomposition and showed that the rates were significantly different.[82] This could mean that a different species to the formate is the key intermediate, one that does not persist on the surface long enough for spectroscopic identification. It could also mean that not all formate species are equal. It is well known that there are a number of different adsorption sites on supported gold catalysts (corner, perimeter etc.) and these have different intrinsic activities in catalytic reactions. It is possible that there are spectator formates and reaction-relevant formates co-existing on the same catalyst.

Bond recently discussed the possible mechanisms of the gold-catalysed WGS reaction.[75] The similarity between the WGS reaction and formic acid decomposition (FAD) was noted and Bond suggested that both reactions could proceed through the same carboxyl intermediate (-COOH), making FAD a simple test reaction for WGS activity. This hypothesis was based on the similar activation energies observed on Au/SiO_2 and Au/Al_2O_3 for both reactions between 100 and 300 ^oC. Other researchers have also identified the similarities between the WGS reaction and FAD. Davis and co-workers examined Pt/CeO_2 catalysts for both reactions and identified a common intermediate on these catalysts: a bidentate formate.[83]

Burch proposed a universal mechanism, taking into account the evidence for the redox and associative mechanism, as well as resolving the conflicting reports in the literature.[34] This is illustrated in Figure 1.4. It was recognised that the reaction mechanism is heavily influenced by the conditions and the effect that the concentration of H_2O or CO_2 could have on directing the mechanism.

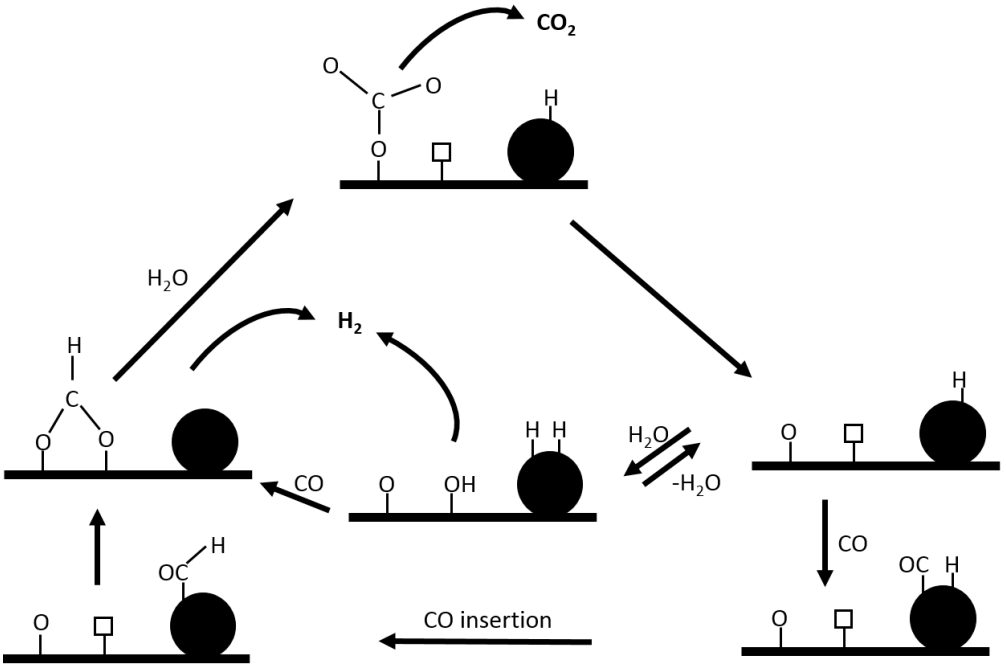

Figure 1.4 Proposed universal reaction mechanism for the WGS reaction. Reproduced from Ref 34 with permission from the PCCP Owner Societies.

1.4. Strategies to stabilise supported metal catalysts

The ultimate aim of this work is to design novel catalysts for the WGS reaction with the aim of improving their stability and understanding the properties that give rise to a stable catalyst. This section outlines the literature pertaining to the catalysts that were investigated in this work. The deactivation mechanism, as described above, is caused by a poor metal-support interaction. It was reasoned that strengthening this interaction would enhance the stability of the catalyst. Two strategies were identified: **Modification of the supported metal** through alloying and **modification of the support** itself. In the former, AuPd was selected as a candidate bimetallic system. Modification of the support involved attempting to introduce sub-surface dopants and to modify the mixed metal oxide.

1.4.1. Modification of the supported metal

Gold-palladium bimetallic systems have been shown to exhibit synergy for a number of chemical reactions, particularly liquid-phase oxidation reactions.[84-88] The term synergy is often used to characterise the effect observed in these systems because the bimetallic catalyst formed of Au and Pd is significantly more active than the equivalent

catalyst comprised of the monometallic catalyst. Specific examples include benzyl alcohol and glycerol oxidation,[88-93] as well as the direct synthesis of hydrogen peroxide[89, 94, 95] and vinyl acetate synthesis.[96] Despite the high activity of AuPd systems for many reactions, gas-phase reactions such as the low-temperature WGS have not been fully investigated. *In lieu* of sufficient studies on the WGS reaction, it is instructive to consider the literature available for these catalysts on CO oxidation. These publications, however, have focussed on non-reducible supports such as SiO_2.[97, 98] Consequently, direct comparisons with reducible supports such as $CeZrO_4$ are problematic because it has been shown that the support is a significant parameter in determining catalytic activity for CO oxidation.[99, 100] Pantaleo *et al.* studied a range of SiO_2 supported AuPd catalysts and found that for a non-reducible support such as SiO_2, Pd was the most active catalyst.[101] The authors attributed the inactivity of Au catalysts to the larger size of Au nanoparticles compared to Pd, although the ability of Pd to activate O_2 should also be considered significant. As Au cannot activate O_2 it is expected that Au was inactive for CO oxidation and this was also reported by Huang *et al.*[98] For TiO_2-supported AuPd catalysts, Guczi *et al.* used a selection of preparation methods to achieve different nanostructured bimetallic catalysts.[102] No significant synergy was observed in those catalysts, regardless of the preparation method, indicating that the presence of core-shell structures do not significantly affect the catalytic activity for CO oxidation. One possible explanation is the segregation of Au and Pd alloys that occurs in various atmospheres, including under exposure to CO, whereby the strong affinity of Pd for CO causes the Pd to migrate to the surface.[103] However, this structure insensitivity was also investigated by Lopez-Sanchez *et al.* using $AuPd/TiO_2$ prepared by colloidal methods. They studied CO oxidation and concluded that the introduction of Pd to Au was not beneficial for the catalyst, however the underlying reasons were not investigated.[104]

Recently, a number of theoretical and model catalysts studies predicted AuPd catalysts to be active for CO oxidation. In a density functional theory (DFT) study, Hwang and co-workers attempted to rationalise AuPd interactions on AuPd(111) surfaces. Their calculations predicted that “partially-poisoned” Pd ensembles facilitate the activation of O_2 and subsequent reaction with CO, making AuPd alloys highly active for CO oxidation.[105] The importance of Pd in dissociating O_2 has also been reported by

Goodman *et al.* in an investigation of model AuPd(100) surfaces.[106] In this study it was shown that the contiguous Pd sites were able to dissociate O_2. It was also highlighted that support and particle size effects should be less important on bimetallic catalysts compared to Au-only catalysts. Subsequently AuPd systems were predicted to exhibit high catalytic activity. It should be noted that these model studies involved low pressures (48 Torr) and thus do not necessarily reflect the dynamic conditions in a catalytic reactor, in addition to the fact that moisture levels have been shown to be of significance in the reaction mechanism.[107, 108] Leitao *et al.* conducted a DFT study that predicted that Au and Pd should be highly active for the WGS reaction due to the low energy barriers associated with H_2O dissociation and CO oxidation but this has not been demonstrated experimentally.[109]

Overall, there is no consensus regarding the efficacy of AuPd systems for CO oxidation and WGS reaction. Of the few experimental reports that have been published, a full explanation of the implications of mixing Pd and Au for this reaction have not been given and while *in situ* vibrational spectroscopy has shed light on how CO interacts with the metal nanoparticles,[103, 110] the literature remains somewhat disjointed on this topic. The AuPd bimetallic system was identified as a candidate for an active, stable catalyst because of its success in so many oxidation reactions, despite the lack of experimental reports for WGS and related reactions. The ease with which these two metals alloy also served as an incentive to explore this bimetallic system.

1.4.2. Modification of the support

Supported gold catalysts often suffer from deactivation through sintering and other mechanisms and as discussed above, the WGS reaction is no exception. There have been many attempts to stabilise such systems. In this section, research that has successfully achieved enhancements in stability through engineering the catalyst support will be described.

In a recent publication, Freund and co-workers showed that sub-surface dopants can significantly affect the properties of surface gold species in CaO model supports.[111] In an undoped CaO (001) film, Au particle growth proceeded in a 3D manner, whereas when Mo was doped into the CaO matrix, 2D growth predominated, as shown in Figure 1.5. This effect was observed and investigated using STM and DFT. DFT showed that the binding energy of gold on the doped CaO was almost three times greater.

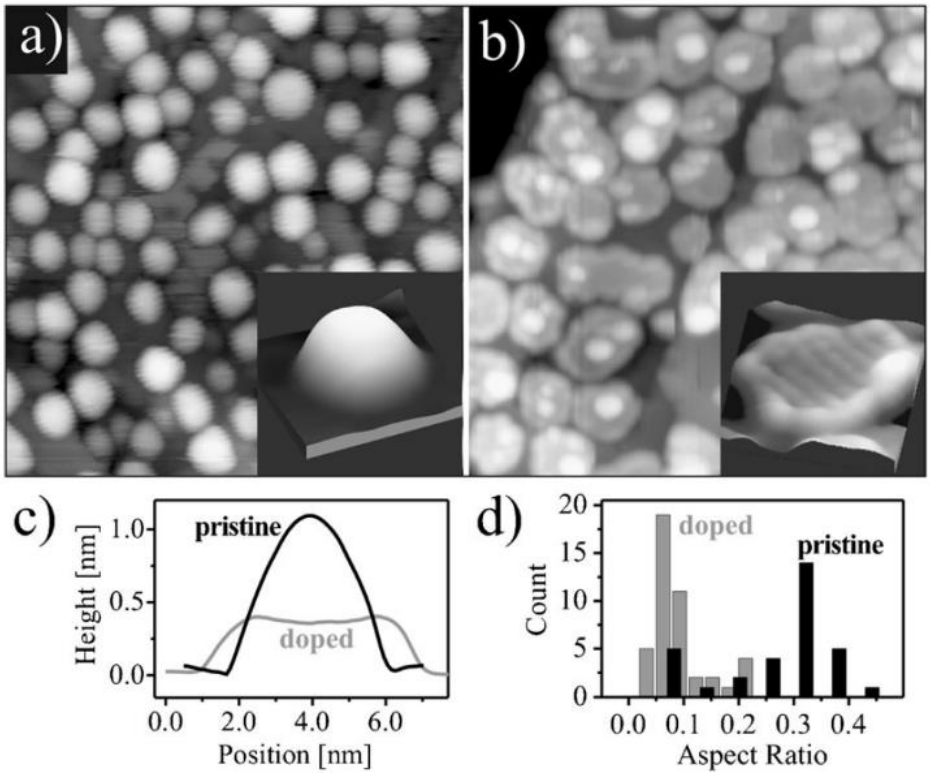

Figure 1.5 The effect of Mo on the structure of Au nanoparticle STM images of a) Au on pristine CaO, b) Au on Mo-doped CaO with the corresponding height profiles (c) and aspect ratios (d). Reprinted from ref 104 with permission from John Wiley and sons.

The donation of electrons from Mo to the gold surface species was confirmed both experimentally and theoretically and led to strong electrostatic interactions between the negatively charged surface gold particles and the CaO film. Earlier reports of similar phenomena exist on ultra-thin films, but in these cases the electronic effect was induced by the metal substrate rather than a dopant.[112, 113] Moreover, it has been demonstrated that surface dopants can induce similar effects.[114, 115] While there has been interest in the doping of substrates to induce morphological and electronic effects on surface species, existing reports have been restricted to model studies on CaO or MgO and no experimental evidence exists for “real” catalysts exhibiting these properties. In the context of the deactivation mechanism of the gold catalyst, as

studied in **Chapter 3**, this method of stabilisation is an ideal candidate for the $Au/CeZrO_4$ catalyst system because it presents an opportunity to stabilise the gold nanoparticles without modifying the elemental composition of the surface.

The formulation of the support is highly tuneable in Ce-based oxides and much research has been carried out in modifying the chemical composition of CeO_2, as briefly discussed in **Chapter 1.1.3**. CeO_2 itself is well known to possess remarkable redox properties and it has been shown, particularly in the context of automotive catalysis,[23] that the addition of metals such as Zr to CeO_2 can further enhance the quality of this material as a catalyst support. Since the early work of Fornasiero[116] who reported that $CeZrO_4$ possessed enhanced redox properties, many researchers have developed Ce-based materials for catalysis, using a number of elements from the periodic table to tune the properties of the final material to meet the desired specifications. $Ce_xZr_{x-1}O_2$ has also been employed as a support for Au in low-temperature water-gas shift[31] and a review of ceria-based catalysts for water-gas shift has recently been published.[117] Zr is not the only metal that can affect the chemical and textural properties of CeO_2. Titanium and aluminium were both identified as being appropriate metals to substitute for Zr to form new mixed metal oxides. The following section describes the literature on these materials in the context of the WGS reaction.

Ceria-titania

Ceria-titania, although not as widely studied as ceria-zirconia has been investigated by numerous research groups as a catalyst support for CO oxidation[118, 119] and dry methane reforming.[120] Similar to ceria-zirconia, the addition of titanium to CeO_2 gives enhanced redox properties. One of the earliest examples of CeO_2-TiO_2 being used as a mixed metal oxide support was by Mastelaro and co-workers, who supported CuO on CeO_2-TiO_2 and reported an enhancement in catalytic activity for methanol oxidation.[121] The reasoning for this was partly ascribed to the enhancement in the textural properties of the materials. In $Ce_{0.09}Ti_{0.82}O_x$ the surface area was 124 $m^2\ g^{-1}$ compared to 79 m^2g^{-1} in the TiO_2 only sample. A high surface area is a desirable property for a catalyst support as it allows a higher loading of supported metal to be deposited with a high dispersion.

Rodriguez and co-workers have made significant contributions to understanding the fundamental processes that occur in the WGS reaction using gold supported on CeO_2/TiO_2 as model catalysts. Recently they showed that $Au/CeO_X/TiO_2(110)$ was remarkably active for low temperature WGS.[56] The activity of this system was far higher than the activity of gold supported on $CeO_2(111)$ or $Au/TiO_2(110)$. It was shown using a combination of DFT and x-ray photoelectron spectroscopy (XPS) that the Ce^{3+} cation is stabilised on $CeO_X/TiO_2(110)$ and this was thought to be the origin of the high activity. Rodriguez and co-workers also demonstrated the high activity of this support can be observed when other metals such as copper and platinum were deposited.[122]

Ramirez-Lopez *et al.* found that the titanium precursor was important in sol-gel syntheses. In a comparison of titanium iso-propoxide and titanium butoxide, it was shown that the former precursor gave materials with higher surface area and oxygen mobility.[123]

Ceria-alumina

Ceria-alumina is not as widely studied as many Ce-based mixed metal oxides but alumina is ubiquitous in industrial catalysis, which is illustrative of its thermal and chemical stability. However, there have been several reports in the literature concerning Au/CeO_2-Al_2O_3 catalysts for water-gas shift that are relevant, most notably performed by Andreeva and co-workers. They reported gold supported on ceria-alumina for WGS prepared using a co-precipitation method to prepare CeO_2 containing 10 or 20 wt% Al_2O_3 and compared it to a conventional Au/CeO_2 catalyst.[57] It was shown that the addition of alumina reduced the catalytic activity of the resultant gold catalysts. This was attributed to deep oxygen vacancies preventing re-oxidation of the catalyst surface, evidenced using Raman and TPR measurements. However, it was also noted that the stability of the gold and ceria particles was enhanced. These catalyst systems were also demonstrated to be active in NO_X reduction using CO.[124, 125]

A subsequent publication by the same group showed the influence of the preparation method in these catalyst systems.[126, 127] Mechano-chemically (MC) prepared CeO_2-Al_2O_3 exhibited high activity and stability for WGS when gold was supported on it, compared to the equivalent catalyst prepared by washcoating. The enhanced stability of the MC prepared catalyst was ascribed to the prevention of particle agglomeration

due to the presence of alumina. The ability of alumina to structurally stabilise catalysts is well established in industrial WGS catalysts.[128] The MC prepared catalyst exhibited superior redox properties and this was thought to be the origin of its higher activity. While preparation through co-precipitation[57] led to deep oxygen vacancies that could not be re-oxidised by water, MC preparation led to a catalyst that retained the redox activity of the CeO_2 support while providing a sintering barrier that enhanced stability. It was suggested that the presence of a 3+ cation created oxygen vacancies in the CeO_2 and so further work was carried out on rare earth metals.

Reina *et al.* studied promoted $Au/CeO_2/Al_2O_3$ catalysts for the low-temperature WGS reaction. These supports were prepared by impregnating the alumina with nitrate precursors of Ce and a dopant (Zn, Cu or Fe).[129] Each of the dopants enhanced the catalyst activity and Fe exhibited the highest activity. This was concluded to be a result of both redox and structural enhancement.

It should be noted that in the works mentioned above ([57, 126, 127, 129, 130]) the reaction conditions were mostly irrelevant to fuel cell applications. CO and H_2O were the only gases present, unlike reformate streams that contain high levels of H_2 and some CO_2. The presence of CO_2 and H_2 have been shown to significantly affect the stability of the catalysts and therefore the stability exhibited in those experiments might not necessarily be seen in actual reformers.

Au/CeO_2-Al_2O_3 was reported to be highly active, when prepared using a sol-gel technique for CO oxidation by Simakov and co-workers[131] but this catalyst has not been studied in the WGS reaction.

Overall, there are several reports that have shown that the addition of alumina to ceria can enhance the activity of a supported gold catalyst for WGS, if prepared using the correct methodology. However, the work published thus far has not fully investigated the stability of this catalyst under relevant WGS reaction conditions. Gold supported on mixed metal oxides of Ce and Al prepared by sol-gel has not been reported for WGS.

1.5. Project aims

The aim of the project was to design a stable catalyst for the low-temperature water-gas shift reaction based on the benchmark $Au/CeZrO_4$ catalyst, while maintaining high catalytic activity. The first objective was to investigate the deactivation mechanism using state-of-the-art microscopy, the subject of **Chapter 3**, and combine this with the current understanding of the deactivation mechanism to inform the design of a novel catalyst. Two approaches to addressing the deactivation were identified: the modification of the supported metal by exploring $AuPd/CeZrO_4$ catalysts, the subject of **Chapter 4**, and the modification of the catalyst support, described in **Chapter 5**. This involved the investigation of sub-surface dopants of Mo and substituting Zr for Ti or Al to form $CeMO_X$ as a support on which to deposit gold.

1.6. References

1. B. H. Davis, H. Knözinger and J. Weitkamp, VCH, Weinheim, 1997.
2. B. Lindstrom and L. J. Pettersson, *Cattech*, 2003, **7**, 130.
3. S. Green, Macmillan Company, New York, 1928.
4. S. Cassisi and M. Salaris, John Wiley and Sons, 2005.
5. I. Chorkendorff and J. W. Niemantsverdriet, *Concepts of Modern Catalysis and Kinetics* Wiley, 2003.
6. G. J. Hutchings, *Journal of Catalysis*, 1985, **96**, 292.
7. M. Haruta, T. Kobayashi, H. Sano and N. Yamada, *Chemistry Letters*, 1987, 405.
8. M. Haruta, *Catalysis Today*, 1997, **36**, 153.
9. D. I. Enache, J. K. Edwards, P. Landon, B. Solsona-Espriu, A. F. Carley, A. A. Herzing, M. Watanabe, C. J. Kiely, D. W. Knight and G. J. Hutchings, *Science*, 2006, **311**, 362.
10. C. L. Bianchi, P. Canton, N. Dimitratos, F. Porta and L. Prati, *Catalysis Today*, 2005, **102**, 203.
11. A. S. K. Hashmi and G. J. Hutchings, *Angewandte Chemie-International Edition*, 2006, **45**, 7896.
12. A. Corma and H. Garcia, *Chemical Society Reviews*, 2008, **37**, 2096.
13. B. K. Min and C. M. Friend, *Chemical Reviews*, 2007, **107**, 2709.
14. F. Tao and Z. Ma, *Physical Chemistry Chemical Physics*, 2013, **15**, 15260.
15. A. Extance, New Catalyst Can Reduce Mercury Emissions, http://www.scientificamerican.com/article/new-catalyst-can-reduce-mercury-emissions/.
16. C. L. Bracey, P. R. Ellis and G. J. Hutchings, *Chemical Society Reviews*, 2009, **38**, 2231.
17. H. G. Lang, S. Maldonado, K. J. Stevenson and B. D. Chandler, *Journal of the American Chemical Society*, 2004, **126**, 12949.
18. A. Sandoval, A. Aguilar, C. Louis, A. Traverse and R. Zanella, *Journal of Catalysis*, 2011, **281**, 40.
19. B. S. Caglayan and A. E. Aksoylu, *Catalysis Communications*, 2011, **12**.
20. *Catalysis by Ceria and Related Materials*, Imperial College Press, second edn., 2013.
21. H. C. Yao and Y. F. Y. Yao, *Journal of Catalysis*, 1984, **86**, 254.
22. Q. Fu, W. L. Deng, H. Saltsburg and M. Flytzani-Stephanopoulos, *Applied Catalysis B-Environmental*, 2005, **56**.
23. J. Kaspar, P. Fornasiero and M. Graziani, *Catalysis Today*, 1999, **50**, 285.
24. J. Rynkowski, J. Farbotko, R. Touroude and L. Hilaire, *Applied Catalysis a-General*, 2000, **203**, 335.

25. G. Zhou and R. J. Gorte, *Journal of Physical Chemistry B*, 2008, **112**, 9869.

26. P. Carstensen, Hansen, Ammonia Plant Saf, 1991, vol. 31, p. 113.

27. T. S. Askgaard, J. K. Norskov, C. V. Ovesen and P. Stoltze, *Journal of Catalysis*, 1995, **156**.

28. J. M. Thomas and W. J. Thomas, *Principles and Practice of Heterogeneous Catalysis*, VCM, 1997.

29. T. R. Ralph and M. P. Hogarth, *Platinum Metals Review*, 2002, **46**.

30. M. E. Scofield, H. Liu and S. S. Wong, *Chemical Society Reviews*, 2015, **44**, 5836.

31. D. Tibiletti, A. Amieiro-Fonseca, R. Burch, Y. Chen, J. M. Fisher, A. Goguet, C. Hardacre, P. Hu and A. Thompsett, *Journal of Physical Chemistry B*, 2005, **109**.

32. C. Bozo, N. Guilhaume and J. M. Herrmann, *Journal of Catalysis*, 2001, **203**, 393.

33. R. Zanella, S. Giorgio, C. H. Shin, C. R. Henry and C. Louis, *Journal of Catalysis*, 2004, **222**, 357.

34. R. Burch, *Physical Chemistry Chemical Physics*, 2006, **8**, 5483.

35. A. Goguet, R. Burch, Y. Chen, C. Hardacre, P. Hu, R. W. Joyner, F. C. Meunier, B. S. Mun, A. Thompsett and D. Tibiletti, *Journal of Physical Chemistry C*, 2007, **111**.

36. Q. Fu, H. Saltsburg and M. Flytzani-Stephanopoulos, *Science*, 2003, **301**, 935.

37. H. Daly, A. Goguet, C. Hardacre, F. C. Meunier, R. Pilasombat and D. Thompsett, *Journal of Catalysis*, 2010, **273**, 257.

38. R. Si and M. Flytzani-Stephanopoulos, *Angewandte Chemie-International Edition*, 2008, **47**, 2884.

39. J. A. Rodriguez, S. Ma, P. Liu, J. Hrbek, J. Evans and M. Perez, *Science*, 2007, **318**, 1757.

40. S. Ricote, G. Jacobs, M. Milling, Y. Y. Ji, P. M. Patterson and B. H. Davis, *Applied Catalysis a-General*, 2006, **303**, 35.

41. T. Bunluesin, R. J. Gorte and G. W. Graham, *Applied Catalysis B-Environmental*, 1998, **15**.

42. M. Shekhar, J. Wang, W.-S. Lee, W. D. Williams, S. M. Kim, E. A. Stach, J. T. Miller, W. N. Delgass and F. H. Ribeiro, *Journal of the American Chemical Society*, 2012, **134**, 4700.

43. L. Ilieva, P. Petrova, I. Ivanov, G. Munteanu, M. Boutonnet, J. W. Sobczac, W. Lisowski, Z. Kaszkur, P. Markov, A. M. Venezia and T. Tabakova, *Materials Chemistry and Physics*, 2015, **157**, 138.

44. A. Luengnaruemitchai, S. Osuwan and E. Gulari, *Catalysis Communications*, 2003, **4**, 215.

45. Y. Denkwitz, A. Karpenko, V. Plzak, R. Leppelt, B. Schumacher and R. J. Behm, *Journal of Catalysis*, 2007, **246**, 74.

46. A. Karpenko, R. Leppelt, J. Cai, V. Plzak, A. Chuvilin, U. Kaiser and R. J. Behm, *Journal of Catalysis*, 2007, **250**, 139.

47. Tana, M. Zhang, J. Li, H. Li, Y. Li and W. Shen, *Catalysis Today*, 2009, **148**, 179.

48. N. Ta, J. Liu, S. Chenna, P. A. Crozier, Y. Li, A. Chen and W. Shen, *Journal of the American Chemical Society*, 2012, **134**, 20585.

49. J. Xu, J. Harmer, G. Li, T. Chapman, P. Collier, S. Longworth and S. C. Tsang, *Chemical Communications*, 2010, **46**, 1887.

50. Y. Lin, Z. Wu, J. Wen, K. Ding, X. Yang, K. R. Poeppelmeier and L. D. Marks, *Nano Letters*, 2015, **15**, 5375.

51. D. Andreeva, V. Idakiev, T. Tabakova, A. Andreev and R. Giovanoli, *Applied Catalysis a-General*, 1996, **134**, 275.

52. M. Boaro, M. Vicario, J. Llorca, C. de Leitenburg, G. Dolcetti and A. Trovarelli, *Applied Catalysis B-Environmental*, 2009, **88**, 272.

53. J. A. Rodriguez, *Catalysis Today*, 2011, **160**, 3.

54. J. Vecchietti, S. Collins, J. Jose Delgado, M. Malecka, E. del Rio, X. Chen, S. Bernal and A. Bonivardi, *Topics in Catalysis*, 2011, **54**, 201.

55. T. Tabakova, L. Ilieva, I. Ivanov, R. Zanella, J. W. Sobczak, W. Lisowski, Z. Kaszkur and D. Andreeva, *Applied Catalysis B-Environmental*, 2013, **136**, 70.

56. J. B. Park, J. Graciani, J. Evans, D. Stacchiola, S. Ma, P. Liu, A. Nambu, J. Fernandez Sanz, J. Hrbek and J. A. Rodriguez, *Proceedings of the National Academy of Sciences of the United States of America*, 2009, **106**, 4975.

57. D. Andreeva, I. Ivanova, L. Ilieva and M. V. Abrashev, *Applied Catalysis a-General*, 2006, **302**, 127.

58. K. Bakhmutsky, G. Zhou, S. Timothy and R. J. Gorte, *Catalysis Letters*, 2009, **129**, 61.

59. X. Wang and R. J. Gorte, *Applied Catalysis a-General*, 2003, **247**, 157.

60. N. L. Wieder, M. Cargnello, K. Bakhmutsky, T. Montini, P. Fornasiero and R. J. Gorte, *Journal of Physical Chemistry C*, 2011, **115**, 915.

61. D. W. Jeong, W. J. Jang, J. O. Shim, W. B. Han, H. S. Roh, U. H. Jung and W. L. Yoon, *Renewable Energy*, 2014, **65**, 102.

62. V. M. Shinde and G. Madras, *Applied Catalysis B-Environmental*, 2013, **138**, 51.

63. H. Daly, F. C. Meunier, R. Pilasombat, R. Burch, A. Goguet and C. Hardacre, *Abstracts of Papers of the American Chemical Society*, 2011, **241**.

64. A. Venugopal, J. Aluha and M. S. Scurrell, *Catalysis Letters*, 2003, **90**, 1.

65. M.-A. Hurtado-Juan, C. M. Y. Yeung and S. C. Tsang, *Catalysis Communications*, 2008, **9**.

66. T. Tabakova, F. B. Boccuzzi, M. Manzoli and D. Andreeva, *Applied Catalysis a-General*, 2003, **252**, 385.

67. R. Si, J. Tao, J. Evans, J. B. Park, L. Barrio, J. C. Hanson, Y. Zhu, J. Hrbek and J. A. Rodriguez, *Journal of Physical Chemistry C*, 2012, **116**, 23547.

68. X. Wang, J. A. Rodriguez, J. C. Hanson, M. Perez and J. Evans, *Journal of Chemical Physics*, 2005, **123**.

69. W. D. Williams, M. Shekhar, W.-S. Lee, V. Kispersky, W. N. Delgass, F. H. Ribeiro, S. M. Kim, E. A. Stach, J. T. Miller and L. F. Allard, *Journal of the American Chemical Society*, 2010, **132**, 14018.

70. N. Guo, B. R. Fingland, W. D. Williams, V. F. Kispersky, J. Jelic, W. N. Delgass, F. H. Ribeiro, R. J. Meyer and J. T. Miller, *Physical Chemistry Chemical Physics*, 2010, **12**, 5678.

71. M. Yang, L. F. Allard and M. Flytzani-Stephanopoulos, *Journal of the American Chemical Society*, 2013, **135**, 3768.

72. M. Flytzani-Stephanopoulos, *Accounts of Chemical Research*, 2014, **47**, 783.

73. M. Yang, S. Li, Y. Wang, J. A. Herron, Y. Xu, L. F. Allard, S. Lee, J. Huang, M. Mavrikakis and M. Flytzani-Stephanopoulos, *Science*, 2014, **346**, 1498.

74. B. Zugic, S. Zhang, D. C. Bell, F. Tao and M. Flytzani-Stephanopoulos, *Journal of the American Chemical Society*, 2014, **136**, 3238.

75. G. Bond, *Gold Bulletin*, 2009, **42**, 337.

76. D. Andreeva, *Gold Bulletin*, 2002, **35**, 82.

77. T. Tabakova, F. Boccuzzi, M. Manzoli, J. W. Sobczak, V. Idakiev and D. Andreeva, *Applied Catalysis a-General*, 2006, **298**, 127.

78. H. Sakurai, T. Akita, S. Tsubota, M. Kiuchi and M. Haruta, *Applied Catalysis a-General*, 2005, **291**.

79. G. Jacobs, E. Chenu, P. M. Patterson, L. Williams, D. Sparks, G. Thomas and B. H. Davis, *Applied Catalysis a-General*, 2004, **258**, 203.

80. R. Leppelt, B. Schumacher, V. Plzak, M. Kinne and R. J. Behm, *Journal of Catalysis*, 2006, **244**.

81. R. Burch, A. Goguet and F. C. Meunier, *Applied Catalysis a-General*, 2011, **409**, 3.

82. F. C. Meunier, D. Reid, A. Goguet, S. Shekhtman, C. Hardacre, R. Burch, W. Deng and M. Flytzani-Stephanopoulos, *Journal of Catalysis*, 2007, **247**, 277.

83. G. Jacobs, P. M. Patterson, U. M. Graham, A. C. Crawford and B. H. Davis, *International Journal of Hydrogen Energy*, 2005, **30**, 1265.

84. M. H. Ab Rahim, Q. He, J. A. Lopez-Sanchez, C. Hammond, N. Dimitratos, M. Sankar, A. F. Carley, C. J. Kiely, D. W. Knight and G. J. Hutchings, *Catalysis Science & Technology*, 2012, **2**.

85. L. Kesavan, R. Tiruvalam, M. H. Ab Rahim, M. I. bin Saiman, D. I. Enache, R. L. Jenkins, N. Dimitratos, J. A. Lopez-Sanchez, S. H. Taylor, D. W. Knight, C. J. Kiely and G. J. Hutchings, *Science*, 2011, **331**.

86. M. Sankar, E. Nowicka, R. Tiruvalam, Q. He, S. H. Taylor, C. J. Kiely, D. Bethell, D. W. Knight and G. J. Hutchings, *Chemistry-a European Journal*, 2011, **17**.

87. A. Hugon, L. Delannoy, J.-M. Krafft and C. Louis, *Journal of Physical Chemistry C*, 2010, **114**, 10823.

88. J. A. Lopez-Sanchez, N. Dimitratos, P. Miedziak, E. Ntainjua, J. K. Edwards, D. Morgan, A. F. Carley, R. Tiruvalam, C. J. Kiely and G. J. Hutchings, *Physical Chemistry Chemical Physics*, 2008, **10**.

89. J. Pritchard, L. Kesavan, M. Piccinini, Q. He, R. Tiruvalam, N. Dimitratos, J. A. Lopez-Sanchez, A. F. Carley, J. K. Edwards, C. J. Kiely and G. J. Hutchings, *Langmuir*, 2010, **26**, 16568.

90. E. Nowicka, J. P. Hofmann, S. F. Parker, M. Sankar, G. M. Lari, S. A. Kondrat, D. W. Knight, D. Bethell, B. M. Weckhuysen and G. J. Hutchings, *Physical Chemistry Chemical Physics*, 2013, **15**, 12147.

91. S. Meenakshisundaram, E. Nowicka, P. J. Miedziak, G. L. Brett, R. L. Jenkins, N. Dimitratos, S. H. Taylor, D. W. Knight, D. Bethell and G. J. Hutchings, *Faraday Discussions*, 2010, **145**, 341.

92. J. Feng, C. Ma, P. J. Miedziak, J. K. Edwards, G. L. Brett, D. Li, Y. Du, D. J. Morgan and G. J. Hutchings, *Dalton Transactions*, 2013, **42**, 14498.

93. N. Dimitratos, J. A. Lopez-Sanchez, D. Morgan, A. F. Carley, R. Tiruvalam, C. J. Kiely, D. Bethell and G. J. Hutchings, *Physical Chemistry Chemical Physics*, 2009, **11**, 5142.

94. L. Ouyang, G.-j. Da, P.-f. Tian, T.-y. Chen, G.-d. Liang, J. Xu and Y.-F. Han, *Journal of Catalysis*, 2014, **311**, 129.

95. J. K. Edwards, B. E. Solsona, P. Landon, A. F. Carley, A. Herzing, C. J. Kiely and G. J. Hutchings, *Journal of Catalysis*, 2005, **236**.

96. Y. F. Han, J. H. Wang, D. Kumar, Z. Yan and D. W. Goodman, *Journal of Catalysis*, 2005, **232**, 467.

97. C. Y. Ma, X. H. Li, M. S. Jin, W. P. Liao, R. G. Guan and Z. H. Suo, *Chinese Journal of Catalysis*, 2007, **28**, 535.

98. K. Qian and W. Huang, *Catalysis Today*, 2011, **164**, 320.

99. M. M. Schubert, S. Hackenberg, A. C. van Veen, M. Muhler, V. Plzak and R. J. Behm, *Journal of Catalysis*, 2001, **197**, 113.

100. M. Comotti, W. C. Li, B. Spliethoff and F. Schuth, *Journal of the American Chemical Society*, 2006, **128**, 917.

101. A. M. Venezia, L. F. Liotta, G. Pantaleo, V. La Parola, G. Deganello, A. Beck, Z. Koppany, K. Frey, D. Horvath and L. Guczi, *Applied Catalysis a-General*, 2003, **251**, 359.

102. A. Beck, A. Horvath, Z. Schay, G. Stefler, Z. Koppany, I. Sajo, O. Geszti and L. Guczi, *Topics in Catalysis*, 2007, **44**, 115.

103. B. Zhu, G. Thrimurthulu, L. Delannoy, C. Louis, C. Mottet, J. Creuze, B. Legrand and H. Guesmi, *Journal of Catalysis*, 2013, **308**, 272.

104. J. A. Lopez-Sanchez, N. Dimitratos, N. Glanville, L. Kesavan, C. Hammond, J. K. Edwards, A. F. Carley, C. J. Kiely and G. J. Hutchings, *Applied Catalysis a-General*, 2011, **391**, 400.

105. H. C. Ham, J. A. Stephens, G. S. Hwang, J. Han, S. W. Nam and T. H. Lim, *Journal of Physical Chemistry Letters*, 2012, **3**, 566.

106. F. Gao, Y. Wang and D. W. Goodman, *Journal of the American Chemical Society*, 2009, **131**, 5734.

107. M. Date, M. Okumura, S. Tsubota and M. Haruta, *Angewandte Chemie-International Edition*, 2004, **43**, 2129.

108. M. Date and M. Haruta, *Journal of Catalysis*, 2001, **201**, 221.

109. M. A. Saqlain, A. Hussain, M. Siddiq and A. A. Leitao, *Rsc Advances*, 2015, **5**, 47066.

110. L. Delannoy, S. Giorgio, J. G. Mattei, C. R. Henry, N. El Kolli, C. Methivier and C. Louis, *Chemcatchem*, 2013, **5**, 2707.

111. X. Shao, S. Prada, L. Giordano, G. Pacchioni, N. Nilius and H.-J. Freund, *Angewandte Chemie-International Edition*, 2011, **50**, 11525.

112. M. Sterrer, T. Risse, M. Heyde, H.-P. Rust and H.-J. Freund, *Physical Review Letters*, 2007, **98**.

113. D. Ricci, A. Bongiorno, G. Pacchioni and U. Landman, *Physical Review Letters*, 2006, **97**.

114. N. Mammen, S. Narasimhan and S. de Gironcoli, *Journal of the American Chemical Society*, 2011, **133**, 2801.

115. N. Mammen, S. de Gironcoli and S. Narasimhan, *Journal of Chemical Physics*, 2015, **143**.

116. P. Fornasiero, G. Balducci, R. DiMonte, J. Kaspar, V. Sergo, G. Gubitosa, A. Ferrero and M. Graziani, *Journal of Catalysis*, 1996, **164**, 173.

117. J. A. Rodriguez, in *Catalysis by Ceria and Related Materials*, eds. A. Trovarelli and P. Fornasiero, Imperial College Press, 2nd edn., 2013, vol. 12, ch. 4, pp. 465-498.

118. S. Rico-Frances, E. O. Jardim, T. A. Wezendonk, F. Kapteijn, J. Gascon, A. Sepulveda-Escribano and E. V. Ramos-Fernandez, *Applied Catalysis B-Environmental*, 2016, **180**, 169.

119. J. A. Rodriguez, R. Si, J. Evans, W. Xu, J. C. Hanson, J. Tao and Y. Zhu, *Catalysis Today*, 2015, **240**, 229.

120. S. S. Kim, S. M. Lee, J. M. Won, H. J. Yang and S. C. Hong, *Chemical Engineering Journal*, 2015, **280**, 433.

121. M. S. P. Francisco, V. R. Mastelaro, P. A. P. Nascente and A. O. Florentino, *Journal of Physical Chemistry B*, 2001, **105**, 10515.

122. J. B. Park, J. Graciani, J. Evans, D. Stacchiola, S. D. Senanayake, L. Barrio, P. Liu, J. F. Sanz, J. Hrbek and J. A. Rodriguez, *Journal of the American Chemical Society*, 2010, **132**.

123. J. Miranda-Sanchez, I. Elizalde, L. Lartundo-Rojas, I. Hernandez-Perez, D. Jaramillo-Vigueras and R. Ramirez-Lopez, *Journal of Sol-Gel Science and Technology*, 2015, **74**, 707.

124. L. Ilieva, G. Pantaleo, J. W. Sobczak, I. Ivanov, A. M. Venezia and D. Andreeva, *Applied Catalysis B-Environmental*, 2007, **76**, 107.

125. L. Ilieva, G. Pantaleo, I. Ivanov, A. M. Venezia and D. Andreeva, *Applied Catalysis B-Environmental*, 2006, **65**, 101.

126. D. Andreeva, I. Ivanov, L. Ilieva, J. W. Sobczak, G. Avdeev and T. Tabakova, *Applied Catalysis a-General*, 2007, **333**, 153.

127. D. Andreeva, I. Ivanov, L. Ilieva, J. W. Sobczak, G. Avdeev and K. Petrov, *Topics in Catalysis*, 2007, **44**, 173.

128. T. Seiyama, *New horizons in catalysis: Proceedings of the 7th International Congress on Catalysis, Tokyo, 30 June-4 July 1980 (Studies in surface science and catalysis)*, Elsevier, 2000.

129. T. R. Reina, S. Ivanova, M. A. Centeno and J. A. Odriozola, *Catalysis Today*, 2015, **253**, 149.

130. D. Andreeva, I. Ivanov, L. Ilieva, M. V. Abrashev, R. Zanella, J. W. Sobczak, W. Lisowski, M. Kantcheva, G. Avdeev and K. Petrov, *Applied Catalysis a-General*, 2009, **357**, 159.

131. E. Smolentseva, A. Simakov, S. Beloshapkin, M. Estrada, E. Vargas, V. Sobolev, R. Kenzhin and S. Fuentes, *Applied Catalysis B-Environmental*, 2012, **115**, 117.

Chapter 2

Experimental

This chapter outlines the experimental methods used in this thesis. Catalyst preparation methods are explained, including the chemicals and their suppliers. In addition, the characterisation methods and the principles that govern them are described. The catalyst testing methods and reactor set-ups are also outlined.

2.1. List of chemicals

The following is a list of the chemicals used in this work, including the suppliers and the purity of the substances.

Table 2.1 List of chemicals used

Substance	Supplier	Purity
$Ce(NO_3)_3.6H_2O$	Sigma Aldrich	99.99%
$ZrO(NO_3)_2.xH_2O$	Sigma Aldrich	99.99%
NH_4OH	Fisher Scientific	28-30 w/w% in water
Na_2CO_3	Sigma Aldrich	>99.0%
$(NH_4)_6Mo_7O_{24}{\cdot}_4H_2O$	Sigma Aldrich	99.98%
$Al[OCH(CH_3)_2]_3$	Sigma Aldrich	>98%
$Ti[OCH(CH_3)_2]_4$	Sigma Aldrich	>97%
$HAuCl_4$	Alfa Aesar	99.99%
$PdCl_2$	Sigma Aldrich	99%
TiO_2 (P25)	Degussa	>99.5%
$CeZrO_4$	(Solvay)	>99%
CO_2	BOC	>99.99%
H_2	BOC	>99.9%
HPLC grade H_2O	Fisher Scientific	-
CO	BOC	>99.997%
N_2	BOC	>99.99%
5000 ppm CO/air	BOC	-

2.2. Catalyst preparation

This section describes the various methods of catalyst preparation that were used in this thesis.

2.2.1. Preparation of $CeZrO_4$ and molybdenum-doped $CeZrO_4$ by sol-gel

$CeZrO_4$ mixed-metal oxides were prepared by a sol-gel method previously reported.[3] In a typical preparation, appropriate molar quantities of $Ce(NO_3)_3.6H_2O$ and $ZrO(NO_3)_2.xH_2O$ were added to deionised water (300 cm^3) at 80 ^oC, whilst stirring vigorously on a hotplate, in order to give the desired 1:1 molar ratio of Ce:Zr. Once the metal precursors had dissolved, NH_4OH (0.5M) was added drop-wise until the pH reached 9. The reaction mixture was then immediately filtered under vacuum and washed with warm distilled water (600 cm^3) before being left to dry in an oven overnight at 110 ^oC. The resultant solid was ground using a mortar and pestle and then calcined under flowing air at 500 ^oC for 5 hours using a ramp rate of 10 $^oC\ min^{-1}$. The final product was pale yellow in colour. A scheme showing the preparation of the $CeZrO_4$ is shown below in Scheme 2.1.

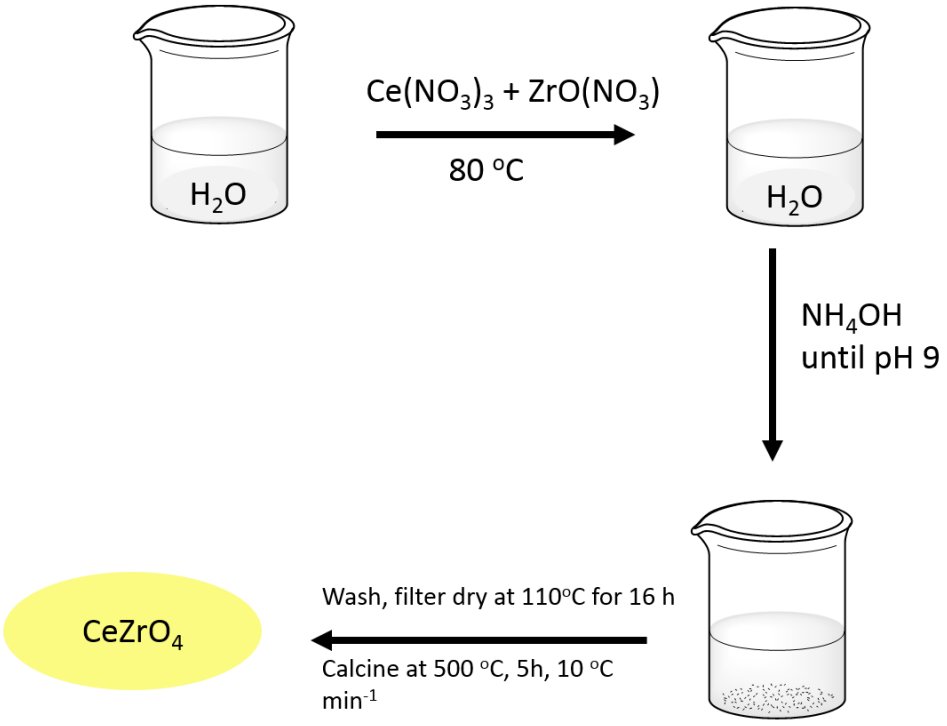

Scheme 2.1 Depiction of sol-gel preparation of $CeZrO_4$

Molybdenum-doped $CeZrO_4$ was prepared through the standard sol-gel route but with the addition of the appropriate amount of $(NH_4)_6Mo_7O_{24}{\cdot}_4H_2O$ with the Ce and Zr metal precursors, to give nominal loadings of 0.1, 1, 2 and 5 wt% Mo-doped $CeZrO_4$.

2.2.2. Preparation of $CeMO_x$ using an ethanoic sol-gel method (where M=Ti or Al)

$Ce_{0.5}Ti_{0.5}O_x$ and $Ce_{0.5}Al_{0.5}O_x$ supports were prepared using a sol-gel method with ethanol as the solvent.[4] The appropriate amount of $Ce(NO_3)_3.6H_2O$ was dissolved in ethanol (150 cm^3). The drop-wise addition of the appropriate amount of M-iso-propoxide precursor ($Al[OCH(CH_3)_2]_3$ or $Ti[OCH(CH_3)_2]_4$) was then carried out before NH_4OH (2M) was also added drop-wise until the pH reached 9. The temperature of the reaction mixture was increased to ~75 ^oC to remove the ethanol. Typically this process lasted for 30 minutes. The reaction mixture was then filtered and washed under vacuum with deionised water (500 cm^3) before being dried overnight in an oven at 110 ^oC. The resulting solid was ground using a mortar and pestle and calcined at 450 ^oC for 5 hours with a ramp rate of 10 $^oC\ min^{-1}$. A typical synthesis of a $Ce_{1-x}Ti_xO_2$ support is presented below in Scheme 2.2.

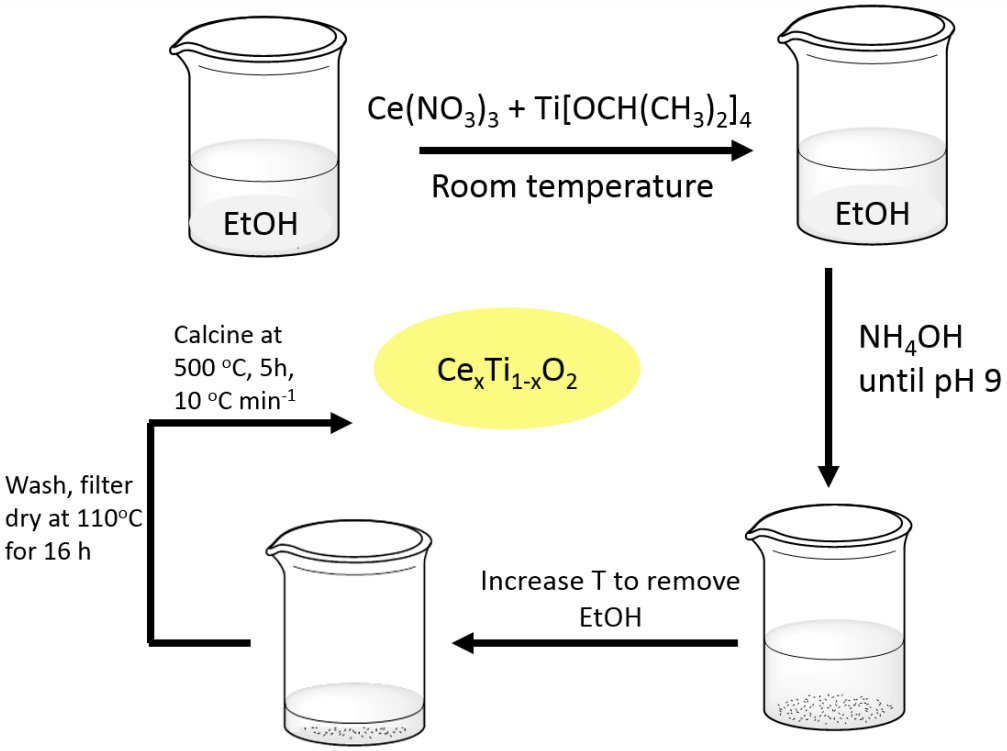

Scheme 2.2 Ethanoic sol-gel preparation of $Ce_{1-x}Ti_xO_2$ catalyst support

For materials where M=Ti, a range of materials was made with different molar ratios, and was denoted as $Ce_xTi_{1-x}O_2$, where x = 0, 0.1, 0.2, 0.5, 0.8 and 0.9 and 1. Table 2.2 below shows the amounts and concentrations used in each preparation.

Table 2.2 Preparation details for preparation of $Ce_aTi_{1-a}O_x$ materials

Sample	Mass of precursor used		Moles of metal used	
	Cerium nitrate (g)	Titanium iso-propoxide (g)	Ce	Ti
CeO_2	8.65	0	0.020	0.000
$Ce_{0.9}Ti0_{.1}O_x$	7.785	0.568	0.018	0.002
$Ce_{0.8}Ti_{0.2}O_x$	6.92	1.136	0.016	0.004
$Ce_{0.5}Ti_{0.5}O_x$	4.325	2.84	0.010	0.010
$Ce_{0.2}Ti_{0.8}O_x$	1.73	4.544	0.004	0.016
$Ce_{0.1}Ti_{0.}$ x	0.865	5.112	0.002	0.018
TiO_2	0	5.68	0.000	0.020

For the TiO_2 support, it was necessary to acidify the reaction mixture using a few drops of concentrated HNO_3 (70%, Fisher) in order to ensure the Ti-precursor stayed in solution before the addition of NH_4OH.

2.2.3. Deposition-precipitation (DP) of precious metals onto a support

DP is a versatile and widely used method that can be used to deposit small nanoparticles of a metal onto a support.[5] In a typical experiment, an aqueous solution of the metal precursor ($HAuCl_4$ and/or $PdCl_2$) was added to deionised water at 60 ^oC. Then the appropriate quantity of support was added before Na_2CO_3 (0.05 M) was added drop-wise until the pH reached 8. The reaction mixture was then stirred for one hour before being filtered under vacuum and washed with deionised water (600 cm^3). The catalyst was dried by placing it in an oven at 110 ^oC for 5 hours. A typical preparation is shown below in Scheme 2.3.

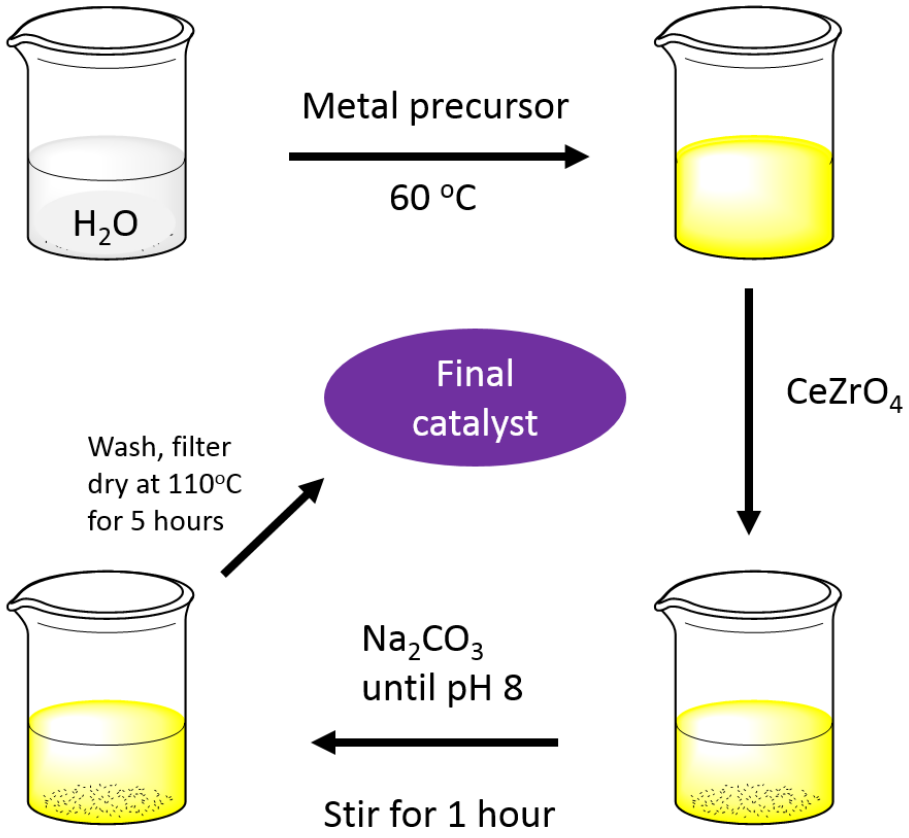

Scheme 2.3 Deposition-precipitation method for the preparation of $Au/CeZrO_4$

2.3. Catalyst characterisation

2.3.1. Powder x-ray diffraction (XRD)

XRD is an important method of structural characterisation, allowing information regarding the crystal structure and crystallite size of a solid sample. When incident x-rays are directed at a powder sample, the photons are diffracted at angles characteristic of well-defined lattice parameters. In order for diffraction peaks to be generated, constructive interference of x-rays must occur. This happens when the distance between scatters i.e. the distance travelled by an x-ray is an integer of its wavelength. This is illustrated Figure 2.1. In a powder sample, where the crystals are aligned randomly, there is a sufficient degree of the sample that is orientated for constructive interference to occur, hence why powder samples are able to give well-defined x-ray diffractograms.[1] Using the Bragg equation the d-spacing can be calculated as follows:

$$n\lambda = 2dsin\theta$$

Where n = the order of reflection (an integer), λ = wavelength of the x-rays, d =the distance between two lattice planes (Å) and θ = angle of the incident x-rays relative to the normal reflecting lattice plane.

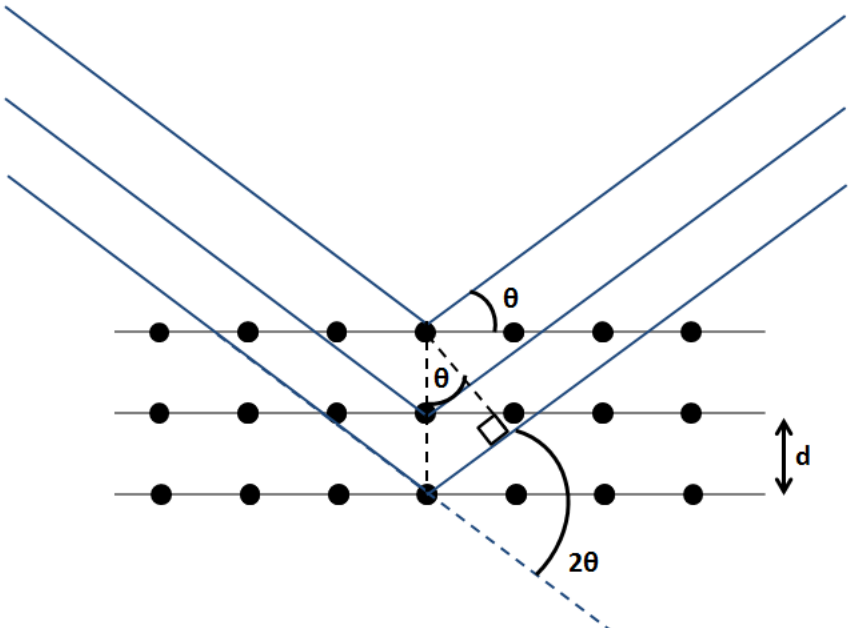

Figure 2.1 Illustration of diffraction of X-rays through a solid

This can then be used to calculate the lattice parameter of a material using a further equation that relates to the crystal system of the sample of interest. In the case of cubic CeO_2, it can be calculated thus:

$$\frac{1}{d^2} = \frac{h^2 + k^2 + l^2}{a^2}$$

Where d = d-spacing (Å), h,k and l = corresponding miller indices for d-spacing reflection and a = lattice parameter (Å).

The lattice parameter, or lattice constant is a measurement of the dimensions of a unit cell of a solid. Modification of the lattice parameter can indicate the presence of another component in a material and is therefore an important parameter to measure. A requirement of XRD is crystallinity, or long-range order. Larger crystallites give more narrow, sharper reflections in a diffractogram but for particles that are below approximately 100 nm in size, line broadening of these reflections occurs due to incomplete destructive interference of out of phase x-rays.[2]

This phenomenon allows information regarding the size of crystallites to be obtained using the Scherrer equation, shown below:

$$< L >= \frac{K\lambda}{\beta cos\theta}$$

Where < L > = dimension of the particle in the direction perpendicular to the reflecting plane, K = constant (usually 1), λ = wavelength of the x-rays, β = peak width and θ = angle of the incident x-rays relative to the normal reflecting lattice plane.

Although XRD cannot accurately determine the sizes of small nanoparticles or elucidate the surface structure of catalysts, this method of characterisation is essential for the determination of structural properties of catalytic materials greater than 3 nm.

Experimental

Powder X-ray diffraction (PXRD) was performed on an X'PertPRO PANalytical instrument. A Cu K_α (1.54Å) radiation source with a nickel filter, calibrated against a Si standard was used. Wide angle measurements were taken in the range of 2θ = 10 – 80°. Approximately 0.3 g of sample was required for each experiment.

2.3.2. N_2 physisorption

N_2 physisorption is an essential tool when characterising materials such as catalyst supports. A specific surface area measurement was taken for each catalyst support that was synthesised. The technique is based on the adsorption of N_2 and described below.

Physisorption is a slightly exothermic process, governed by Van der Waals' interactions and occurs over mono- and multi-layers of adsorbates. It is used to discern the total surface area of a material and does not discriminate between the active phase of a supported catalyst (such as metal nanoparticles) and the catalytically inert support itself. This is exploited in N_2 physisorption by generating an adsorption isotherm of N_2 at very low temperatures.

Isotherms are recorded by measuring the quantity of N_2 adsorbed at different pressures, and the shape of the resultant isotherm can reveal a great deal about the solid sample. Figure 2.2 shows the six adsorption isotherms exhibited by different

types of materials. Typically, Type I is indicative of monolayer-only adsorption.[2] Type II shows further adsorption after a monolayer has formed, indicating multi-layer formation that is indicative of a material with a large distribution of pore sizes.[2] Type III indicates multi-layer formation of the adsorbate without a well-defined monolayer and is not typically observed for N_2 adsorption on catalyst surfaces. Type IV is related to Type II but shows finite multi-layer formation, indicating the complete filling of pores.[2] This is exhibited by mesoporous materials. Type V is a similar to Type IV, but without the formation of a monolayer. Finally, Type VI occurs when the temperature of the analysis is near the melting point of the adsorbed gas and are characteristic of non-porous materials with a homogeneous surface.[2]

Point B is the point where saturation of the surface occurs and multi-layer adsorption proceeds. Application of the Brunauer–Emmett–Teller (BET) method to deduce the surface area of the support typically takes place at pressures up until this point of inflection.

The BET equation is given below:

$$\frac{P}{V_a(P_0 - P)} = \frac{1}{V_m C} + \frac{C - 1}{V_m C}\left(\frac{P}{P_0}\right)$$

Where P = pressure, P_0 = saturation pressure, V_a = volume of gas adsorbed, V_m = volume of monolayer, and C = multilayer adsorption parameter.

The surface area can then be determined as follows:

$$s.a. = \frac{V_m \sigma N_a}{mv}$$

Where σ = moleculer area of N_2 (0.162 nm^2), N_a = Avogadro's number, m = mass of sample, v = molar volume of gas.

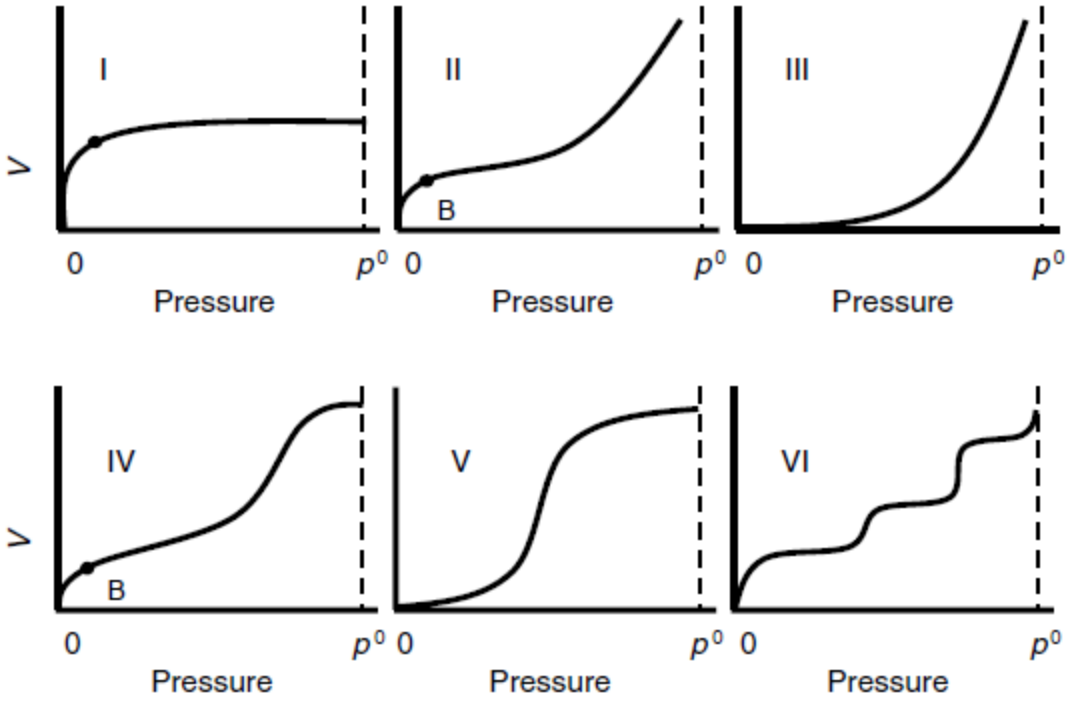

Figure 2.2 Six adsorption isotherms that arise from different pore architectures.[1]

Experimental

Nitrogen porosimetry was performed at -196 °C on a Quantachrome Quadrasorb SI instrument after each sample was evacuated for 2 h at 120 °C. Surface areas were calculated using Brunauer–Emmet–Teller (BET) theory over the range P/P_0 = 0.05-0.2.

2.3.3. H_2-Temperature-programmed reduction (TPR)

TPR is a widely-used characterisation method that allows precise determination of the temperature of reduction to be measured, which in turn can be used to extract kinetic information and infer other properties of a catalyst. Typically, the sample is exposed to H_2 gas and the temperature is increased over time and the instrument measures the consumption of the gas as a function of temperature[6] by a thermal conductivity detector (TCD) as shown in Scheme 2.4 or by a mass spectrometer. This methodology allows different reduction processes (e.g. surface and bulk reduction of a metal oxide) to be distinguished and quantified.

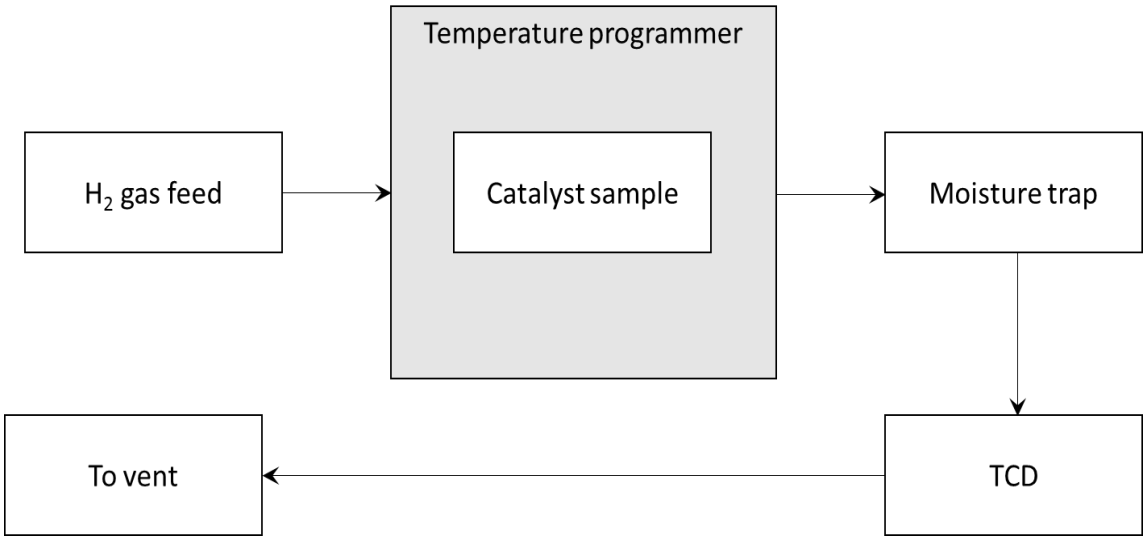

Scheme 2.4 Typical TPR set-up featuring a TCD as the analysis method

H_2-TPR can give vital information pertaining to the redox properties of a catalyst support, an important parameter of water-gas shift catalyst supports.[7] Quantification of the H_2 consumption in a TPR trace can enable the calculation of the stoichiometry of the starting oxide[2] as well as indirect information regarding the metal dispersion of a supported metal catalyst.

Experimental

H_2-TPR was carried out on a Thermo TPRO 1100 instrument. The gas feed was 10% H_2/Ar, which was fed in at 50 ml min^{-1} and the temperature was increased up to 800 ^oC at a ramp rate of 10 ^oC min^{-1} after pre-treatment at 110 ^oC in Ar for 45 minutes. In each experiment, 0.050 g of catalyst was used, which was placed in a quartz tube between two pieces of quartz wool.

2.3.4. X-ray photoelectron spectroscopy (XPS)

XPS is an important characterisation tool in catalysis for gaining information on the surface of a sample. It enables the determination of the elemental composition of a solid surface as well as the identification of the oxidation states of the elements within the sample and can even show evidence of metal alloying in nanocrystals.[8] The basis of XPS is the photoelectric effect, which is depicted in Figure 2.3.[2] In an XPS experiment, the sample being analysed absorbs an x-ray photon and a photo-electron is emitted. The kinetic energy of this electron can be measured and the binding energy calculated. The hole left by the emitted electron leaves an excited ionised atom, which relaxes through the filling of the core hole by an electron from a higher shell. Consideration of

the work function of each metal and the relative sensitivity factors enables quantitative information to be sought. Due to the short mean free path of electrons in solids, XPS is described as a surface sensitive technique, although in actual fact, the first twenty atomic layers can be probed, depending on the experimental parameters.[1] The binding energy is calculated by using the equation:

$$E_k = hv - E_b - \varphi$$

Where E_k = kinetic energy, h = Planck's constant, v = frequency of exciting electron, E_b = binding energy and φ = work function of the spectrometer.

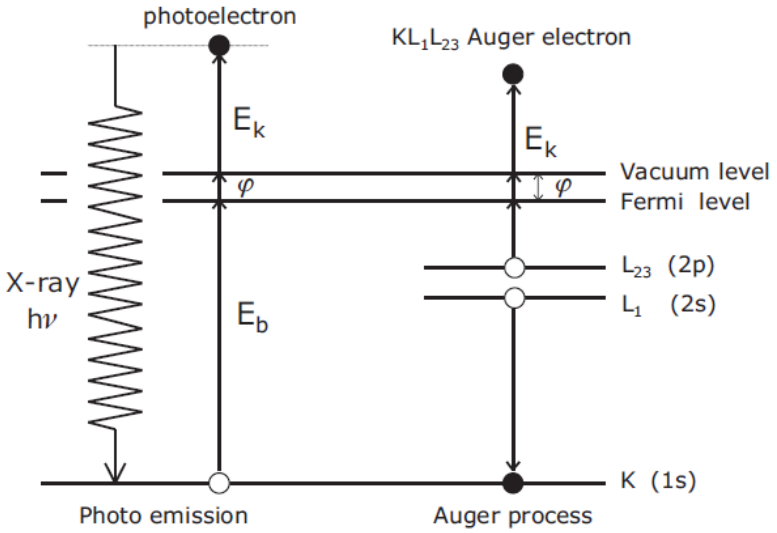

Figure 2.3 The photoemission of an electron.

Each binding energy is characteristic of the element that the photo-electron originates from. This gives specific peaks in an XP spectrum that can be used to identify and quantify which elements are present in the sample and what oxidation state they are in. This is because the binding energy is dependent on numerous factors, referred to as either initial state effects (caused by the atom before photoemission) or final state effects (caused by the response of the core-ionised atom after photoemission).[2] In supported catalysis, the binding energy of a given XPS feature will be determined by both of these effects. The binding energy can then be used to determine the oxidation states present, evidence of alloying[8] and an indication of relative metal particle sizes of a supported metal.[9]

Furthermore, XPS can be used to infer information regarding the dispersion of the supported metal catalyst. This can be achieved by measuring the ratio of the supported metal concentration and the support concentration, C_m/C_s. Well dispersed metals will show a higher ratio, whereby more of the supported metal is detectable by XPS. Conversely, poorly dispersed metals will show a relatively low C_m/C_s as more of the supported metal is inaccessible to detection by XPS. This of course requires that the same number of moles of metal is on the surface of each catalyst.

Experimental

Measurements were made on a Kratos Axis Ultra-DLD XPS spectrometer, Figure 2.4, equipped with an AlKα X-ray 300 W source by Dr David Morgan, Cardiff University. The binding energies were standardised against a C 1s reference (284.7 eV). Peaks were fitted as Gaussian Lorentzian curves GL(30) using CasaXPS software. All spectra were fitted with Shirley backgrounds with the exception of the Ce 3d spectrum, which was fitted using a U Tougaard background.

Figure 2.4 Kratos Axis Ultra-DLD XPS spectrometer

2.3.5. Diffuse-reflectance Fourier-transform infrared spectroscopy (DRIFTS)

Infrared (IR) spectroscopy is a versatile tool for probing different properties of materials, particularly surface adsorption sites. In this work, carbon monoxide was used as a probe molecule to elucidate information regarding the adsorption sites of various catalysts. This method of characterisation is referred to as CO-DRIFTS. The general principles of infrared spectroscopy are described below, as well as the the concept of Fourier Transform spectroscopy and diffuse reflectance spectroscopy.

The basis of infrared spectroscopy exploits the fact that molecules possess discrete levels of vibrational and rotational energy, which are related to their structure. Photons are absorbed by a molecule or functional group with the same energy to the incident photons, so the vibrations are resonant. Adsorption of IR radiation (1–1000 mm or 10,000–10 cm^{-1}) therefore reveals structural information about the sample. In order for a sample to be "IR active" the vibration of the molecule must result in a change in the dipole moment. In a symmetrical diatomic molecule such as hydrogen or nitrogen there is no change in the dipole moment and they are said to be IR inactive.

A Fourier transform (FT) is a mathematical operation widely used in spectroscopic characterisation that has greatly increased the power of IR spectroscopy. Conventional spectrometers use one wavelength of light sequentially and measure the absorbance or reflectance at a given wavelength. FT spectrometers use a light source of multiple wavelengths. These enter a Michelson interferometer, a configuration of mirrors that enables each wavelength of the beam to be transmitted and blocked, periodically. This occurs due to wave interference which is modulated by a moving mirror. The FT is used to generate a spectrum from the interferogram collected using the Michelson interferometer. A diagram of a Michelson interferometer is shown below in Figure 2.5.[10]

The development of diffuse-reflectance methodologies have enabled powders to be easily analysed with no sample preparation other than filling the sample well with the desired material. Ellipsoidal mirrors mounted above the sample concentrate scattered photons from a wide range of angles toward the detector.

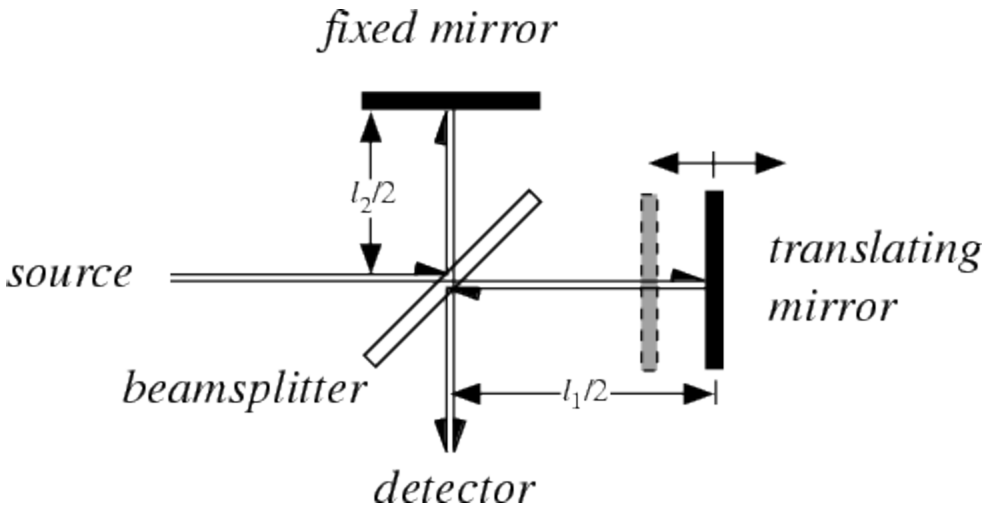

Figure 2.5 Diagram of a Michelson interferometer in a typical FTIR set-up

Experimental

DRIFTS measurements were taken on a Bruker Tensor 27 spectrometer fitted with a mercury cadmium telluride (MCT) detector and ZnSe windows. A sample was loaded into the Praying Mantis high temperature (HVC-DRP-4) *in situ* cell before exposure to N_2 and then 1% CO/N_2 at a flow rate of 50 cm^3 min^{-1}. A background was obtained using KBr and measurements were recorded every minute at room temperature. Once the CO adsorption bands in the DRIFT spectra ceased to change, the gas feed was changed back to N_2 and measurements were made until no change in subsequent spectra was observed. Unless stated otherwise, all catalysts were analysed in this way.

2.3.6. Raman spectroscopy

Raman spectroscopy is a form of vibrational spectroscopy similar to IR spectroscopy. When incident radiation comes into contact with a sample, it can be absorbed, transmitted or scattered. Raman spectroscopy exploits the inelastic scattering of photons, known as Raman scattering. This is equivalent to an energy change, or a shift in the frequency of the scattered radiation compared to incident radiation. The shift can be positive or negative, depending on whether there is an energy gain or loss. If a molecule gains energy, it is known as Stokes scattering while a loss in energy is termed anti-stokes scattering. If there is no energy change, this is elastic scattering, also known as Rayleigh scattering. A summary of these energetic processes is given in Figure 2.6, below.

Also featured in Figure 2.6 is fluorescence. This is an undesirable process that can occur when a sample is illuminated with a laser of a frequency that promotes electrons to an excited electronic state that decays over multiple transitions to the ground state. This can occur over the entire Raman spectrum and obscure or hide Raman features.

There are requirements for a molecule to be Raman active, known as selection rules. While In IR spectroscopy the molecule must have a change in the dipole moment, in Raman spectroscopy there must be a change in the polarizability. This relates to how the electronic structure in a molecule deforms in an electric field. Symmetrical molecules can be Raman active, but not IR active.

Only a very small fraction of the photons that are present are due to Raman scattering and so an extremely sensitive detector is needed for this. A charge coupled device (CCD) is a suitable detector, which is made of a semiconductor. Electrodes on the surface of the CCD transfer electronic charge from one side of the semiconductor to the other. The intensity of the charge is proportional to the photons that are detected and therefore can be used quantitatively.

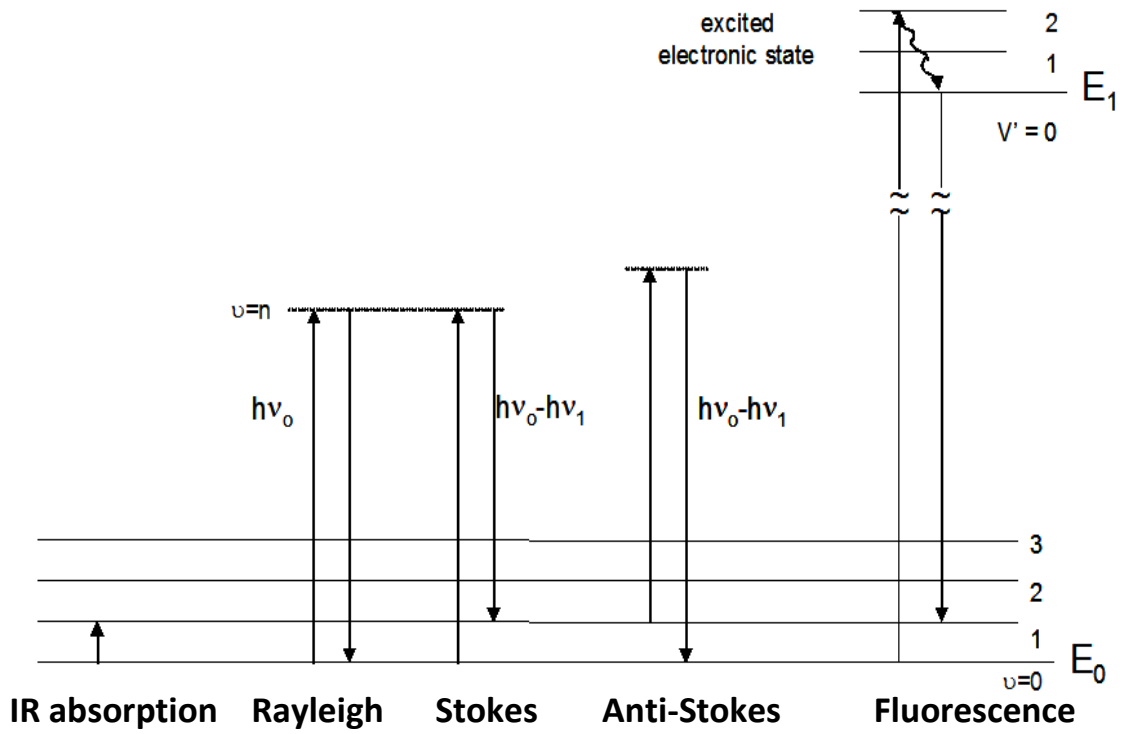

Figure 2.6 Scheme showing vibrational energetic processes, where υ represent vibrational energy levels.

Experimental

Raman spectroscopy was carried out using a Renishaw ramascope using spectrophysics 514 nm HeNe laser at a power of 20 mW. Spectra were obtained in the region of 500-2000 cm^{-1}. Approximately 50 mg of sample was used.

2.3.7. Microwave plasma atomic emission spectroscopy (MP-AES)

Microwave plasma atomic emission spectroscopy (MP-AES) is a powerful tool for conducting elemental analysis of catalyst samples. In this application, a nitrogen plasma is used to excite and vaporise the atoms in a liquid sample. This causes the electrons in the sample to go from a ground state to an excited state. When the atoms relax, a specific quantum of energy is released, in the form of photons. These have a wavelength that is characterised by the element of origin.

The photons are detected by a charge-coupled device (CCD). Each wavelength is analysed sequentially, which although increases the time per sample, achieves very high sensitivity.

This method also allows multiple wavelengths pertaining to the same element to be quantified – this reduces the possibility of interference from other elements that have similar emission wavelengths. The diagram in Scheme 2.5 shows a depiction of the MP-AES methodology, while Figure 2.7 shows a photograph of the instrument.

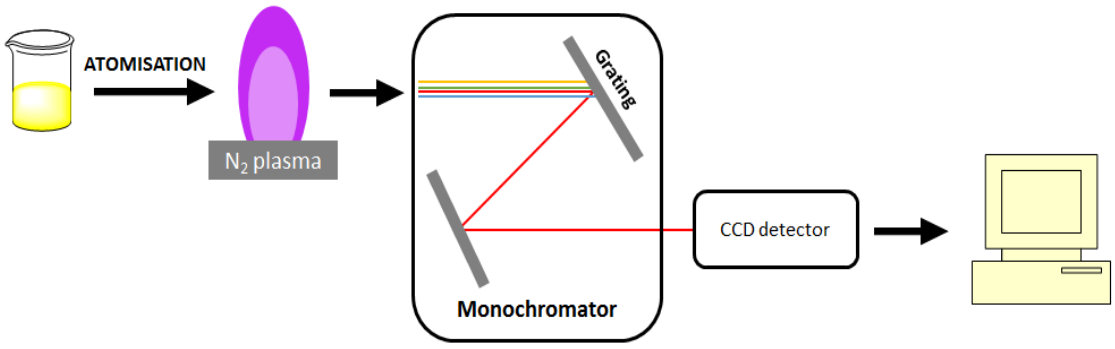

Scheme 2.5 Processes involved in the MP-AES methodology

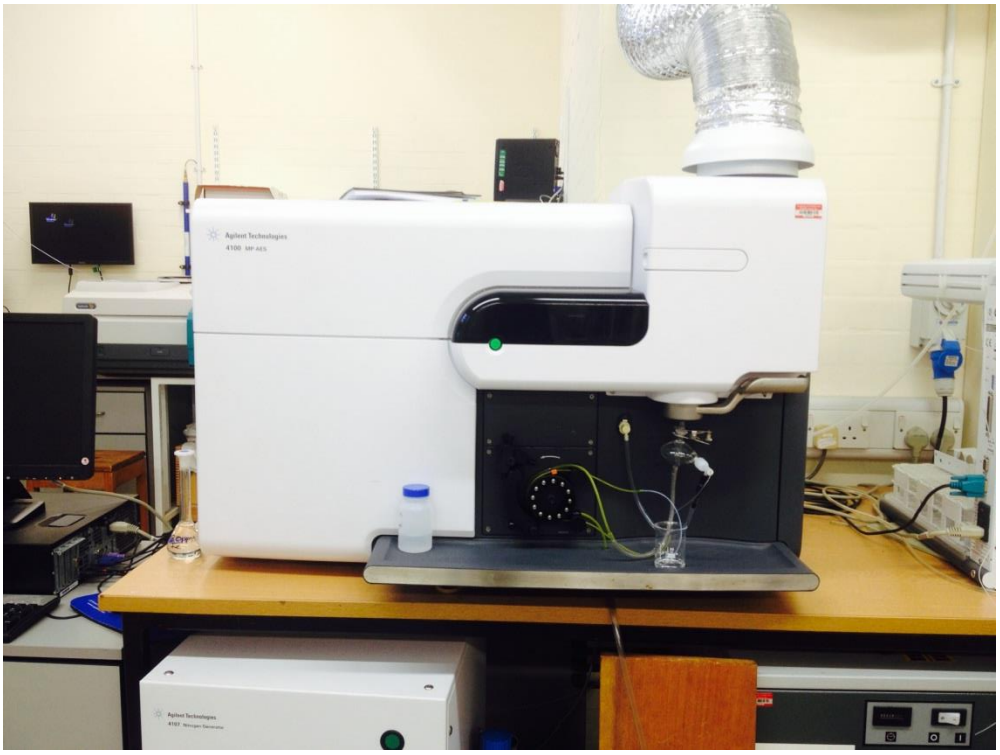

Figure 2.7 Agilent 4100 MP-AES instrument

Experimental

The metal loadings of the catalysts were determined using an Agilent 4100 MP-AES spectrometer equipped with a nitrogen plasma. The catalyst sample (50 mg) was digested in *aqua regia* (4 cm^3) overnight and the sample was diluted in deionised water up to a total volume of 50 cm^3. Any remaining solids were filtered before analysing the final solution.

2.3.8. Thermo-gravimetric analysis (TGA)

TGA is a widely used characterisation tool that involves precisely measuring the mass of a sample as it is exposed to a specific environment. This can involve different gas environments and temperature programs. For example, the change in the physical or chemical state of a sample can be measured as temperature is increased under an oxidising environment. This type of analysis can be used to model calcination procedures and establish when the decomposition of a sample has taken place. Typically, the data is represented as mass loss as a function of temperature, allowing identification of water desorption, complete decomposition or reduction temperatures to be identified. In this work it was briefly used as a tool to establish an appropriate calcination program. In some applications, TGA can be coupled with IR spectroscopy or

mass spectrometry to identify and quantify desorption products. Furthermore, when the TGA analysis is carried out with an inert reference, the heat change can be measured in the sample relative to the reference. This is known as differential thermal analysis, DTA. DTA allows determination of whether a process is an exo- or endo-thermic one and enables further insights to be made. Scheme 2.6 shows a typical set-up for a TGA instrument.

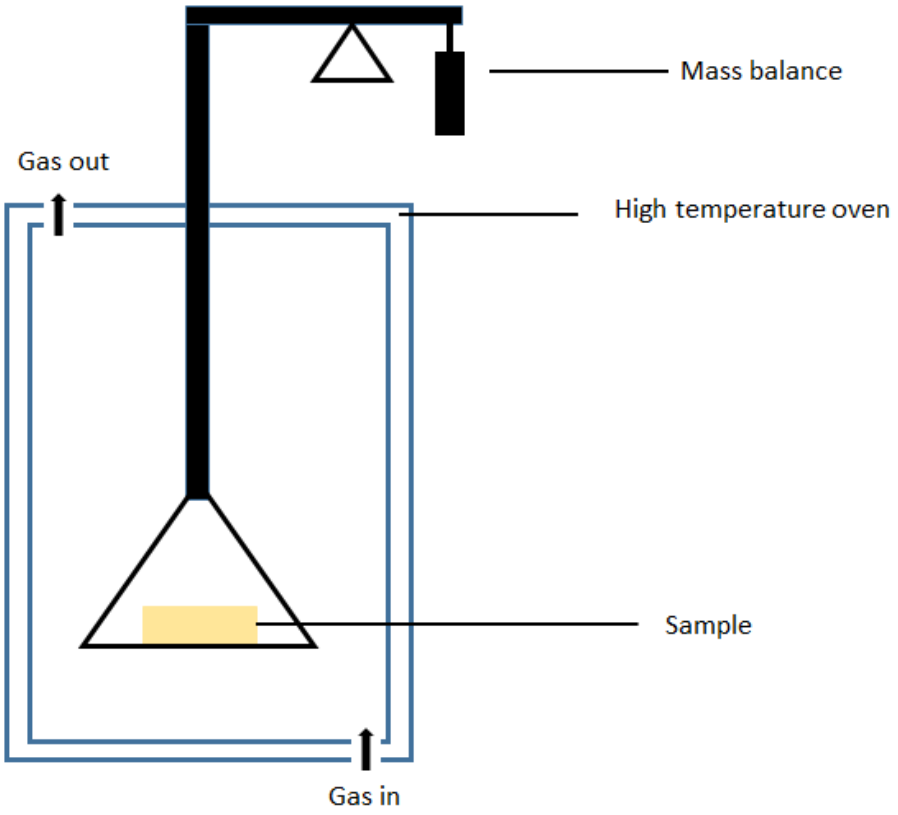

Scheme 2.6 Set-up of typical TGA instrument

Experimental

TGA analysis was carried out on a Perkin Elmer TGA 4000. Approximately 50 mg of catalyst was used. The samples were heated up to 800^{o}C at a ramp rate of 30 ^{o}C min^{-1} under 20 ml min^{-1} of flowing air.

2.3.9. Electron microscopy

Electron microscopy covers a range of techniques including scanning electron microscopy (SEM) and transmission electron microscopy (TEM). Both of these techniques exploit the fact that electrons have characteristic wavelengths below 1 Å. While the resolution of conventional optical microscopes is limited to hundreds of nanometres, electron microscopes can achieve atomic resolution. Figure 2.8 below

depicts the Scheme representation of two relevant electron microscopy techniques.[2] Typically SEM instruments have resolutions limited to 5 nm although in practice this is often higher, while TEM can achieve atomic resolution. In a TEM instrument a beam of electrons is irradiated at a sample. Using condenser lenses, the electron beam is made into parallel rays that continue towards the sample. The focussed electron beam comes into contact and is attenuated by the solid sample.

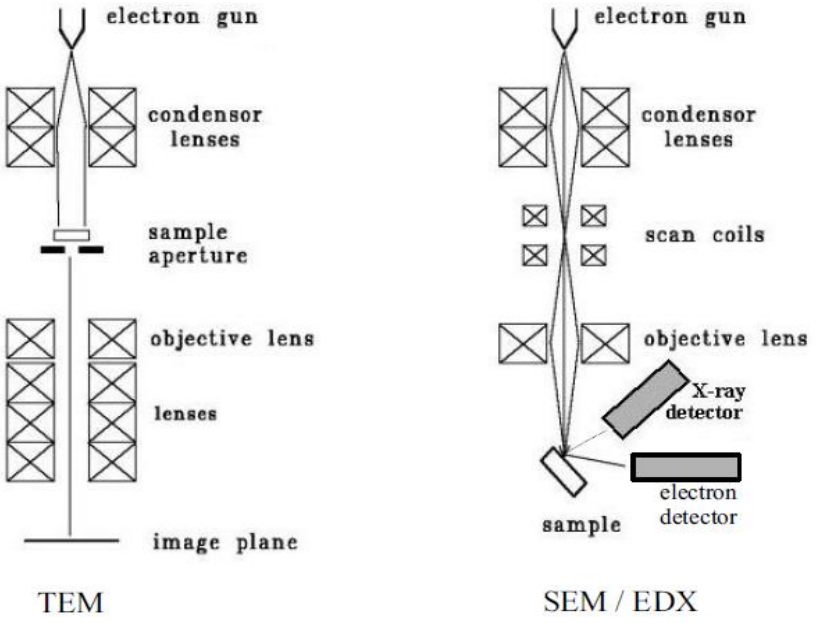

Figure 2.8 Scheme of transmission electron microscopy (TEM) and scanning electron microscopy (SEM) equipped with an energy dispersive x-ray (EDX)

The attenuation depends on the density and thickness of the sample. The transmitted electrons then go on to form a “bright field” image. A proportion of the electrons will be diffracted by the sample. These can be detected by an annular dark field detector (ADF) and produce a dark field image. Many innovations have been applied to TEM to enhance the quality and quantity of information that can be extracted. The advent of scanning transmission electron microscopy (STEM) has meant that in combination with a high angle annular dark field (HAADF) detector, it is possible to generate images whereby the contrast is determined by the atomic number of an element, making the identification of nanoparticles on a support much easier, assuming a sufficient mass contrast between the two components.

SEM uses a scanning electron beam that detects the secondary or backscattered electrons. This means the contrast is determined by the topology of the sample. The backscattered electrons typically come from deeper in the sample and are related to the atomic number of the constituent elements, as larger atoms will scatter the electrons more efficiently.

Experimental

SEM-EDX was carried out using JEOL 6610LV equipped with an Oxford Instruments energy dispersive X-ray (EDX) analyser. A Co standard was used to calibrate the EDX instrument.

STEM HAADF was carried out at Lehigh University by Sultan Althahban under the supervision of Professor Christopher Kiely. A JEOL ARM 200CF AC-STEM instrument was used and the samples were prepared using the dry dispersion route: The catalyst powder was ground between two clean glass slides and then dry transferred onto a holey carbon TEM grid.

2.4. Catalytic testing

2.4.1. Water-gas shift

Water-gas shift screening was carried out in a custom-made fixed-bed flow reactor shown in Figure 2.9 and Scheme 2.7. Typically the catalyst (0.150 g) was suspended between two pieces of glass wool in a steel reactor tube fitted with a stainless steel mesh to hold the catalyst in place within the bed. The catalyst bed was gently heated to reaction temperature (150 ^{o}C) under a flow of N_2 at 7 ^{o}C min^{-1}. The gas feed consisted of 2% CO, 2% CO_2, 7.5% H_2O, 8.1% H_2 and N_2 to balance and was left to stabilise for 20 minutes before the reaction was started. This gas mixture is of a similar composition to a relevant syn gas mixture, although it is more dilute. The gases were introduced to the catalyst bed using mass flow controllers (Bronkhorst). The water was passed through a liquid-flow controller (Bronkhorst) into a controlled evaporator mixer heated to 140 ^{o}C where it was mixed with the carrier gas, N_2. The total flow rate was 100 ml min^{-1}. The products were quantified using an on-line Gasmet Dx4000 Fourier Transform infrared spectrometer (FTIR).

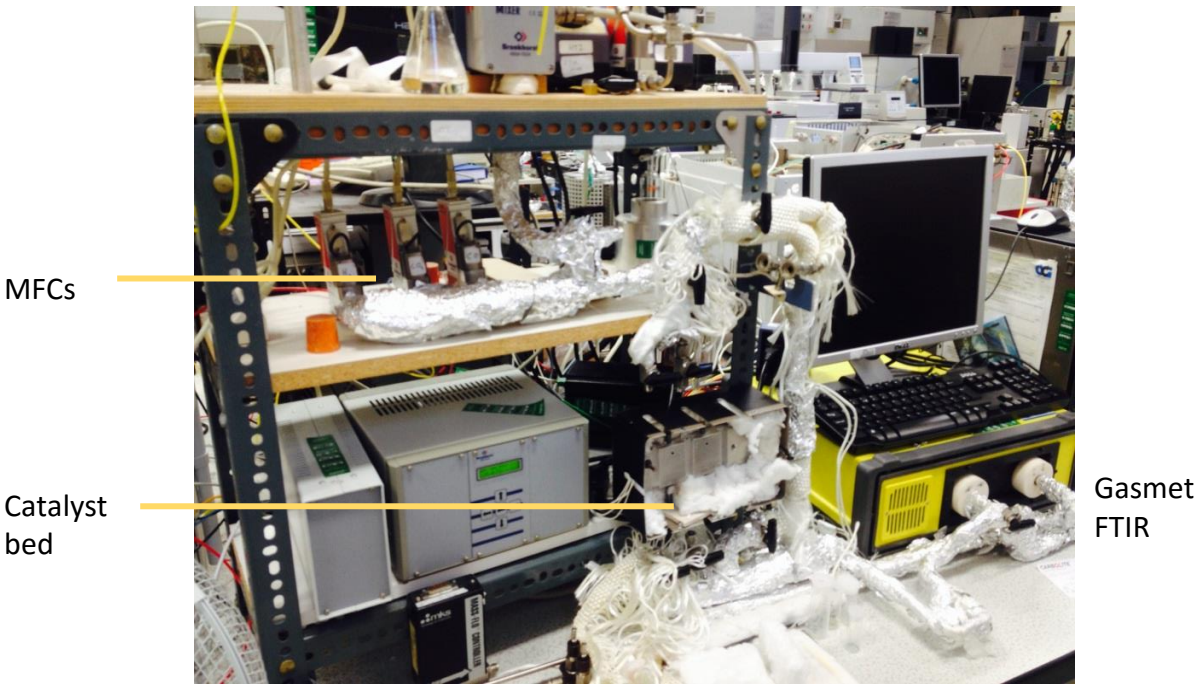

Figure 2.9 Photograph of the water-gas shift reactor

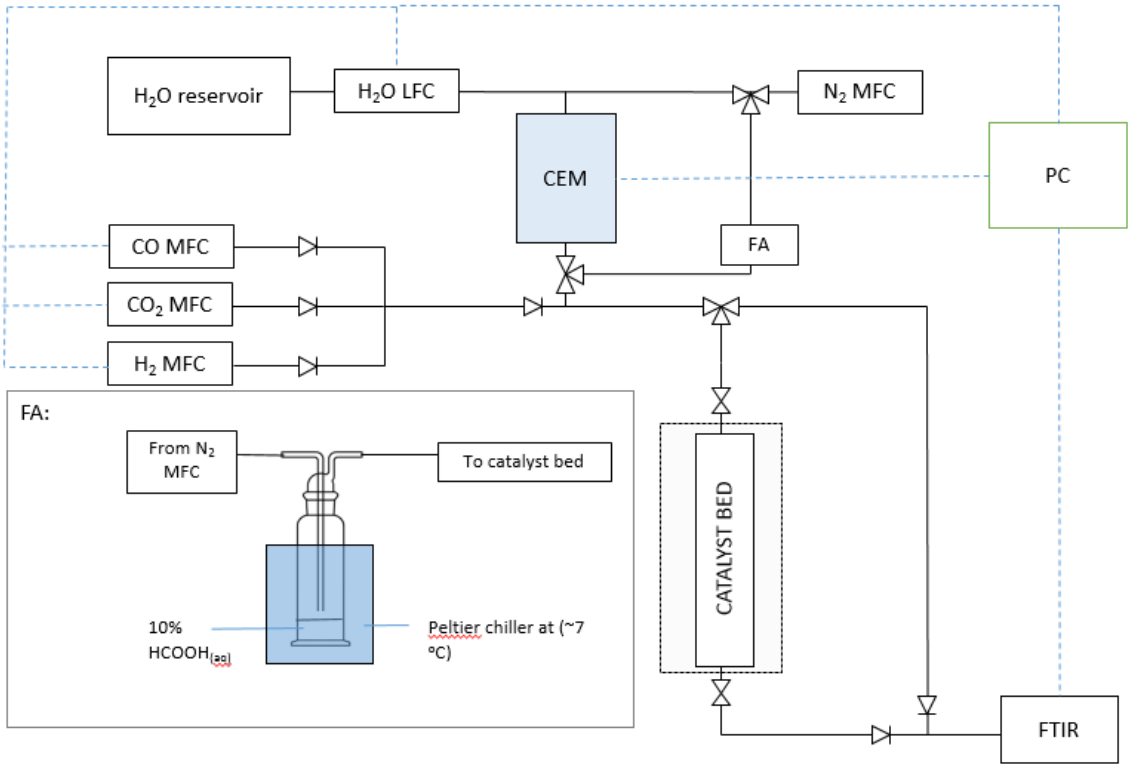

Scheme 2.7. WGS reactor set-up and in-set: modification of reactor to accommodate FAD. Where MFC = mass-flow controller, LFC = liqui-flow controller, CEM = controlled evaporator mixer and FTIR = Fourier transform infrared spectrometer

The above reactor set-up was selected to replicate the conditions previously reported by Hardacre and co-workers who pioneered the $Au/CeZrO_4$ catalyst for the WGS reaction.[3, 11-15]

2.4.2. CO oxidation

CO oxidation was performed on a fixed bed flow reactor, shown in Scheme 2.8. In a standard reaction, the catalyst (0.020 g) was fitted between two pieces of glass wool in the glass U-tube, which was suspended in a silicone oil bath heated to 35 ^{o}C. N_2 was used to purge the U-tube before 5000 ppm CO/synthetic air (BOC) was introduced at 20 ml min^{-1} *via* MFCs (Brooks). The products were analysed by an on-line Varian gas chromatograph (GC) fitted with a thermal conductivity detector (TCD). The column was a custom Supelco 100/120 carbosieve SII – 10' x ¼''.

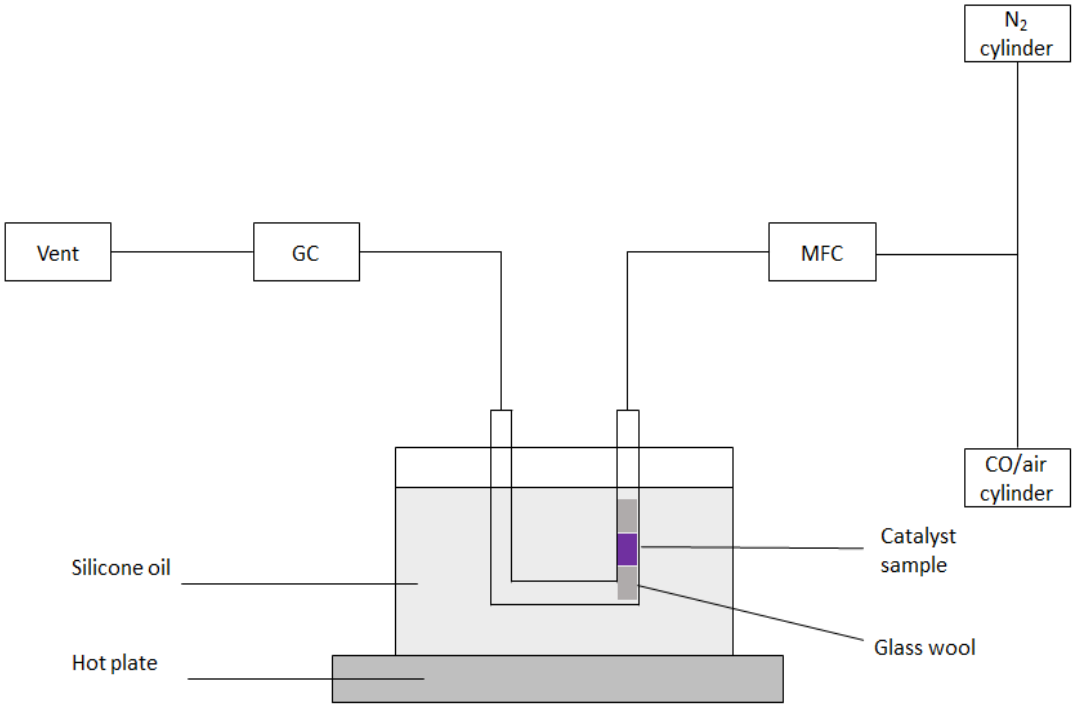

Scheme 2.8 reactor Scheme of the CO oxidation set-up

2.4.3. Formic acid decomposition (FAD)

FAD reactions were conducted using the same reactor as described for WGS experiments with one modification: A Drechsler bottle was installed containing 10% formic acid in water (inset, Scheme 2.6). A Peltier chiller was used to cool the bottle to

7 ^{o}C and the N_2 was passed through the bottle, giving a consistent flow of 1700 ppm of formic acid and 1500 ppm of H_2O through the catalyst bed. Experiments were conducted at 85 ^{o}C and 0.050 g of catalyst was used. The total flow rate was 100 ml min^{-1}. The decomposition of formic acid was quantified using the on-line FTIR instrument used in the WGS reactions.

2.4.4. Benzyl alcohol oxidation

Benzyl alcohol oxidation experiments were carried out by Dr Ewa Nowicka, at Cardiff University in a 50 cm^3 glass stirred reactor as previously reported.[16] In a typical reaction, the catalyst (0.02g) and substrate (1g) were charged into the reactor which was then purged with oxygen three times before closing and the pressure was maintained at 1 barg. The reactor was kept in a heating block, which was preheated to the reaction temperature (120 ^{o}C). The reaction mixture was stirred at 1000 rpm using a magnetic bar inside the reactor. After 1h reaction, the stirring was stopped and the reactor was rapidly cooled in an ice-bath.

After cooling, the reactor was opened slowly and the contents were centrifuged. An aliquot of the clear supernatant reaction mixture (0.5 cm^3) was diluted with mesitylene (0.5 cm^3, external standard for GC analysis.). For the analysis of the products, a GC (a Varian star 3800 cx with a 30 m CP-Wax 52 CB column) was employed.

2.4.5. Product analysis

Gas chromatography

Gas chromatography is a powerful tool that is widely used to separate and quantify molecules in the gas-phase. In this work it was utilised in the context of CO oxidation and benzyl alcohol oxidation. The basic principle involves the injection (and vaporisation, if necessary) of a sample, which is then separated using a column in an oven and then the detection of each component that allows identification and quantification of the sample. In reality, there are countless parameters that are optimised and tailored according to the properties of the analytes. The detector used must be appropriate for the sample being analysed.

For analysis of the CO oxidation products, a thermal conductivity detector (TCD) was used. For the analysis of benzyl alcohol oxidation, a flame ionisation detector was used (FID).

A TCD consists of a temperature-controlled cell that compares the conductivity of an analyte to that of a reference gas, typically hydrogen or helium. A Wheatstone bridge is usually applied to achieve this. Most gases have a lower conductivity than He or H_2 and so when an analyte enters the detector, the resistance will increase and a signal is measured. One of the main advantages of a TCD is its ability to detect CO_2, which would not be possible with an FID. A FID consists of hydrogen flame in excess oxygen, a cathode and an anode above the flame. The sample is combusted in the flame, which causes a change in current to be detected at the anode. This change in current is amplified to produce a signal that can achieve extremely sensitive levels. The main drawback is that it is a destructive technique, although this was not a concern in the analysis of reaction products in benzyl alcohol oxidation.

The GC was calibrated by passing known concentrations of CO_2/air through the GC. The counts corresponded to a CO conversion and this was used to work out the percentage of CO that was oxidised to CO_2.

For the benzyl alcohol oxidation experiments, the GC was calibrated using standards of known products to calculate a response factor. The response factor was then used to convert the counts on the GC into concentration that represented the conversion to a reaction product.

Fourier Transform Infrared Spectroscopy

For WGS and FAD, FTIR was employed to analyse the products of the reactions. The FTIR was set-up such that it analysed the gas mixture on-line, using a 400 cm^3 cell. A spectrum was recorded every minute. The activity of the catalysts has been reported in terms of the number of moles of the substrate converted per hour per moles of supported metal on the catalyst throughout the thesis. For example for WGS and CO oxidation, the units are $mol_{COconverted}\ h^{-1}\ mol_{metal}^{-1}$. This is calculated using the formula below:

$$\text{Activity} = \frac{(\text{CO conversion }\%)(\text{moles of CO per hour in the gas feed})}{(100)(\text{Moles of total supported metal on the catalyst})}$$

For other reactions, the same formula was applied but the appropriate flow rates and conversions were substituted. The actual metal loadings were determined using MP-AES.

This method of quantifying catalytic activity is important because in the DP method of catalyst preparation, it is common for the nominal loadings of metals to be significantly different from the actual metal loadings and so reporting the “CO conversion” is not sufficient.

2.5. References

1. G. Rothenberg, *Catalysis: Concepts and green applications*, Wiley VCH, 1 edn., 2008.

2. I. Chorkendorff and J. W. Niemantsverdriet, *Concepts of Modern Catalysis and Kinetics* Wiley, 2003.

3. R. Pilasombat, H. Daly, A. Goguet, J. P. Breen, R. Burch, C. Hardacre and D. Thompsett, *Catalysis Today*, 2012, **180**.

4. J. Rynkowski, J. Farbotko, R. Touroude and L. Hilaire, *Applied Catalysis a-General*, 2000, **203**, 335.

5. K. de Jong, ed. K. de Jong, Wiley-VCH Verlag GmbH & Co, 2009, ch. 6.

6. A. Jones, *Tempature-Programmed Reduction for Solid Materials Characterization*, 1986.

7. Q. Fu, A. Weber and M. Flytzani-Stephanopoulos, *Catalysis Letters*, 2001, **77**.

8. A. M. Venezia, L. F. Liotta, G. Pantaleo, V. La Parola, G. Deganello, A. Beck, Z. Koppany, K. Frey, D. Horvath and L. Guczi, *Applied Catalysis a-General*, 2003, **251**, 359.

9. D. Goodman, in *Dekker Encyclopedia of Nanoscience and Nanotechnology*, eds. C. Contescu and K. Putyera, CRC Press, Second edn., 2008, pp. 611-619.

10. http://scienceworld.wolfram.com/physics/FourierTransformSpectrometer.html

11. D. Tibiletti, A. Amieiro-Fonseca, R. Burch, Y. Chen, J. M. Fisher, A. Goguet, C. Hardacre, P. Hu and A. Thompsett, *Journal of Physical Chemistry B*, 2005, **109**.

12. A. Goguet, R. Burch, Y. Chen, C. Hardacre, P. Hu, R. W. Joyner, F. C. Meunier, B. S. Mun, A. Thompsett and D. Tibiletti, *Journal of Physical Chemistry C*, 2007, **111**.

13. F. C. Meunier, D. Reid, A. Goguet, S. Shekhtman, C. Hardacre, R. Burch, W. Deng and M. Flytzani-Stephanopoulos, *Journal of Catalysis*, 2007, **247**, 277.

14. H. Daly, A. Goguet, C. Hardacre, F. C. Meunier, R. Pilasombat and D. Thompsett, *Journal of Catalysis*, 2010, **273**, 257.

15. H. Daly, F. C. Meunier, R. Pilasombat, R. Burch, A. Goguet and C. Hardacre, *Abstracts of Papers of the American Chemical Society*, 2011, **241**.

16. M. Sankar, E. Nowicka, R. Tiruvalam, Q. He, S. H. Taylor, C. J. Kiely, D. Bethell, D. W. Knight and G. J. Hutchings, *Chemistry-a European Journal*, 2011, **17**.

Chapter 3

The deactivation of $Au/CeZrO_4$ during the low-temperature water-gas shift reaction

3.1. Introduction to the deactivation mechanism and the aims of the chapter

This short opening results chapter aims to understand the deactivation mechanism of the benchmark catalyst described in **Chapter 1**. A combination of XPS and HAADF STEM was used to characterise fresh and used samples of the catalyst after exposure to WGS reaction conditions.

3.1.1. The deactivation of $Au/CeZrO_4$ under water-gas shift conditions

An in-depth discussion of the literature regarding the benchmark catalyst can be found in **Chapter 1**. The following is a summary of the significant publications relevant to the benchmark Au catalyst and similar systems.

The most rigorous investigation into the $Au/CeZrO_4$ catalyst was carried out by Goguet *et al.* who used a combination of high-pressure XPS, EXAFS and XANES, DFT and DRIFTS to elucidate active sites and deactivation mechanism of 1.7wt% $Au/CeZrO_4$.[1] It was shown that deactivation occurred due to the loss of metal-support interaction that reduced the number of active site of the catalyst, which as discussed in **Chapter 1**, is the metal-support interface. Carbonate deposition was ruled out using TPO and DRIFTS and sintering[2] was excluded from *in situ* EXAFS data that showed no change in the co-ordination number of Au throughout the reaction. It was also shown that high concentrations of water caused the catalyst to deactivate more rapidly. DFT calculations rationalised this by showing that the dissociation of water near a gold cluster causes restructuring at the interface, which the authors concluded was consistent with the de-wetting of the nanoparticle.

Similar effects have been reported for copper catalysts in the presence of water: Hansen *et al.* showed using *in situ* microscopy that the nanoparticles underwent reversible shape changes in different gaseous atmospheres.[3] These effects were thought to be caused by adsorbate-induced changes in surface energies and interfacial energy changes. Under a wet atmosphere, the copper nanoparticles changed from a hemi-spherical shape to a more spherical one.

There are contrasting reports in the literature concerning the deactivation of gold supported on Ce-based supports for the water-gas shift reaction and indeed other similar reactions such as CO oxidation. This is no doubt due to subtle but significant differences in the catalyst system and the preparation method used. For example, the build-up of carbonates on the surface of the catalyst has been reported to be involved in deactivating Au/CeO_2, but it has been reported that on $CeZrO_4$, this is less likely to occur.[1] Although the explanation for this was not given, it might be related to the high number of hydroxyl groups that are present on $CeZrO_4$ which occur as a result of defect sites. It is known that OH groups facilitate the decomposition of carbonates and so it is logical that a surface high in OH groups should not be susceptible to carbonate accumulation.[4] Marks and co-workers' recent microscopic investigation of Au/CeO_2 illustrates how a subtle difference in a catalyst can greatly affect the properties and deactivation mechanism in WGS: Gold supported on CeO_2 nanorods did not sinter during the WGS reaction but gold supported on CeO_2 nanocubes did.[5] This showed that the facet of the support is critical in determining the adhesion of a supported metal particle and therefore the catalyst stability in certain reactions.

3.1.2. The aims of the chapter

The aim of this opening chapter is to further understand the deactivation mechanism of an $Au/CeZrO_4$ catalyst through spectroscopic and microscopic characterisation of the fresh and used samples. While many research groups have studied this system, there is still much to be learned about this highly active catalyst. The objective was also to use the knowledge gained from this work to inform the design of future catalysts in this reaction.

3.2. The catalytic activity of $Au/CeZrO_4$ for the low-temperature water-gas shift reaction

$Au/CeZrO_4$ was subjected to the standard test conditions described in **Chapter 2** (150°C, 52,000 h^{-1}, 2% CO, 2% CO_2, 7.5% H_2O, 8.1% H_2 + N_2 to balance) for 48 h on-stream. The time on-line data is presented in Figure 3.1, which shows the normalised CO conversion against time. This is calculated by measuring an initial conversion of the catalyst, in this case after 60 minutes on-stream and normalising all subsequent conversions to this value. This allows the deactivation to be considered relative to its initial activity.

Figure 3.1 shows that after 48 h just 50% of the initial catalyst activity remained and while the most rapid deactivation took place in the first 6 h, the catalyst continued to deactivate throughout the entire experiment. The change in the rate of deactivation is significant and could be due to multiple processes occurring during deactivation. At approximately 22 h on-line, there is a noticeable increase in the catalyst activity. This is most likely an artefact, due to fluctuations in the water concentration that are common in the reactor set-up. After the experiment was complete, the catalyst sample was recovered and analysed using XPS and HAADF STEM.

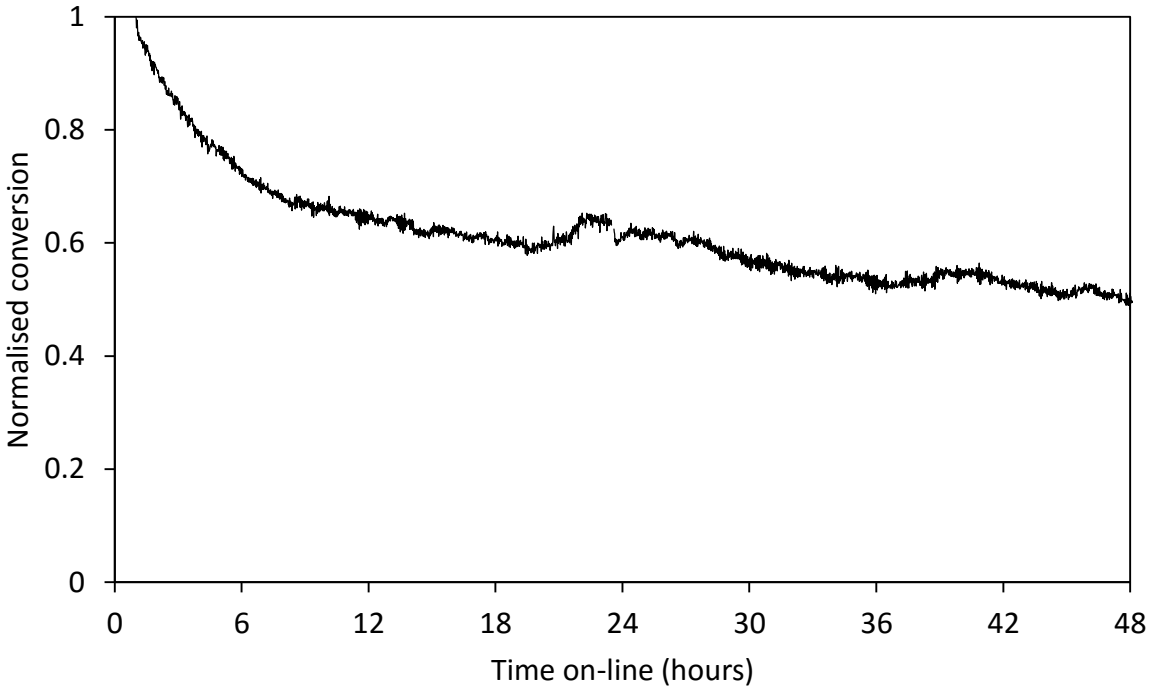

Figure 3.1 Time on-line data for $Au/CeZrO_4$ under standard WGS conditions. Reaction conditions: 150 °C, 0.15 g catalyst, 100 ml min^{-1} Gas feed: 2% CO, 2% CO_2, 7.5% H_2O, 8.1% H_2 and N_2.

3.3. X-ray photoelectron spectroscopy of fresh and used $Au/CeZrO_4$

XPS is widely used to characterise a catalyst in order to gain an insight into the chemical state of the surface of a catalyst. In this study, the focus was to compare the Au 4f spectra of the catalysts and look for changes in the nature of the supported metal. However, the Ce 3d and O 1s spectra were also analysed to establish the chemical changes that occurred on the support, although the proposed deactivation mechanism focusses on the nature of the gold nanoparticles rather than the support. In addition, high resolution spectra of the Cl and Na regions were collected (not shown) as these potential poisons could have remained from the catalyst preparation. In all cases, no contaminants were detected.

3.3.1. The Au 4f spectrum

The fresh and used spectra are presented in Figure 3.2 below in addition to the composition and binding energy of each Au species, presented in Table 3.1. The Au 4f spectrum consists of several features that correspond to different Au species in the sample. There are three features in the fresh and used sample: Au^0, $Au^{\delta+}$ and Au^{3+}. Au^0 and Au^{3+} correspond to the different oxidation states of Au and are found at 84 eV and 86.2 eV, respectively in the fresh sample.

These values are consistent with those reported in the literature for similar systems.[6-8] The feature at 85 eV is at the binding energy typically associated with Au^+ although this has also been assigned to small metallic Au species, hence its assignment as $Au^{\delta+}$.

Table 3.1 XPS analysis of Au 4f signal including the surface ratio of the Au 4f and Zr 3d regions

Sample	Au species composition (%)			Binding energy of assigned species (eV)			Au surface concentration
	Au^0	$Au^{\delta+}$	Au^{3+}	Au^0	$Au^{\delta+}$	Au^{3+}	Au 4f/Zr 3d ratio
Fresh	65.2	26.5	8.4	83.9	85.0	86.2	0.056
Used	83.2	11.2	5.6	84.1	85.1	86.4	0.049

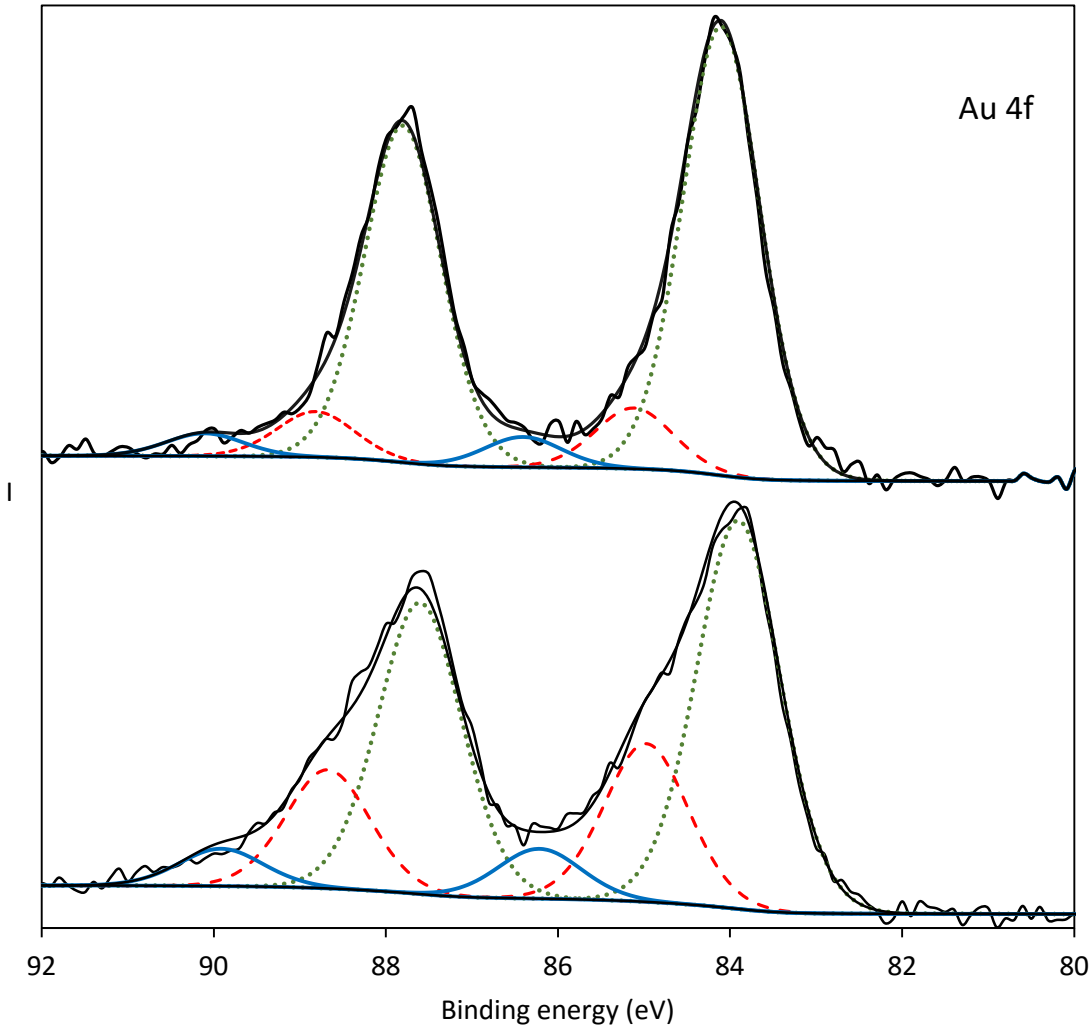

Figure 3.2 XP spectra of fresh (bottom) and used (top) Au/$CeZrO_4$ catalyst. Each sample shows the presence of multiple species as Au^0 (dotted green line), $Au^{\delta+}$ (dashed red line) and Au^{3+} (solid blue line). The fresh catalyst shows a higher abundance of Au^{3+} and $Au^{\delta+}$ compared to the used sample.

There is a precedent for this feature to be assigned to small nanoparticles of Au, although there is still some debate in the literature. The variation of the Au 4f binding energy as a function of Au coverage (and therefore Au particle size) on yttria-stabilised ZrO_2 was observed by Zafeiratos and Kennou[9] and was attributed to a change in the final state i.e. the screening and delocalisation of the photoemission core holes[10-12] as well as initial state effects, which include factors such as the oxidation state, co-ordination number and particle size of gold.[11, 12] It is agreed by many groups that this is the origin of the signal at 85 eV in these systems.[13-17]

On the other hand, Boyd *et al.* studied Au supported on TiO_2, TiO_2-ZrO_2 and Zeolite Y for CO oxidation and Au/Fe_2O_3 for low-temperature WGS and identified the co-existence of Au^0, Au^+ and Au^{3+} using Mössbauer spectroscopy.[18] Furthermore, the CO oxidation activity of each catalyst correlated well with the amount of Au^+ in the sample. This suggests that perhaps this feature in the Au 4f XP spectra is due to ionic Au, the binding energy of which was reported to be 84.9 eV for gold/titania-zirconia, rather than small particles although the possibility of both contributing to this feature is also reasonable. One final consideration in the assignment of this feature to small gold particles is the fact that there are likely to be many nanoparticles of different sizes that all contribute to the region where the $Au^{\delta+}$ feature has been fitted. Fitting many peaks in this region might more accurately reflect particle size distribution of gold particles in the catalyst although this of course would not be realistic. Instead, fitting one peak and assigning this to "small particles" is perhaps the simplest way to represent the different Au species in the catalyst that are small enough to induce an appreciable shift in the binding energy. Overall, the majority of the literature is consistent with the assignment of the peak centred at 85.2 eV to small particles and so this feature is tentatively assigned as such.

The identity of this feature is significant as it is less abundant in the surface of the used sample. The fresh Au/$CeZrO_4$ consists of 26.5% $Au^{\delta+}$ and the used sample has just 11.2% of this feature. As this feature has been assigned to small gold particles, it was concluded that this reduction in $Au^{\delta+}$ is consistent with particle agglomeration under reaction conditions. It should also be noted that in the reducing conditions of the WGS reactor, reduction of Au^+ and Au^{3+} would also be expected. Further evidence of particle agglomeration was found by measuring the Au/Zr ratio from the XPS data. In the fresh sample, this ratio was 0.056 however in the used sample it was 0.049. This ratio shows the amount of gold detectable by XPS in relation to the zirconium, of which the latter would not be expected to change significantly under the WGS testing conditions. A decrease in this value indicated that less of the gold was detectable by XPS, which is consistent with particle agglomeration due to XPS probing only the uppermost atomic layers. This finding was further evidence for the agglomeration of gold particles under reaction conditions. There was a reduction in 12.5% of the original value, which is comparable to that reported by Goguet *et al.* who observed a decrease of 16% in a

high-pressure XPS study. The authors ascribed this to a change of morphology in the Au nanoparticles, from hemi-spherical to spherical, rather than particle agglomeration. However, the Au 4f signal was noisy and the peak fitting not shown. In addition to this, the sample was treated in equi-molar quantities of CO, H_2, H_2O and CO_2 at a pressure of 400 mTorr and the temperature ramped from 150^{o}C to 300^{o}C. It might be that under these gentler conditions no sintering takes place, especially in light of the reports that high concentrations of water are thought to be responsible for the high rate of deactivation in these systems.[1] It also possible that the change in surface Au/Zr ratio is due to both agglomeration and morphological changes.

In addition to the change in the composition of Au species in the fresh and used samples there was a shift in the binding energy (BE) of the Au signals of 0.1-0.2 eV, as shown in Table 3.1. As described above, the final BE depends on the initial state (determined by particle size, oxidation state etc.) and the final state (screening of holes created by photoemission). Cies *et al.* reported that successive oxidation-reduction treatments caused a reversible shift in the BE of the Au 4f signal in an Au/$CeZrO_4$ catalyst.[12] After reduction, the BE shifted from 84.5 eV to 84.3 eV. This was concluded to be the result of an initial state effect caused by the change in charge transfer from the reduced support to the supported metal. In this work, a shift in the opposite direction was observed. This is no doubt due to other initial state effects such as changes in the particle size of the gold also contributing to the final BE. In this instance no significance in the binding energy position can be inferred due to the many contributing factors that determine it.

3.3.2. The Ce 3d spectrum

The Ce 3d spectrum was analysed to assess whether significant changes to the support occurred under the reaction conditions. The Ce 3d spectra of the fresh and used samples are shown in Figure 3.3. Deconvolution of the Ce 3d spectrum is challenging due to the many features that contribute to the line shape. Various models have been proposed to fit the spectra, most notably by Burroughs and co-workers[19] and this was the basis for the deconvolution of the Ce 3d spectra throughout this work. The notation consists of v and u labels for peaks from the $3d_{5/2}$ and $3d_{3/2}$ spin-orbit coupling, respectively. v, v'' and v''' correspond to Ce^{4+} states while v_0 and v'

correspond to Ce^{3+}. The same assignments apply for the u labelled peaks, i.e. u, u' and u''' correspond to Ce^{4+}.

In the fresh and used samples there is evidence of Ce^{3+} and Ce^{4+}, which is consistent with Ce-containing mixed metal oxides due to the creation of defect sites by the second metal, although some reduction under the X-ray beam is also possible.[20-22] The peak fitting model was a good fit for the XPS data although not perfect. The Ce oxidation state composition is shown in Table 3.2. There is evidence of some cerium reduction in the used sample. The fresh sample contains 65.8% Ce^{4+} but this figure was 59.7% in the used sample. In order to illustrate the change in the Ce^{3+} signal, the corresponding features are shown in red. There is a visible decrease in the size of these peaks. The partial reduction in Ce is not unexpected given the reducing conditions of

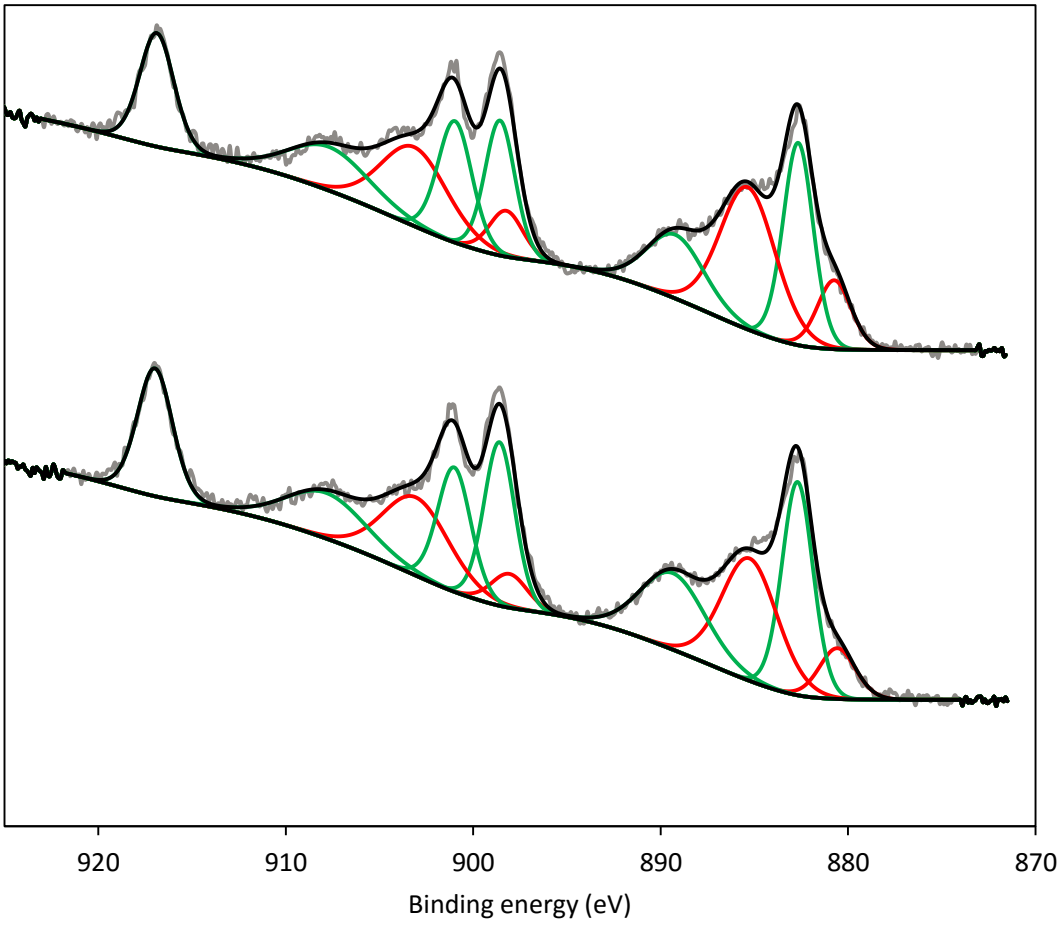

Figure 3.3 Ce 3d spectra of fresh (bottom) and used (top) catalysts. Features due to Ce^{3+} are shown in red and features due to Ce^{4+} are shown in green.

the reaction although its significance in the context of the deactivation of this system is not obvious.

Table 3.2 XPS data of fresh and used $Au/CeZrO_4$ catalysts showing the concentration of different Ce oxidation states and the BE and composition of different O species.

Sample	Ce species composition (%)		Species composition (%)		Binding energy (eV)	
	Ce^{3+}	Ce^{4+}	O'	O''	O'	O''
Fresh	34.2	65.8	72.6	27.5	529.8	531.6
Used	40.3	59.7	70.0	30.0	529.8	531.6

Previous reports have ascribed the deactivation of Pt/CeO_2 to the over-reduction of the support.[23] Zalc *et al.* showed that catalyst deactivation was more rapid when higher concentrations of H_2 were present in the gas feed. However, these observations do not necessarily apply to the benchmark catalyst and a mechanistic explanation was not given. In fact, it has been demonstrated that anion vacancies caused by the partial reduction in ceria supports are necessary for the efficient activation of water.[24] However, it has been suggested that if there is too much hydrogen in the gas-feed, the rate of water activation becomes rate-limiting and the activity is reduced.[24] Over-reduction was not considered significant in studies on $Au/CeZrO_4$.[1] There is no evidence that the reduction observed in this work is sufficient to cause water dissociation to become rate-limiting although in order to fully rule this out, further studies should be undertaken with different concentrations of H_2 and perhaps kinetic isotope studies involving D_2.

3.3.3. The O 1s spectrum

The O 1s signal was also investigated to establish which oxygen containing species are present in each sample. The peak fitting is presented in Figure 3.4. While the spectrum is relatively simple, there are theoretically many possible species that could be detected, including carbonate/carbonyl species, hydroxyl groups, lattice oxygen bonded to Zr or Ce and oxygen bonded to Au. In addition to this, the full width half maximum (FWHM) of each species can vary significantly. Assignment of the O 1s species was made in the context of the existing literature and the complimentary data available.

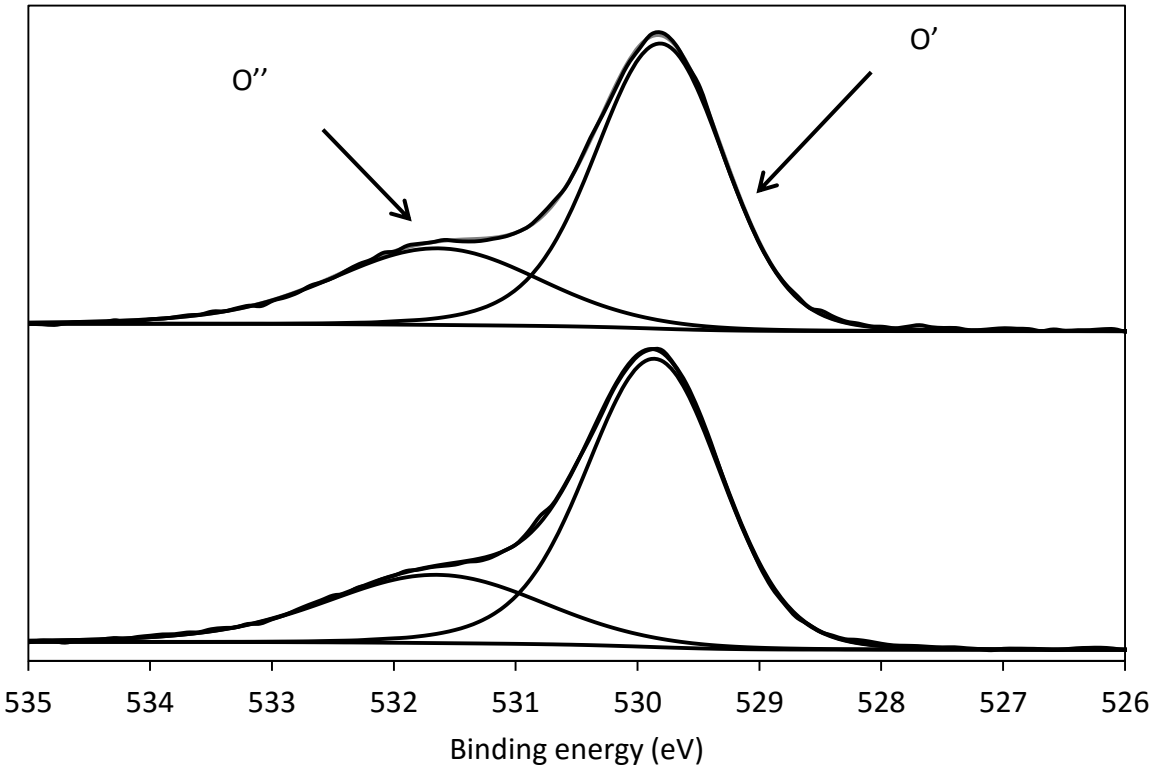

Figure 3.4 O 1s spectrum of fresh (bottom) and used (top) sample

For example, in the used sample a higher degree of hydroxyl groups would be expected due to the partial reduction in the support, as evidenced from the Ce 3d spectrum. This is indeed what is observed, although the difference is only slight, as shown in Table 3.2. There are two features in the observed O 1s signal. The feature at 529.8 eV, O', is due to lattice oxygen from the metal oxide support. The smaller feature at 531.6 eV, O'', is due to weakly bound hydroxyl and carbonate species, as well as adsorbed oxygen.[20-22, 25, 26] However, the presence of carbonates in the fresh and used samples can be disregarded by consideration of the C 1s peak. A sharp feature (calibrated to 284.7 eV) and due to carbon-carbon bonding from adventitious carbon was observed in this region, but a feature relating to carbon-oxygen bonds, typically at 286-288.5 eV was not detected, indicating that there were not a detectable level of carbonate species on the sample. The build-up of carbonates has been identified as a possible cause of deactivation on Au/CeO_2 but no evidence of this was found in this work. It should be noted however, that under the UHV conditions of an XPS experiment, weakly bound carbonates that accumulated during the reaction could have desorbed.

In conclusion, XPS was used to elucidate many details regarding the surface of the catalyst in the fresh and used samples. Changes in the binding energy of the Au 4f signal, in addition to changes in the Au/Zr ratio suggested that particle agglomeration occurred under the reaction conditions tested. The Ce 3d spectrum showed that the support does get reduced under reaction conditions although the significance of this in the deactivation mechanism remains unclear. The O 1s and C 1s spectra revealed no significant build-up of carbonates was present on the sample.

3.4 STEM HAADF of fresh and used $Au/CeZrO_4$

An extensive electron microscopic analysis of fresh and used samples of $Au/CeZrO_4$ was carried out in order to determine if there was any evidence of sintering or changes in particle morphology. The electron microscopy was carried out at Lehigh University by Mr Sultan Althahban and Professor Christopher Kiely, using a JEOL ARM 200CF AC-STEM instrument. More details can be found in **Chapter 2.3.9**.

3.4.1. Characterising the $CeZrO_4$ support

Initial work set out to identify the morphology and crystallite size of the support. It was found that in the $CeZrO_4$ used in this work, there was a bimodal particle size distribution whereby small crystallites of $CeZrO_4$, 2-3 nm in size were present as well as larger crystallites that were approximately 8-15 nm in diameter. Interestingly, the majority of the Au particles imaged were supported on the larger crystallites. Figure 3.5 below shows the two morphologies of the support. Previous reports of supported

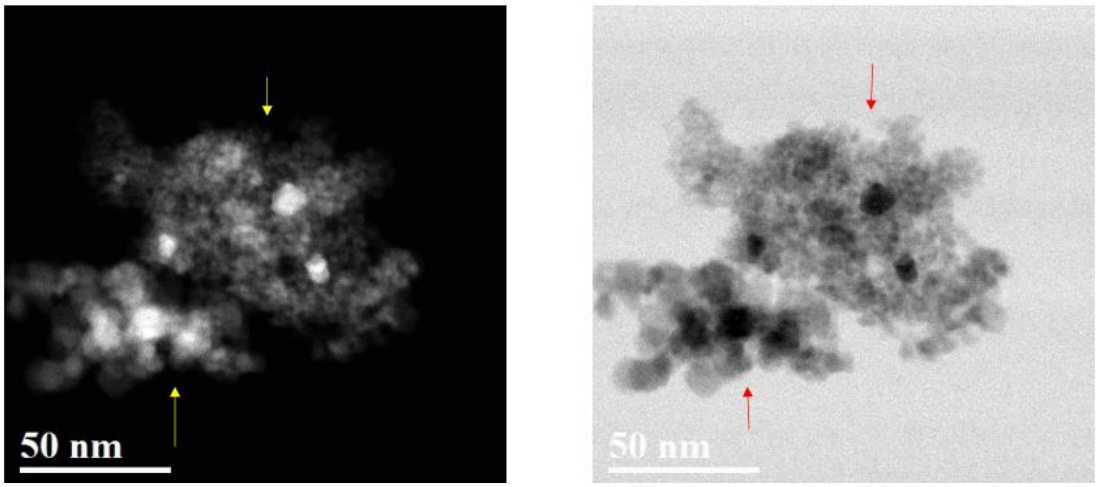

Figure 3.5 STEM HAADF (left) and BF (right) images of the $CeZrO_4$ support. Nanocrystalline $CeZrO_4$ can be seen in the top right of the image while the large crystallites make up the lower left image.

gold catalysts have shown that the loss of surface area of the support contributed to catalyst deactivation.[27] While there have not been any reports of this type of deactivation occuring on $CeZrO_4$ supports, high resolution electron microscopy of this kind offers a great opportunity to test for this and so the crystallite size of the support was also noted.

3.4.2. Fresh $Au/CeZrO_4$

As stated above, both the particle size and morphology were considered important in the deactivation mechanism. Examination of the micrographs of the fresh catalyst showed that there were several morphologies and metal particle sizes present in the sample. Figure 3.6 shows a representative selection of bright and dark field images of various magnifications of Au nanoparticles. It can be seen that there were clear variations in the size of the supported metal particles, which is commonly observed in supported metal catalysts prepared in this way. The gold nanoparticles contrasted reasonably well with the $CeZrO_4$ support. An extensive investigation was carried out in order to identify the most abundant gold nanoparticle morphologies in the sample as well as calculate a particle size distribution for the metal nanoparticles.

Figure 3.7 (top image) shows an example of a large, rounded gold nanoparticle that exhibited five-fold twinning. These types of particles were present on the catalyst, but not in high-abundance. On the other hand, large numbers of well facetted gold particles were observed, as shown in Figure 3.7 (middle image) and labelled with the arrows. The morphology of the gold particle could be important for high catalytic activity as this will determine the surface energy of the gold species and therefore the binding strength of CO molecule. Marks and co-workers investigated the effect of WGS conditions on gold supported on ceria nanocubes and nanorods at 250^{o}C. While both catalysts deactivated rapidly, Au/CeO_x nanorods retained the same gold nanoparticle size throughout the WGS reaction. However, there was a significant change in the morphology of the nanoparticles. In the fresh sample, there were rafts and layers of gold atoms and these were not observed in the used sample. The gold nanoparticles in the Au/CeO_x nanocubes catalyst did increase in size during the WGS reaction as well as morphologically change, showing the important role of different support facets. Unfortunately morphological distribution data is very difficult to generate due to the

numerous variety of shapes and surface properties that are possible so conclusions regarding the morphology of the supported gold are qualitative and cautious. Gold paticles trapped in crevices in the support and on grain boundaries were also observed in the fresh sample, as shown in Figure 3.7 (bottom image).

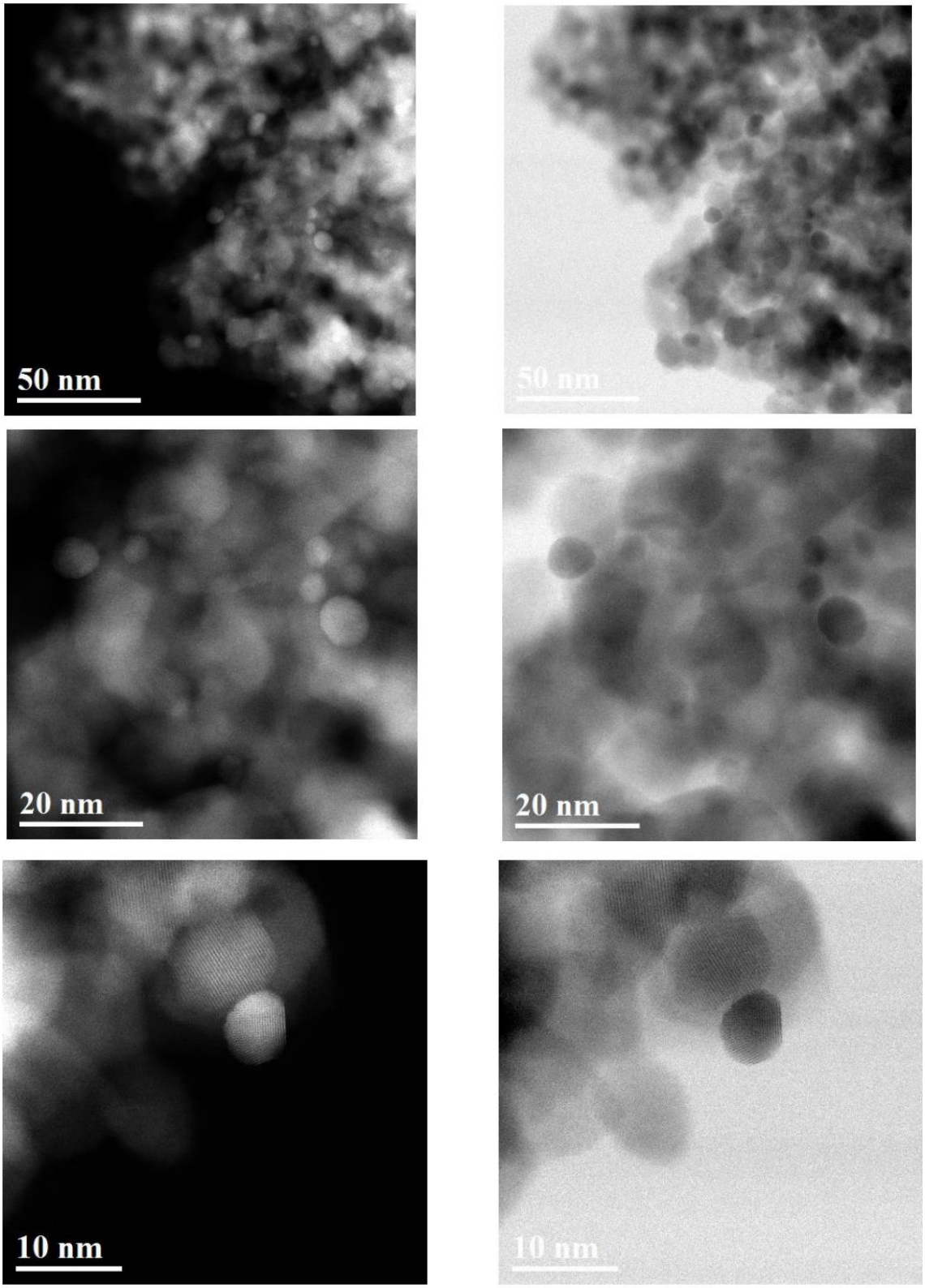

Figure 3.6 STEM HAAADF (left) and BF (right) images of the fresh Au/$CeZrO_4$ at different magnifications

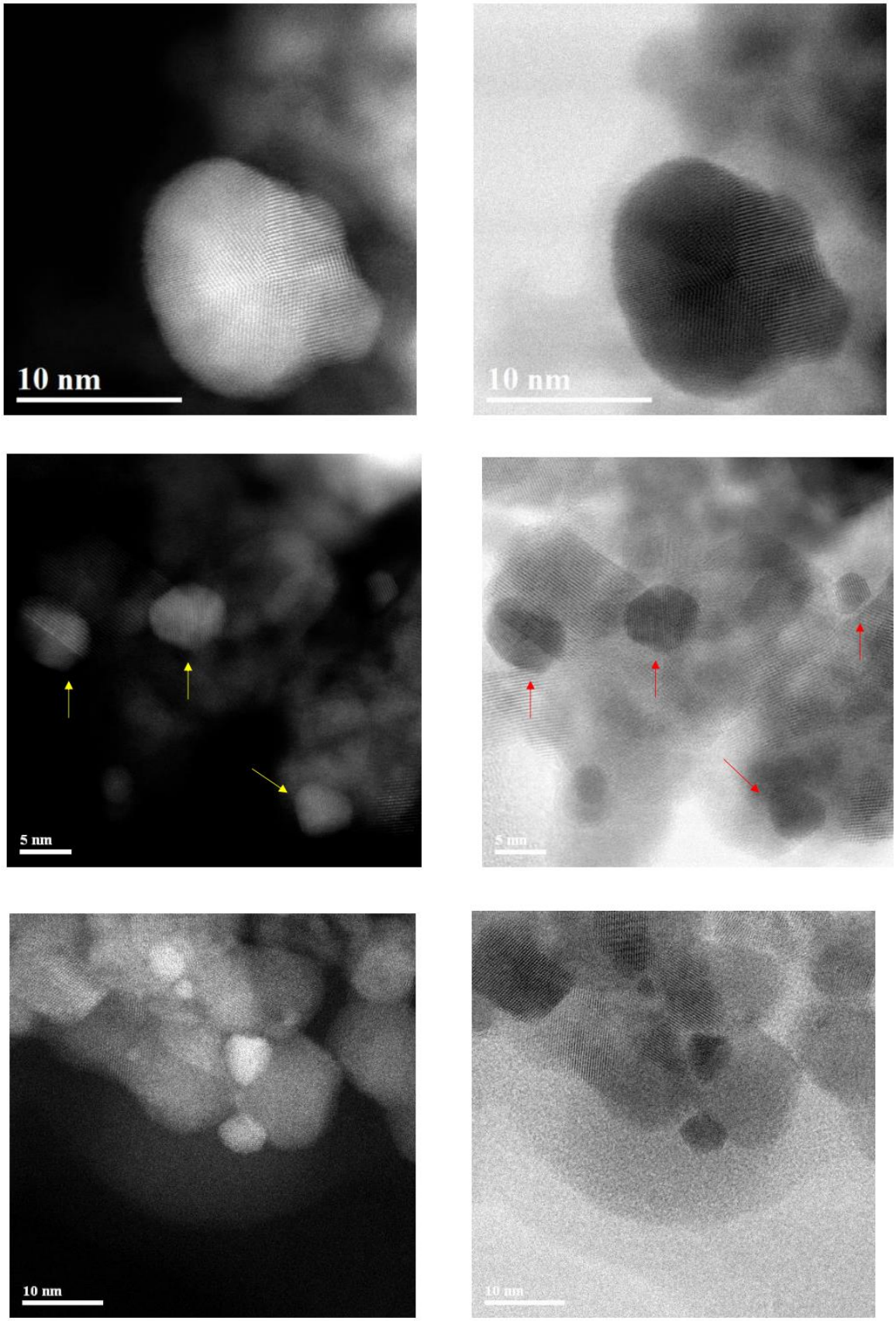

Figure 3.7 Top: Dark field (left) and bright field (right) image of top: a large, round Au nanoparticle exhibiting five-fold twinning. Middle: Au nanoparticles exhibiting cuboctoherdal shape with well-defined facets and edges Bottom: image of Au particle positioned in crevice of support

This perhaps suggests that the adhesion of the gold nanoparticle is rather weak. The particle size distribution was generated from a statistically relevant number of micrographs and is presented in figure 3.8. The mean particle size was measured as 4.5 nm.

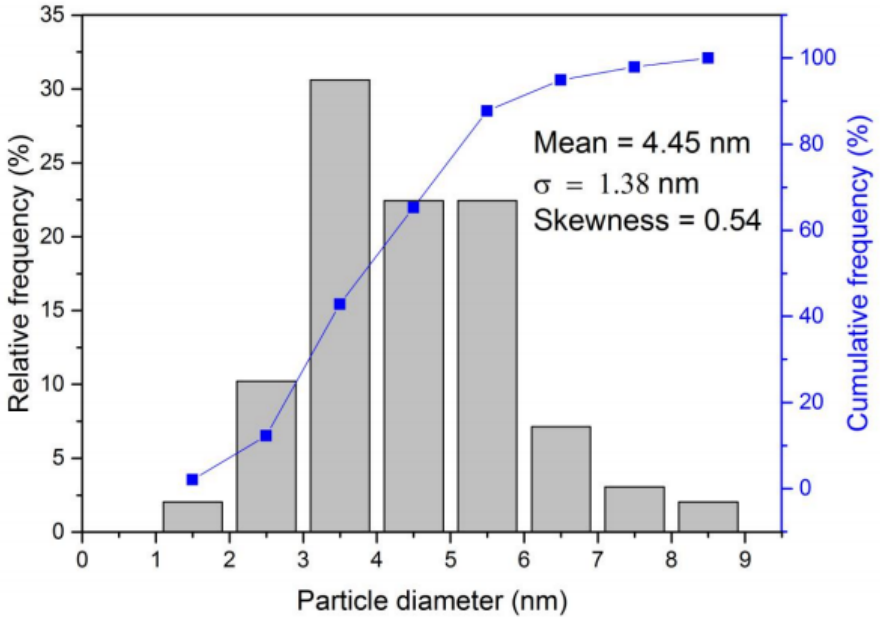

Figure 3.8 Particle size distribution for the fresh Au/$CeZrO_4$ catalyst. The mean particle size was 4.5 nm.

3.4.3. The used Au/$CeZrO_4$

The used sample was subjected to the same characterisation process as the fresh catalyst, whereby the particle size and morphology was investigated. It should be noted that the $CeZrO_4$ support exhibited the same bimodal particle size as the fresh catalyst and no evidence of particle growth of $CeZrO_4$ was observed, showing that the morphology or surface area of the support was not a significant in the deactivation mechanism. Figure 3.9 below shows a number of micrographs of the used sample, where a high abundance of large, round gold nanoparticles was observed. Qualitatively, the gold particles appeared less facetted and rounder compared to the fresh sample. This was observed in the smaller gold particles in addition to the larger ones, as shown in Figure 3.10 that depicts a small, round gold nanoparticle in the top image and a slightly bigger, rounded nanoparticle in the bottom image.

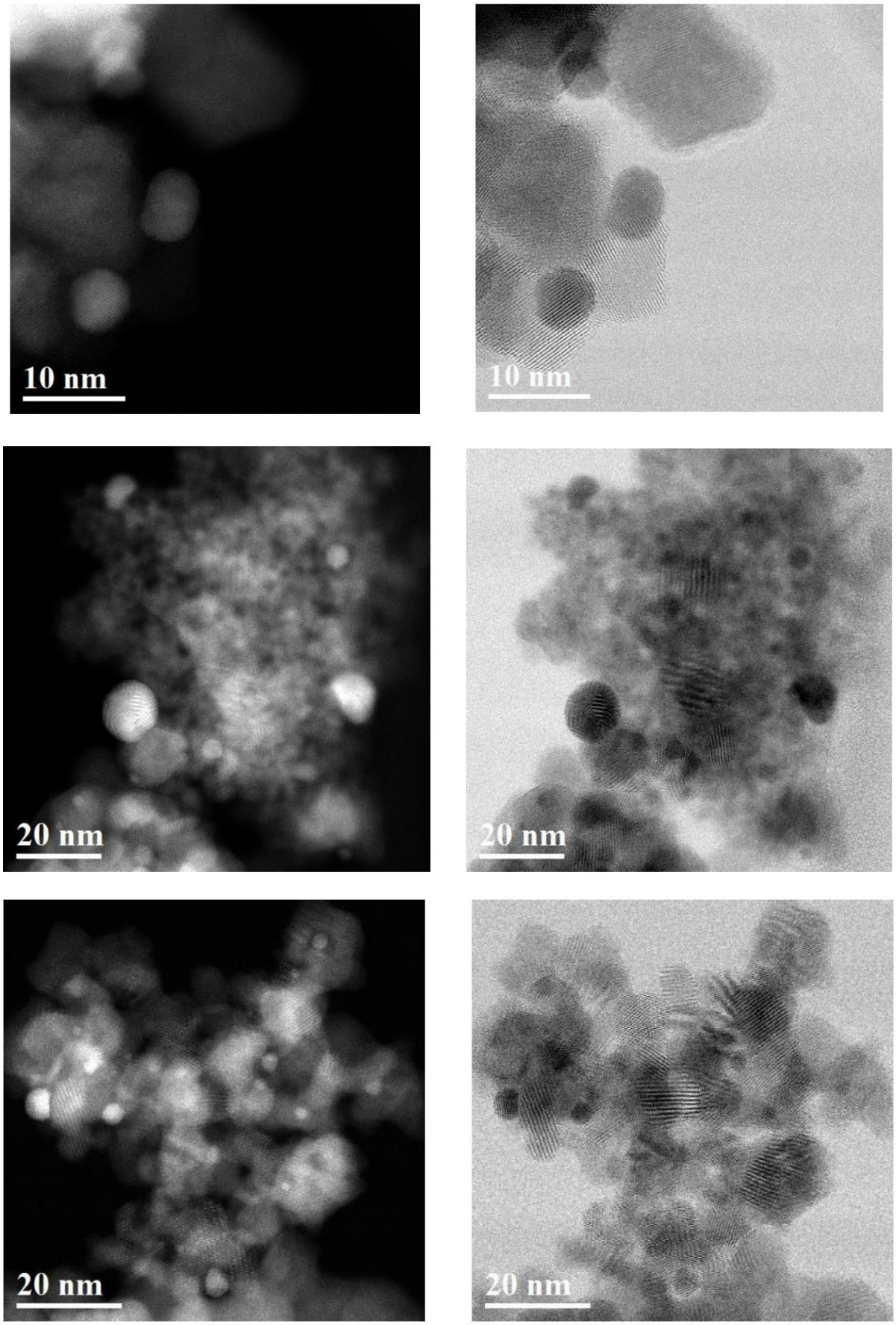

Figure 3.9 HAADF (left) and BF (right) Au nanoparticles in the used sample, with an abundance of large particles, exhibiting rounded morphologies.

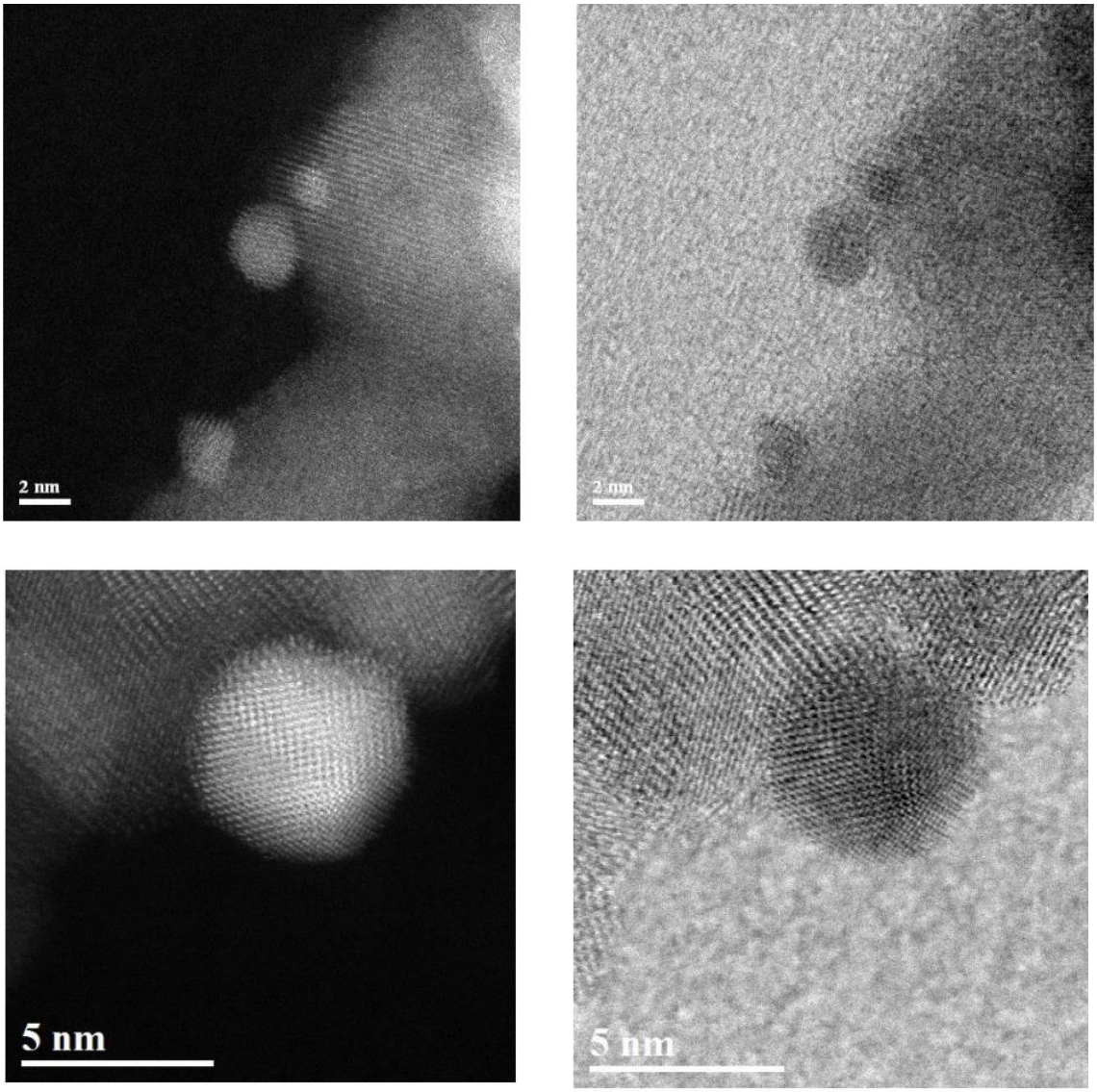

Figure 3.10 HAADF (left) and BF (right) images of small Au nanoparticles that exhibit well rounded morphologies

The calculated particle size distribution of the gold particles in the used sample is given in Figure 3.11. The mean particle diameter was 7.5 nm. This is significantly larger than the fresh sample and shows evidence of particle agglomeration occurring during the WGS reaction, consistent with the XPS data. In addition to the qualitative change in shape of the gold nanoparticles, two phenomena have been observed during the WGS reaction on the benchmark catalyst. These data support, to some extent, the work of Goguet *et al.* who proposed that morphological change caused catalyst deactivation in the WGS reaction.[1] Evidence of such a morphological change was observed, although sintering of the gold was also seen. The work of Marks and co-workers on Au/CeO_2[5] illustrates the sensitivity of the catalyst system in question and helps to explain the discrepancies between different reports in the literature.

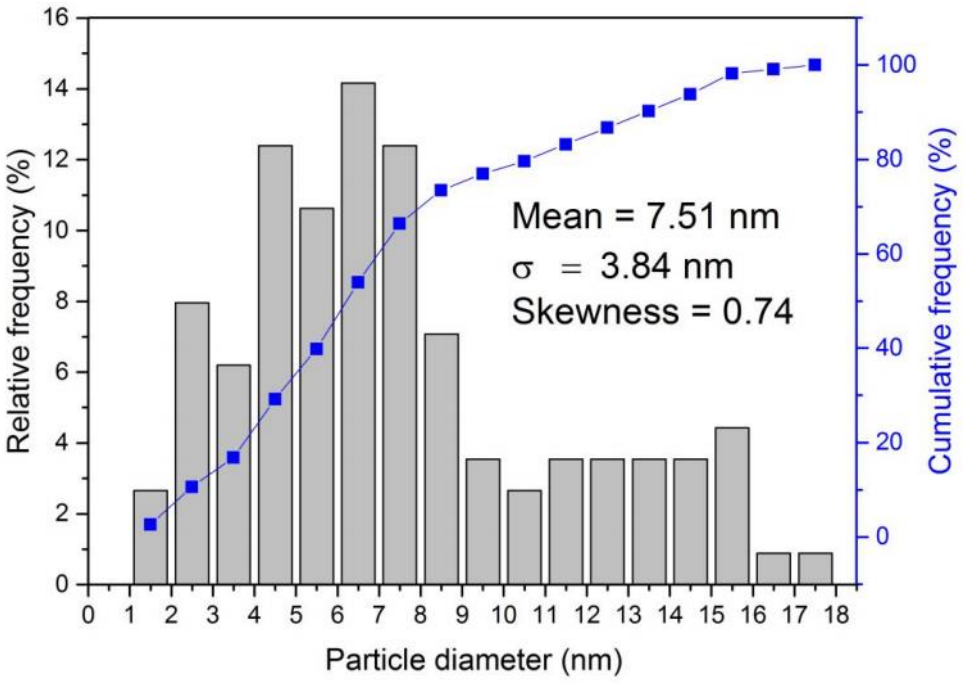

Figure 3.11 Particle size distribution for used $Au/CeZrO_4$ sample

3.5. Conclusions

In this short opening results chapter, a combined XPS and HAADF STEM study invesitgated the differences in fresh and used $Au/CeZrO_4$ after 48 h in a WGS reactor. XPS showed that partial reduction of the support occurred under the reaction conditions, which was expected. Thorough analysis of the Au 4f signal revealed that particle agglomeration and possibly reduction of gold was also a relevant process during the reaction. The HAADF STEM data corroborated the sintering observations and also showed morphological changes in the gold species, although these were not quantified and their significance was not established. Recent reports have disregarded sintering as a cause of deactivation in the WGS reaction although in these cases, microscopic evidence was not given. This is the first detailed microscopic study on the $Au/CeZrO_4$ system to date and has enhanced the understandng of the deactivation mechanism by showing that sintering is relevant, although it does not necessarily occur on all $Au/CeZrO_4$ catalysts. Whether morphological change or particle agglomeration occurs, the underlying property that needs to be addressed in future catalyst design is the adhesion or interaction between the precious metal and the support. Fundamental studies in this area have helped to illuminate the understanding of the metal-support

interaction but the fruits of this work have not been carried into the discovery of stable Au-based WGS catalysts.

This chapter served to identify a number of processes that occur during the WGS reaction on an $Au/CeZrO_4$ but could not evaluate the importance of each of the processes to the loss in activity and therefore much future work remains to be done. For example, *in situ* spectroscopy (and microscopy) offers a great opportunity to observe processes occuring in real time. EXAFS for example could be utilised to measure the growth of Au nanoparticles as the reaction proceeds. *In situ* CO-DRIFTS could also provide evidence of changes in the nature of the gold nanoparticle during the reaction that *ex situ* techniques might not resolve. Environmental TEM has proven to be a powerful tool for observing morphological changes in nanoparticles under various gaseous atmospheres[28] and could provide a powerful insight into how the particles change in different conditions.

3.6. References

1. A. Goguet, R. Burch, Y. Chen, C. Hardacre, P. Hu, R. W. Joyner, F. C. Meunier, B. S. Mun, A. Thompsett and D. Tibiletti, *Journal of Physical Chemistry C*, 2007, **111**.

2. D. Tibiletti, A. Amieiro-Fonseca, R. Burch, Y. Chen, J. M. Fisher, A. Goguet, C. Hardacre, P. Hu and A. Thompsett, *Journal of Physical Chemistry B*, 2005, **109**.

3. P. L. Hansen, J. B. Wagner, S. Helveg, J. R. Rostrup-Nielsen, B. S. Clausen and H. Topsoe, *Science*, 2002, **295**, 2053.

4. R. Burch, *Physical Chemistry Chemical Physics*, 2006, **8**, 5483.

5. Y. Lin, Z. Wu, J. Wen, K. Ding, X. Yang, K. R. Poeppelmeier and L. D. Marks, *Nano Letters*, 2015, **15**, 5375.

6. A. M. Venezia, G. Pantaleo, A. Longo, G. Di Carlo, M. P. Casaletto, F. L. Liotta and G. Deganello, *Journal of Physical Chemistry B*, 2005, **109**, 2821.

7. P. Bera and M. S. Hegde, *Catalysis Letters*, 2002, **79**, 75.

8. M. P. Casaletto, A. Longo, A. Martorana, A. Prestianni and A. M. Venezia, *Surface and Interface Analysis*, 2006, **38**, 215.

9. S. Zafeiratos and S. Kennou, *Surface Science*, 1999, **443**, 238.

10. C. Kuhrt and M. Harsdorff, *Surface Science*, 1991, **245**, 173.

11. C. R. Henry, *Surface Science Reports*, 1998, **31**, 235.

12. J. M. Cies, E. del Rio, M. Lopez-Haro, J. J. Delgado, G. Blanco, S. Collins, J. J. Calvino and S. Bernal, *Angewandte Chemie-International Edition*, 2010, **49**, 9744.

13. D. Dalacu, J. E. Klernberg-Sapieha and L. Martinu, *Surface Science*, 2001, **472**, 33.

14. E. A. Willneff, S. Braun, D. Rosenthal, H. Bluhm, M. Havecker, E. Kleimenov, A. Knop-Gericke, R. Schlogl and S. L. M. Schroeder, *Journal of the American Chemical Society*, 2006, **128**, 12052.

15. P. Rodriguez, D. Plana, D. J. Fermin and M. T. M. Koper, *Journal of Catalysis*, 2014, **311**, 182.

16. K. Luo, D. Y. Kim and D. W. Goodman, *Journal of Molecular Catalysis a-Chemical*, 2001, **167**, 191.

17. Y. Zhou, E. W. Peterson and J. Zhou, *Catalysis Today*, 2015, **240**, 201.

18. D. Boyd, S. Golunski, G. R. Hearne, T. Magadzu, K. Mallick, M. C. Raphulu, A. Venugopal and M. S. Scurrell, *Applied Catalysis a-General*, 2005, **292**, 76.

19. P. Burroughs, A. Hamnett, A. F. Orchard and G. Thornton, *Journal of the Chemical Society-Dalton Transactions*, 1976, 1686.

20. L. Liu, Z. Yao, B. Liu and L. Dong, *Journal of Catalysis*, 2010, **275**, 45.

21. M. Alifanti, B. Baps, N. Blangenois, J. Naud, P. Grange and B. Delmon, *Chemistry of Materials*, 2003, **15**, 395.

22. X. Yao, C. Tang, Z. Ji, Y. Dai, Y. Cao, F. Gao, L. Dong and Y. Chen, *Catalysis Science & Technology*, 2013, **3**, 688.

23. J. M. Zalc, V. Sokolovskii and D. G. Loffler, *Journal of Catalysis*, 2002, **206**, 169.

24. G. Bond, *Gold Bulletin*, 2009, **42**, 337.

25. T.-Y. Li, S.-J. Chiang, B.-J. Liaw and Y.-Z. Chen, *Applied Catalysis B-Environmental*, 2011, **103**, 143.

26. G. Avgouropoulos and T. Ioannides, *Applied Catalysis B-Environmental*, 2006, **67**, 1.

27. B. A. A. Silberova, M. Makkee and J. A. Moulijn, *Topics in Catalysis*, 2007, **44**, 209.

28. Q. Jeangros, T. W. Hansen, J. B. Wagner, C. D. Damsgaard, R. E. Dunin-Borkowski, C. Hebert, J. Van Herle and A. Hessler-Wyser, *Journal of Materials Science*, 2013, **48**, 2893.

Chapter 4

Gold-palladium catalysts supported on $CeZrO_4$ for low-temperature water-gas shift and related reactions

4.1. Introduction and aims of the chapter

In **Chapter 3** it was shown that the deactivation mechanism of the benchmark gold catalyst (2wt% Au/$CeZrO_4$) involved sintering as well as morphological changes, with the latter previously reported.[1] This chapter describes the work carried out to attempt to stabilise the benchmark catalyst through modification of the supported metal, which was hoped would enhance the interaction between the support and the supported metal. One of the most promising candidate metals to introduce to the gold catalyst was identified as palladium. This is because of the successful application of this bimetallic system to a wide range of oxidation reactions and the facile formation of AuPd alloys. A full investigation into the implications of introducing Pd to an Au catalyst was carried out which included catalyst screening as well as rigorous characterisation.

4.1.1. Gold-palladium catalysts for WGS and CO oxidation

A full review of the literature concerning gold-palladium bimetallic catalysts for WGS and the related reaction, CO oxidation was presented in **Chapter 1**. This section serves as a summary of the key publications in this field in order to provide the context for the results discussed herein.

Publications on AuPd catalysts for WGS are extremely limited, with one experimental report.[2] Tsang and co-workers prepared catalysts using a co-precipitation method and subsequently calcined the materials at 400 ^{o}C. Therefore these catalysts were not comparable to those prepared by deposition precipitation and the absence of rigorous characterisation left many questions unanswered. A theoretical study using DFT

predicted that AuPd catalysts would highly active for WGS due to the low energy barriers for the activation of H_2O and CO that were calculated.[3] However, this was based on a (100) AuPd surface rather than a supported nanoparticle so consideration of the support was not made, and given the importance of the metal-support interaction it is difficult to conclude that this study would be a sound prediction for supported AuPd catalysts.

In an analysis of the reaction mechanism of the gold-catalysed WGS reaction, Bond identified the potential of the AuPd system in the WGS reaction.[4] Specifically, he identified the success of this bimetallic catalyst in the decomposition of formic acid and speculated that the WGS reaction shared a common reaction intermediate. Therefore it was concluded that formic acid decomposition (FAD) could serve as a simple test reaction for WGS catalysts. In addition, Bond discussed the reaction mechanism of CO oxidation and compared it with that of the WGS reaction, highlighting the similarities and differences of each.

In the absence of rigorous research on the WGS reaction for AuPd catalysts, publications on CO oxidation were considered. While reports of AuPd catalysts supported on SiO_2 exist,[5, 6] no publications based on supports with considerable redox properties such as Ce-based oxides were found. There are several theoretical reports that predict AuPd catalysts to be highly active for CO oxidation based on the ability of Pd to activate O_2 and Au to activate CO.[7, 8]

As a result of this, the AuPd catalysts prepared in this chapter were screened for CO oxidation and formic acid decomposition in addition to WGS. CO oxidation was carried out to test the predictions made by theorists that AuPd should be active for CO oxidation and because no publications on this system have been reported. FAD was carried out to test Bond's hypothesis that the catalysts should behave similarly in the WGS reaction.[4] Also of interest was the activity trends of the catalysts in the different reactions, which could indicate fundamental similarities or differences in the mechanistic pathways of WGS, CO oxidation and formic acid decomposition.

4.1.2. Aims of the chapter

The aims of the work presented in this chapter are to investigate the applicability of gold-palladium bimetallic catalysts for the low-temperature WGS reaction and to test

the predictions made by computational and experimental chemists that gold-palladium bimetallic catalysts should be active for WGS. This also involved investigating how the addition of Pd affected the resultant bimetallic catalyst and how this compared with the properties of a monometallic Au catalyst. The mechanistically relevant CO oxidation and FAD were also studied in an attempt to extract mechanistic details of the WGS reaction and further understand the requisite properties for active WGS catalysts. Finally, clarification of the disparate literature was attempted in order to explain seemingly contradictory reports. A range of characterisation tools were employed in order to understand the nature of the catalyst but also to evaluate the importance of different catalyst properties and determine which of these properties is essential for an active catalyst.

4.2. Catalytic testing of AuPd/$CeZrO_4$

4.2.1. Au, Pd and AuPd/$CeZrO_4$ for the WGS reaction

Initial investigations into the AuPd system focussed on comparing the activity and stability of the benchmark monometallic Au catalyst with monometallic Pd and a bimetallic AuPd catalyst. Thus, these three catalysts were prepared and tested under the standard conditions described in **Chapter 2.1.3**. The AuPd catalyst was prepared to achieve an equi-molar amount of Au and Pd with a total nominal loading of 2 wt%. Figure 4.1 shows the activity and stability of these catalysts. The activity was measured after 1h on-stream and reflects the actual metal loading as determined by MP-AES and described in **Chapter 2.2.6**. Measurements were taken after one hour because this ensured the reactor had reached steady-state conditions, as evidenced by the time on-line data presented later in this chapter (Figure 4.2). This also represented a time-frame that clearly illustrated the short-term activity of the catalysts. The benchmark catalyst, Au/$CeZrO_4$ is significantly (3.6 times) more active per mole of metal than Pd/$CeZrO_4$ and more than 12 times more active than the equi-molar bimetallic catalyst. The fact that the bimetallic catalyst gave the lowest conversion was unexpected as there are many reports that describe the synergistic effect of combining gold and palladium to form bimetallic catalysts. This synergy is characterised by the bimetallic catalyst exhibiting higher activity than the equivalent quantity of either of the monometallic ones. In the case of the water-gas shift reaction, the opposite is true: The combination of these two supported metals resulted in a catalyst of lower activity

than the sum of the activity of the monometallic catalysts. This effect was called anti-synergy. The deactivation rate was calculated using the loss in activity over the first hour on-line. Using this method, all three catalysts deactivated at similar rates, which was approximately 5% h^{-1}.

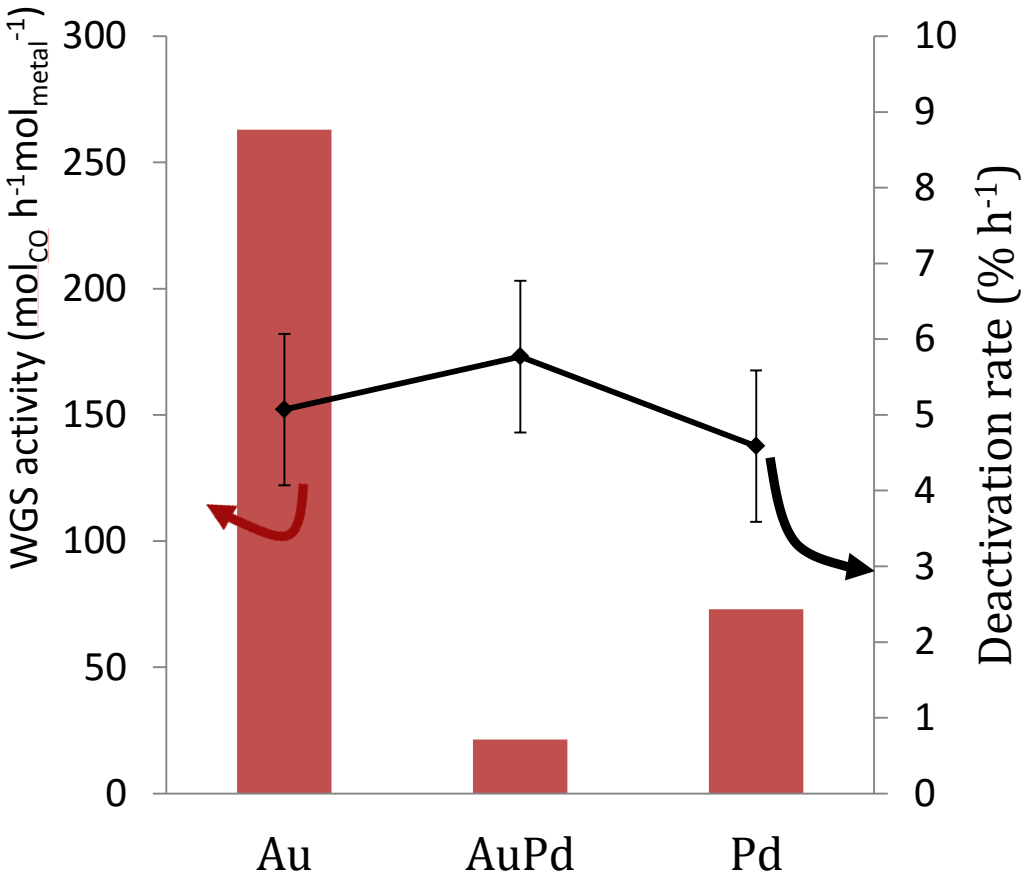

Figure 4.1 The catalytic activity of Au, AuPd and Pd supported on $CeZrO_4$ after 1 h on-line(bars, left axis) and the rate of deactivation (black diamonds, right axis). Reaction conditions: 150 °C, 0.15 g catalyst, 100 ml min^{-1} Gas feed: 2% CO, 2% CO_2, 7.5% H_2O, 8.1% H_2 and N_2.

4.2.2. Further investigations: The effect of the Au:Pd ratio

In order to fully investigate this catalytic system, a number of bimetallic catalysts were prepared with a range of AuPd molar ratios, as described in **Chapter 2.1.3.** MP-AES was carried out in order to determine the actual metal loadings and Au:Pd molar ratios of the catalysts. The results are given in Table 4.1. The activity of the catalysts was reported in terms of the number of moles of the substrate converted per hour per moles of supported metal on the catalyst. In the DP method of catalyst preparation, it is common for the nominal loadings of metals to differ from the actual metal loadings and so reporting the "CO conversion" is not sufficient for accurate catalyst comparisons. The catalyst $Au_{93}Pd_7/CeZrO_4$ illustrates this well (Table 4.1).

Table 4.1 Elemental analysis of $Au_xPd_y/CeZrO_4$ catalysts determined using MP-AES

Nominal Au loading (%)	Actual molar ratios (Au_xPd_y)[a]	mmol metal g^{-1}			Total weight loading (%)
		Au	Pd	Total	
100	Au	0.075	0.000	0.075	1.47
99	$Au_{99}Pd_1$	0.083	0.001	0.084	1.65
95	$Au_{93}Pd_7$	0.096	0.003	0.099	1.93
91	$Au_{86}Pd_{14}$	0.075	0.012	0.087	1.60
75	$Au_{67}Pd_{33}$	0.059	0.029	0.088	1.47
68	$Au_{64}Pd_{36}$	0.061	0.035	0.096	1.58
62	$Au_{55}Pd_{45}$	0.050	0.040	0.090	1.41
50	$Au_{44}Pd_{56}$	0.044	0.056	0.100	1.46
15	$Au_{12}Pd_{88}$	0.016	0.121	0.137	1.61
9	Au_8Pd_{92}	0.015	0.163	0.178	2.02
0	Pd	0.000	0.162	0.162	1.72

While the nominal loading of Au on this catalyst was lower than that of $Au/CeZrO_4$, MP-AES showed that the actual Au loading was higher. This explained why $Au_{93}Pd_7/CeZrO_4$ achieved higher catalytic conversions than the mono-metallic Au catalyst.

However, when the WGS activity is calculated as described above, the actual metal loadings are considered and the catalytic activity in the WGS reaction was lower than that of the mono-metallic Au catalyst, as seen in Figure 4.2. The notation of bimetallic catalysts throughout this chapter is that the bimetallic catalysts are Au_xPd_y where x and y represent the molar percentage of that metal as determined from MP-AES analysis. The exceptions are the monometallic catalysts which are simply referred to as either $Au/CeZrO_4$ or $Pd/CeZrO_4$.

The nanostructure of the Au_xPd_y catalysts is also of importance as this has been shown to be important for determining catalytic activity and selectivity.[9, 10] However, forming specific nanostructures such as a core-shell morphology typically involves careful synthesis procedures which have not been used here. Furthermore, the determination

of the nanostructure is very challenging and beyond the scope of the current study. Therefore, based on the catalyst preparation method it is unclear what type of nanostructure was synthesised and more importantly what the nanostructure of these catalysts is under reaction conditions.

As described in **Chapter 1**, the poor stability of $Au/CeZrO_4$ was the motivation for modifying the catalyst although the retention of high activity was of course also a fundamental requirement. A range of $AuPd/CeZrO_4$ catalysts were screened for 90 minutes under WGS reaction conditions although some screening tests were terminated prematurely due to the poor performance of the catalyst. The time on-line data is shown in Figure 4.2. The activity of each catalyst varies heavily with the Au:Pd loading: $Au/CeZrO_4$ remains the most active catalyst and any combination of Au and Pd is significantly less active per mole of metal on the catalyst. The fact that such low conversions were observed in the bimetallic catalysts means that even if these systems were more stable, their applicability in fuel cell technology would not be appropriate.

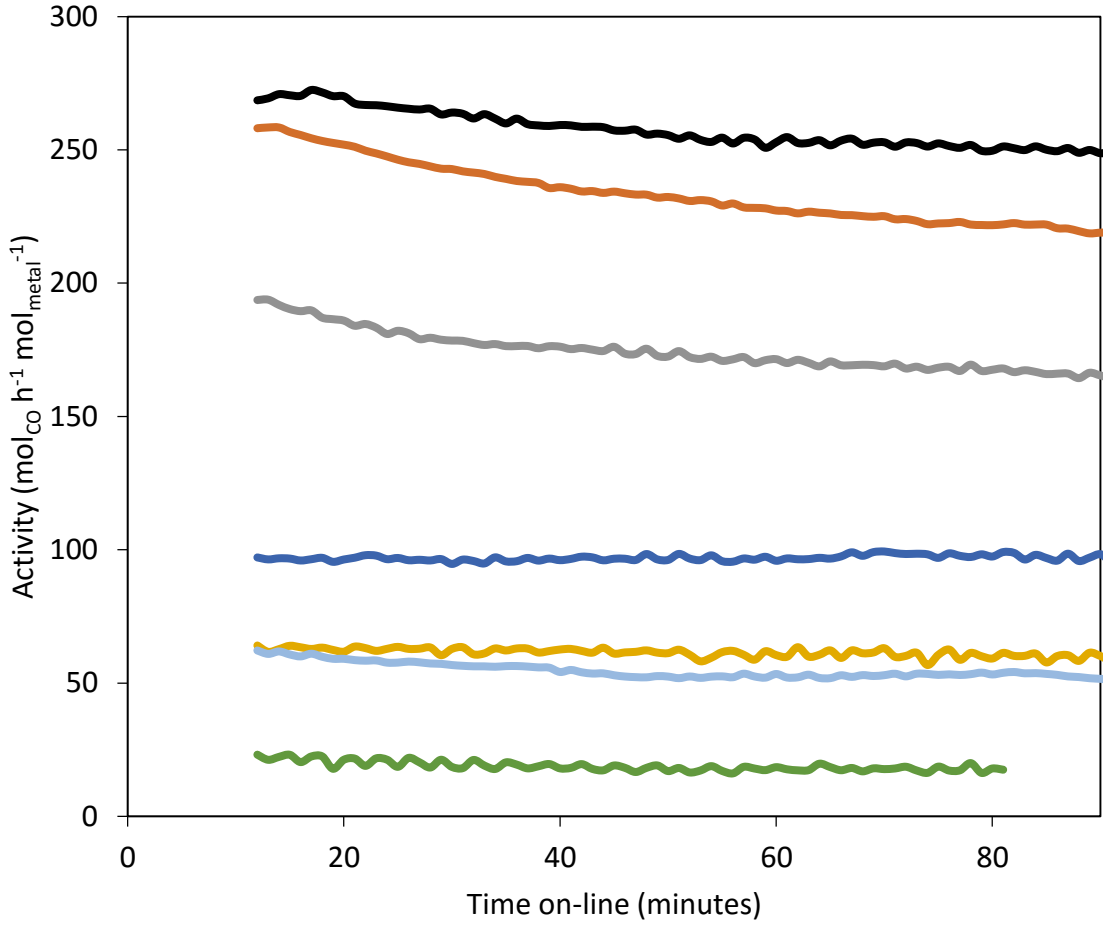

Figure 4.2 Time on-line water-gas shift data for a selection of $Au_xPd_y/CeZrO_4$ catalysts. From top to bottom: Au, $Au_{93}Pd_7$, $Au_{86}Pd_{14}$, $Au_{55}Pd_{45}$, $Au_{67}Pd_{33}$, Pd and $Au_{44}Pd_{56}$. Reaction conditions: 150 °C, 0.15 g catalyst, 100 ml min^{-1} Gas feed: 2% CO, 2% CO_2, 7.5% H_2O, 8.1% H_2 and N_2.

Despite this, the stability of the catalysts was measured to assess if there were in fact improvements which could be understood and exploited in future catalyst design.

The normalised conversion of the series of AuPd catalysts is shown in Figure 4.3. This is calculated by normalising each data-point against the highest conversion observed in that reaction. In this case, each data-point is normalised against the conversion after approximately 10 minutes on-stream. There appears to be a large variation in the stability of the catalysts over the initial two hours on-line. The most stable catalyst over this period was $Au_{55}Pd_{45}/CeZrO_4$, which maintained the vast majority of its initial activity after 2 hours. Interestingly, the least active catalyst was $Au_{44}Pd_{56}/CeZrO_4$, which lost over 20% of its initial activity in the first hour. It should be noted that the data points are not well correlated due to the low conversion achieved by this catalyst so small deviations in the concentration of CO have large effects on the normalised

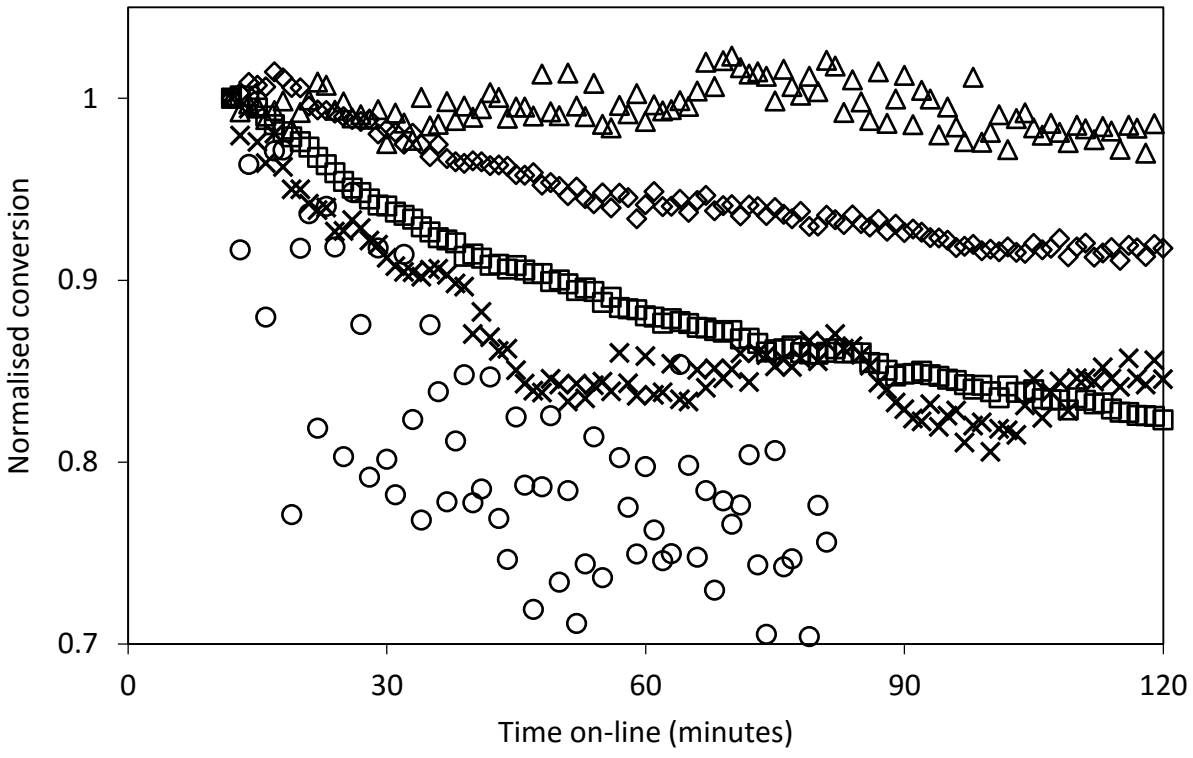

Figure 4.3 Normalised conversion showing initial stability for $Au/CeZrO_4$ (diamonds), $Au_{93}Pd_7/CeZrO_4$ (squares), $Au_{55}Pd_{45}/CeZrO_4$ (triangles), $Au_{44}Pd_{56}/CeZrO_4$ (circles) and $Pd/CeZrO_4$ (crosses). Reaction conditions: 150 ^oC, 0.15 g catalyst, 100 ml min^{-1} Gas feed: 2% CO, 2% CO_2, 7.5% H_2O, 8.1% H_2 and N_2.

conversion. Despite this, it can be seen that $Au_{44}Pd_{56}/CeZrO_4$ deactivates rapidly. It should be noted that the time scale of this stability measurement is not relevant in the

context of an industrial process. Ideally, the catalyst stability should be measured over more than 120 minutes. In light of this, overnight screening experiments were conducted and the stability of the catalysts analysed over 16 h. Figure 4.4 shows the deactivation rate of a selection of AuPd/$CeZrO_4$ catalysts. The normalised conversion represents the loss in activity from 3h to 16 h on-line. This ensured the system had stabilised before the deactivation rate was calculated. After consideration of the long term stability, the $Au_{55}Pd_{45}$/$CeZrO_4$ catalyst no longer appeared to be the most stable. It retained 89% of its original conversion while the benchmark catalyst retained 88%; a difference that was considered to be within experimental error.

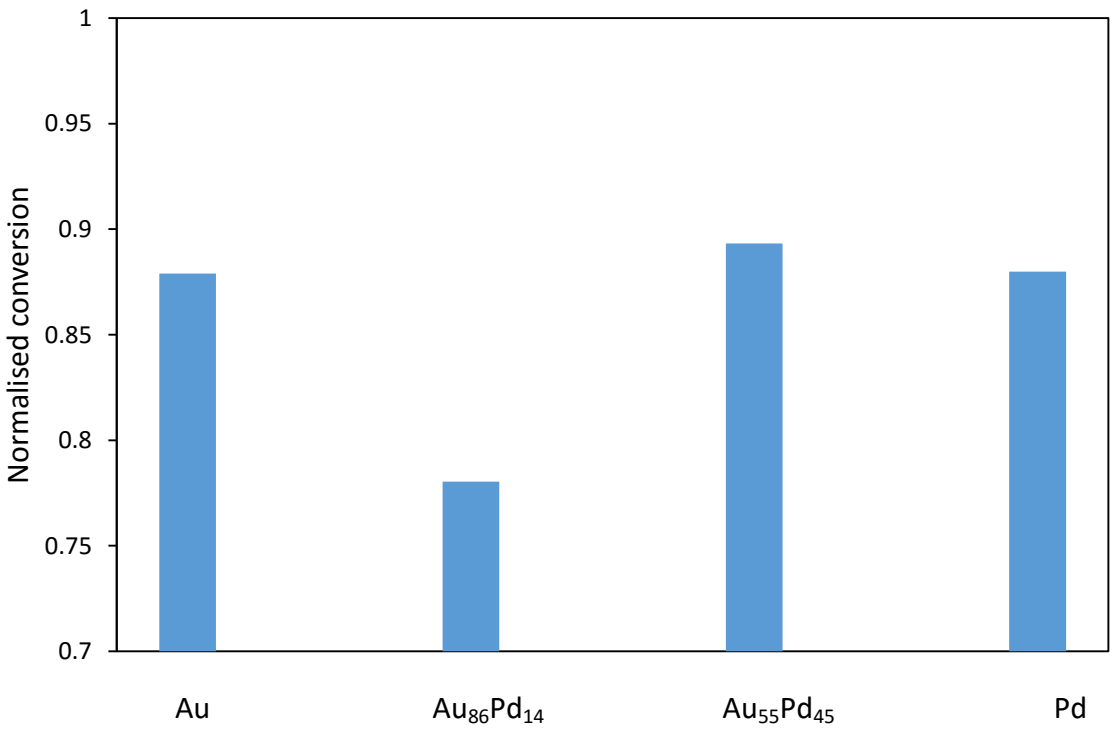

Figure 4.4 Deactivation of a selection of AuPd/$CeZrO_4$ catalysts after 16 h on-line. Normalised conversion calculated over the period of 3 - 16 h. Reaction conditions: 150 °C, 0.15 g catalyst, 100 ml min^{-1} Gas feed: 2% CO, 2% CO_2, 7.5% H_2O, 8.1% H_2 and N_2.

Despite the failure of this system to satisfy the original aim of the project, further work on this catalyst system was carried out in order to understand how the combination of two metals resulted in decrease of activity with the aim of enhancing the understanding and design of future WGS catalysts.

4.2.3. The activity of Au_xPd_y/$CeZrO_4$ for WGS and related reactions

As discussed in **Chapter 1**, AuPd was predicted to be highly active for WGS[3, 4] and CO oxidation[7] and formic acid decomposition was identified as a possible test reaction for

WGS catalysts.[4] The next section of this chapter describes the work carried out to test these hypotheses by screening the series of prepared catalysts for CO oxidation and formic acid decomposition as well as the oxidation of benzyl alcohol. In order to observe the relationship between the Au:Pd molar ratio and the catalytic activity for the reactions of interest, the data was presented as the activity plotted against the Au mol content, determined using MP-AES.

Low-temperature water-gas shift

The effect of the Au:Pd ratio on the catalytic activity in WGS is illustrated in Figure 4.5. The activity measurement of each catalyst was made after one hour of exposure to the reaction gases. As described above, $Au/CeZrO_4$ was the most active catalyst and the introduction of Pd resulted in a sharp decrease in activity. The catalysts that exhibited the poorest conversions had an Au mol content of 10-40%. Interestingly, Pd was more active than the Pd-rich bimetallic catalysts. The overall trend across the range of

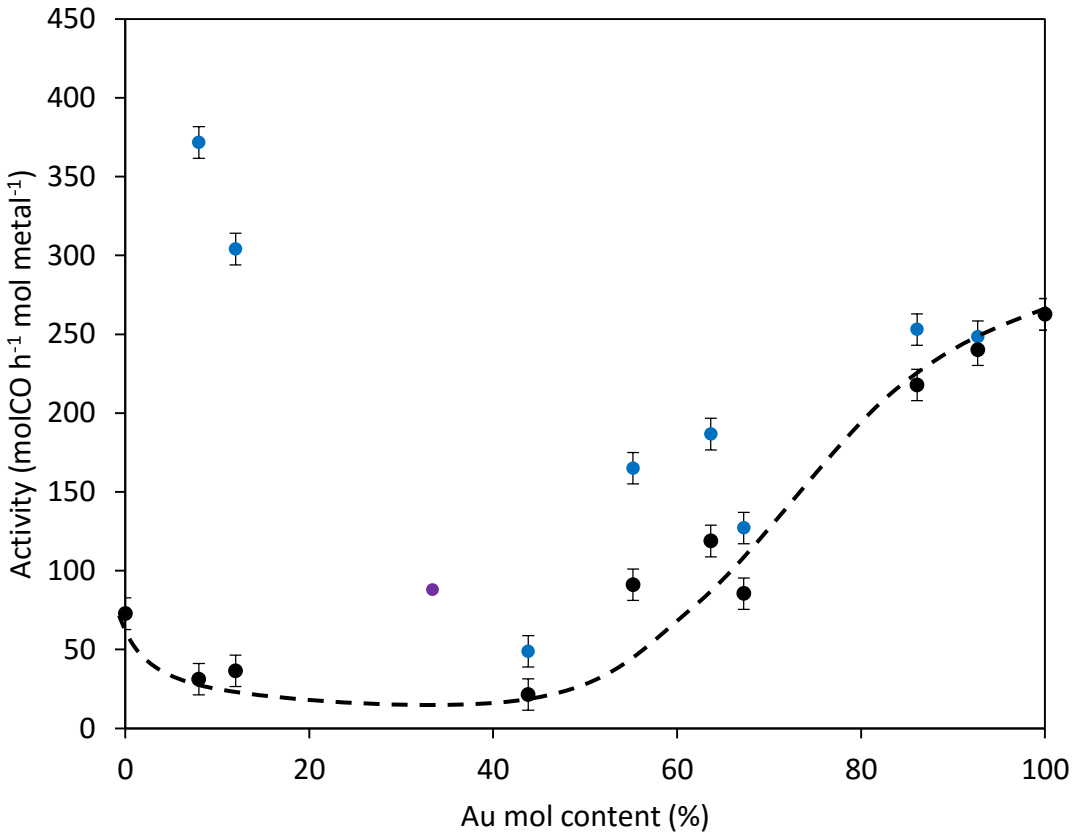

Figure 4.5 The water-gas shift activity of a range of $Au_xPd_y/CeZrO_4$ catalysts measured per mole of total metal (black circles) and moles of Au on the catalyst (blue circles). The purple data point is a physical mixture of Au and Pd. Activity measured after 1 h on-stream. Reaction conditions: 150 °C, 0.15 g catalyst, 100 ml min^{-1} Gas feed: 2% CO, 2% CO_2, 7.5% H_2O, 8.1% H_2 and N_2.

catalysts is notable and shows that the overall activity of these catalysts is not simply the sum of the two monometallic catalyst's activity. If that was the case, a straight line would be expected across the range of catalysts. The majority of the literature on AuPd catalysts reports a "synergy" between the two metals because the presence of both Au and Pd in the catalyst formulation resulted in a significantly more active catalyst. Benzyl alcohol oxidation is a prototypical example. However, in the WGS reaction the opposite effect was observed: The presence of Au and Pd in the catalyst formulation gave a catalyst that was significantly less active than the monometallic equivalent catalysts. This effect was therefore characterised as *anti-synergy.* Interestingly, when a physical mixture of the Au and Pd catalysts was tested for WGS activity, it was found that the WGS activity was more active than the bimetallic catalysts. This is represented by the purple data point in Figure 4.5. The physical mixture was 75 mg of $Pd/CeZrO_4$ and 75 mg of $Au/CeZrO_4$, which corresponded to a molar Au content of 35%. The higher activity of this data-point supports the hypothesis that the interaction between Au and Pd is central to the catalytic activity trend observed in Figure 4.5.

For the Au-rich catalysts where the Au mol content was above 50%, the catalytic activity was very sensitive to the Au:Pd molar ratio. Conversely, the Pd-rich catalysts where Au mol content was below 50%, very similar catalytic conversions were measured. This implies that while the nanostructure/elemental composition of the supported metal is changing, the catalytically active component is not. One possible explanation for this observation considers the mobility of the Au and Pd atoms under reaction conditions. It has been shown experimentally that the distribution of Pd atoms in bimetallic AuPd nanoparticles is dynamic and dependent on its environment. Zhu *et al.* used density functional theory (DFT) calculations and diffuse reflectance Fourier transform infrared spectroscopy (DRIFTS) to study the surface nanostructure of $AuPd/Al_2O_3$ under an atmosphere of CO at room temperature.[11] They found that over time, the linear stretching modes of CO adsorbed on Au decreased in $AuPd/Al_2O_3$. Furthermore, the bands associated with linear and non-linear CO on Pd increased concomitantly. The explanation for this was the surface enrichment of Pd in the presence of CO. The DFT investigation supported the DRIFTS data and showed that Pd preferentially occupies under co-ordinated edge sites of AuPd nanoparticles. These under-co-ordinated edge sites are thought to be the active site for the gold-catalysed

reaction[12] and it is intuitive that this would also be the case for the palladium-catalysed reaction. In addition, Delannoy *et al.* used DRIFTS and environmental transmission electron microscopy (ETEM) to observe the restructuring of an AuPd/TiO_2 catalyst. Under a CO/O_2 feed, the Pd segregated to edge sites of the catalyst to form a $Au_{core}Pd_{shell}$ nanostructure.[13]

Several other researchers have also reported the segregation of Pd[8, 14-16] and other metals[17-19] to the surface in the presence of CO in Au-containing bimetallic catalysts. Although this effect has not been demonstrated under WGS conditions, CO is present as a reactant and therefore could interact with the nanoparticles in a similar way. This could explain the similarity of the catalytic activity in the Pd-rich catalysts: When there is an excess of Pd in the bimetallic nanoparticles and it is exposed to CO, Pd will occupy all the under co-ordinated edge sites. Therefore the catalytic activity will be dominated by the rate of the Pd-catalysed reaction; Au becomes a spectator species.

For comparison, the catalytic activity per mole of Au was also plotted in Figure 4.5, represented by the blue circles. As Pd was introduced to the catalyst, the activity per mole of Au decreased, suggesting that the Au in the bimetallic catalysts was less active than the Au in the monometallic catalyst. This observation is consistent with an increase in the particle size of the bimetallic catalysts and suggests that the interaction of Au and Pd affects the chemical properties of the Au.

The final notable observation is that the monometallic Pd catalyst was more active than the Pd-rich bimetallic catalysts. In the context of the above discussion, whereby it seems likely that in the Pd-rich catalysts the chemistry is dominated by Pd, the reason for the enhanced activity of the Pd catalyst could simply be metal dispersion/particle size, which could be measured using electron microscopy.

Overall, the inverted-volcano plot observed for the WGS reaction suggests that there are significant chemical differences between the catalysts tested that go beyond the AuPd ratio. These differences will be explored in the later part of this chapter.

CO oxidation

The WGS activity of the AuPd catalysts was then compared with their activity in CO oxidation. CO oxidation is one of the most studied reactions in catalysis, not just for its practical application to purify gases but also as a test reaction for supported metal

catalysts. However literature on AuPd catalysts for this reaction is sparse. CO oxidation has frequently been compared to the WGS reaction for its mechanistic similarities. Bond noted that in both reactions, CO reacts with a water molecule that forms an intermediate,[4] which is then oxidised to produce CO_2. In CO oxidation, the intermediate can be oxidised by O_2, but in water-gas shift this could occur with an additional water molecule.[4] It is therefore instructive to compare the activity trends in the WGS reaction with those in CO oxidation. Similarities or differences in the activity trends could help to enhance the understanding of the reaction steps of each reaction. The catalytic activity of each catalyst for CO oxidation is shown in Figure 4.6. The activity was measured after 1 h on-stream. It can be seen that the overall activity trend is remarkably similar to that of the WGS reaction: Au remains the most active catalyst, while Pd-rich bimetallic catalysts displayed the poorest activity. Also, the Pd catalyst was more active than the bimetallic catalysts. In the above section, the mobility of Pd in the bimetallic nanoparticles was postulated as a possible relevant process that explains the activity trends.

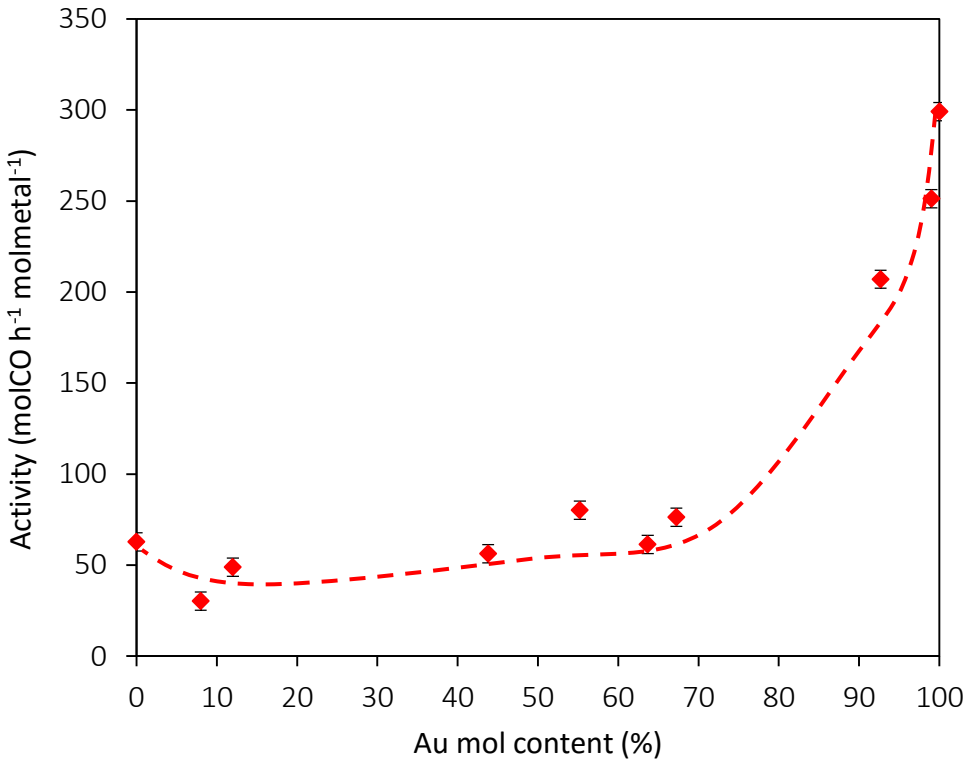

Figure 4.6 The CO oxidation activity of AuPd/$CeZrO_4$ catalysts. Activity measured after 1h on-stream. Reaction conditions: 35°C, 0.020 g catalyst, 20ml min^{-1} 5000 ppm CO/air.

While this explanation remains a hypothesis, the similarity in the activity trends suggests that there are underlying parallels between these two reactions and perhaps the segregation of Pd is occurring in both reactions and this affects the activity of these catalysts.

Formic acid decomposition (FAD)

As discussed above, AuPd catalysts were identified by Bond as candidates for highly active water-gas shift catalysts.[4] In addition to this, Bond suggested that FAD could be used as a test reaction to screen for WGS activity. This hypothesis was tested by modifying the WGS reactor to accommodate FAD experiments, as described in **Chapter 2**. The catalytic activity data for a selection of AuPd/$CeZrO_4$ catalysts is presented in Figure 4.7. It can be seen that the activity trend approximates that of the WGS and CO oxidation reactions, whereby Au is the most active catalyst and the introduction of Pd results in a decrease in activity. While there are fewer data points in the Pd-rich region, the same activity insensitivity to Au:Pd ratio is observed in this region of the graph. The $Au_{55}Pd_{45}/CeZrO_4$ catalyst had a slightly higher conversion than catalysts with similar Au:Pd ratios but this was also observed for CO oxidation and WGS. It could indicate

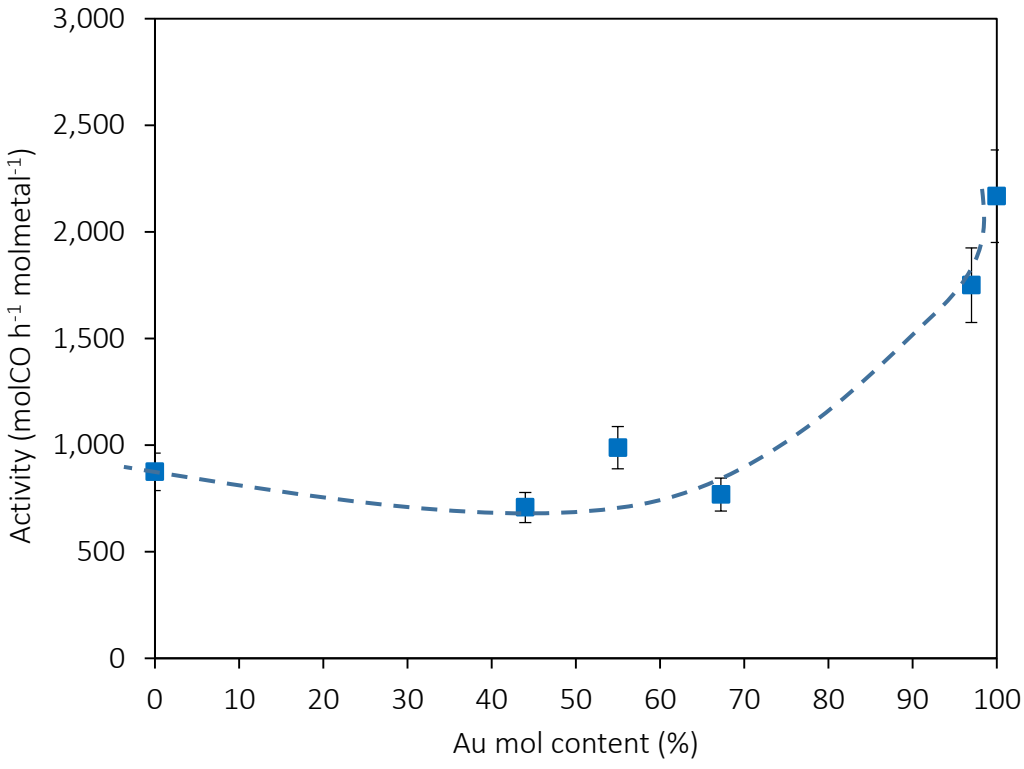

Figure 4.7 The FAD activity of a selection of AuPd/$CeZrO_4$. Activity measured after 1h on-stream. Reaction conditions: 0.050g catalyst, 85 °C, Total flow: 100 ml min^{-1}. 1700 ppm HCOOH, 1500 ppm H_2O + N_2.

that this catalyst has smaller metal particles than the others. With the exception of Pd, each catalyst exhibited 100% selectivity to H_2 and CO_2. Pd exhibited 97.5% selectivity to CO_2 and H_2 and 2.5% selectivity to $CO+H_2O$.

While numerous accounts of FAD have been reported, including many recent studies that explore the viability of formic acid as a hydrogen storage compound, the experimental conditions are typically different from those used in this study. Furthermore, many studies concern gold and palladium supported on non-reducible metal oxides including carbon, SiO_2, Al_2O_3 and TiO_2[20-23] or are used as electrocatalysts[24] and so comparisons are problematic.

However, one study conducted by Davis *et al.* is of particular relevance to this work: The authors explored the link between WGS and FAD for Pt/CeO_2 catalysts. As well as identifying similar kinetic isotope effects in their studies on FAD with literature results for WGS, they also postulated existence of a common intermediate: a bidentate formate species. The authors reported that the support was crucial to the formation of the intermediate. Specifically, the reducibility of the CeO_2 facilitated bridging OH groups that could then react with either CO or formic acid to ultimately produce the same intermediate species. Therefore it is feasible that the same intermediate is formed on the Au catalyst, although further work would be needed to demonstrate it fully.

Another study that recognises similarities between WGS and FAD was conducted by Iglesia *et al.*[23] who suggested that both reactions require Au clusters that were invisible to TEM for high activity, i.e. very small metal nanoparticles. This was shown by the decrease in activity of their Au/Al_2O_3 catalyst after thermal treatments as a result of sintering. Interestingly, the same catalysts were screened for CO oxidation activity, the same decrease in activity was not observed. It was concluded that the active species for CO oxidation must be the larger, TEM visible particles. This is inconsistent with the findings of this study, where it has been observed that in each reaction, the same activity trend is observed.

Several literature reports identify Pd as being more active than Au[21, 22, 25] for FAD which was not observed in this investigation. However the discrepancy of those reports with the findings in this work can be explained by the significant difference in both the

experimental conditions and the supports used in the studies. The sensitivity of the reaction conditions on the catalytic activity was demonstrated by Ross and co-workers who showed that the activity of Au/TiO_2 catalysts are significantly improved by the addition of water into the reactor.[21] They attributed this effect to the water-gas shift reaction taking place. Likewise, in a subsequent paper by the same group it was shown that Pd/Al_2O_3 catalysts are significantly inhibited by the presence of CO, possibly due to the strong chemisorption that occurs when Pd is exposed to CO.[22]

The segregation of Au and Pd under reaction conditions, specifically under exposure to CO, was earlier postulated as an explanation for the activity trends for WGS and CO oxidation. The fact that FAD exhibits the same trend does not disprove this. In fact, the segregation of Au and Pd in bimetallic catalysts has been reported in media other than CO, for example in the hydrogenation of 1,5-cyclooctadiene.[26] Therefore it is possible that segregation would occur under the FAD reaction conditions. The similarity in activity trends is likely to be caused by a property such as metal particle size. Perhaps each reaction mechanism favours a small metal particle size and this is reflected in the variation across the series of AuPd catalysts prepared. Another possible commonality is the active site in each of the reactions: the metal-support interface. It is known that the role of the support is to activate the water molecule and produce OH groups proximal to the metal nanoparticle in each of the reactions.

The results obtained are in agreement with the reports that identified mechanistic similarities in FAD and WGS and suggest there are underlying similarities, possibly reaction intermediates or possibly active sites. These data do not provide concrete conclusions regarding the mechanisms or active sites for these reactions but are incentives for further work in this area.

Benzyl alcohol oxidation

The synergistic effect of AuPd bimetallic catalysts is well documented for benzyl alcohol oxidation, as described earlier. In order to confirm that the catalysts used in this study were relevant to the ones described in the literature, a selection of AuPd catalysts were tested for this reaction. The results are shown in Figure 4.8 which includes the activity data for all the reactions that were screened. In line with previous studies, the $AuPd/CeZrO_4$ catalysts also displayed remarkable synergy for benzyl

alcohol oxidation.[27-29] This synergy demonstrates that the activity trends for WGS and CO oxidation were in fact valid and the catalysts prepared in this work were comparable to those reported in the literature.

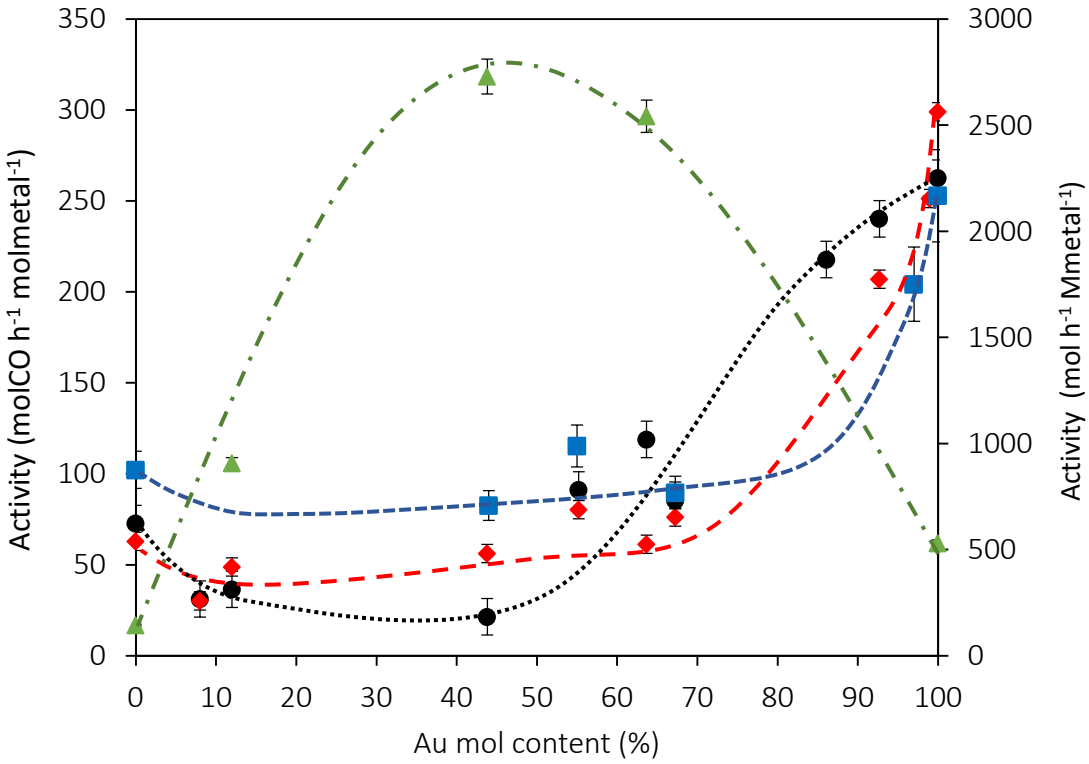

Figure 4.8 The catalytic activity of $Au_xPd_y/CeZrO_4$ for water-gas shift (●), CO oxidation (♦), formic acid decomposition (■) and benzyl alcohol oxidation (▲). Activity measurements recorded after one hour on-stream.

4.2.4. The effect of the support: Comparison with AuPd/TiO_2 catalysts

The effect of the support was probed to determine whether the anti-synergy observed in this work was a property induced by the $CeZrO_4$ support or whether it was a property of AuPd catalysts in general. A range of catalysts supported on TiO_2 were prepared by deposition precipitation method, as described in **Chapter 2.1.3.** Catalyst were characterised by MP-AES to determine the metal loadings of the final catalysts, as was done with the $CeZrO_4$ catalysts. It was found that Au/TiO_2 was not active for WGS under the reaction conditions used, consistent with previous reports.[30] Therefore each catalyst was screened for CO oxidation activity under the same conditions as the $CeZrO_4$ catalysts. The activity trends are presented in Figure 4.9. The elemental

composition of each of the Au_xPd_y/TiO_2 catalysts, as determined by MP-AES, is given below in Table 4.2.

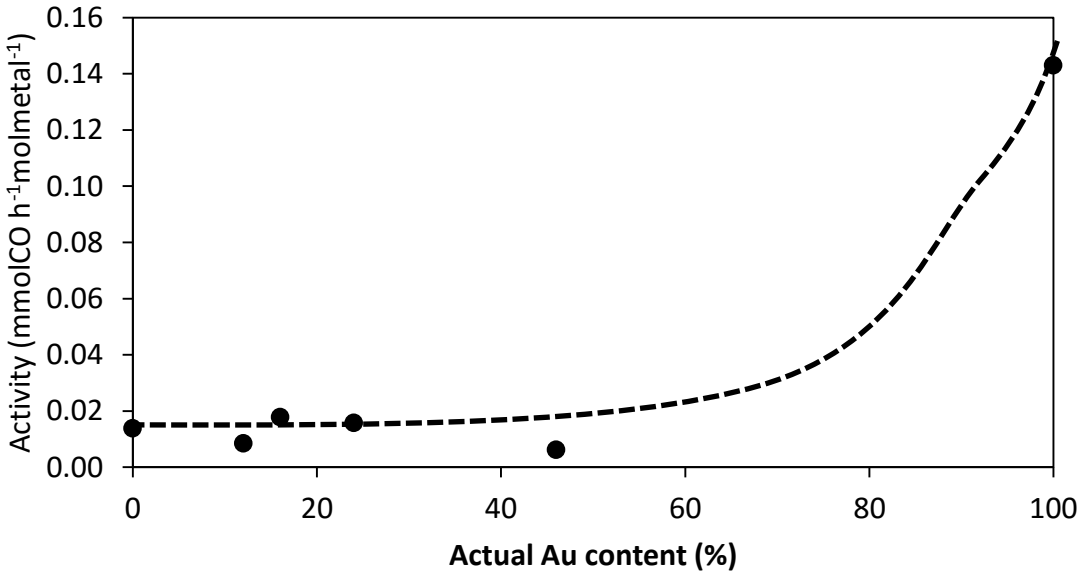

Figure 4.9 CO oxidation activity of $AuPd/TiO_2$ catalysts. Reaction conditions: 35°C, 0.020 g catalyst, 20ml min^{-1} 5000 ppm CO/air.

It can be seen that the activity trends observed for the $AuPd/TiO_2$ catalysts are similar to those found in the $AuPd/CeZrO_4$ catalysts whereby Au/TiO_2 was the most active catalyst for CO oxidation and the Pd-rich bimetallic catalysts were the least active, although the monometallic Pd did not outperform the Pd-rich bimetallic catalysts. Similar to the $CeZrO_4$ catalysts, where Au mol content was less than 50% the activity did not vary significantly with the gold-palladium molar ratio.

The actual metal loadings determined using MP-AES and then confirmed using XPS are very different from the nominal loadings. The discrepancies are essentially due to the low yields of gold and high yields of palladium deposited onto the support. This is illustrated by the fact that the monometallic Au/TiO_2 catalyst was measured to have 0.52 wt% gold compared to the $Au/CeZrO_4$ catalyst, that consisted of 1.47 wt% gold. Surprisingly, the monometallic Pd catalyst had a loading of 2.67 wt% palladium, higher than the nominal loading. If the concentration of the aqueous $PdCl_2$ precursor solution was higher than thought, this could explain this observation. However, the concentration of the precursor was verified using MP-AES. This leaves the possibility that the dispersion of the metal was very inhomogeneous and the sample analysed happened to contain high concentrations of Pd, although this is unlikely. The origin of the differences in metal loadings must be the difference in the surface charge of the

support. If the isoelectric point of the $CeZrO_4$ support is higher than that of P25 TiO_2, which is reasonable according to literature values,[31] the surface charge will be more negative for TiO_2 at pH 8, meaning that the affinity of the negatively charged hydroxylated gold species will be lower on TiO_2 than $CeZrO_4$. Therefore, less gold will be deposited on the surface. A lower pH e.g. 6 or 7 would yield higher gold loadings although this would also affect the speciation of the gold precursor – at lower pH, there will be a higher abundance of chlorinated gold species, which have been shown to lead to larger particles.[32]

The significant variations in metal loading across the range of catalysts mean that the comparison of the catalyst activity becomes problematic, because while the activity is normalised against the moles of metal on that catalyst, the dispersion of the metals will be limited at higher metal loadings. This could explain why the Pd catalyst was not as active as expected. Overall, the preparation of the TiO_2 supported catalyst was not optimised but the activity trend observed closely resembled that of the $CeZrO_4$-supported catalysts.

Table 4.2 shows that there were large discrepancies in the elemental analysis of the XPS and MP-AES loadings. The mol% of Au was consistently higher in the XPS analysis than the MP-AES analysis. The origin of this difference could be due to a surface enrichment of gold in the bimetallic metal particles under the conditions of the XPS experiment.

Table 4.2 Elemental analysis of AuPd/TiO_2 catalysts determined by MP-AES and XPS

Catalyst (Nominal loadings)	Total metal loading (wt%) (MP-AES)	Mol% Au (MP-AES)	Mol% Au (XPS)
Au	0.52	100	100
$Au_{80}Pd_{20}$	0.64	34	46
$Au_{60}Pd_{40}$	1.19	22	24
$Au_{40}Pd_{60}$	1.61	14	16
$Au_{20}Pd_{80}$	2.21	7	12
Pd	2.67	0	0

It is also possible that the gold is better dispersed than the Pd: It is likely that at pH 8, there is a relatively poor interaction of the gold species with the TiO_2 support and so the gold is highly dispersed, making it easier to detect than the Pd, which could exist in large particles.

4.3. Rationalising the activity trends through catalyst characterisation

In Section 4.1 a range of AuPd/$CeZrO_4$ catalysts were tested for several reactions and a number of interesting trends were found, namely the anti-synergistic effect of AuPd catalysts for WGS, CO oxidation and FAD. In order to explain these observations, a number of characterisation tools were utilised in order to try and rationalise these trends.

4.3.1. H_2-temperature-programmed reduction (TPR)

H_2-TPR was conducted in order to assess the redox properties of the catalyst. It was important to investigate how the composition of gold and palladium affected the reducibility of the catalyst and whether or not this was a significant factor in determining the catalyst performance. The data is presented below in Figure 4.10. Firstly the $CeZrO_4$ support was analysed. This material has been extensively studied in the literature and the reduction processes have been reported before.[33, 34] $CeZrO_4$ has three distinct reduction features (Figure 4.10, inset).

The feature at 345 ^oC corresponds to the surface reduction while the larger feature at 550 ^oC is related to the bulk reduction of the $CeZrO_4$ material. In addition, a weak feature at 150^oC is visible which was not due to Ce reduction. It is most likely due to weakly bound surface species such as carbonates or water, or an impurity that wasn't removed during the pre-treatment step.

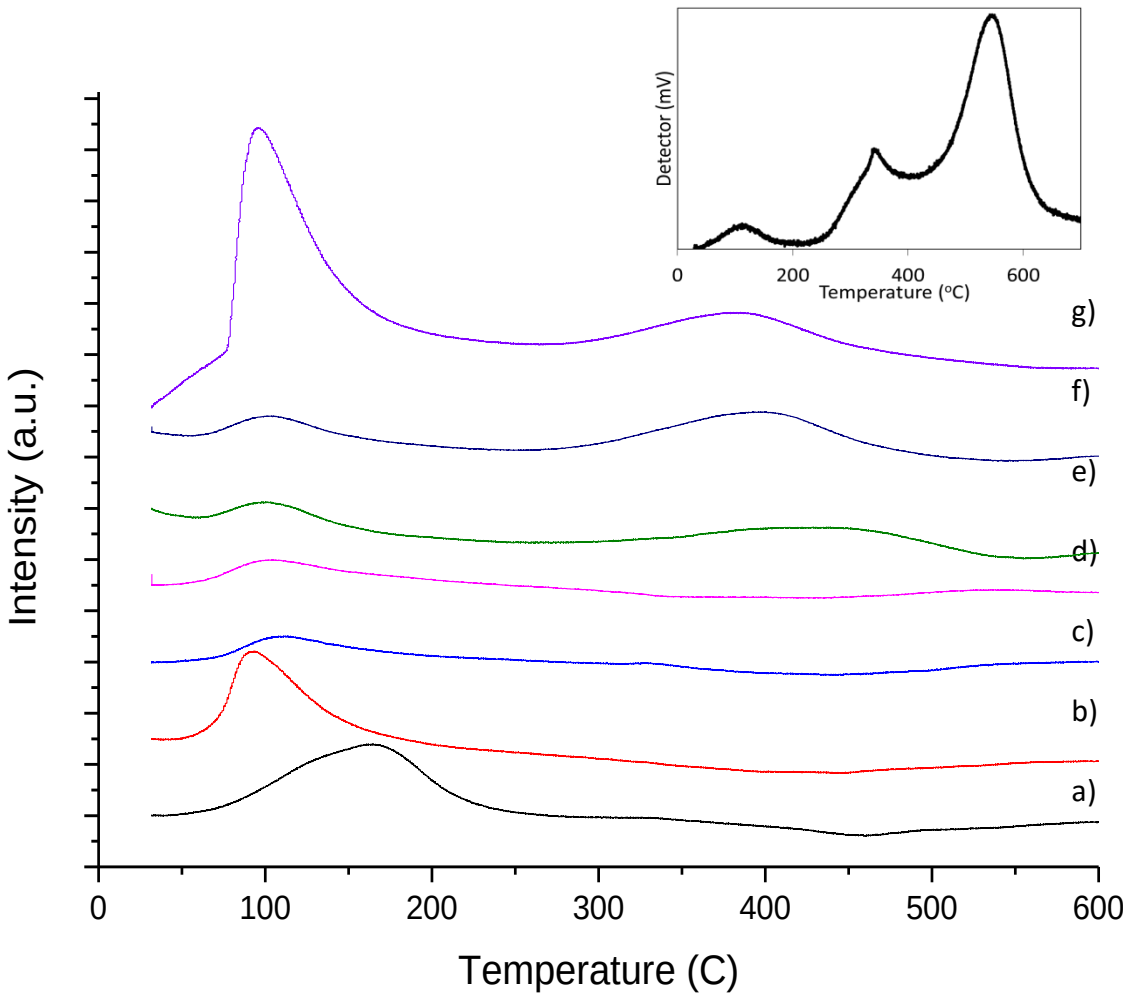

Figure 4.10 H_2-TPR profiles of $Au_xPd_y/CeZrO_4$ catalysts. Inset: $CeZrO_4$ a) Au, b) $Au_{86}Pd_{14}$, c) $Au_{67}Pd_{33}$, d) $Au_{44}Pd_{56}$, e) $Au_{12}Pd_{88}$, f) Au_8Pd_{92} and g) Pd

The effect of the addition of precious metals to the redox properties of metal oxides is well understood: The reduction of the material occurs at a much lower temperature than the bare metal oxide when metals such as Au, Pd and Cu are deposited. This proceeds through a hydrogen spillover mechanism.[35, 36] The hydrogen spillover mechanism of reduction describes the dissociative adsorption of hydrogen onto a supported metal such as Pd or Au followed by the migration of the adsorbed species to the support material. This then diffuses across the surface and reduces the support. Significantly, in the absence of the spillover material, the reduction would not otherwise occur. A schematic of the process is presented below in Schematic 4.1.

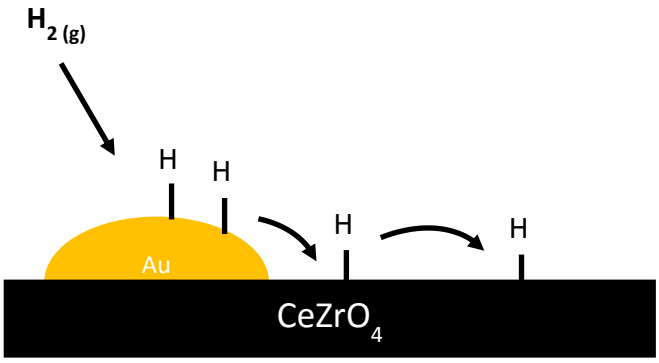

Schematic 4.1 Schematic diagram of the hydrogen spillover effect. Gaseous H_2 dissociatively adsorbs onto the support metal and then diffuses onto the surface, reducing the support.

The $Au/CeZrO_4$ catalyst has one distinct reduction feature centred at 165 ^oC while the $Pd/CeZrO_4$ catalyst has a very intense reduction peak at 95 ^oC. These correspond to the surface reduction of the catalyst through the hydrogen spillover mechanism described above. There are broad features in each of the supported metal catalyst samples which although less well-defined are also due to hydrogen spillover. Broad shoulders are visible on each of the catalysts at higher temperatures, at 400 ^oC for the $Pd/CeZrO_4$ catalyst. These relate to the bulk reduction of the material which was characterised by a feature at 550^oC for the bare support. The downshift of the bulk reduction temperature shows that the bulk reduction is also more facile when Au or Pd is deposited.

There was no correlation in the reducibility of the catalysts and the resultant catalytic activity for WGS. In the context of the WGS reaction, the reducibility is related to the activation of water whereby a lower reduction temperature would indicate more facile activation of water in the WGS reaction. Therefore in the series of mono- and bi-metallic catalysts tested, the activation of water is not likely to be a rate-limiting step, or a correlation between the WGS activity and the temperature of surface reduction would be expected. However, a relationship between the hydrogen consumption per mole of metal on the catalyst and the catalyst activity for WGS could be drawn. This correlation is shown in Figure 4.11. Here it can be seen that catalysts that consumed more H_2 during the TPR experiment, or were more reducibile, dispalyed higher catalytic activity for WGS. This correlation can be understood in the context of the hydrogen spillover mechanism that occurs on supported metal catalysts: The number

of spillover sites on the catalyst is determined by the dispersion of the metal particles. Catalysts with a higher dispersion should have more spillover sites therefore this correlation could be an indirect measure of the dispersion of the metals on the catalyst and it is unsurprising that this correlates well with WGS activity.

The $Pd/CeZrO_4$ catalysts is a clear out-lier in this trend. This catalyst consumed a relatively large quantity of H_2 and yet did not exhibit high catalytic activity. It is well known that the adsorption of CO on Pd is much stronger than on Au and if the formation of a reaction intermediate is perturbed by this strong adsorption, this could explain why the WGS activity was not as high as expected, given the hydrogen consumption. However, the catalytic activity for FAD also follows the same trend as WGS, which suggests that the interaction with CO is not relevant.

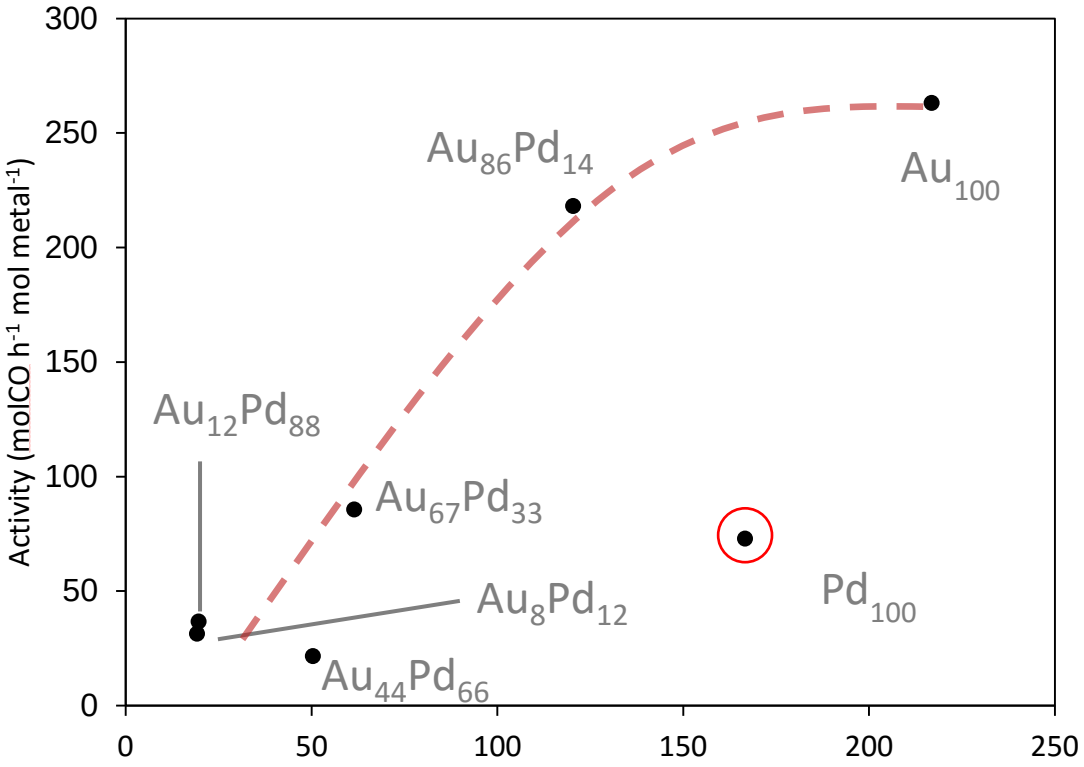

Figure 4.11 The relationship between the H_2 consumption and WGS activity in $AuPd/CeZrO_4$ catalysts

In summary, the H_2-TPR revealed that the surface reducibility of the catalyst was not a significant factor in determining the catalytic activity in the water-gas shift reaction, and by extension CO oxidation and FAD. However, a strong correlation between the hydrogen consumption and the catalytic activity of each catalyst was observed. This was rationalised through differences in the metal dispersion in different catalysts and

represents the first evidence for explaining the catalytic activity trends observed in the first part of this chapter.

4.3.2. XPS

XPS was carried out on the series of catalysts to gain evidence for the interactions between gold and palladium as well as the composition of gold species present. In addition to this, the Cl 2s region of the XP spectrum was also measured and the absence of a signal in this region confirmed that that no residual chloride species were present.

Figure 4.12 shows the Au 4f XP spectrum and the region comprising Zr 3p, Pd 3d and Au 4d and the deconvolution of the peaks. The binding energy of the Au $4f_{7/2}$ signal in each catalyst is listed below in Table 4.3. The ionisation of the Au 4f shell causes spin-orbit splitting that results in a doublet of $4f_{7/2}$ and $4f_{5/2}$ peaks, which are separated by 3.7 eV.[37] The observed binding energy of the Au $4f_{7/2}$ peak varied according to the AuPd ratio, whereby increasing Pd content resulted in a smaller binding energy, with the most dramatic shift in the Au_8Pd_{92} catalyst which exhibited a peak at 83.6 eV compared to 84.1 eV in the monometallic Au catalyst. This shift is due to the electronic modification of the Au species by Pd and suggests interactions between the Au and the Pd.[38, 39] This type of electronic modification suggests the formation of an alloy. Similar shifts have been observed on SiO_2-supported AuPd catalysts although the extent of the shifts was different.[38] The magnitude and direction of the binding energy shift is dependent on both initial and final state effects, the former of which is affected by the catalyst support.[40] Therefore quantitative comparisons between catalysts on different supports were not appropriate.

Analogous shifts in the binding energy of the Pd species were also observed. However, the overlap of the Zr 3p and Au 4d spectra with the Pd 3d spectrum makes deconvolution of the peaks very challenging. The positions of the features are shown in Table 4.3. The spin-orbit components are separated by 5.26 eV. The binding energy of the Pd $3d_{5/2}$ peak in each catalyst was indicative of Pd^{2+}.[41, 42] Quantifying the ratio of Pd^0 to Pd^{2+} was not possible due to the overlap in the XPS signal of Pd 3d and Zr 3p.

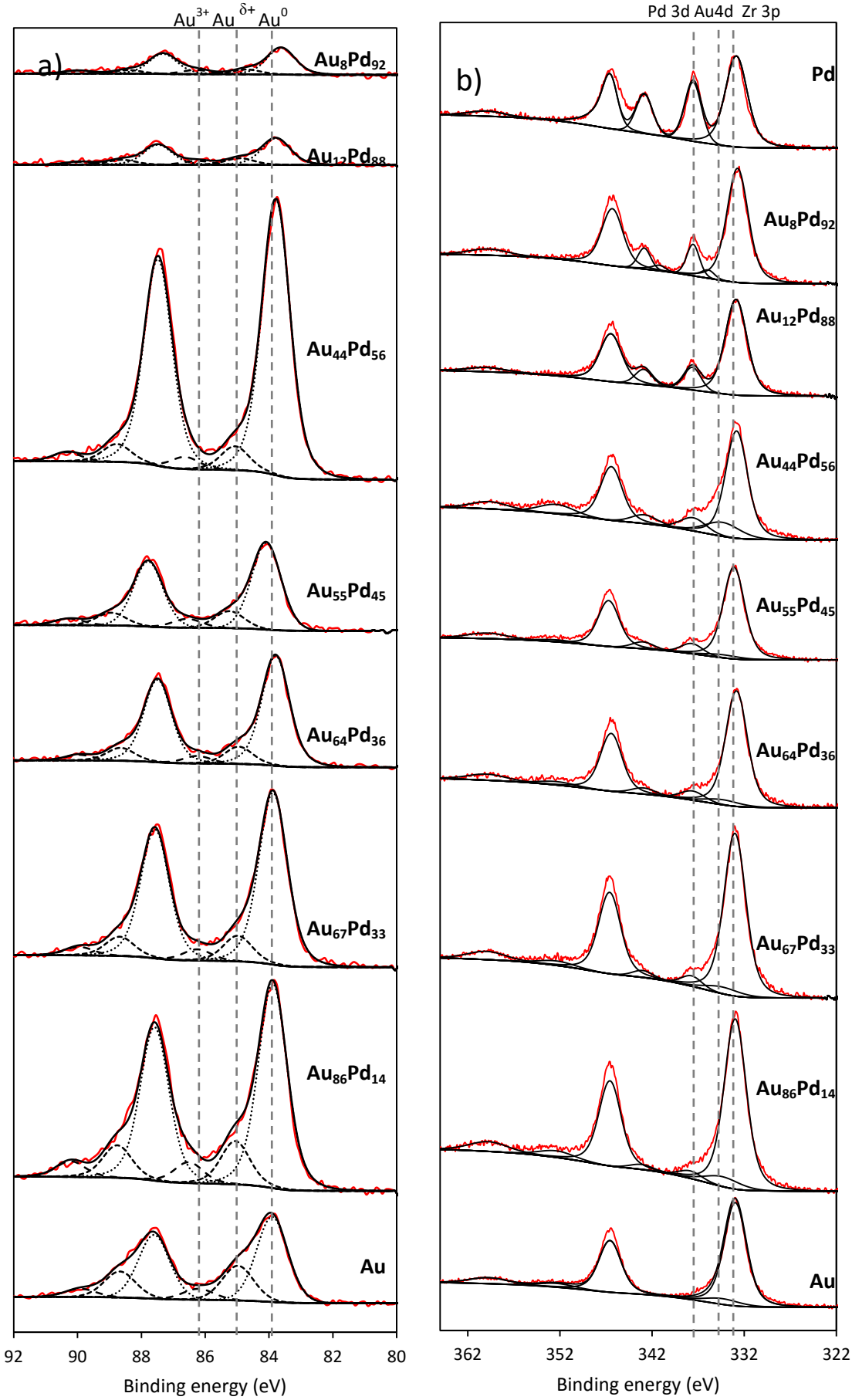

Figure 4.12 XPS analysis of a) Au 4f and b) Pd 3d, Zr 3p and Au 4d spectrum showing deconvolution of peaks.

In the Pd catalyst, the $3d_{5/2}$ peak had a binding energy of 337.6 eV whereas in the $Au_{86}Pd_{14}$ catalyst it was 337.9 eV. Interestingly, several catalysts did not exhibit a significant shift in the position of the peak. In fact, noticeable shifts were seen only when there was an excess of Au in the sample. However, due to the overlapping peaks in this region of the XP spectrum, the exact position of the Pd 3d peak could not be precisely determined.

Table 4.3 XPS analysis of Au 4f and Pd 3d spectra for $Au_xPd_y/CeZrO_4$ catalysts

Catalyst	Composition of different Au species CeZrO4 catalysts (%)			Binding energy (eV)			
	Au^0	$Au^{\delta+}$	Au^{3+}	Au^0	$Au^{\delta+}$	Au^{3+}	Pd^{2+}
Au	65.1	26.5	8.4	84.1	85.2	86.6	-
$Au_{86}Pd_{14}$	76.1	16.1	7.8	83.9	85.1	86.5	337.9
$Au_{67}Pd_{33}$	82.3	12.3	5.4	83.9	85.1	86.2	337.7
$Au_{64}Pd_{36}$	81.6	12.8	5.6	83.8	84.9	86.2	337.6
$Au_{55}Pd_{45}$	77.1	15.1	7.8	84.1	85.2	86.6	337.7
$Au_{44}Pd_{56}$	88.5	7.7	3.9	83.8	85.1	86.6	337.5
$Au_{12}Pd_{88}$	71.6	17.8	10.6	83.8	84.9	86.3	337.6
Au_8Pd_{92}	75.0	13.3	11.7	83.6	84.7	86.3	337.6
Pd	-	-	-	-	-	-	337.6

The different oxidation states of Au were inferred based on the Au 4f spectrum due to the overlaps associated with the Au 4d spectrum. A summary of the different Au species are also shown in Table 4.3. In the Au and AuPd catalysts, there was evidence of Au^0 and Au^{3+} which correspond to peaks with binding energies of 84.1 eV, and 86.6 eV, respectively for the Au catalyst.[37, 43, 44] There is also the presence of a third species, $Au^{\delta+}$ that has a binding energy close that of Au^+ at 85 eV. This was due to "small gold nanoparticles", as previously reported[1] and discussed in **Chapter 3.**

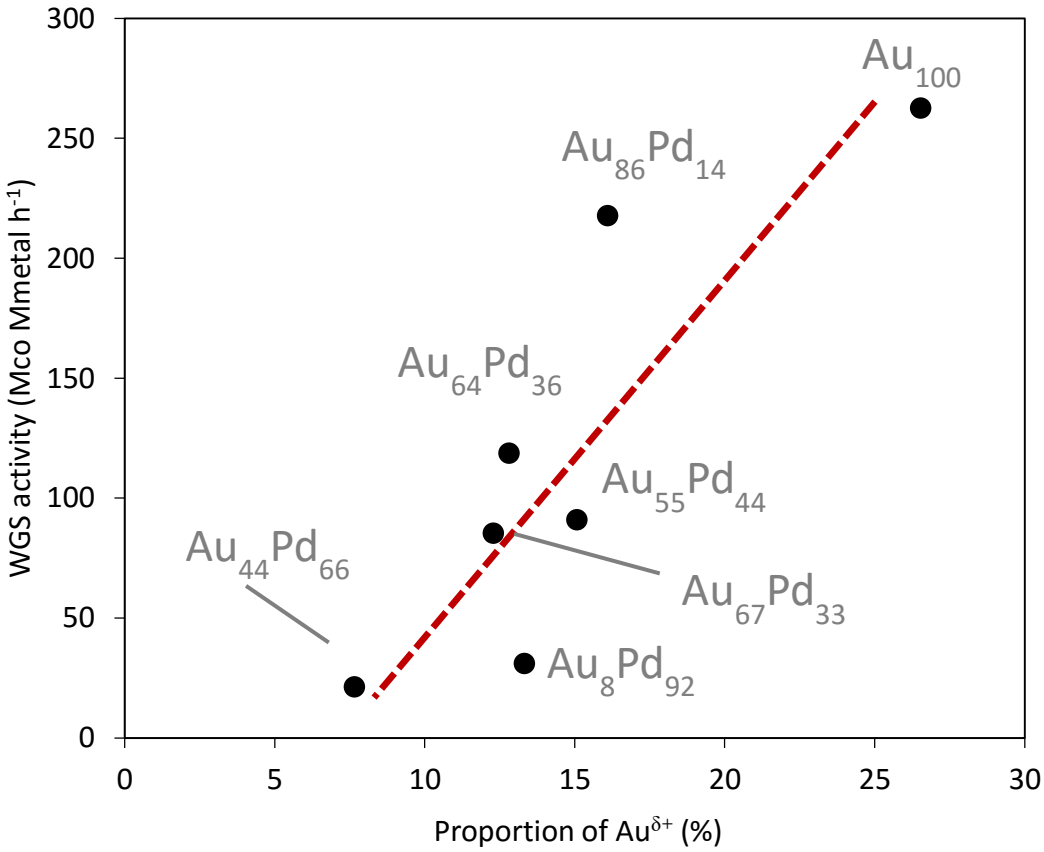

Figure 4.13 Correlation between the concentration of $Au^{\delta+}$ and the catalytic activity in water-gas shift

In the Au catalyst, $Au^{\delta+}$ accounts for 26.5% of the total Au species. As Pd is introduced, there is significant decrease in the proportion of $Au^{\delta+}$, which could indicate larger particle sizes. When the concentration is correlated against the catalytic activity in WGS, there is a strong correlation: Catalysts with higher concentrations of $Au^{\delta+}$ are much more active than those with a small proportion of $Au^{\delta+}$ This is shown in Figure 4.13. The Pd-rich catalyst $Au_8Pd_{92}/CeZrO_4$ does not follow the trend as strongly as the other catalysts with higher molar quantities of Au. This observation can be rationalised by the fact that while there may be an appreciable quantity of $Au^{\delta+}$ the majority of the supported metal is Pd and so the catalytic activity will be largely dominated by the properties of this metal, rather than the Au.

The XPS data presented above are consistent with the TPR data described earlier. This further provides evidence of variations in metal particle size across the range of catalysts. It should be noted that the same catalysts that consumed large quantities of hydrogen in the TPR experiment were also observed to have a large amount of $Au^{\delta+}$

according to XPS. Correlation of the hydrogen consumption and $Au^{\delta+}$ yields a straight line in the catalysts in $Au_xPd_y/CeZrO_4$ catalysts where x > 44 i.e. catalysts with a relatively large amount of Au. This correlation is shown in Figure 4.14.

Overall, XPS was implemented to gain valuable information regarding the nature of the supported metals. A correlation between a feature assigned to small gold particles and catalyst activity was made, which corroborated the findings in the H_2-TPR studies (Figure 4.14). Further, evidence of binding energy shifts in the Pd 3d and particularly the Au 4f spectra were found which was interpreted as evidence for the interaction between the two supported metals.

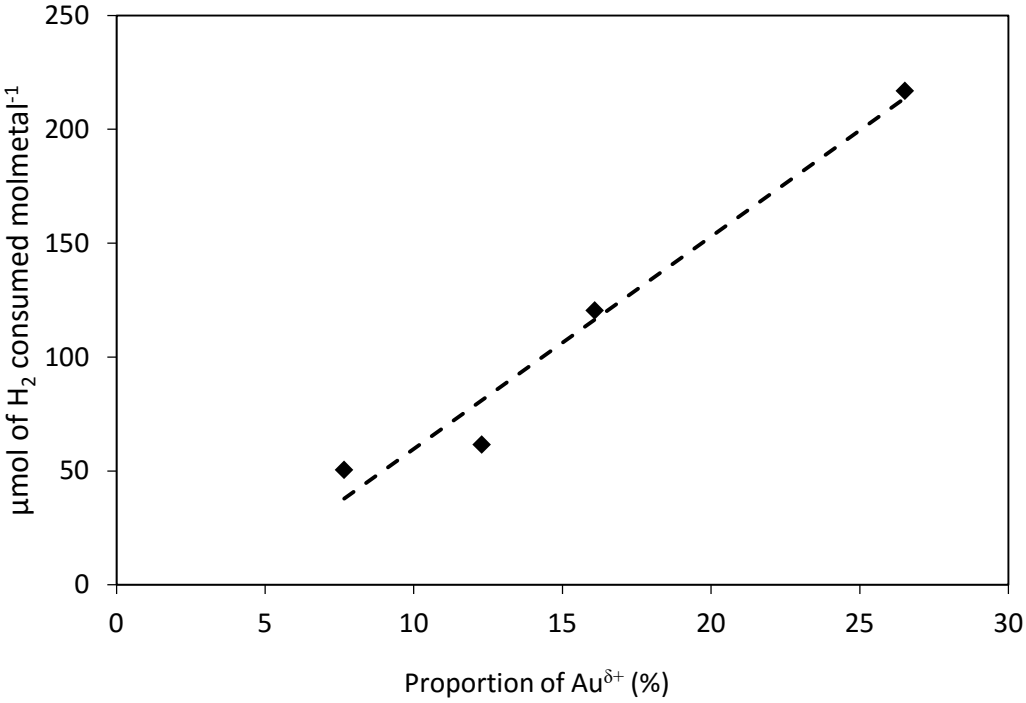

Figure 4.14 Correlation between the hydrogen consumption in a H_2-TPR experiment and the proportion of $Au^{\delta+}$ in a range of $AuPd/CeZrO_4$

4.3.3. *In situ* CO-Diffuse Reflectance Infrared Fourier Transform Spectroscopy (DRIFTS)

The CO-DRIFTS spectrum of each catalyst was investigated in the region of 1800-2200 cm^{-1} which includes the stretching modes of CO adsorption on Au and Pd. This technique has been extensively reported before to probe the interaction of CO and precious metal supported catalysts.[11, 45-50] Assignments of specific bands to CO

adsorption on Au or Pd in different oxidation states have been made,[51] however, it has been shown that CO can reduce PdO to Pd in supported Pd/CeO_2 catalysts at room temperature[52] so lower temperatures are needed to ensure that the oxidation states are representative of the sample and the reduced components are not exaggerated. However, the limitations of the equipment used in this experiment restricted the temperature range to room temperature or above. Conducting analysis at room temperature still represents an opportunity to observe the relative population of different vibrational bands attributable to Au or Pd. The colour change observed in the post-analysis samples indicated that reduction had occurred under the experimental conditions and therefore no information regarding the oxidation states of the metals was sought. Instead, the focus was to analyse the position and intensity of the different CO bands and the contribution from each stretching mode in order to gain an insight into how CO interacts with the catalyst. Unless stated otherwise, all spectra refer to samples that have been exposed to CO such that there was no change in subsequent DRIFTS spectra. The higher wavenumber region of the spectra (2200 – 2000 cm^{-1}) has previously been assigned to linearly adsorbed carbonyl species and features at lower wavenumbers (2000-1800 cm^{-1}) have been assigned to two-fold (bridged) or three-fold (hollow) adsorption of CO on Pd or AuPd.[49, 53] CO-DRIFTS data for a range of $Au_xPd_y/CeZrO_4$ catalysts are presented in Figure 4.15.

The mono-metallic Au catalyst features just one band at 2113 cm^{-1}, caused by the linear adsorption of CO on Au.[51] This band corresponds to the adsorption of CO on metallic Au. There is a slight asymmetry of this feature that could indicate the presence of an adsorption mode at a higher frequency, 2125 cm^{-1}, which is due to CO-$Au^{\delta+}$.[51] The CO-DRIFTS spectrum observed in this work is consistent with previous reports for the $Au/CeZrO_4$ catalyst.[51, 54] The mono-metallic Pd catalyst consists of two features: firstly, there is an intense band at 2092 cm^{-1} which corresponds to the linear adsorption of CO on Pd and secondly there is a broad feature that begins at 1960 cm^{-1}, where two-fold and three-fold adsorption of CO on Pd occurs.[48, 55]

Significantly, the adsorption band of CO-Au rapidly reduces in magnitude as Pd is introduced. The CO-DRIFTS spectrum of $Au_{67}Pd_{33}$ is dominated by Pd adsorption modes, suggesting that the surface of the catalyst is predominately formed of Pd. This explains to some extent why the catalytic activity of the bimetallic catalysts so quickly

decreases: The surface of the catalyst quickly becomes dominated by Pd, even when Au is in excess and so the catalytic activity is determined by the activity of the Pd active sites, which are of course less active than the Au ones.

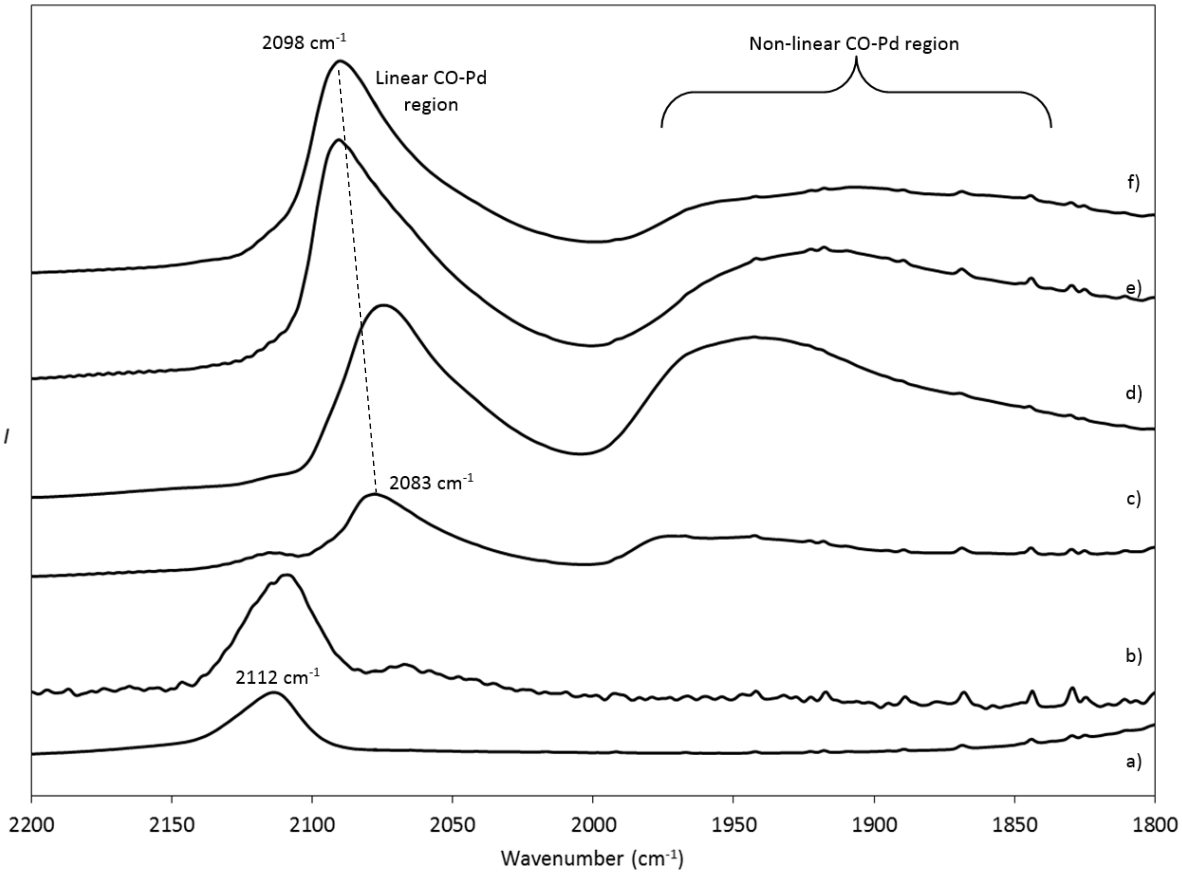

Figure 4.15 CO-DRIFTS spectra for selected AuPd/$CeZrO_4$ catalysts: a) Au, b) $Au_{93}Pd_7$, c) $Au_{67}Pd_{33}$, d) $Au_{44}Pd_{56}$, e) $Au_{12}Pd_{88}$ and f) Pd.

In addition, there are important differences in the relative intensity of the different absorption modes. As Pd content increases, the non-linear adsorption regions increase, which is explained by a higher proportion of Pd in the surface of the particles leading to a higher likelihood of contiguous Pd sites that give rise to non-linear CO adsorption. It is important to recognise the importance of different adsorption modes in this region. It has been experimentally demonstrated that the linear modes of CO adsorption on Pd are due to adsorption of CO molecules at the edge of the nanoparticle, on under co-ordinated Pd species.[48, 55] In the context of the metal-support interface active site model, these adsorption modes become catalytically significant. The non-linear adsorption modes are typically due to molecules adsorbing on extended metal surface such as the top of the nanoparticle. These are likely to be

less important in the reaction mechanism and could possibly be considered spectator sites.

In order to measure the contribution of different adsorption modes in each catalyst, an "adsorption ratio" was calculated for each of the Pd-containing catalysts. The adsorption ratio is a measure of the linear component of the spectrum relative to the non-linear component, as shown in Figure 4.16. It is important to note that while the linear component makes up one type of adsorption, the non-linear component can comprise several modes: 2-fold, 3-fold and 4-fold adsorption.[11] It also important to realise the limitations of the adsorption ratio. No quantitaive information can be sought from comparsion between the two features, as the extinction co-efficients of the various species adsorbed on the surface are not known and time-consuming to calculate. However, qualitative information can be gained from comparing the adsorption ratios between different catalyst samples.

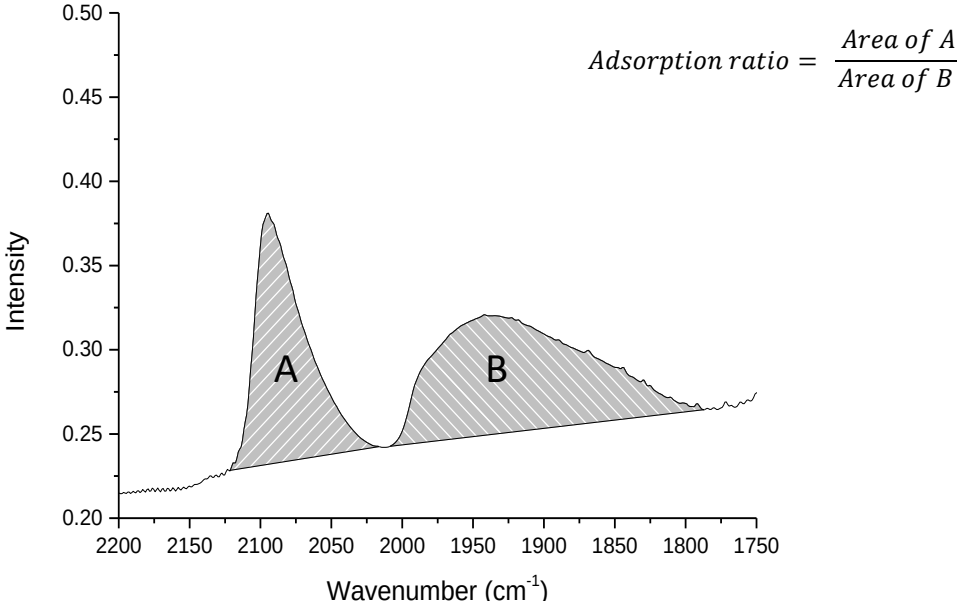

Figure 4.16 CO-DRIFTS spectrum of an AuPd catalyst showing how the adsorption ratio is calculated

Figure 4.17 shows the correlation between the adsoprtion ratio of the AuPd catalysts and the catalytic activity. Similar to the correlations observed in the H_2-TPR and XPS data, a strong positive correlation can be plotted whereby the catalysts with the highest adsorption ratios are the most active catalysts.

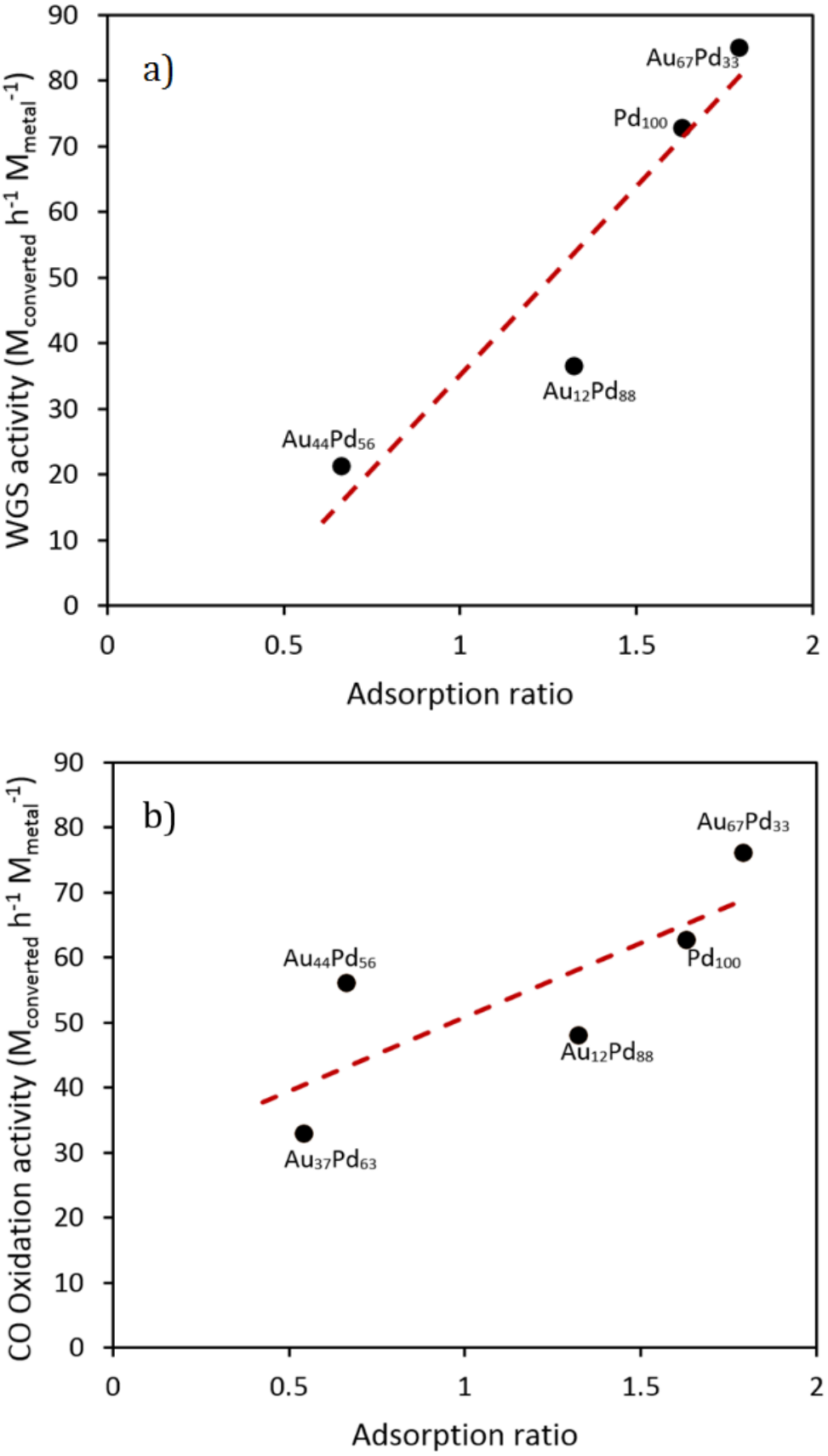

Figure 4.17 The correlation between the adsorption ratios measured in *in situ* CO-DRIFTS experiments and the catalytic activity in a) WGS and b) CO oxidation.

This correlation is easily understood in the context of the origins of the different adsorption modes, as explained above. The adsorption ratio measures the contribution from linear or edge sites compared to the non-linear or top sites. Therefore the adsorption ratio is analogous to metal particle size or interfacial area. Catalysts with large adsorption ratios will have fewer non-linear, bridged adsorption sites compared to catalysts with larger metal particles whose CO-DRIFTS spectrum will feature a larger degree of top adsorption sites compared to edge sites. This is based on an assumption regarding the shape of the nanoparticles: that they are hemi-spherical or cub-octohedral particles. High resolution microscopy could verify this and is the subject of a later section in this chapter. Significantly, it can be seen that the Pd catalyst had a higher adsorption ratio than $Au_{44}Pd_{56}$ and $Au_{12}Pd_{88}$, both of which were less active than the monometallic Pd catalyst. This could serve as evidence that the monometallic Pd catalyst had a smaller particle size than the Pd-rich bimetallic catalysts, which would explain the monometallic catalysts superior activity for WGS. This analysis is restricted to Pd-rich catalysts as the catalytic activity of these catalysts is dominated by into the catalyst surface by probing the Pd adsorption modes.

4.3.4. Electron microscopy

A selection of Au, Pd and AuPd/$CeZrO_4$ catalysts were analysed using a TEM/STEM microscope as detailed in **Chapter 2** in order to estimate the particle size distribution and morphology of the AuPd/$CeZrO_4$ catalysts. The following samples were studied:

- Au/$CeZrO_4$
- $Au_{93}Pd_7$/$CeZrO_4$
- $Au_{55}Pd_{45}$/$CeZrO_4$
- Pd/$CeZrO_4$

The data for the monometallic Au/$CeZrO_4$ catalyst was previously presented in **Chapter 3** however, this is relevant to this work and therefore a brief summary of the findings presented in **Chapter 3** will be given below, before the presentation of the Pd-containing catalysts.

$Au/CeZrO_4$

The particle size distribution is shown below in Figure 4.18 in addition to a dark field image of typical Au nanoparticles, exhibiting well faceted edges.

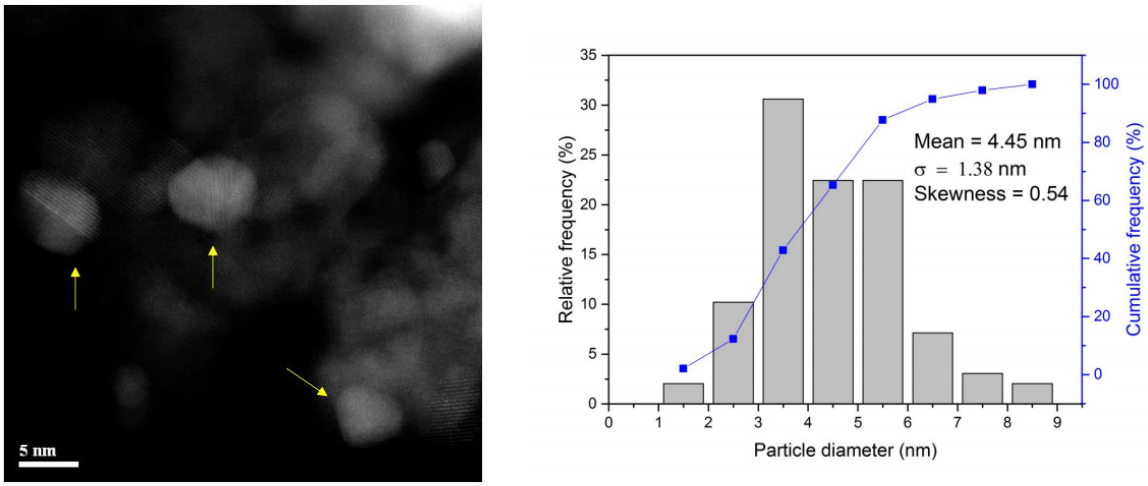

Figure 4.18 Left: Dark field image of Au nanoparticles exhibiting cub-octoherdal shape with well-defined facets and edges and right: particle size distribution of Au particles in $Au/CeZrO_4$

$Au_{93}Pd_7/CeZrO_4$

$Au_{93}Pd_7/CeZrO_4$ was selected for microscopic analysis because the effect of adding a small amount of Pd to the catalyst had not yet been established. Understanding how the presence of a small amount of Pd affects the nanostructure of the resultant catalyst would help to explain the activity trend of the AuPd catalysts for WGS. Figure 4.19 shows that the Au nanoparticles reside in crevices between the support grains, similar to that of the monometallic Au catalyst. This suggests that the metal-support interaction is not strong in the bimetallic catalysts. The morphology was also investigated and evidence of cub-octohedral nanoparticles were found (Figure 4.20). Moreover, larger, rounder metal particles (Figure 4.21, bottom) and particles that were multiply twinned and more icosahedral in nature (Figure 4.21, top and middle) were present. The particle size distribution was measured (Figure 4.24, top) and the mean particle size was found to be 6.2 nm, significantly larger than the monometallic Au catalyst (4.5 nm).

The STEM HAADF data for the $Au_{93}Pd_7$ catalyst revealed that the introduction of a small amount of Pd results in a significant increase in the mean particle size. However, the cause of this increase must be explained and could be due to several factors. It is important to note that in the absence of elemental analysis, it is not clear whether the metal particles presented here are bimetallic alloys or largely monometallic particles.

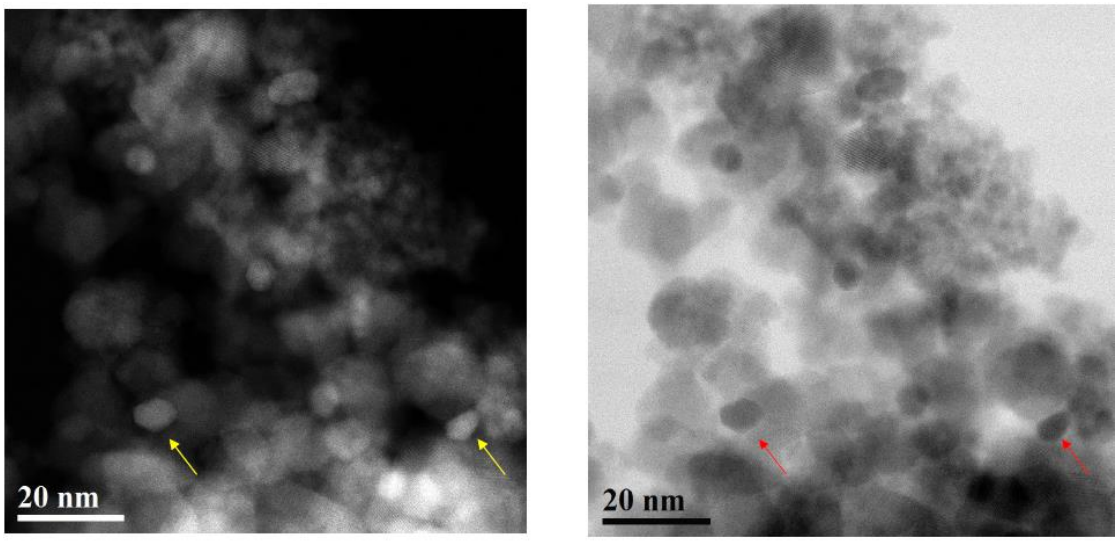

Figure 4.19 DF (left) and BF (right) images of $Au_{93}Pd_7/CeZrO_4$ catalyst with Au particles in crevices between support grains

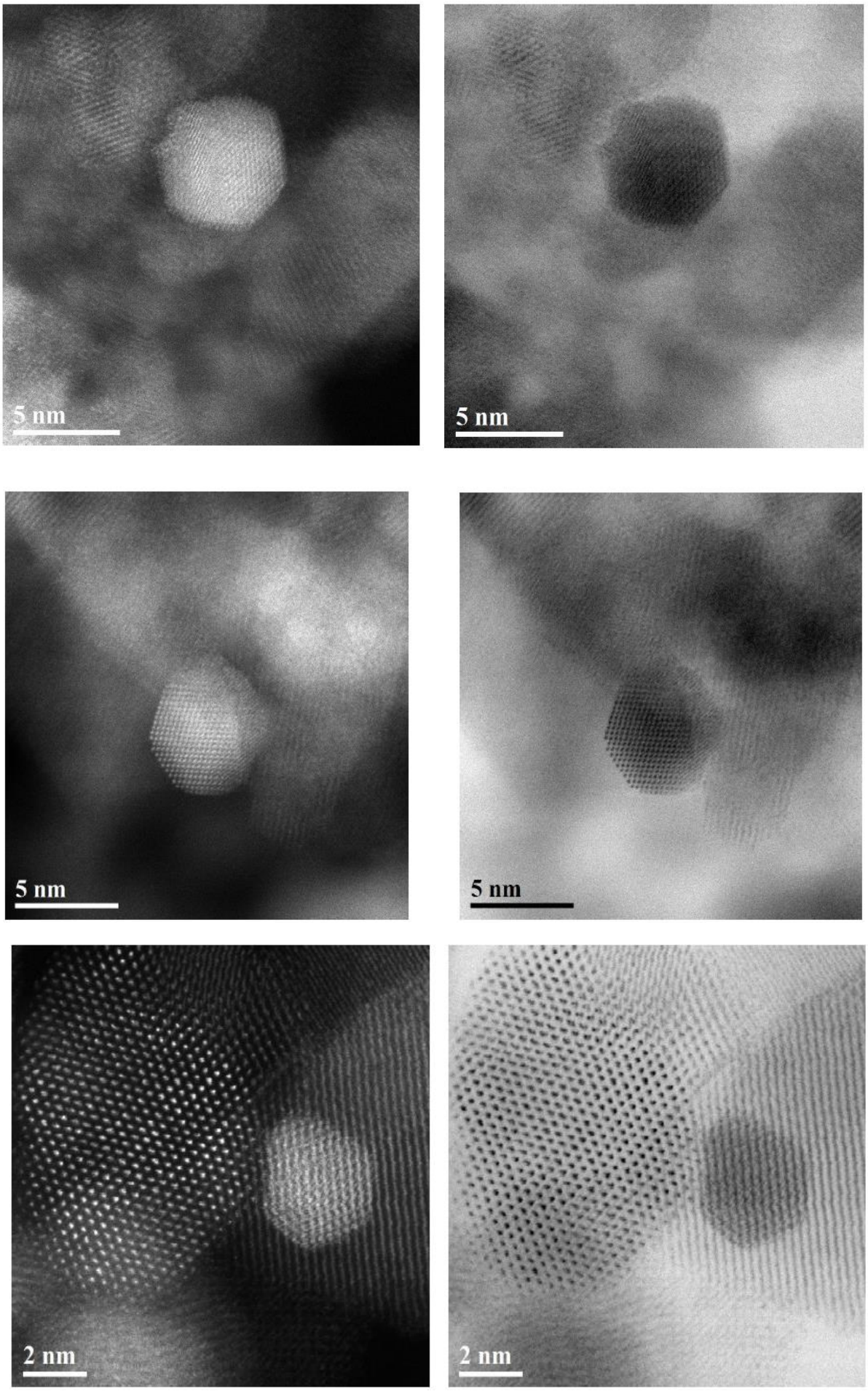

Figure 4.20 DF (left) and BF (right) STEM images of $Au_{93}Pd_7/CeZrO_4$ sample exhibiting well facetted cub-octahedral morphologies

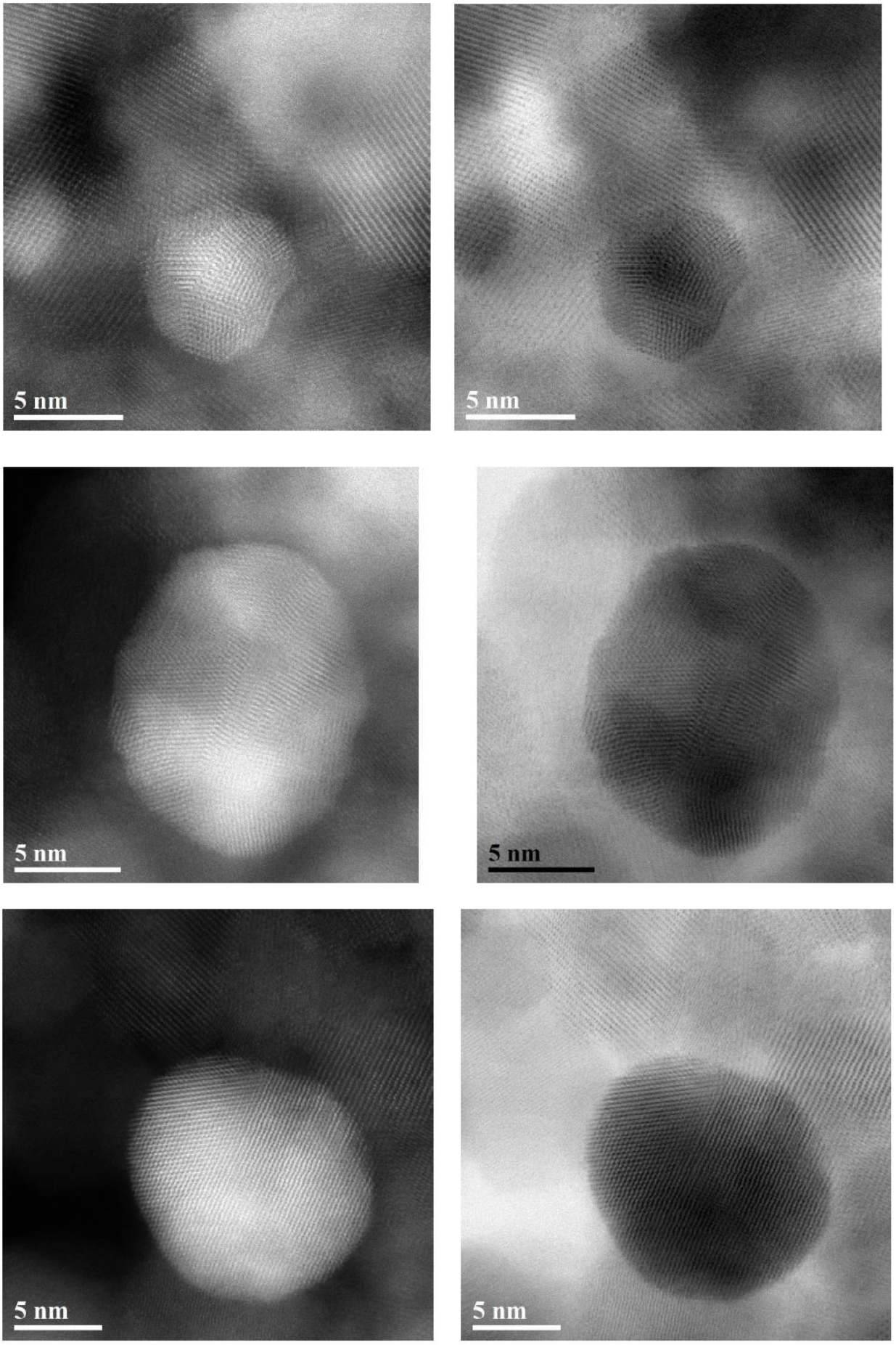

Figure 4.21 DF (left) and BF (right) STEM images of $Au_{93}Pd_7/CeZrO_4$ showing larger Au particles with icosahedral morphology (top, middle) and rounder, less clearly facetted particles (bottom)

$Au_{55}Pd_{45}/CeZrO_4$

In the $Au_{55}Pd_{45}$ sample, the Au:Pd molar ratio is close to 1 and so this catalyst was appropriate for analysis by STEM HAADF because it is often reported as being the most active bimetallic catalyst for oxidation reactions and it was among the least active for WGS in the AuPd bimetallic series tested in this work. Further, there is high chance of imaging bimetallic particles. Figure 4.22 shows examples of metal particles in this sample, which are large and rounded. Also present were twinned icosahedral particles, similar to those observed in the $Au_{93}Pd_7$ sample. The particle size distribution is presented in Figure 4.24 and the mean particle size was calculated to be 6.4 nm – significantly larger than the monometallic Au catalyst and very similar to that of the $Au_{93}Pd_7$ catalyst.

$Pd/CeZrO_4$

Figure 4.23 shows the STEM HAADF data for the monometallic Pd catalyst. Resolving the metal nanoparticles was very challenging, due to the lower mass of Pd contrasting poorly with the $CeZrO_4$ support. It is immediately apparent that the Pd particles are very small, most likely below 1 nm in diameter. Generating morphological and particle size distribution data for this sample was not possible, due to the difficulty in resolving the small metal clusters/particles. However, it can be concluded that the particles present in the monometallic catalyst are qualitatively smaller than the AuPd and Au catalyst prepared in this work.

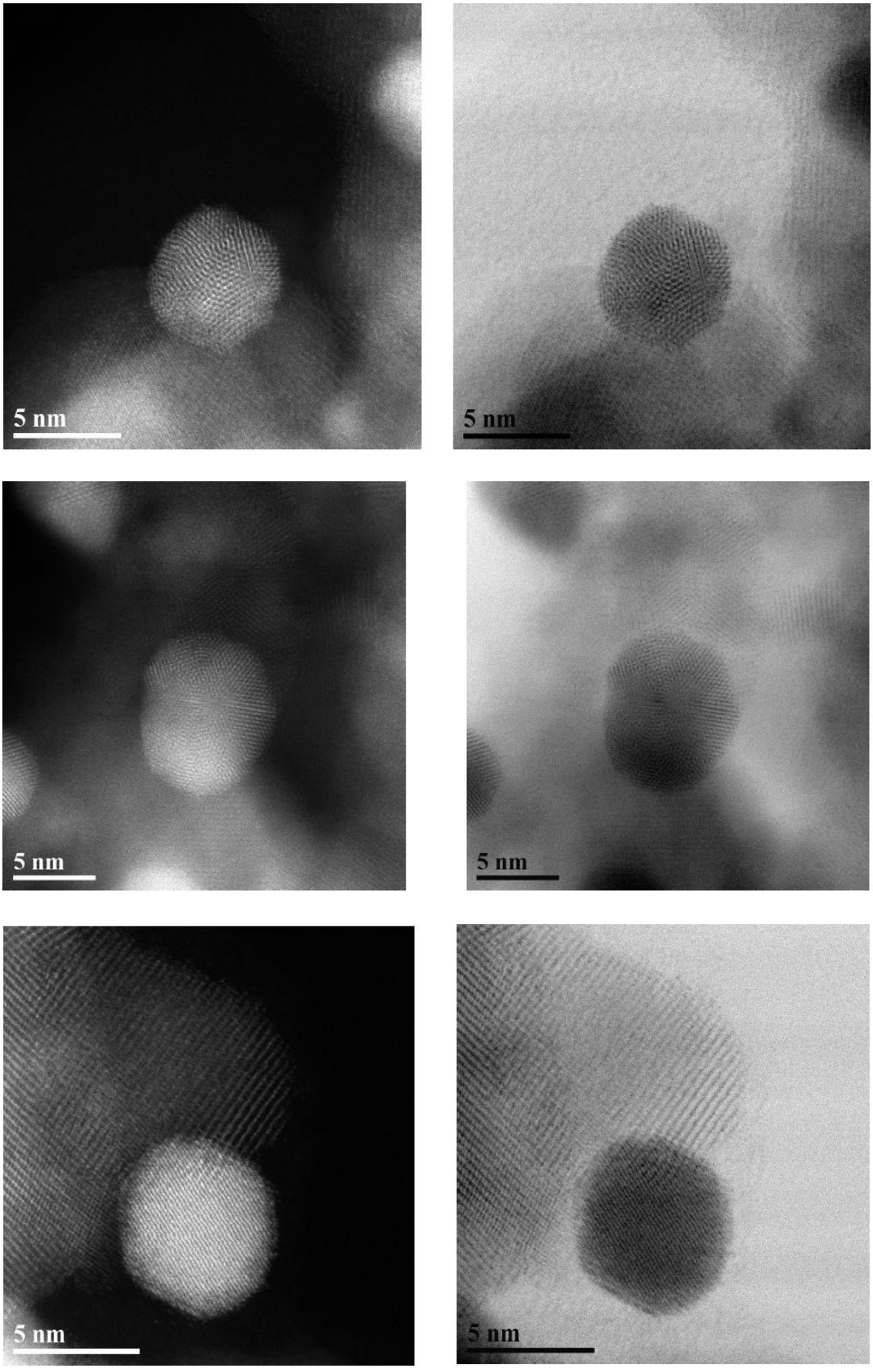

Figure 4.22 DF (left) and BF (right) images of metal nanoparticles in $Au_{55}Pd_{45}/CeZrO_4$ exhibiting round, icosahedral morphology (top and middle) and cuboctohedral morphology (bottom).

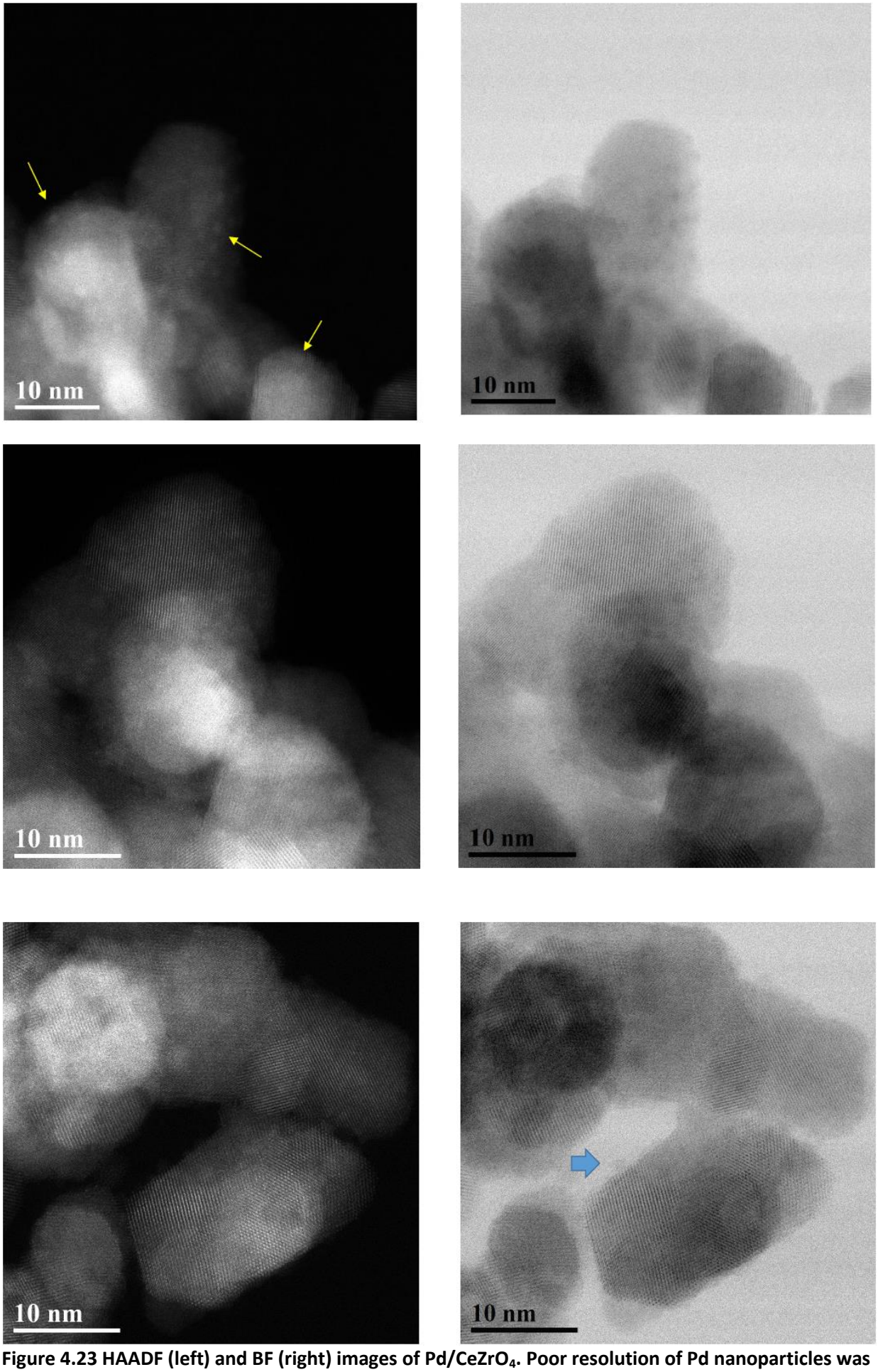

Figure 4.23 HAADF (left) and BF (right) images of $Pd/CeZrO_4$. Poor resolution of Pd nanoparticles was caused by poor Z contrast with support

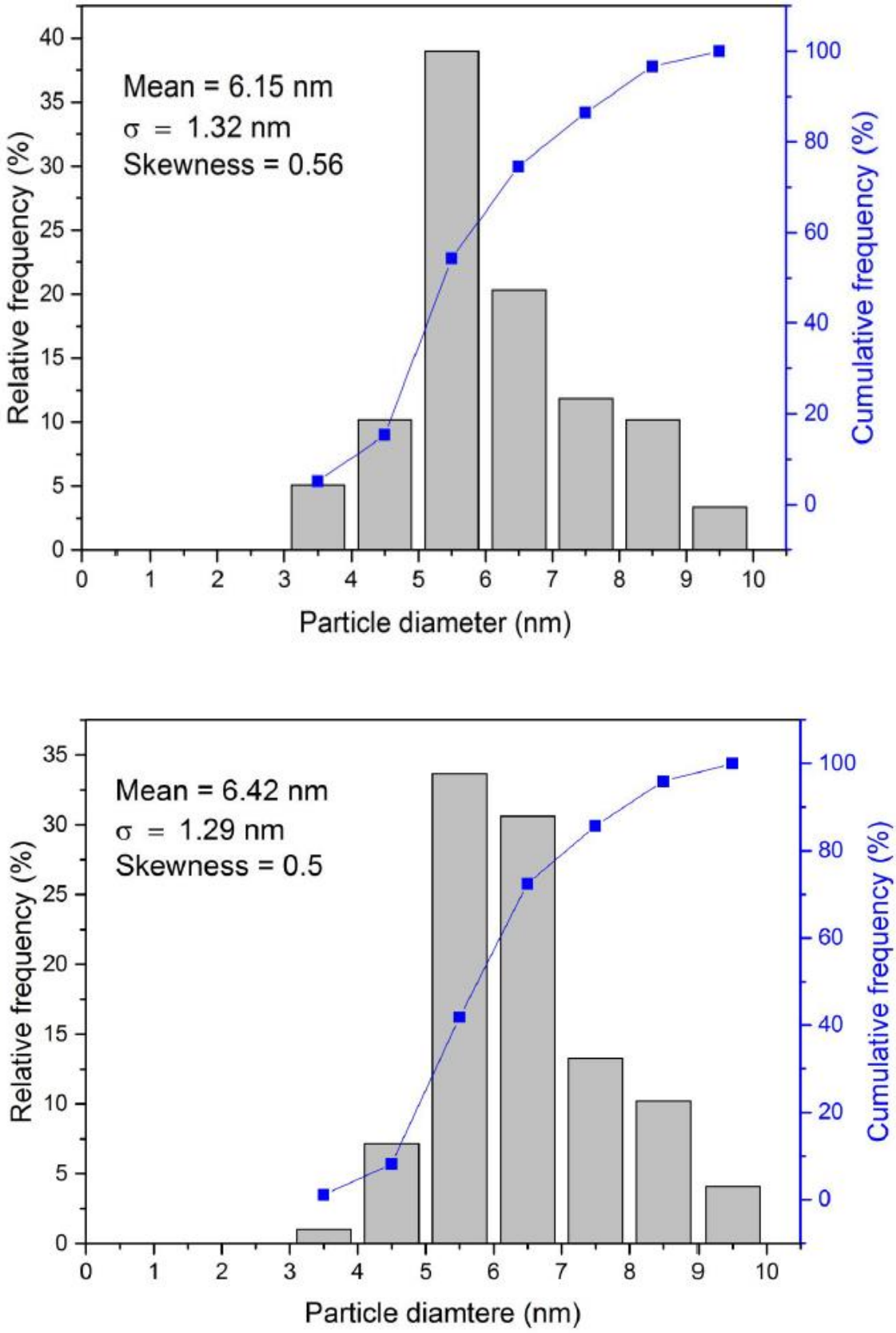

Figure 4.24 Particle size distribution of $Au_{93}Pd_7/CeZrO_4$ (top) and $Au_{55}Pd_{45}/CeZrO_4$ (bottom)

Overall, STEM HAADF was used to successfully resolve the size and shape of a selection of Au and AuPd catalysts. It was found that in the Au-containing catalysts, the monometallic Au catalyst had the smallest average particle size. $Au_{93}Pd_7$ was studied in order to assess the effect of introducing a small amount of Pd into an Au catalyst to form a bimetallic system. There was a significant increase in the particle size of this bimetallic catalyst. The least active catalyst for WGS, $Au_{55}Pd_{45}$ was also investigated using microscopy. Interestingly, the mean particle size of this catalyst was very similar to that of the $Au_{93}Pd_7$ catalyst, despite a large difference in the catalytic activity of these two materials. Finally, the monometallic Pd catalyst exhibited the smallest metal nanoparticles, which could only be estimated to be below 1 nm due to the difficulties in distinguishing the supported Pd from the support. This of course means that it is possible that monometallic Pd particles in bimetallic catalysts were not identified.

The morphology of the nanoparticles was shown in **Chapter 3** to change under reaction conditions and previous work has shown the shape of the nanoparticles to be related to the deactivation of the benchmark catalyst.[1] In this microscopy study, the shape of the nanoparticles was also investigated, although compiling statistically relevant distributions of morphologies was not possible. However, qualitative observations were made: Typically, monometallic Au exhibited small cub-octohedral nanoparticles, with well facetted edges. Also present were larger, icosahedral particles often with multiple twins that had less well defined facets and a more rounded morphology. The $Au_{93}Pd_7$ sample also consisted of a mixture of well facetted cuboctohedral particles and larger, rounder icosahedral particles. The $Au_{55}Pd_{45}$ sample typically consisted of the larger, rounder particles but there was also evidence of well facetted smaller particles. Generally, the smaller particles tended to be well facetted while the larger ones were rounder, although counter-examples were also found. The importance of well facetted or rounded particles for high catalytic activity in WGS remains unclear, although it is feasible that these surfaces would have sufficiently different interactions with reactants such as CO, to have implications for the overall catalytic activity in the WGS reaction. A further complication lies in the absence of elemental identification: it is likely that there are monometallic Au particles as well as bimetallic ones in the $Au_{93}Pd_7$ and $Au_{55}Pd_{45}$ samples and differentiating between these

would allow insights to be made such as the distribution of each element in a given particle and how the elemental formulation of a particle affects its size and shape.

The microscopy data acquired for the selected supported $CeZrO_4$ catalysts is entirely consistent with the other characterisation presented in this chapter. H_2-TPR, CO-DRIFTS and XPS all gave indirect evidence of particle size differences between the catalyst samples and this has been corroborated by STEM HAADF.

4.3.5. XRD

XRD profiles of a range of bimetallic catalysts are presented in Figure 4.25. While XRD is used for bulk characterisations, it is also possible to detect reflections due to precious metals supported on metal oxides[56-58] if the loading and crystallinity of the metals is sufficient.

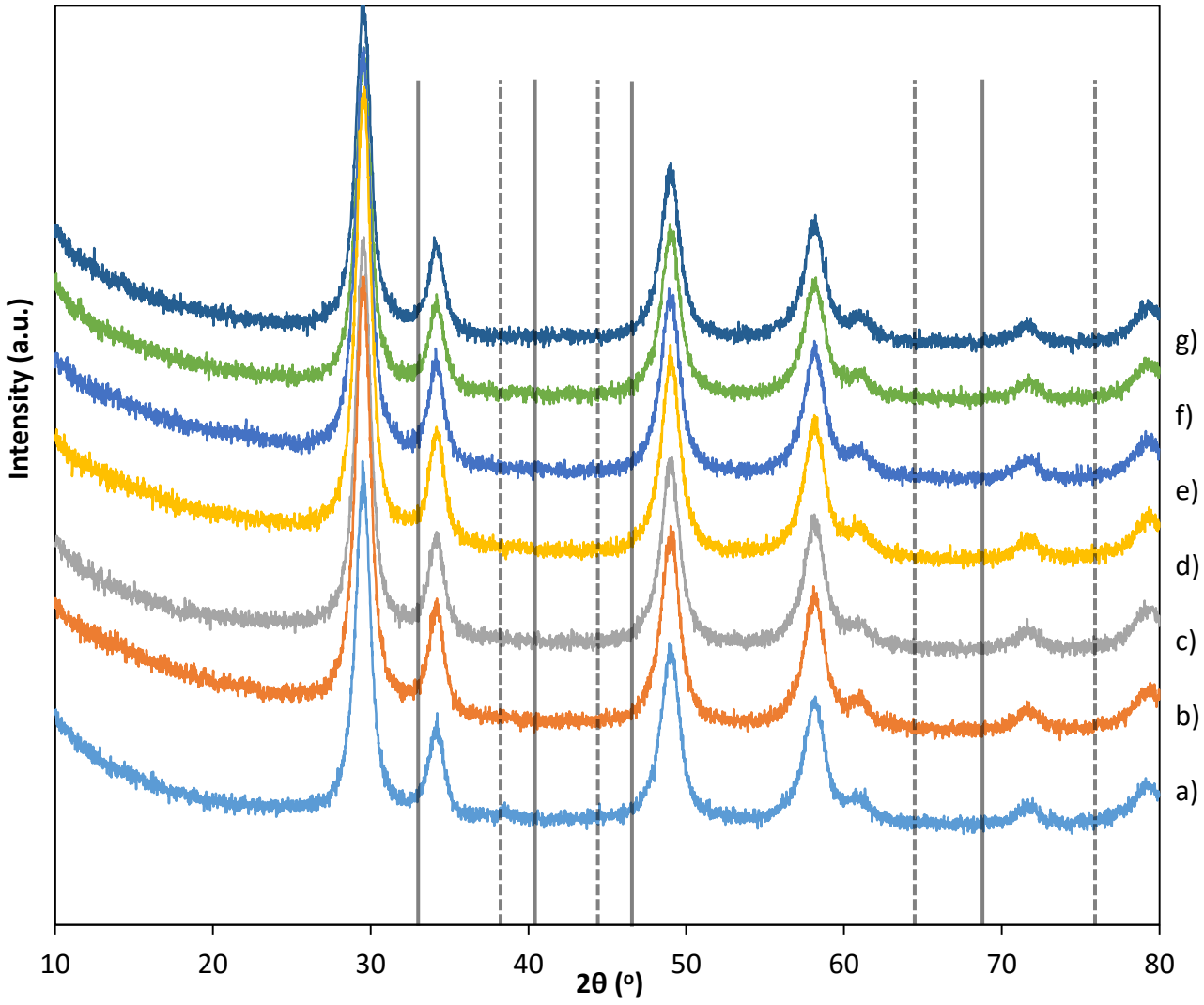

Figure 4.25 XRD stack of $AuPd/CeZrO_4$ catalysts. a) Au, b) $Au_{86}Pd_{14}$, c) $Au_{55}Pd_{45}$, d) $Au_{44}Pd_{56}$, e) $Au_{12}Pd_{88}$, f) Au_8Pd_{92} and g) Pd The position where reflections due to Au (dashed lines) and Pd (solid lines) are marked on the diffractogram.

In this context, XRD can serve as a quick, useful tool to assess if a catalyst features well dispersed metal species or not; evidence of Au or Pd reflections would indicate poor dispersion and large metal particle size. The reflections due to Au would be expected at 2θ = 38.3°, 44.3°, 64.7° and 76.8° that are due to the (111), (200), (220) and (311) planes, respectively of metallic Au.[58, 59] These are indicated by the dashed lines in Figure 4.25. Reflections due to Pd would be expected at 2θ = 40.4, 46.7 and 68.1°, which are due to the (111), (200) and (220) phases, respectively. A PdO reflection would be expected at 32.6°C. These are indicated by the solid lines in Figure 4.25. There are no reflections at any of positions where Au or Pd would occur, indicating that there is not enough long-range order in the samples to give rise to reflections due to the supported metals. This is evidence of well dispersed supported metals, which is consistent with the previous characterisation data although based on the size of the average particle size from STEM, reflections due to Au/Pd would be expected. The absence of such relfections could indicate that the STEM was not representative of the sample and that the smaller species were missed.

The reflections that are present are due to the $CeZrO_4$ support and are typical of a tetragonal crystal structure (ICDD card: 01-081-1549). The position of each of the most intense reflections does not vary significantly with the Au:Pd ratios, suggesting that no incorporation of supported metal into the lattice has occurred.

4.4. Conclusions

In this chapter, the viability of AuPd/$CeZrO_4$ for the WGS reaction prepared by DP was explored. It has been shown that the introduction of Pd to an Au/$CeZrO_4$ catalyst has a severe, detrimental effect on the catalytic activity. The stability of the bimetallic catalysts was not higher than that of monometallic Au. The activity of the catalysts that had 0-50 mol% of Au did not vary significantly, which was rationalised by consideration of the mobility of Pd within the bimetallic nanocrystal, although this was not investigated experimentally. Where the Au mol% was 50-100% there was a large variation in the activity for WGS, whereby the higher the Au content, the higher the activity.

The mechanistically similar CO oxidation and formic acid decomposition reactions were also investigated: Screening of the AuPd/$CeZrO_4$ catalysts for these reactions gave

almost identical activity trends; each reaction showing an anti-synergistic trend across different Au:Pd molar ratios. This confirmed the prediction made by Bond that FAD could be used as a simple test reaction for WGS catalysts.[4] The observation that FAD shares the same trend as CO oxidation and WGS suggested that are underlying similarities between these three reactions. Characterisation showed that the interfacial area of the catalysts varied across the series and this was correlated with catalytic activity. Catalysts with higher dispersion or a higher interfacial area of supported metal were more active for WGS, FAD and CO oxidation. Therefore it can be concluded that each of these reactions requires a well dispersed supported metal, with the metal-support interface likely serving as the active site. This is in contrast to benzyl alcohol oxidation, where the most active catalyst for this reaction was an AuPd catalyst with the molar ratio of nearly one. Therefore the active site for this reaction is different to that of WGS, FAD and CO oxidation.

The fact that WGS, FAD and CO oxidation requires a similar catalytic active site could be exploited in the identification and design of future catalysts for these reactions. Catalysts active for FAD could also prove to be active for WGS and CO oxidation, although it is unclear if the activity trends observed in the AuPd catalysts would be applicable to other systems.

A range of AuPd/TiO_2 catalysts were prepared and screened for CO oxidation. Similar activity trends were seen and suggested that the processes that govern the activity are determined by the nature of the supported metal nanoparticle rather than the support.

Numerous characterisation methods were employed to rationalise the anti-synergistic trends: H_2-TPR showed a correlation between the consumption of hydrogen in the TPR experiment and the catalytic activity in WGS. This was rationalised by consideration of the metal dispersion and hydrogen spillover sites on the catalyst surface that implied the metal particle size was important in determining the catalyst activity. *In situ* CO-DRIFTS corroborated the H_2-TPR findings by showing a correlation between the mode of CO adsorption and catalyst activity. The mode of CO adsorption indicated details about the structure of the nanoparticle that led to the same conclusion as H_2-TPR: Metal particle size determined the catalyst activity in WGS (and by extension, CO oxidation and FAD). XPS analysis of the Au 4f spectrum showed the presence of a

species that was assigned to small gold nanoparticles in each of the Au-containing catalysts. The concentration of this species in each catalyst was correlated with the WGS activity and a liner relationship was found, whereby catalysts that possessed a high level of $Au^{\delta+}$ were more active. Shifts in the binding energy of the Au 4f and Pd 3d signal were interpreted as evidence for the interaction of the two metals, showing the likely formation of an alloy in the bimetallic catalysts.

HAADF STEM was employed to learn about the morphology of the nanoparticles and the mean particle size. The smallest nanoparticles were found on the monometallic Pd catalyst. The monometallic Au catalyst featured nanoparticles with a mean size of 4.5 nm, compared to $Au_{95}Pd_5$, which had a mean particle size of 6.2 nm indicating that very little Pd is needed to significantly affect the final catalyst. The possibility of increased chloride in the reaction mixture during the catalyst preparation was suggested as a possible cause of the increased particle size although this is still not well understood. $Au_{55}Pd_{45}$ exhibited a mean particle size of 6.4 nm, the largest of any of the catalysts analysed using this technique. It also had the lowest catalytic activity. The particle size trends were consistent with the other characterisation tools used. The morphology of the nanoparticles was also investigated and qualitative conclusions were drawn: smaller metal nanoparticles tended to have well facetted edges, while the larger ones tended to be rounder. There was an abundance of small, well facetted cub-octohedral particles in the monometallic Au catalysts, which appeared to be less abundant in the bimetallic catalysts. However, formulation of quantitative information regarding the population of different particle shapes was not possible and the importance of different morphologies/facets was not understood.

The current literature regarding CO oxidation and AuPd systems is somewhat conflicting. While numerous studies predict that AuPd catalysts should be effective WGS and CO oxidation catalysts based on theoretical calculations, the experimental reports have not shown this. Of the few reports that include AuPd catalysts for CO oxidation, supports such as SiO_2 are used which are inherently less active and not comparable with the more widely studied, relevant supports such as Fe_2O_3, CeO_2 and TiO_2. The conflicting literature in this area can be summarised as follows: The theoretical reports do not take into account the dynamic structure of the bimetallic nano-alloy, which has been demonstrated to be susceptible to metal segregation.

Therefore simulations that assume specific arrangements of Au and Pd atoms may not be accurate representations of real catalysts. Mechanistically, the metal oxide support plays an important role in both WGS and CO oxidation so studying non-reducible supports does not enhance the understanding of AuPd catalysts that consist of the reducible supports described above. This work has shown that on $CeZrO_4$ and TiO_2, the combination of Au and Pd is not conducive to highly active catalysts in WGS and CO oxidation. The origin of this anti-synergistic effect is undoubtedly due to the observed particle size differences between the bimetallic catalysts in addition to the observation that the surface of bimetallic catalysts was dominated by Pd.

4.5. References

1. A. Goguet, R. Burch, Y. Chen, C. Hardacre, P. Hu, R. W. Joyner, F. C. Meunier, B. S. Mun, A. Thompsett and D. Tibiletti, *Journal of Physical Chemistry C*, 2007, **111**.

2. M.-A. Hurtado-Juan, C. M. Y. Yeung and S. C. Tsang, *Catalysis Communications*, 2008, **9**.

3. M. A. Saqlain, A. Hussain, M. Siddiq and A. A. Leitao, *Rsc Advances*, 2015, **5**, 47066.

4. G. Bond, *Gold Bulletin*, 2009, **42**, 337.

5. C. Y. Ma, X. H. Li, M. S. Jin, W. P. Liao, R. G. Guan and Z. H. Suo, *Chinese Journal of Catalysis*, 2007, **28**, 535.

6. K. Qian and W. Huang, *Catalysis Today*, 2011, **164**, 320.

7. H. C. Ham, J. A. Stephens, G. S. Hwang, J. Han, S. W. Nam and T. H. Lim, *Journal of Physical Chemistry Letters*, 2012, **3**, 566.

8. F. Gao, Y. Wang and D. W. Goodman, *Journal of the American Chemical Society*, 2009, **131**, 5734.

9. A. M. Henning, J. Watt, P. J. Miedziak, S. Cheong, M. Santonastaso, M. H. Song, Y. Takeda, A. I. Kirkland, S. H. Taylor and R. D. Tilley, *Angewandte Chemie-International Edition*, 2013, **52**, 1477.

10. W. Jones, R. Su, P. P. Wells, Y. Shen, N. Dimitratos, M. Bowker, D. Morgan, B. B. Iversen, A. Chutia, F. Besenbacher and G. Hutchings, *Physical Chemistry Chemical Physics*, 2014, **16**, 26638.

11. B. Zhu, G. Thrimurthulu, L. Delannoy, C. Louis, C. Mottet, J. Creuze, B. Legrand and H. Guesmi, *Journal of Catalysis*, 2013, **308**, 272.

12. H. Daly, F. C. Meunier, R. Pilasombat, R. Burch, A. Goguet and C. Hardacre, *Abstracts of Papers of the American Chemical Society*, 2011, **241**.

13. L. Delannoy, S. Giorgio, J. G. Mattei, C. R. Henry, N. El Kolli, C. Methivier and C. Louis, *Chemcatchem*, 2013, **5**, 2707.

14. F. Gao, Y. Wang and D. W. Goodman, *Journal of Physical Chemistry C*, 2010, **114**, 4036.

15. V. Soto-Verdugo and H. Metiu, *Surface Science*, 2007, **601**, 5332.

16. E. K. Gibson, A. M. Beale, C. R. A. Catlow, A. Chutia, D. Gianolio, A. Gould, A. Kroner, K. M. H. Mohammed, M. Perdjon, S. M. Rogers and P. P. Wells, *Chemistry of Materials*, 2015, **27**, 3714.

17. S. A. Tenney, J. S. Ratliff, C. C. Roberts, W. He, S. C. Ammal, A. Heyden and D. A. Chen, *Journal of Physical Chemistry C*, 2010, **114**, 21652.

18. S. A. Tenney, W. He, J. S. Ratliff, D. R. Mullins and D. A. Chen, *Topics in Catalysis*, 2011, **54**, 42.

19. J. Kiss, L. Ovari, A. Oszko, G. Potari, M. Toth, K. Baan and A. Erdohelyi, *Catalysis Today*, 2012, **181**, 163.

20. Q.-Y. Bi, X.-L. Du, Y.-M. Liu, Y. Cao, H.-Y. He and K.-N. Fan, *Journal of the American Chemical Society*, 2012, **134**, 8926.

21. D. A. Bulushev, S. Beloshapkin and J. R. H. Ross, *Catalysis Today*, 2010, **154**, 7.

22. D. A. Bulushev, S. Beloshapkin, P. E. Plyusnin, Y. V. Shubin, V. I. Bukhtiyarov, S. V. Korenev and J. R. H. Ross, *Journal of Catalysis*, 2013, **299**, 171.

23. M. Ojeda and E. Iglesia, *Angewandte Chemie-International Edition*, 2009, **48**, 4800.

24. W. Zhou and J. Y. Lee, *Electrochemistry Communications*, 2007, **9**, 1725.

25. W.-Y. Yu, G. M. Mullen, D. W. Flaherty and C. B. Mullins, *Journal of the American Chemical Society*, 2014, **136**, 11070.

26. P. Concepcion, S. Garcia, J. Carlos Hernandez-Garrido, J. Juan Calvino and A. Corma, *Catalysis Today*, 2016, **259**, 213.

27. M. Sankar, E. Nowicka, R. Tiruvalam, Q. He, S. H. Taylor, C. J. Kiely, D. Bethell, D. W. Knight and G. J. Hutchings, *Chemistry-a European Journal*, 2011, **17**.

28. Y. Hou, X. Ji, G. Liu, J. Tang, J. Zheng, Y. Liu, W. Zhang and M. Jia, *Catalysis Communications*, 2009, **10**.

29. J. A. Lopez-Sanchez, N. Dimitratos, P. Miedziak, E. Ntainjua, J. K. Edwards, D. Morgan, A. F. Carley, R. Tiruvalam, C. J. Kiely and G. J. Hutchings, *Physical Chemistry Chemical Physics*, 2008, **10**.

30. R. Burch, L. Gladden and S. Golunski, *Platinum Metals Review*, 2010, **54**.

31. M. Kosmulski, CRC Press, 2001.

32. F. Moreau, G. C. Bond and A. O. Taylor, *Journal of Catalysis*, 2005, **231**, 105.

33. P. Fornasiero, G. Balducci, R. DiMonte, J. Kaspar, V. Sergo, G. Gubitosa, A. Ferrero and M. Graziani, *Journal of Catalysis*, 1996, **164**, 173.

34. J. Kaspar, P. Fornasiero and M. Graziani, *Catalysis Today*, 1999, **50**, 285.

35. S. S. E. Collins, M. Cittadini, C. Pecharroman, A. Martucci and P. Mulvaney, *Acs Nano*, 2015, **9**, 7846.

36. V. V. Rozanov and O. V. Krylov, *Uspekhi Khimii*, 1997, **66**, 117.

37. A. M. Venezia, G. Pantaleo, A. Longo, G. Di Carlo, M. P. Casaletto, F. L. Liotta and G. Deganello, *Journal of Physical Chemistry B*, 2005, **109**, 2821.

38. A. M. Venezia, L. F. Liotta, G. Pantaleo, V. La Parola, G. Deganello, A. Beck, Z. Koppany, K. Frey, D. Horvath and L. Guczi, *Applied Catalysis a-General*, 2003, **251**, 359.

39. P. A. P. Nascente, S. G. C. Decastro, R. Landers and G. G. Kleiman, *Physical Review B*, 1991, **43**, 4659.

40. D. Goodman, in *Dekker Encyclopedia of Nanoscience and Nanotechnology*, eds. C. Contescu and K. Putyera, CRC Press, Second edn., 2008, pp. 611-619.

41. V. I. Parvulescu, V. Parvulescu, U. Eudruschat, G. Filoti, F. E. Wagner, C. Kubel and R. Richards, *Chemistry-a European Journal*, 2006, **12**, 2343.

42. P. A. Deshpande, M. S. Hegde and G. Madras, *Applied Catalysis B-Environmental*, 2010, **96**, 83.

43. P. Bera and M. S. Hegde, *Catalysis Letters*, 2002, **79**, 75.

44. M. P. Casaletto, A. Longo, A. Martorana, A. Prestianni and A. M. Venezia, *Surface and Interface Analysis*, 2006, **38**, 215.

45. M. A. Bollinger and M. A. Vannice, *Applied Catalysis B-Environmental*, 1996, **8**, 417.

46. A. R. Wilson, K. Sun, M. Chi, R. M. White, J. M. LeBeau, H. H. Lamb and B. J. Wiley, *Journal of Physical Chemistry C*, 2013, **117**, 17557.

47. S. Marx, F. Krumeich and A. Baiker, *Journal of Physical Chemistry C*, 2011, **115**, 8195.

48. T. Dellwig, G. Rupprechter, H. Unterhalt and H. J. Freund, *Physical Review Letters*, 2000, **85**, 776.

49. K. I. Hadjiivanov and G. N. Vayssilov, *Advances in Catalysis, Vol 47*, 2002, **47**, 307.

50. L. Ouyang, G.-j. Da, P.-f. Tian, T.-y. Chen, G.-d. Liang, J. Xu and Y.-F. Han, *Journal of Catalysis*, 2014, **311**, 129.

51. R. Pilasombat, H. Daly, A. Goguet, J. P. Breen, R. Burch, C. Hardacre and D. Thompsett, *Catalysis Today*, 2012, **180**.

52. H. Q. Zhu, Z. F. Qin, W. J. Shan, W. J. Shen and J. G. Wang, *Journal of Catalysis*, 2004, **225**, 267.

53. E. A. Redina, O. A. Kirichenko, A. A. Greish, A. V. Kucherov, O. P. Tkachenko, G. I. Kapustin, I. V. Mishin and L. M. Kustov, *Catalysis Today*, 2015, **246**, 216.

54. H. Daly, A. Goguet, C. Hardacre, F. C. Meunier, R. Pilasombat and D. Thompsett, *Journal of Catalysis*, 2010, **273**, 257.

55. K. Duan, Z. Liu, J. Li, L. Yuan, H. Hu and S. I. Woo, *Catalysis Communications*, 2014, **57**, 19.

56. X. Zhang, Y. Zhu, X. Yang, Y. Zhou, Y. Yao and C. Li, *Nanoscale*, 2014, **6**, 5971.

57. X. Wang, T. Dornom, M. Blackford and R. A. Caruso, *Journal of Materials Chemistry*, 2012, **22**, 11701.

58. M. Y. M. Abdelrahim, S. R. Benjamin, L. Ma Cubillana-Aguilera, I. Naranjo-Rodriguez, J. L. Hidalgo-Hidalgo de Cisneros, J. Jose Delgado and J. Ma Palacios-Santander, *Sensors*, 2013, **13**, 4979.

59. J. Heo, D.-S. Kim, Z. H. Kim, Y. W. Lee, D. Kim, M. Kim, K. Kwon, H. J. Park, W. S. Yun and S. W. Han, *Chemical Communications*, 2008, 6120.

Chapter 5

Ce-based metal oxide supports for the low-temperature water-gas shift reaction

5.1. Introduction and aims of the chapter

The role of the support in a water-gas shift catalyst (WGS) has been the subject of much research in recent years.[1] In precious metal supported catalysts that feature Ce-based supports, e.g. $CeZrO_4$ it is now known that the role of support is more than to simply immobilise the metal nanoparticles. It is responsible for dissociating water on the surface of the catalyst which then reacts at the metal-support interface with an adsorbed CO molecule.[1, 2] The deactivation mechanism of the $Au/CeZrO_4$ catalyst fundamentally concerns the interaction between the metal and the support, as discussed in **Chapter 3.** We showed that morphological changes and particle agglomeration occur under WGS reaction conditions therefore optimisation of the metal-support interaction should be considered integral to developing a stable catalytic system. The work presented in this chapter concerns the attempts made to modify the support with the aim of enhancing the metal-support interaction in order to minimise the agglomeration or morphological change under reaction conditions of the supported gold. This was attempted through two routes: firstly through the addition of sub-surface dopants and secondly by the substitution of Zr to form a new mixed metal oxide support. A full literature review of Ce-based supports for WGS catalysts is presented in **Chapter 1.3**. Below, a brief summary of the key findings that were the motivation for this work is presented.

5.1.1. Strategies to achieving stability through support modification

Increasing the interaction between the metal and the support is an ongoing field of investigation. Recent advances made by Freund and co-workers showed that the addition of sub-surface dopants could affect the properties of a surface gold nanoparticle.[3-5] The addition of Mo beneath the surface of CaO resulted in a more 2D like gold structure at the surface. The prospect of anchoring a gold species without affecting the chemical composition of the surface is an appealing one so the stability of Au supported on Mo-doped $CeZrO_4$ was investigated for WGS.

Other strategies to achieving stable catalysts involve the adjustment of the chemical formulation of the support. The modification of CeO_2 to form novel mixed metal oxides has led to the discovery of many materials with superior properties to CeO_2.[6] Ceria-titania is no exception and has been successfully used as a catalyst support for a number of reactions, including CO oxidation[7, 8] and dry methane reforming.[9] The addition of Ti to Ce has been reported to produce a mixed metal oxide with enhanced redox properties, due to the introduction of oxygen vacancies and small crystallite sizes.[7, 10, 11] The pioneering surface science studies of Rodriguez and co-workers have shown in model studies, that Au/CeO_2-TiO_2 yields a remarkably active catalyst for the WGS reaction.[12] However, despite research interest in this area, $Ce_{0.5}Ti_{0.5}O_x$ has not been directly compared to $CeZrO_4$ supported catalysts for activity or stability in the WGS reaction. Therefore the potential of this support in the low-temperature WGS reaction is unknown. In addition, the optimisation of the support has not been carried out.

$Ce_{0.5}Al_{0.5}O_x$ is not as widely studied as many Ce-based mixed metal oxides but there are reports concerning Au supported on $Ce_{0.5}Al_{0.5}O_x$ for the WGS reaction[13, 14] and CO oxidation.[15] In addition, the successful application of alumina to stabilise industrial catalysts makes it an appealing oxide to investigate.[16] However, the properties of the catalyst have been shown to be highly dependent on the preparation method.[13, 17] In many of the reports on ceria-alumina catalysts for the WGS reaction[13, 14, 17-19] the reaction conditions were not representative of the typical gas composition that would exist in a fuel cell reformer. Therefore reports of high stability and activity are not necessarily

relevant in the context of fuel cell applications. Gold supported on mixed metal oxides of Ce and Al prepared by the sol-gel method has not been reported for WGS, despite promising results achieved in similar systems. Therefore the activity and stability of gold supported on $Ce_{0.5}Al_{0.5}O_x$ and $Ce_{0.5}Ti_{0.5}O_x$ were investigated and compared to $Au/CeZrO_4$.

5.1.2. Chapter aims

The aim of this chapter was to attempt to stabilise the benchmark gold catalyst through modification of the support. Mo-doped $CeZrO_4$ was investigated as a catalyst support to enhance the stability of a supported gold catalyst. $Ce_{0.5}Ti_{0.5}O_x$ and $Ce_{0.5}Al_{0.5}O_x$ were prepared and compared to a standard $Au/CeZrO_4$ catalyst and the best candidate was selected for further investigation. The properties of the supports were examined by using numerous tools to characterise the novel materials and establish the most significant properties required for active WGS catalysts.

5.2. Mo-doped $CeZrO_4$ as a support for WGS catalysts

The use of sub-surface dopants was considered to be an appropriate strategy for preventing the deactivation of $Au/CeZrO_4$ given that the deactivation mechanism concerns the morphology and strength of interaction between gold and the support. Thus, a number of doped supports were prepared with various amounts of Mo-doped into the support that was synthesised in a conventional sol-gel methodology, as described in **Chapter 2.2.1.** Mo-doped $CeZrO_4$ was prepared with X wt% Mo-$CeZrO_4$, where X = 0.1, 1, 2 or 5. The supports were then characterised using XPS and XRD, before being used as supports for 2 wt% Au catalysts that were prepared using the conventional DP method described in **Chapter 2.2.3.**

5.2.1. Characterisation of Mo-doped $CeZrO_4$

XRD

A stack of the XRD patterns of the Mo-doped $CeZrO_4$ supports are presented in Figure 5.1 as well as an undoped $CeZrO_4$ support for comparison. Each of the samples exhibited a similar diffraction pattern, each consistent with the cubic crystal system of CeO_2. The reflections at 2θ = 29, 33, 47, 56 and 59^o are due to the (111), (200), (220), (311) and (222) planes. These are indicated by an asterisk (*) in Figure 5.1. The samples containing Mo might be expected to exhibit reflections due to molybdenum oxides, such as MoO_3. An intense reflection due to MoO_3 would be expected at $2\theta = 25^o$ however there is no feature in this region, showing that if MoO_3 is present, it is not sufficiently crystalline to be detected using XRD. This 'XRD invisibility' is common in supported metal catalysts and could indicate that the Mo is well dispersed in the material.

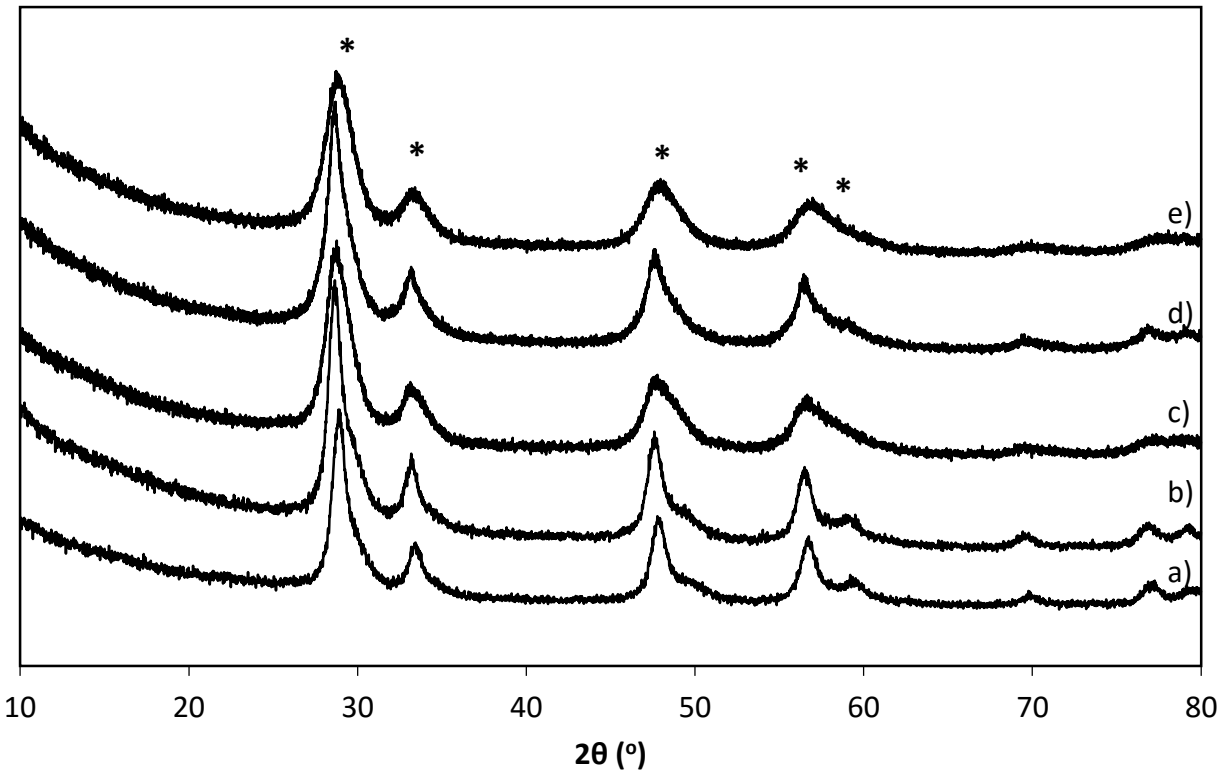

Figure 5.1 XRD stack of Mo-doped $CeZrO_4$ supports: a) un-doped $CeZrO_4$, b) 0.1 wt% Mo-$CeZrO_4$, c) 1 wt%Mo-$CeZrO_4$, d) 2 wt%Mo-$CeZrO_4$ and e) 5 wt%Mo-$CeZrO_4$. * indicate reflections due to cubic CeO_2.

The position of the most intense reflection, at 29^{o}, varies between samples. Table 5.1 shows the lattice parameter of each Mo-doped sample. The un-doped $CeZrO_4$ lattice parameter was calculated to be 5.33 Å. Each of the Mo-doped $CeZrO_4$ exhibit larger lattice parameters than the un-doped materials, which could be because of distortion of the lattice due to the inclusion of Mo, although the ionic radii of Mo cations is considerably smaller than Ce so it is intuitive that there would be an overall decrease in the lattice parameter if Mo was substituted for Ce.

Table 5.1 Lattice parameter and surface composition of doped supports determined using XRD and XPS

Nominal Mo loading (wt %)	Lattice constant (Å)	Elemental composition (at %)				Ce:Zr molar ratio
		Ce	Zr	O	Mo	
0.1	5.37	17.1	8.7	74.2	0	2.0
1	5.37	12.9	8.0	72.9	6.2	1.6
2	5.40	14.8	8.4	76	0.9	1.8
5	5.37	12.1	10.7	74	3.2	1.1

However, it well known that the Ce:Zr molar ratio also affects the lattice parameter[20, 21] of the materials and so variations in this between the Mo-doped samples can also contribute to the difference in lattice constant. Zhang *et al.* showed the relationship between the lattice parameter and Ce concentration in a series of solid solutions annealed at 1200 ^{o}C. Where Ce concentration is 60%, the lattice parameter is at a minimum of 5.34 Å. Deviations above or below this value resulted in larger lattice parameters. Based on the calculated lattice parameters, the Ce:Zr ratios of these materials could potentially vary significantly from the nominal 1:1 ratio. Given the relatively small quantity of Mo that was added to the $CeZrO_4$, it is likely that the cerium and zirconium content is a more significant contributor to the lattice constant than the Mo content and so the presence of Mo cannot be inferred from this parameter.

Overall, XRD showed that there was no evidence of long-range ordered Mo in the doped $CeZrO_4$ supports. Each material exhibited a cubic structure typical of Ce-based mixed metal oxides, showing that the addition of Mo did not prevent the formation of the expected mixed metal oxide phase. While the bulk properties of the material are important, the surface of the Mo-doped material was also of interest and therefore characterisation of this part of the support was carried out.

XPS

XPS was carried out on the doped supports in order to gain quantitative information regarding the surface concentration of Mo in the catalyst and the chemical state of the other constituent elements present. A stack of the Mo 3d region of the XP spectrum is shown below in figure 2 for the Mo-doped supports. There is the existence of one species in each of the samples that has been assigned to Mo^{6+} in the form of MoO_3 with a binding energy at 232.8 eV, corresponding to the Mo $3d_{5/2}$ peak. The 0.1% Mo-$CeZrO_4$ did not exhibit a peak in this region, showing that there was not a significant quantity of Mo on the surface of the catalyst. The surface concentration of Mo in each sample was calculated for the other supports and the surface elemental composition is shown above in Table 5.1. The concentration of Mo in each sample does not reflect the nominal value. 1% Mo-$CeZrO_4$ displayed the highest surface concentration of Mo, at 6.2 at%, almost twice as much as the 5% Mo-$CeZrO_4$ which had 3.2 at%. This shows the lack of control of metal loading in this preparation method. The purpose of introducing the Mo during the synthesis of the support was to ensure minimal levels of surface Mo, as the stabilising effect requires the Mo to be sub-surface. In the majority of the samples, this was not achieved, although it is unclear whether the Mo migrated or segregated to the surface during the drying or calcination step from the bulk, or precipitated there during the synthesis.

If the $CeZrO_4$ precursor precipitated before the Mo, it is feasible that the Mo would be deposited on the surface. XPS analysis at different stages of the preparation could clarify this. The atomic % of the constituent elements is also presented in Table 5.1.

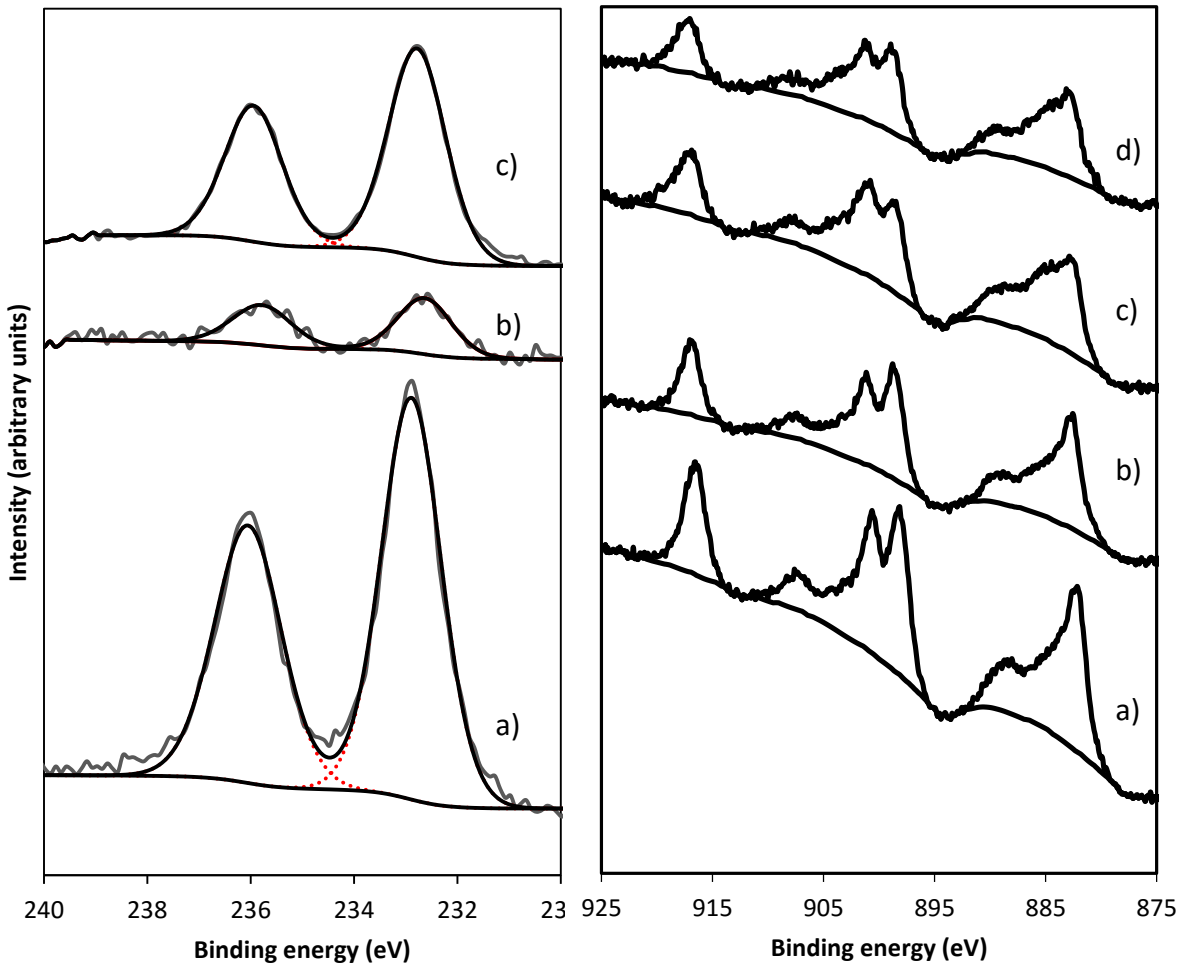

Figure 5.2 Left: Mo 3d spectra a) 1 wt% Mo-$CeZrO_4$, b) 2 wt% Mo-$CeZrO_4$ and c) 5 wt% Mo-$CeZrO_4$ and right: Ce 3d of a) 0.1 wt% Mo-$CeZrO_4$, 1 wt% Mo-$CeZrO_4$, 2 wt% Mo-$CeZrO_4$ and 5 wt% Mo-$CeZrO_4$.

The variation in Ce content is significant: the 0.1% Mo-$CeZrO_4$ had a Ce:Zr ratio of 2.0 whereas the 5% Mo-$CeZrO_4$ had a ratio of 1.1. This does not necessarily reflect the bulk composition, although the ease with which Ce and Zr form solid solutions means that it is an adequate approximation. It is unclear how the Mo precursor, ammonium heptamolybdate, could affect the Ce:Zr ratio in the resultant material, especially as there is no correlation between the nominal or actual Mo content and the Ce:Zr ratio.

Table 5.2 Relative compositions of different Ce and O species present in the Mo-doped $CeZrO_4$

Nominal Mo loading (wt %)	Species composition (%)			
	Ce^{3+}	Ce^{4+}	O'	O''
5	42.5	57.5	57.7	42.3
2	42.7	57.3	56.9	42.6
1	34.6	65.4	53.9	46.1
0.1	31.5	68.5	56.7	42.9

While the surface composition of elements is extremely important, the bulk composition is also a relevant parameter to measure as it would enhance the understanding of structure of the material. This is challenging however, as SEM-EDX is not sensitive enough to accurately quantify small amounts of Mo and so this method cannot be used. The total digestion of the sample and the subsequent analysis using MP-AES was attempted, but the digestion media used was not sufficient to digest these materials. The Ce 3d spectrum of each of the Mo-doped supports is also shown in figure 2. The deconvolution of the Ce 3d is challenging, due to the large number of features within. As with the data in **Chapter 3,** the fitting was modelled on the early work of Burroughs.[22] Table 5.2 shows the relative concentrations of Ce^{3+} and Ce^{4+}. This can indicate the number or defect sites on the surface of the catalyst, which are the activation sites of water in the WGS reaction.[13, 23, 24] The samples with a higher nominal loading of Mo have a higher amount of Ce^{3+} compared to the un-doped supports. This could be due to the formation of defect sites as a result of the Mo on the surface although the surface concentration of Mo, as determined from the Mo 3d spectra, does not correlate with the concentration of Ce^{3+}.

Table 5.2 also shows the composition of the different oxygen species in each of the Mo-doped samples. There are differences in the shape of the spectra across the range of samples. This is illustrated in Figure 5.3, which shows a stack of O 1s spectra for the samples. Accurate deconvolution of the O 1s region is challenging, with multiple O features present in the Mo-containing samples over a relatively small region. Furthermore, the full width half maximum (FWHM) of these features heavily influences

the relative concentrations and while the lattice oxygen signal is generally fitted with a smaller FWHM than for example hydroxyl O, it is unclear exactly how wide each signal should be. However, the peaks have been fitted and are tentatively assigned as follows: The peak at 529 eV corresponds to lattice oxygen bonded to a metal, O', while the broader feature at 531 eV corresponds to hydroxyl groups, labelled O''.[25, 26] There is not a significant difference between the line shape of the samples. For the 0.1 wt% and 2 wt% samples, a third peak was fitted. The line shape of these samples had a shoulder at 533 eV, most likely due to a carbon-oxygen bond, perhaps a carbonate species.[27-29] This observation is consistent with a corresponding carbonate signal in the C 1s spectrum. The quantity of oxygen due to carbonate makes up a very small part of the total O 1s signal and should not affect the quantitative interpretation of the other features significantly. The origin of the carbonate is unknown, but is likely due to adventitious carbon contamination.

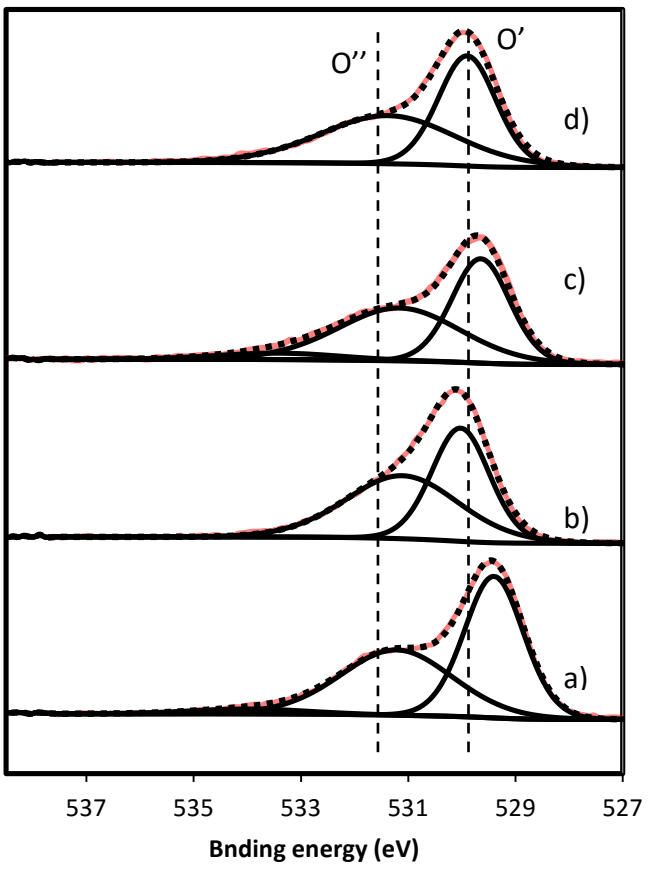

Figure 5.3 O 1s spectra of a): 0.1 wt% Mo-CeZrO$_4$, b) 1 wt% Mo-CeZrO$_4$, c) 2 wt% Mo-CeZrO$_4$ and d) 5 wt% Mo-CeZrO$_4$.

The characterisation of the Mo-doped materials was challenging. XRD showed that the doped materials all exhibit a cubic crystal system, consistent with ceria-zirconia but did not show any evidence of Mo. The variation in lattice parameter was most likely due to variations in the Ce and Zr content in the materials. XPS confirmed that there were large variations in the molar ratio of Ce and Zr although these variations did not correlate with the lattice parameter. The presence of multiple phases was highlighted as a possibility for this. XPS also showed the presence of Mo on the surface of the materials although the concentration did not scale with the nominal loadings, suggesting a poor degree of control in the sol-gel preparation method. Differences between the Ce^{3+}/Ce^{4+} concentration were also identified but these did not correlate with the Mo content or Ce:Zr ratio. While many characteristics of these materials were not well resolved, it was shown that a series of Mo-doped ceria-zirconia material were successfully synthesised.

5.2.2. The activity and stability of Au/Mo-$CeZrO_4$

The Mo-doped supports were used to prepare a range of 2 wt% Au/X wt%Mo-$CeZrO_4$ catalysts using the standard DP method. They were then tested and screened for their activity and stability in the low-temperature WGS reaction. Catalyst screening showed that the introduction of Mo into the support severely reduced the catalytic activity of the resultant catalyst. As discussed above, while only one variable was changed in the preparation method, the resultant materials contained more differences than just the Mo content, for example the Ce:Zr ratio. As shown above, there was an appreciable amount of Mo on the surface of many doped $CeZrO_4$ samples. Figure 5.4 shows a plot of the actual Mo content as determined by XPS and the catalytic activity compared to an un-doped catalyst. As the surface Mo content increases, the WGS activity decreases. Mo has previously been identified as a poison on Pd/CeO_2 catalysts for the WGS reaction.[30] Gorte and co-workers showed that Mo exchanged with surface hydroxyl groups and disrupted the redox properties of the catalyst.

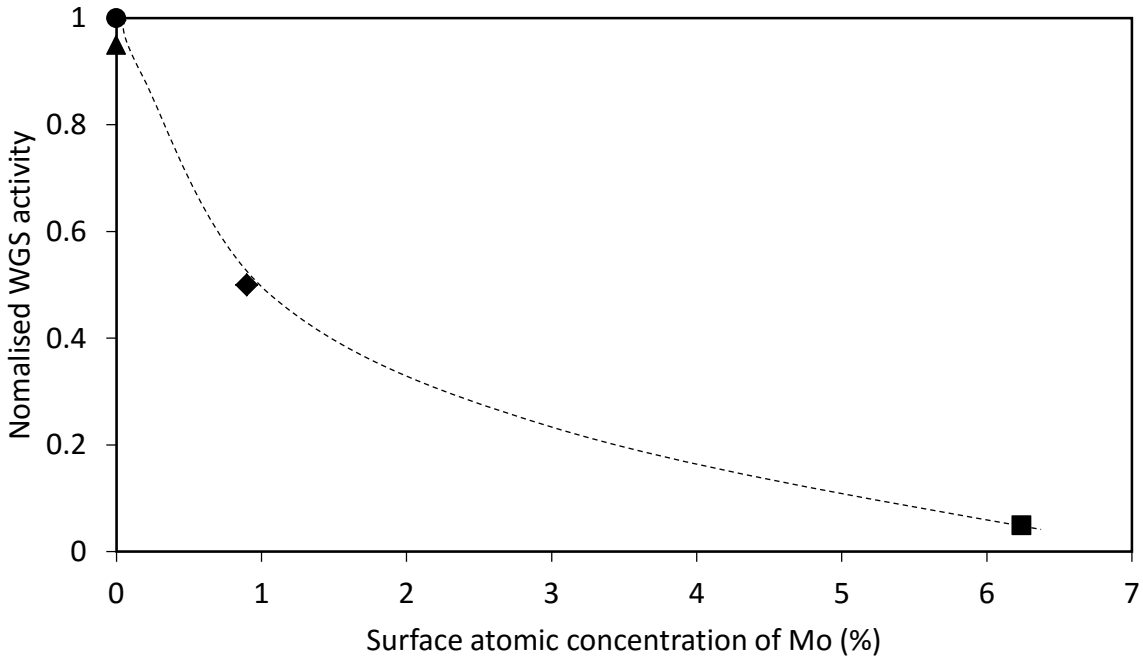

Figure 5.4 Comparison of the WGS activity of Au catalysts as a function of the surface Mo concentration determined using XPS where Au/$CeZrO_4$ (●), Au/0.1 wt%Mo-$CeZrO_4$ (▲), Au/2 wt%Mo-$CeZrO_4$ (♦) and Au/1 wt%Mo-$CeZrO_4$ (■).

The only catalyst that exhibited a similar activity as the un-doped catalyst was Au/0.1% Mo-$CeZrO_4$, which exhibited the same activity within experimental error. In light of this, the stability of this catalyst was studied over a longer time period (16 h). The stability of the benchmark catalyst and Au/0.1%Mo-$CeZrO_4$ is shown below in Figure 5.5. The stability of each catalyst is almost identical. According to XPS, there was no Mo at the surface of the catalyst, and most bulk techniques are not sensitive enough to measure low quantities of the dopant. Therefore it was not possible to establish if any sub-surface Mo was present in the catalyst sample.

In conclusion, the doping of $CeZrO_4$ with Mo was not effective in enhancing the stability of the benchmark catalyst. The sol-gel route for preparing Mo-doped $CeZrO_4$ was not effective as Mo was present on the surface and the Ce:Zr ratios were variable. The catalysts displayed poor activity in the WGS reaction, most likely due to the poisoning effect of Mo that was previously reported.[31] The degree of control required to achieve the optimum level of sub-surface dopant in the material at the correct distance from the surface is unrealistically high using sol-gel or co-precipitation methods, which could

explain why no reports exist on powder samples exhibiting the remarkable effect seen in Freund and co-workers' model catalysts.[5] The prospect of exploiting the stabilising effect of sub-surface dopants remains an appealing one, but advances in catalyst preparation and the understanding of the sub-surface dopant effect must be made in order to realistically apply this to powder catalysts.

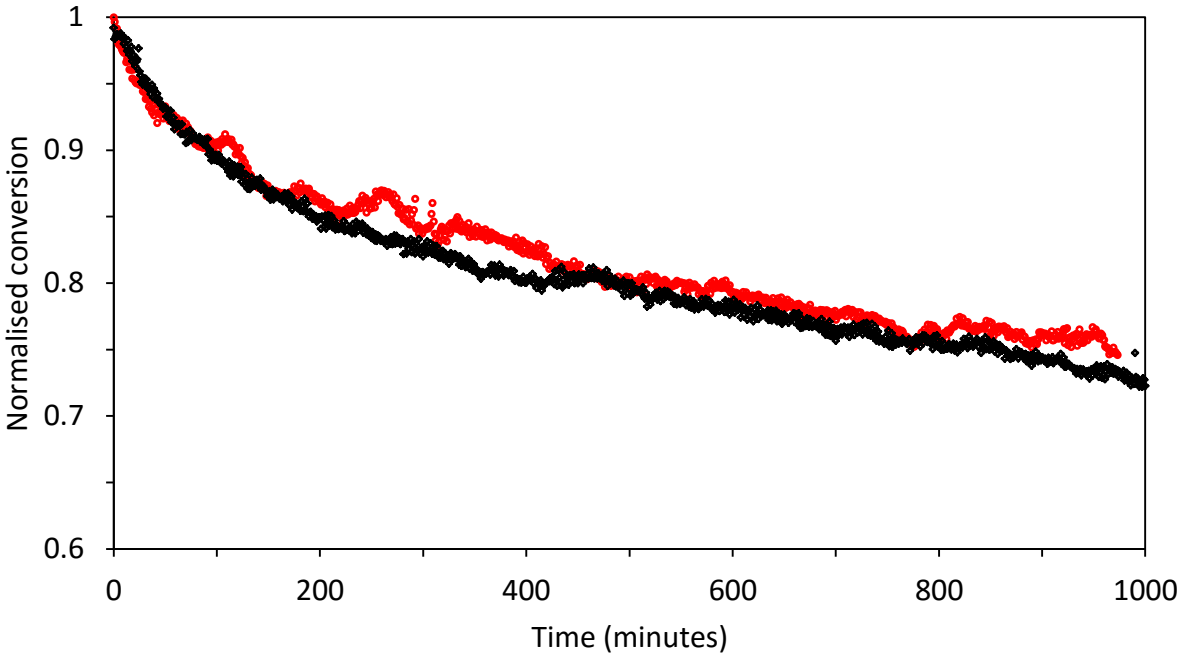

Figure 5.5 Comparison of the stability of Au/$CeZrO_4$ (red circles) and Au/0.1%Mo-$CeZrO_4$ (black diamonds) during a 16 h time on-line study

5.3. Substitution of Zr for M (where M=Al or Ti)

5.3.1. The activity and stability of $CeMO_x$ materials

The importance of the Zr cation in the $CeZrO_4$ mixed metal oxide was investigated by substituting Zr for Ti or Al. These materials were prepared with nominally equi-molar quantities of Ce and Ti or Al, to form $Ce_{0.5}Ti_{0.5}O_x$ or $Ce_{0.5}Al_{0.5}O_x$ using a sol-gel synthesis and compared to a $CeZrO_4$ support prepared in the same way, as described in **Chapter 2.2.2.** The sol-gel method is extensively used in catalysis to produce well-dispersed, high surface area mixed-metal oxides. It has also been shown to yield high numbers of defect

sites in CeO_2 based materials,[32] which is desirable as these sites are responsible for the activation of water in the WGS reaction[24] and can function as nucleation sites for metal nanoparticles.[33-35]

Titanium was selected as an appropriate metal to substitute Zr with for many reasons, as described in the introduction to this chapter. Despite being reported before, $Au/Ce_{0.5}Ti_{0.5}O_x$ has not been investigated in the context of the catalyst stability in the WGS reaction, nor has the preparation of the material been properly optimised. Accordingly, it remains unclear how this mixed metal oxide compares to such supports as $CeZrO_4$ or $Ce_{0.5}Al_{0.5}O_x$. Aluminium is a widely used element in catalysis, particularly in its oxidic form as a thermally robust support. While Ce doped onto Al_2O_3 has been studied for WGS, with promising results as a support for Au, the mixed metal oxide is not as well studied and its stability and activity compared to $Au/CeZrO_4$ has not been reported. Overall, the research carried out on the aforementioned supports has provided a strong basis for carrying out further work on these materials but the large variation in the experimental conditions used by different research groups has prevented a consensus being reached on which material is the optimum support. The aim of **Chapter 5.3** is to evaluate the activity and stability of gold supported on $CeZrO_4$, $Ce_{0.5}Ti_{0.5}O_x$ and $Ce_{0.5}Al_{0.5}O_x$ in a manner that allows direct comparisons to be made regarding the activity and stability. Furthermore, extensive characterisation was carried out with the aim of identifying the key properties that give rise to active and stable supports for gold catalysts for the WGS reaction.

TGA analysis in flowing air was performed on the catalysts prior to calcination in order to establish the most appropriate calcination temperature. The data is presented below in Figure 5.6. The decomposition of both precursors was complete at 500 ^{o}C and so this was selected as the calcination temperature. This is also consistent with similarly prepared Ce-based oxides.[7, 36] Once the supports were synthesised, gold was deposited using the standard DP method described in **Chapter 2.2.3** to achieve nominal loadings of 2 wt% Au. These were then tested for WGS activity and stability and compared to the $Au/CeZrO_4$ catalyst investigated in **Chapter 3**. The time on-line data for the three catalysts is shown in Figure 5.7 (top graph). It can be seen that the highest conversion was by the $CeZrO_4$ and

$Ce_{0.5}Ti_{0.5}O_x$ supported catalysts while the $Ce_{0.5}Al_{0.5}O_x$ achieved the poorest conversion. Although the $CeZrO_4$-supported catalyst achieved an initially higher conversion than the $Ce_{0.5}Ti_{0.5}O_x$, the difference is within error and so the activity of the two catalysts can be considered to be the same within experimental error. In addition to the activity, the stability of the catalysts was measured and is represented by the normalised conversion graph shown in Figure 5.7 (bottom graph). The most stable catalyst was $Au/Ce_{0.5}Ti_{0.5}O_x$, followed by $Au/CeZrO_4$ while the least stable catalyst was $Au/Ce_{0.5}Al_{0.5}O_x$. After 10 h on-line, $Au/Ce_{0.5}Ti_{0.5}O_x$, $Au/CeZrO_4$ and $Au/Ce_{0.5}Al_{0.5}O_x$ retained 82%, 73% and 60% of their initial activity. This represents a significant difference in stability.

This observation was initially unexpected, as there is a precedent for using Al_2O_3 to stabilise many catalysts and Au/CeO_2-Al_2O_3 has also been reported to be stable.[14] However, the importance of preparation method has also been noted: Physical grinding of $Ce(NO_3)_3$ onto Al_2O_3 followed by calcination was reported to stabilise the resultant gold catalyst while wash-coating did not improve stability.[13] This finding showed the importance of preparation methods in determining the final properties of the material.

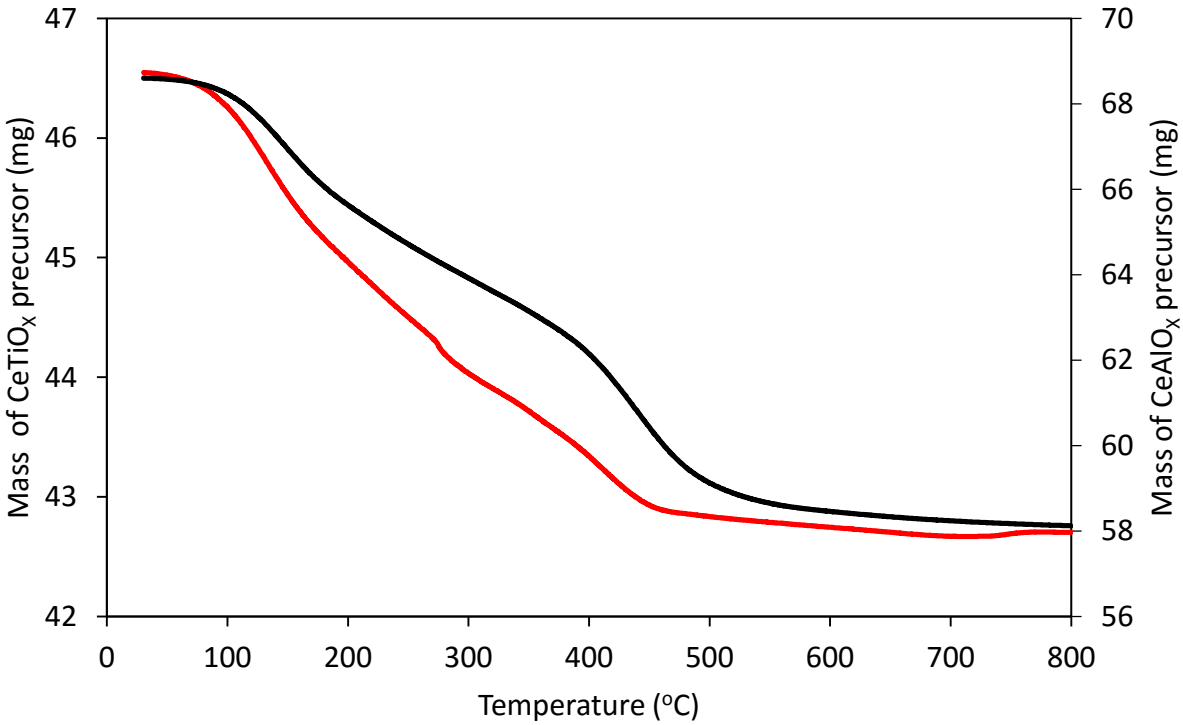

Figure 5.6 TGA profiles of $Ce_{0.5}Ti_{0.5}O_x$ (red) and $Ce_{0.5}Al_{0.5}O_X$ (black) precursors.

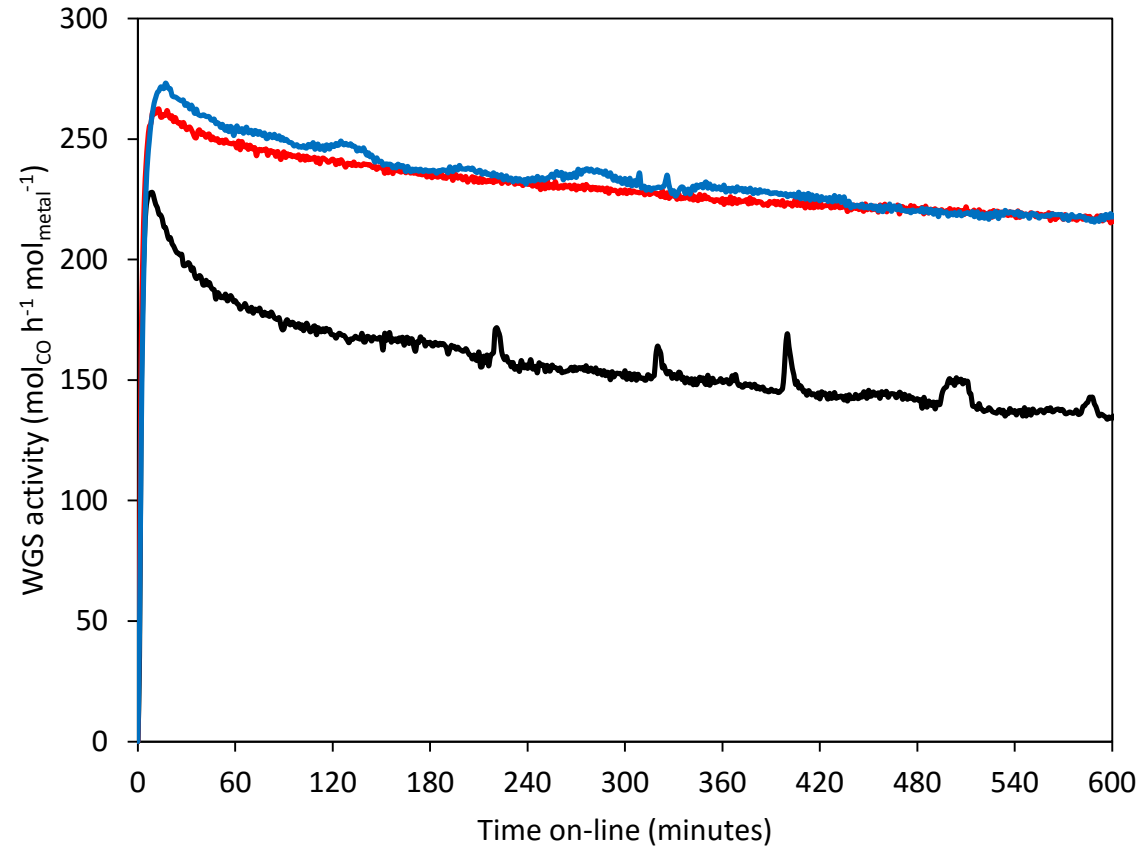

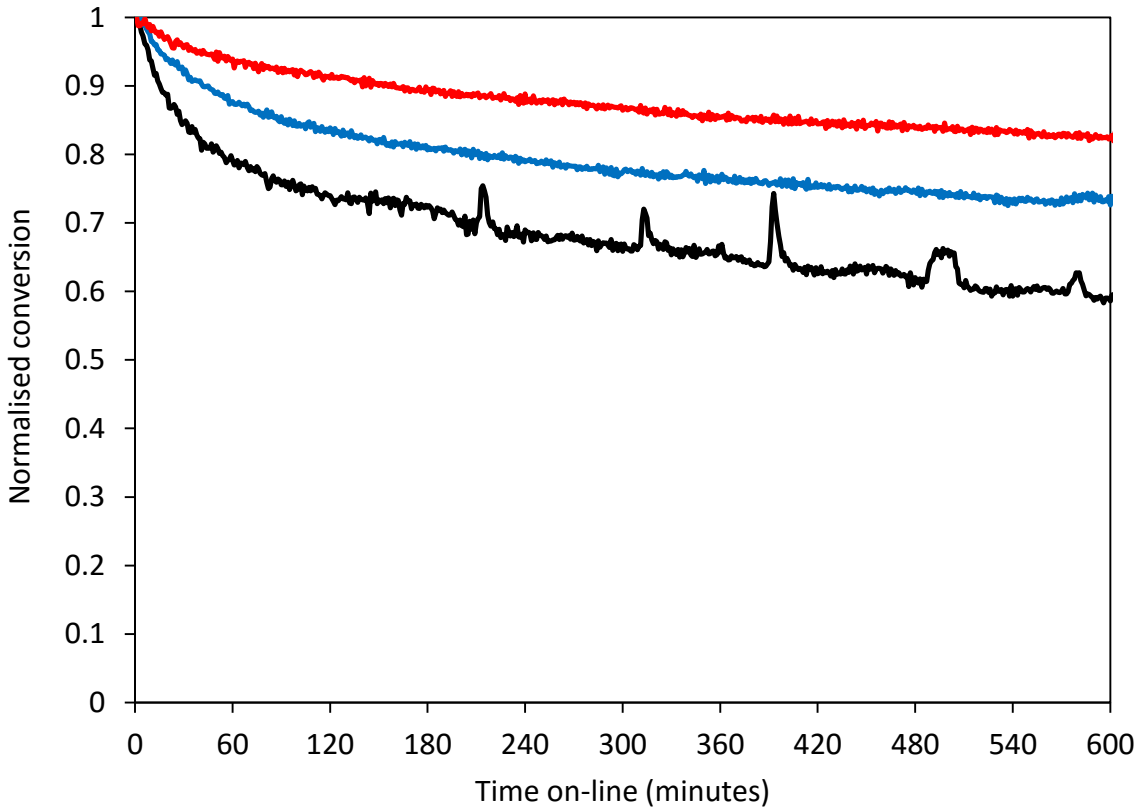

Figure 5.7 Activity (top graph) and stability (bottom graph) data for $Au/CeZrO_4$ (blue), $Au/Ce_{0.5}Ti_{0.5}O_x$ (red) and $Au/Ce_{0.5}Al_{0.5}O_x$ (black)

5.3.2. Characterisation of $CeZrO_4$, $Ce_{0.5}Ti_{0.5}O_x$ and $Ce_{0.5}Al_{0.5}O_x$

MP-AES

In order to identify the properties of each catalyst that gave rise to the observed stability and activity, extensive characterisation of the materials was carried out. Firstly, MP-AES analysis of digested samples of each catalyst showed the actual metal loadings of gold on the surface, shown in Table 3. One of the first differences of note is the variation in total metal loading between the samples. Au/$CeZrO_4$ had the highest Au loading of 1.59 wt%, compared to the $Ce_{0.5}Al_{0.5}O_x$ and $Ce_{0.5}Ti_{0.5}O_x$ catalysts that had 1.45 and 1.30 wt% Au, respectively. The cause of the discrepancies in the actual metal loading could be related to the surface charge of the support during the catalyst preparation. This is determined by the point of zero charge (PZC) of the material. The PZC is an important parameter to consider when preparing catalysts *via* the DP route as this defines the strength of interaction between the gold species in solution and the support itself. Supports with a lower PZC will become negatively charged at a lower pH which will mean that the surface charge at pH 8 (used in the preparation of these catalysts) will be different to that of a support with a high PZC. A stronger interaction between the metal precursor and the support will give higher metal loadings but poorer dispersion.

N_2 physisorption

The specific surface area of a support is an important property to measure as supports with higher surface areas typically can facilitate high metal loadings while retaining high dispersion and therefore they can support more active sites per mole of supported metal. The measured specific surface area is shown in Table 5.3. The surface area of $Ce_{0.5}Ti_{0.5}O_x$ and $Ce_{0.5}Al_{0.5}O_x$ was 143 and 158 $m^2\ g^{-1}$, respectively. The $CeZrO_4$ had the lowest specific surface area, which was measured as 83 $m^2\ g^{-1}$.

XRD

XRD was used to gain an insight into the size of the crystallites as well as the phase(s) present in the support. Figure 5.8 shows the diffraction pattern of $Ce_{0.5}Al_{0.5}O_x$ and $Ce_{0.5}Ti_{0.5}O_x$ as well as $CeZrO_4$ for reference. The XRD pattern of $CeZrO_4$ was consistent with a cubic crystal structure, corresponding to other reports.[20] Reflections at 2θ = 28.9°, 33.4°

and 47.8° are the (111), (200), (220) and (311) planes of the fluorite-type structure. The $Ce_{0.5}Ti_{0.5}O_x$ support exhibits a similar structure with analogous reflections at 2θ = 28.6°, 33.2° and 47.6°. These represent an approximate shift of 0.2° in the angle of reflections in the material. $CeZrO_4$ exhibits a small feature at 59.4° which is due to the (222) plane of the cubic crystal structure. This feature is not present in the $Ce_{0.5}Ti_{0.5}O_x$ sample, most likely due to the line broadening caused by a small crystallite size. Table 5.3 shows the lattice parameter of the materials based on the cubic crystal structure. The differences in the positions of the reflection correlate to a difference of 0.05 Å in the dimension of the unit cell. The difference in the size of the unit cell could be due to a number of factors. Firstly, the substitution of Zr for Ti would naturally result in a difference as the size of the Zr^{4+} and the Ti^{4+} cationic radius. The Zr^{4+} ionic radius is significantly larger than that of the Ti^{4+}. Therefore it is unexpected that the $Ce_{0.5}Ti_{0.5}O_x$ support exhibits a larger lattice parameter.

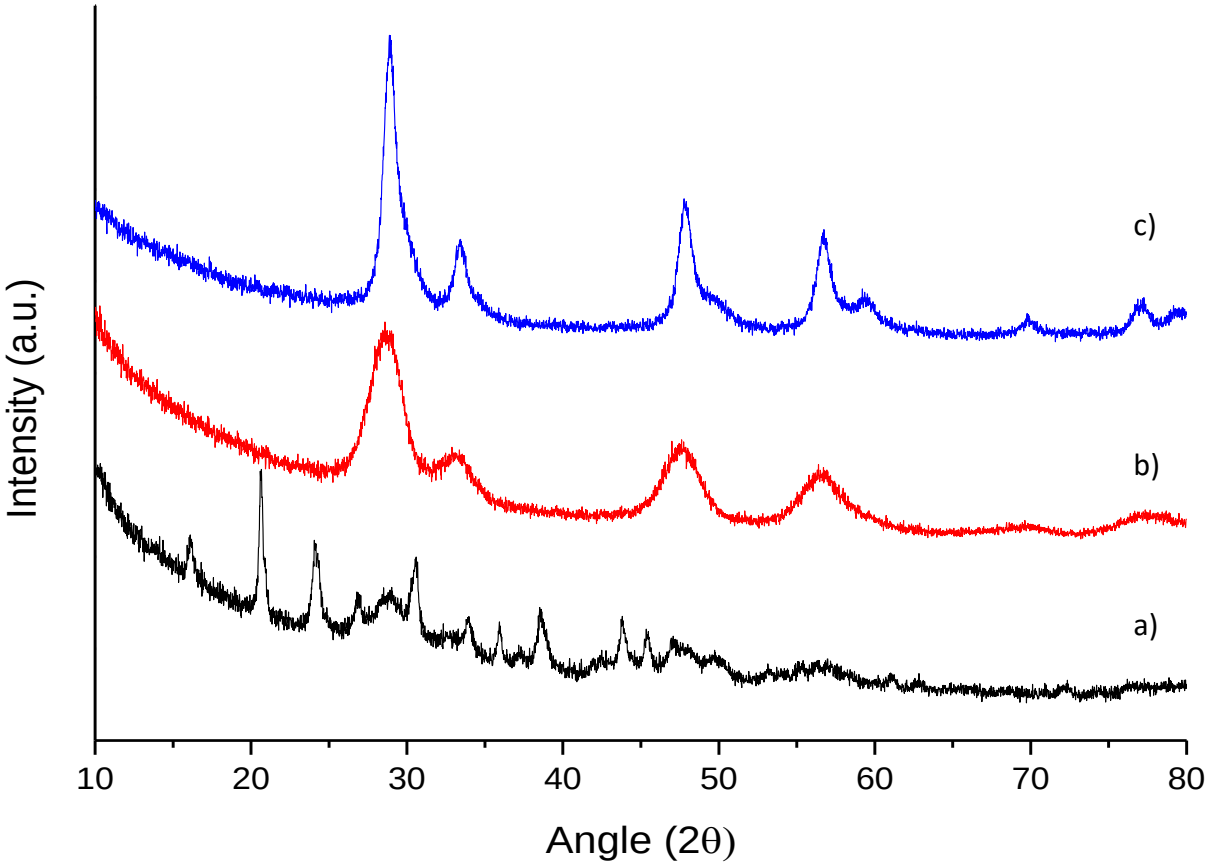

Figure 5.8 XRD patterns of a) $Ce_{0.5}Al_{0.5}O_x$, b) $Ce_{0.5}Ti_{0.5}O_x$ and c) $CeZrO_4$.

It has been shown that in ceria and ceria-terbia mixed metal oxides, a decrease in the crystallite size results in a decrease in the lattice parameter.[37, 38] In the case of the $Ce_{0.5}Ti_{0.5}O_x$ and the $CeZrO_4$ solutions, the $Ce_{0.5}Ti_{0.5}O_x$ material exhibits the smaller crystallite size, determined using the Scherrer equation and presented in Table 5.3. The estimated crystallite size for $Ce_{0.5}Ti_{0.5}O_x$ and $CeZrO_4$ were 4.2 nm and 7.1 nm, respectively. Therefore it would be expected that the $Ce_{0.5}Ti_{0.5}O_x$ have a smaller lattice parameter. Another consideration is the extent of the incorporation of the Ti into the CeO_2 lattice and the actual molar ratio of the Ce:Ti. CeO_2 prepared using a conventional sol-gel methodology has a lattice parameter of 5.39 Å, as shown in **Chapter 5.3.2** below. This value was consistent with previous reports.[20] The $Ce_{0.5}Ti_{0.5}O_x$ material has a very similar value to this, suggesting that the lattice of both materials is similar, although it should be noted that the CeO_2 material had a larger crystallite size (12.3 nm).

The $Ce_{0.5}Al_{0.5}O_x$ material exhibited a very different diffraction pattern to that of the Zr- and Ti-containing materials. While there were very broad shoulders in the region where the reflections of a cubic crystal system would appear, the diffractogram was dominated by sharp features that were difficult to match with the International Centre for Diffraction Data (ICDD) database. The broad cubic crystal shoulders could indicate well dispersed or amorphous CeO_2 that is almost undetectable by XRD. The sharper reflections are consistent with cerium carbonate hydroxide hydrate, $Ce_2(CO_3)_2(OH)_2.H_2O$ according to the best matched XRD pattern from the ICDD (Reference code: 00-046-0369). The formation of this phase is unexpected as the TGA analysis of the precursor showed that at 500 ^oC, complete oxidation of the material had occurred. The precursor was subjected to an atmosphere of flowing air for 5 h, which was expected to be sufficient for the formation of the oxide, and was sufficient in the $CeZrO_4$ and $Ce_{0.5}Ti_{0.5}O_x$ materials. The estimation of the crystallite size was 37 nm, significantly higher than the $Ce_{0.5}Ti_{0.5}O_x$ and $CeZrO_4$. It is possible that the large crystallite size prevented the full oxidation of the materials. The incomplete formation of the oxide would be expected to have a deleterious effect on the redox properties; the oxygen mobility would be expected to be poor.

It has previously been shown that the particle size of CeO_2 affects the WGS activity in Au/CeO_2 catalysts.[23, 35] Flytzani-Stephanopoulos and co-workers prepared a range of Au/CeO_2 catalysts with different crystallite sizes and surface areas. Weakly bound Au was removed using NaCN leaching and it was found that CeO_2 supports with smaller crystallite sizes retained a larger proportion of the Au. The origin of this effect was thought to be because of the increased oxygen vacancies present in small crystallites of CeO_2, which has previously been reported.[34, 39, 40] It has also been suggested that smaller crystallite sizes thermodynamically favour the creation of oxygen defects.[41] Therefore small crystallite sizes are desirable as it leads to a strong interaction between the supported metal and the support.

In addition to the enhanced metal-support interaction that small CeO_2 particles facilitate, the redox properties are also highly dependent on the crystallite size of the support. Below crystallite sizes of 10-15 nm of CeO_2, the facile formation of oxygen defects and Ce^{4+} -> Ce^{3+} is observed.[33, 34, 39] This "critical size" is significant because the $Ce_{0.5}Ti_{0.5}O_x$ crystallite size was calculated to be 4.2 nm whereas in $Ce_{0.5}Al0.5O_x$ it was 37 nm. Therefore it would be expected that the $Ce0.5Ti0.5O_x$ sample would exhibit superior redox properties to the $Ce0.5Al_{0.5}O_x$. Furthermore, it was reported by Tsang and co-workers that at particle sizes smaller than 4.7 nm superoxide species (O_2^-) are generated which further increased the amount of reducible oxygen.[10]

Overall, the XRD data highlighted the structural differences in the materials and showed that while solid solutions of $CeZrO_4$ or $Ce_{0.5}Ti_{0.5}O_x$ are easily prepared, this is not the case for $Ce_{0.5}Al_{0.5}O_x$.

H_2-temperature programmed reduction (TPR)

H_2-TPR was carried out on the three supports to measure the redox properties of the materials. The reduction of CeO_2 and Ce-based oxides has been widely studied and the TPR profile of such materials is characterised by two processes: surface and bulk reduction.[10, 26] The temperature at which the surface and bulk reduction occurs is dependent on several factors, including the crystallite size and morphology as well as the concentration of defects.[34] As discussed above, the concentration of defect sites and the

crystallite size are related. The H_2-TPR profile of each support is shown in Figure 5.9. $Ce_{0.5}Ti_{0.5}O_x$ exhibits the lowest reduction peak at 380 ^oC, which was due to the surface reduction of Ce^{4+} to Ce^{3+}. The analogous reduction temperatures of $Ce_{0.5}Al_{0.5}O_x$ and $CeZrO_4$ occur at very similar temperatures – 500 ^oC although the hydrogen consumption is much greater in the $CeZrO_4$ sample, suggesting greater oxygen mobility. The hydrogen consumption is shown in Table 3. The origin of the enhanced hydrogen consumption of the $CeZrO_4$ support is most likely related to the inclusion of Zr in the lattice and the high oxygen storage capacity that results. The enhanced reducibility of $CeZrO_4$ is well known and has been extensively studied in the context of automotive catalysts.[6] Murota *et al.* showed that the surface reduction peak of the $CeZrO_4$ became stronger compared to the bulk reduction feature with the addition of Zr.[42] This was one of the first demonstrations of the enhanced oxygen mobility of $CeZrO_4$. The $Ce_{0.5}Al_{0.5}O_x$ exhibited the poorest hydrogen consumption and is most likely related to the incomplete formation of the mixed metal oxide as well as the large crystallite size. In addition, $Ce_{0.5}Al_{0.5}O_x$ materials have been reported to exhibit poor redox properties when prepared by co-precipitation.[13, 14]

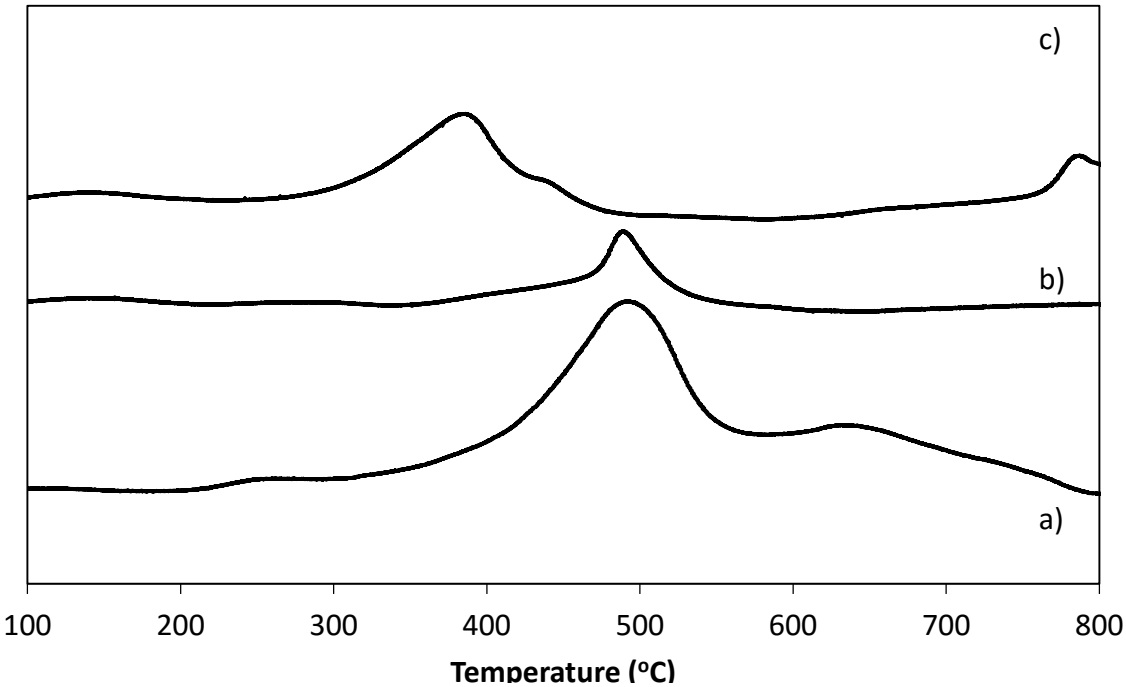

Figure 5.9 H_2-TPR traces for Ce-based supports of a) $CeZrO_4$, b) $Ce_{0.5}Al_{0.5}O_x$ and c) $Ce_{0.5}Ti_{0.5}O_x$

Raman spectroscopy

Raman spectroscopy was utilised in order to supplement the analysis of the phases of the support as well as reveal information regarding the defect sites in the mixed metal oxides.[40] The data is presented in Figure 5.10. The characteristic feature of CeO_2 is a band at 460 cm^{-1} which is the result of F_{2g} stretching mode of a fluorite-type structure, in this case due to CeO_2.[40] The positions of the F_{2g} band vary across the $CeMO_X$ supports. The shift in the position of the F_{2g} band is most likely due to a number of factors. Herman *et al*. found that the size of a CeO_2 nanoparticle affected both the position of the band as well as the line shape. Smaller particles gave broader, more asymmetric bands at lower energies.[43] In addition to this, the intensity of the band has been shown to be proportional to the particle size of CeO_2.[44] Another feature of interest exists in the spectrum: At 600 cm^{-1} a very weak band induced by defects in the sample is present to various extents across the $CeMO_x$ supports, labelled as O_v. The assignment of this band to oxygen defects is well reported[40, 43, 45, 46] and a method for comparing the population of oxygen vacancies in a sample has been developed,[40, 45, 47] which involves calculating the ratio of the peak area of the F_{2g} feature and the O_v feature.

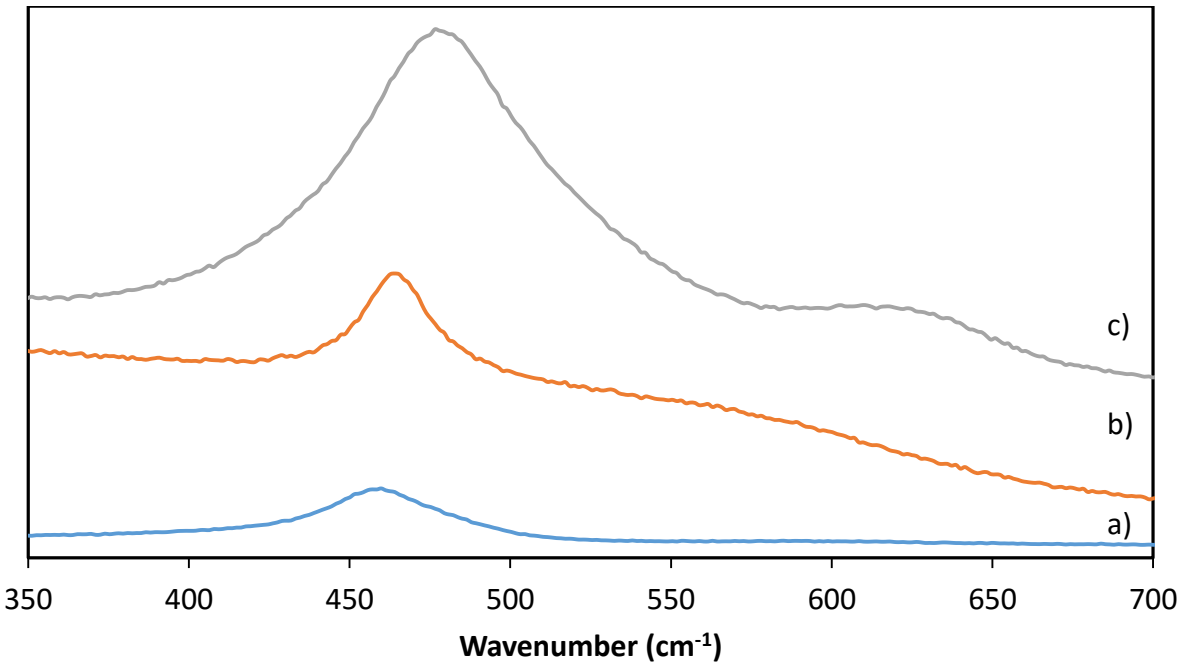

Figure 5.10 Raman spectra for CeMOx supports: a) $Ce_{0.5}Al_{0.5}O_x$, b) $Ce_{0.5}Ti_{0.5}O_x$ and c) $CeZrO_4$.

The width and magnitude of the F_{2g} mode is related to the particle size of the material and so this method minimises contributions from particle size variations.

Table 5.3 shows the calculated values for the ratio of the O_v to F_{2g} mode. $Ce_{0.5}Ti_{0.5}O_x$ exhibits the highest concentration of oxygen vacancies according to this measurement with a ratio of 0.20. $CeZrO_4$ exhibited a ratio of 0.046 while $Ce_{0.5}Al_{0.5}O_x$ had the lowest ratio of 0.035. While the $Ce_{0.5}Ti_{0.5}O_x$ had a significantly larger ratio of O_v to F_{2g}, the $CeZrO_4$ and $Ce_{0.5}Al_{0.5}O_x$ had similar values, implying that there was not a significant difference in the concentration of oxygen vacancies. The importance of oxygen vacancies for a catalyst support in the WGS reaction is well known: Fu *et al.* showed that the defect sites in CeO_2 are important for the anchoring of Au on the support; a high density of defects gives rise to a high number of Au nucleation sites, yielding a catalyst with a high number of active sites. In addition to this, the work of Zhou *et al.* recently showed that the oxidation state of Ce influences the growth of Au nanoparticles on CeO_2 supports.[48] Specifically, on reduced CeO_2 Au nanoparticles were flatter in shape compared with those on fully oxidised CeO_2.

Table 5.3 Physical and chemical properties of $CeMO_x$ supports

Sample	Wt % Au (MP-AES)	Specific surface area ($m^2\ g^{-1}$)	Crystallite size (Å) (XRD)	Lattice parameter, a (Å) (XRD)	Hydrogen consumption in TPR (μmol)	Ov/F2g (Raman)
$Ce_{0.5}Ti_{0.5}O_x$	1.30	143	42	5.40	26.0	0.20
$Ce_{0.5}Al_{0.5}O_x$	1.45	158	370	-	13.4	0.03
$CeZrO_4$	1.59	83	71	5.35	40.1	0.05

XPS

XPS was used to analyse the nature of the supported gold and the mixed metal oxide supports. The Au 4f spectrum was measured and the various gold species in each catalyst was identified by deconvolution of the line shape. A stack of the Au 4f spectrum for each of the three catalysts of interest is shown in Figure 5.11, which also includes the Ce 3d spectra for each of the samples. There are a three gold species present in each catalyst, indicated by the dashed lines in Figure 5.11 and quantified in Table 5.4. They have been

assigned to the following Au states, consistent with the convention established in **Chapter 3**: Firstly, the most intense peak at 84.0 eV in the $Au/CeZrO_4$ catalyst is due to metallic Au. Secondly, there is a peak at 85.4 eV that corresponds to "small gold nanoparticles" as explained in **Chapter 3**. Finally, there is evidence of Au^{3+} at 86.9 eV. The position of each XPS feature is shown below in Table 5.4. This also shows the composition of each gold species.

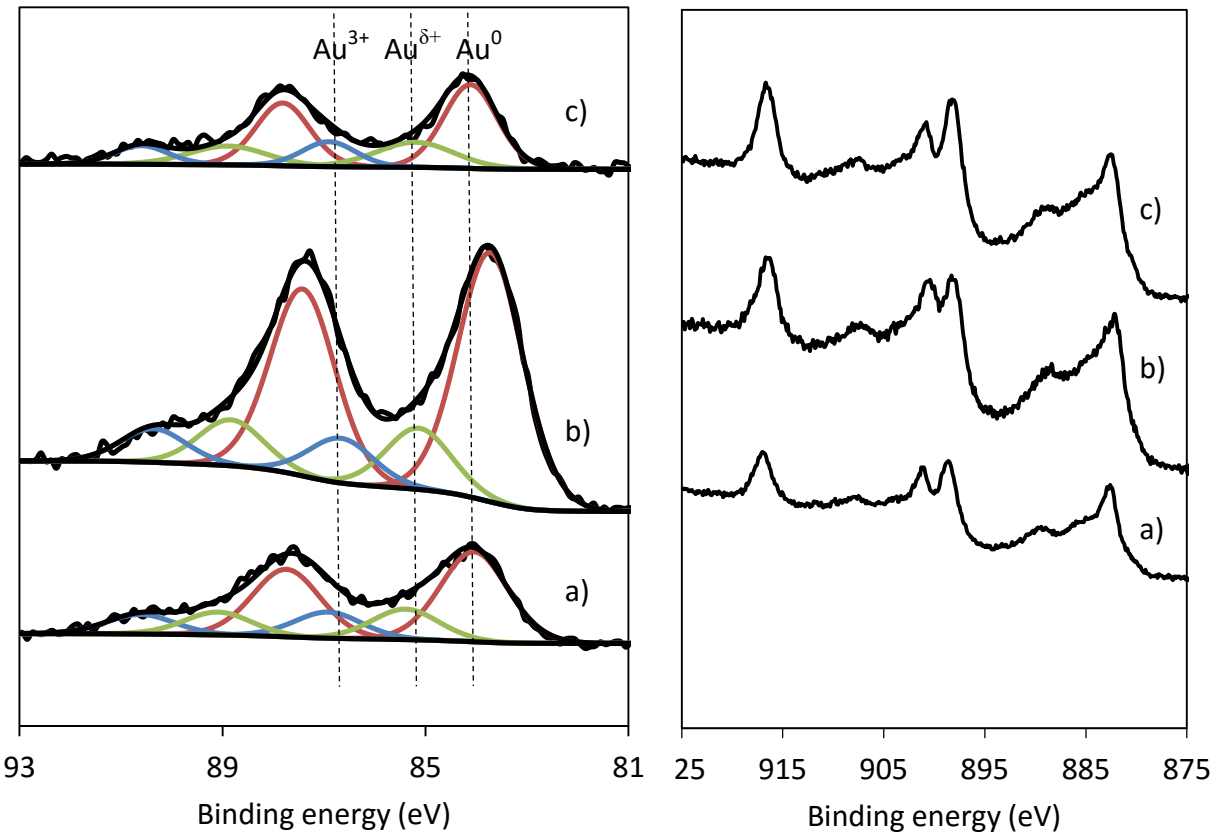

Figure 5.11 XP spectra of Au 4f (left) and Ce 3d (right) regions. From bottom to top: $Au/CeZrO_4$, $Au/Ce_{0.5}Al_{0.5}O_x$ and $Au/Ce_{0.5}Ti_{0.5}O_x$

In **Chapters 3** it was shown that the feature assigned to small gold nanoparticles was much smaller in the used $Au/CeZrO_4$ catalyst after a WGS reaction, suggesting sintering was occurring. In **Chapter 4** the concentration of the same feature was plotted against the catalytic activity for $AuPd/CeZrO_4$ catalysts, showing the importance of a small particle size in WGS catalysts. In this chapter the concentration of the $Au^{\delta+}$ feature was calculated in order to gain an insight into the relative size of the Au nanoparticles. Based on the

catalytic activity, the concentration of the $Au^{\delta+}$ feature should go in the following order: $Au/Ce_{0.5}Ti_{0.5}O_x \geq Au/CeZrO_4 > Au/Ce_{0.5}Al_{0.5}O_x$. The observed trend is not consistent with this which suggests that the support was crucial to determining the catalyst activity as well as the nature of the Au. While the $Au/Ce_{0.5}Al_{0.5}O_x$ catalyst exhibited the lowest concentration of $Au^{\delta+}$, the differences between the three catalysts was not significant and did not fit well with the catalytic activity trend. However, consideration of the Au^{3+} concentration showed a relationship more reflective of the activity measurements: $Au/CeZrO_4$ and $Au/Ce_{0.5}Ti_{0.5}O_x$ had approximately the same concentration of Au^{3+} (17.8 and 17.2%, respectively) whereas the $Au/Ce_{0.5}Al_{0.5}O_x$ sample contained 12.6% Au^{3+}. The chemical significance of this species is related to the formation of nanoparticles upon exposure to WGS conditions. Tibiletti *et al.* first reported the high activity of $Au/CeZrO_4$ catalysts for the WGS reaction and used several characterisation tools, including *in situ* techniques to elucidate the nature of the gold before and during the reaction. Scanning transmission election microscopy (STEM) was used on the fresh catalyst to identify isolated gold ions. This was consistent with EXAFS and XANES findings, which also showed the rapid reduction of Au^{3+} to form metallic clusters containing approximately 50 atoms.[24] In the context of this work, it appears that a high concentration of Au^{3+} could be a precursor to a high concentration of small Au clusters. However, it is difficult to decouple the effect of the support and the effect of the gold species in determining the overall catalytic activity.

Table 5.4 Composition of Au species and position of Au 4f signal in the $Au/CeMO_X$ catalysts

Sample	% Concentration			Binding energy (eV)		
	Au^0	$Au^{\delta+}$	Au^{3+}	Au^0	$Au^{\delta+}$	Au^{3+}
Au $Ce_{0.5}Ti_{0.5}O_x$	58.0	24.9	17.2	84.1	85.2	86.9
Au $Ce_{0.5}Al_{0.5}O_x$	70.2	17.2	12.6	83.7	85.1	86.7
Au $CeZrO_4$	61.4	20.8	17.8	84.0	85.4	86.9

The binding energy of the Au 4f signal of each sample is presented in Table 5.4. It shows a variation in the position of the Au $4f_{7/2}$ peak which is most likely due to the variation in

the composition of the support. Goodman showed that the binding energy is a result of many factors, including initial state effects such as the electronic interaction between the gold and the support.[49] Another consideration in the position of the Au 4f band is the oxidation state of cerium in the support. It was shown by Zhou and co-workers that the higher the degree of Ce reduction, the higher the positive shift in binding energy of the Au 4f spectrum.[48] This was due to differences in the size and shape of the gold nanoparticles, exemplifying the importance of the nature of the support in the growth of metal nanoparticles. Overall, the position of the Au 4f band is a combination of many factors that cannot be separated and so inferring significance from it could be misleading.

The Ce 3d spectrum was analysed to observe the existence of different Ce species. It is complex and consists of many peaks. The spectrum is annotated, showing which features are the result of Ce^{3+} and Ce^{4+} cations. Although tentative Ce^{3+}/Ce^{4+} ratios have been calculated, it is recognised that there are large degrees of uncertainties associated with the values. A more detailed explanation of Ce 3d fitting was given in **Chapter 3**. The oxidation state of Ce is significant. Firstly, the oxidation state of Ce gives information regarding the number of oxygen vacancies in the sample. These are important for the nucleation of gold particles during the preparation of catalysts and activating water during the WGS reaction.[24, 33-35] Secondly, Zhou *et al.* recently showed that the extent of reduction affects the size and shape of gold nanoparticles.[48] Therefore understanding the nature of Ce can help to understand the properties of the support and explain their catalytic activity. Table 5 shows the Ce^{3+}/Ce^{4+} molar ratios from XPS. The values for $Ce_{0.5}Al_{0.5}O_x$ and $Ce_{0.5}Ti_{0.5}O_x$ are very similar. $CeZrO_4$ exhibits higher concentrations of Ce^{3+} than the two other supports but the difference is small.

Also important is the surface composition of the supports. This is also given in Table 5. In each case, there is a higher than expected ratio of metal:oxygen. This phenomenon is well known and is attributed to weakly bound hydroxyl or carbonate species on the surface.[50, 51] The surface concentration of carbon was not included in the surface concentration as it was deemed to be adventitious but given the uncertainty of the chemical composition of $Ce_{0.5}Al_{0.5}O_x$, it is instructive to consider whether there was a large amount of surface

carbon present on the $Ce_{0.5}Al_{0.5}O_x$ as this would be consistent with the XRD pattern of cerium hydroxy carbonate hydrate. The concentration of C on the $Ce_{0.5}Ti_{0.5}O_x$, $Ce_{0.5}Al_{0.5}O_x$ and $CeZrO_4$ was 9.4, 7.3 and 14.6 at%, respectively. This shows that in $Ce_{0.5}Al_{0.5}O_x$, the surface is not composed of a carbonate. In addition to the metal:oxygen ratio of $Ce_{0.5}Al_{0.5}O_x$ that is similar to $Ce_{0.5}Ti_{0.5}O_x$ and $CeZrO_4$, it is likely that the surface is oxidic. The presence of Al_2O_3 at the surface would give a slightly lower surface concentration of oxygen, which was consistent with the data in Table 5.5.

Table 5.5 XPS analysis of Au/$CeMO_X$ catalysts

Sample	Ce oxidation states (At %)		Surface elemental composition (At %)			Surface metal ratios	
	Ce^{3+}	Ce^{4+}	Ce	M	O	Ce:M	Metal:Oxygen
Au/$Ce_{0.5}Ti_{0.5}O_x$	38.4	61.6	12.0	16.9	70.6	0.71	0.41
Au/$Ce_{0.5}Al_{0.5}O_x$	35.9	64.1	9.62	22.5	68.7	0.43	0.44
Au/$CeZrO_4$	36.8	63.2	16.6	9.24	73.4	1.8	0.35

SEM-EDX

SEM-EDX was carried out to investigate the bulk elemental composition of the synthesised supports. In addition to this, the homogeneity of the material was also assessed by calculating the variation between three different sites of interest. The results are shown in Table 5.6. As described in **Chapter 2**, the bulk elemental composition was calculated by investigating three sites of interest on the support. The variation of the Ce:M was then calculated by expressing the standard deviation of each sample as a percentage of the average Ce:M ratio. For example, the $Ce_{0.5}Al_{0.5}O_x$ exhibited a Ce:Al ratio of 1.42 and the average variation was 44.6%. This means that on average, there was a difference of 44.6% between the measured Ce:Al ratios at each site. This represents a very large variation and shows that the material is not homogeneous in nature.

The $Ce_{0.5}Ti_{0.5}O_x$ support exhibited a molar ratio of 0.94, close to the nominal value of 1. In addition, the two metals were homogeneously dispersed through the material, showing an average variation of 5.1% between different sites. The $CeZrO_4$ support exhibited a Ce:Zr ratio of 1.23, slightly higher than the nominal value of 1. The standard deviation was calculated as 15.5% showing it to be more homogeneous than $Ce_{0.5}Al_{0.5}O_x$ but less so than $Ce_{0.5}Ti_{0.5}O_x$. $Ce_{0.5}Al_{0.5}O_x$ had the highest average Ce:M ratio of 1.42 although the high

average variation between sites means that in certain areas, the Ce:Al ratio was significantly different.

Table 5.6 EDX analysis of $CeMO_X$ supports showing the bulk composition and the standard deviation across three sites of interest.

Sample	EDX	
	Ce:Ti molar ratio	Average variation (%)
$Ce_{0.5}Ti_{0.5}O_x$	0.94	5.1
$Ce_{0.5}Al_{0.5}O_x$	1.42	44.6
$CeZrO_4$	1.23	15.5

It is instructive to compare the surface and bulk composition of the material, in particular the Ce:M ratio. The surface Ce:Al ratio of $Ce_{0.5}Al_{0.5}O_x$ was 0.43 but the bulk ratio was 1.42. This is a significant difference and highlights the importance of characterising the surface of catalysts as well as the bulk. While there is an excess of Ce in the bulk of the material, there is an excess of Al at the surface of the material, where the chemical reactions take place. It should also be noted that the support could be as inhomogeneous as the bulk and so while the sample analysed had a large amount of Al at the surface, other parts of the support could have a more Ce-enriched surface.

Summary

The initial work into modifying the support through substituting Zr for Al or Ti showed that $Ce_{0.5}Ti_{0.5}O_x$ was a promising support to investigate further. The combination of these two metals gave a more stable catalyst than the benchmark $Au/CeZrO_4$ catalyst. Characterisation showed that the $Ce_{0.5}Ti_{0.5}O_x$ had a higher surface area and smaller crystallite size than the $CeZrO_4$ supported catalyst in addition to good redox properties. Furthermore, Raman spectroscopy showed significant oxygen vacancies in the support. EDX confirmed that the ratio of Ce:Ti was close to the nominal value and the material was homogenous in nature.

5.4. $Ce_aTi_{1-a}O_x$ as a catalyst support

Preliminary studies indicated that $Au/Ce_{0.5}Ti_{0.5}O_x$ was more stable than $Au/CeZrO_4$ under WGS conditions. In order to investigate this in more detail, the Ce:Ti molar ratio of the support was varied using the same sol-gel method as used previously. Furthermore, the monometallic metal oxide supports were also synthesised using the same procedure.

The following supports were prepared:

- TiO_2
- $Ce_{0.1}Ti_{0.9}O_x$
- $Ce_{0.2}Ti_{0.8}O_x$
- $Ce_{0.5}Ti_{0.5}O_x$
- $Ce_{0.8}Ti_{0.2}O_x$
- $Ce_{0.9}Ti_{0.1}O_x$
- CeO_2

For the mixed metal oxides, the supports are referred to as $Ce_aTi_bO_x$, where a and b refer to the nominal molar ratios of each metal or as $Ce_{0.5}Ti_{0.5}O_x$ to signify the series of catalysts prepared. Using the standard DP method used throughout this work, 2 wt% Au was deposited onto each of the supports.

5.4.1. The catalytic activity and stability of $Au/Ce_aTi_{1-a}O_x$

The range of catalysts described above was tested under the standard WGS conditions described in **Chapter 2.3.1.** The catalytic activity is shown below in Figure 5.12. The activity data is presented as a function of the Ce:Ti ratio. The Ce:Ti ratio of the support is a significant factor in determining the catalytic activity. The most active catalyst was $Au/Ce_{0.2}Ti_{0.8}O_X$, which exhibited conversions of 300 mol CO h^{-1} mol_{metal}^{-1}. The Au/CeO_2 catalyst is active but exhibits poor conversions. The introduction of Ti to the support results in a significant increase in the catalytic activity: The substitution of just 10 mol% of Ce for Ti resulted in just under an 8-fold increase in WGS activity. The WGS activity increases with additional Ti content in the catalyst until it reaches a maximum at 20 mol% Ce. Interestingly, $Au/Ce_{0.1}Ti_{0.9}O_x$ was not active for WGS, which given that $Au/Ce_{0.2}Ti_{0.8}Ox$

was the most active catalyst, was surprising. The role of the CeO_x component in the catalyst is to provide sites of the activation of water. Au/TiO_2 is not active for WGS at low temperatures because of the poor ability of TiO_2 to achieve this.[24, 52] In the case of the $Au/Ce_{0.1}Ti_{0.9}O_x$ the small quantity of CeO_x present might not generate many sites for the activation of water.

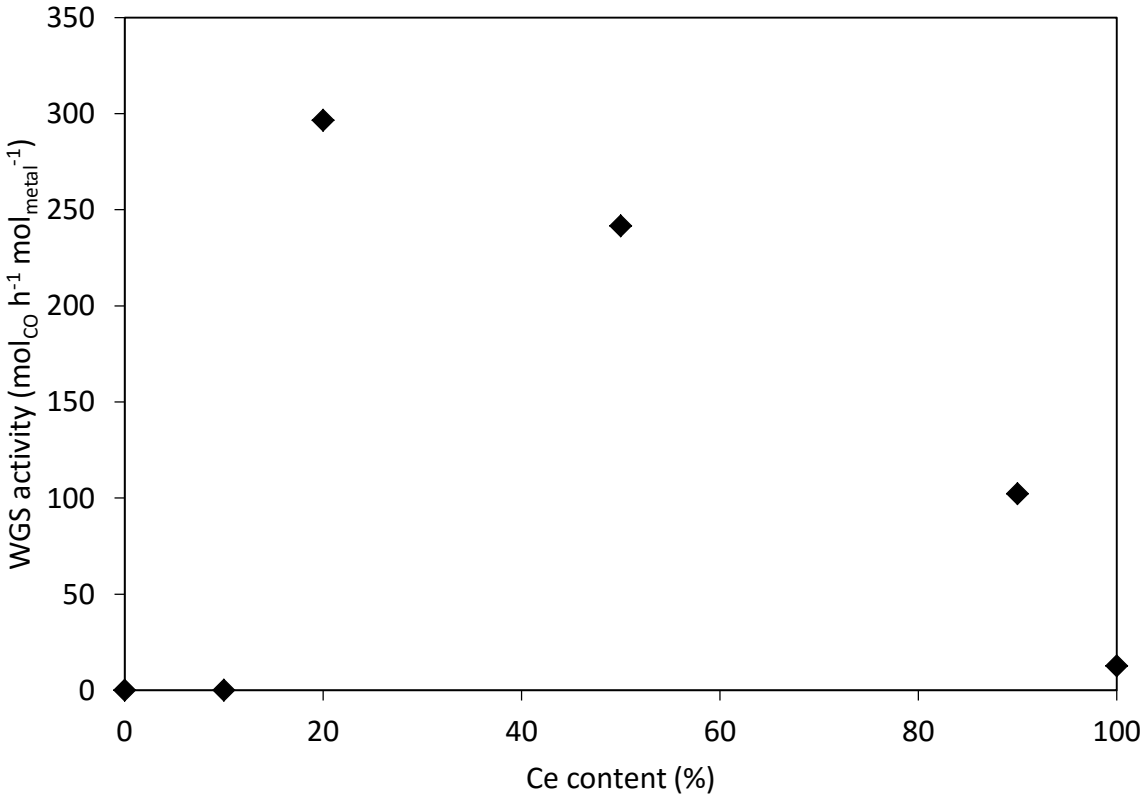

Figure 5.12 WGS activity for $Au/Ce_aTi_{1-a}O_x$ catalysts after 90 minutes on-line.

The stability of these catalysts was measured by plotting the normalised conversion of each of the active catalysts over 16 hours, using the conversion after 90 minutes as the first measurement to allow for complete stabilisation of the system. These data are presented in Figure 5.13, below. There is a large variation in the stability of each catalyst. The least active catalyst was Au/CeO_2, which retained just 55% of its activity over the time-period studied. There is a high degree of error associated with this dataset because of the low conversions exhibited. This was also found in similar datasets in **Chapter 4**. As

in the activity plot, the addition of a small amount of Ti enhanced the catalysts stability. $Au/Ce_{0.9}Ti_{0.1}O_x$ retained approximately 62% of its original activity although this was still less stable than the two most active catalysts: $Au/Ce_{0.2}Ti_{0.8}O_X$ and $Au/Ce_{0.5}Ti_{0.5}O_X$. Both of these catalysts had remarkably similar deactivation rates, retaining 84% of their original activity.

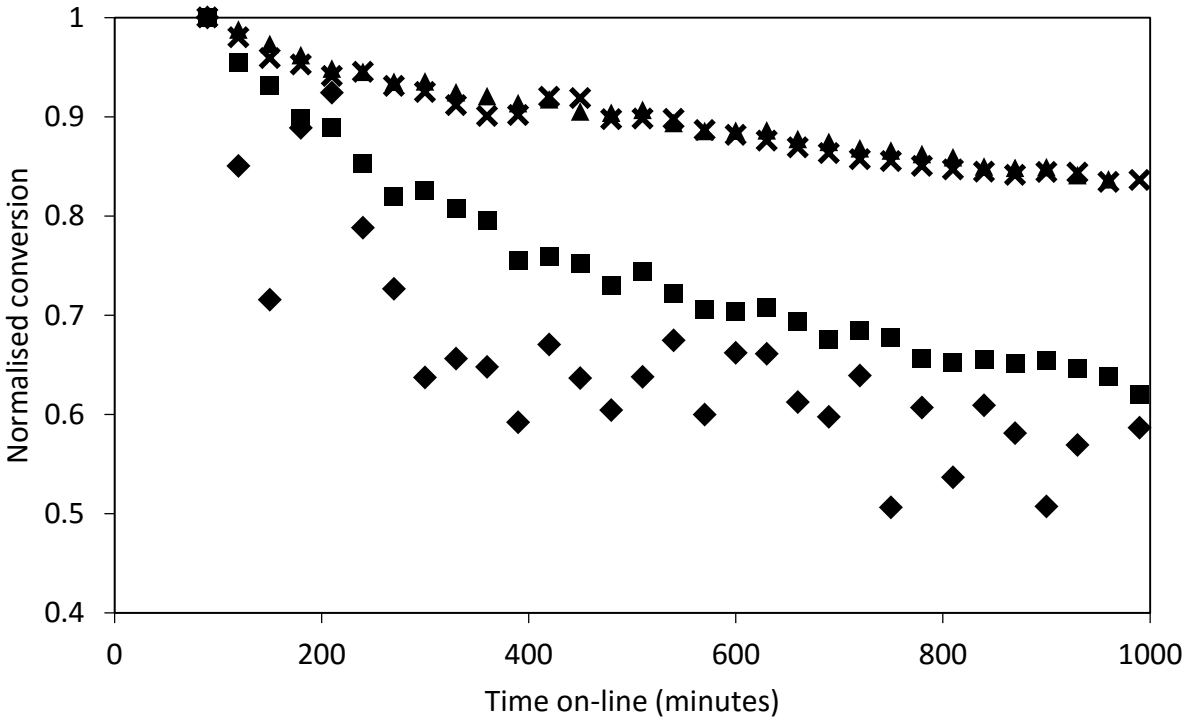

Figure 5.13 Normalised conversion plot for a selection of $Au/Ce_{0.5}Ti_{0.5}O_x$ catalysts: Au/CeO_2 (♦), $Au/Ce_{0.9}Ti_{0.1}O_X$ (■), $Au/Ce_{0.5}Ti_{0.5}O_X$ (▲) and $Au/Ce_{0.2}Ti_{0.8}O_X$ (×).

The testing data of the gold supported on ceria-titania led to the following conclusions. Firstly, the mixed metal oxide system is more effective than either monometallic metal oxide as a support in the WGS reaction, with $Ce_{0.2}Ti_{0.8}Ox$ exhibiting the highest stability and activity. Furthermore, under the reaction conditions investigated, the catalysts are not active when the Ce content of the mixed metal oxide is less than 20 mol%. The stability studies showed that $Au/Ce_{0.2}Ti_{0.8}O_x$ and $Au/Ce_{0.5}Ti_{0.5}O_x$ were the most stable catalysts. In order to learn why these catalysts were more active and more stable,

extensive characterisation was carried out to measure the textural, physical and chemical properties of the synthesised supports in order to identify the key properties for an active WGS catalyst support.

5.4.2. Characterisation of $Au/Ce_aTi_{1-a}O_x$

The activity data presented in Figure 5.12 was calculated using the moles of metal determined using MP-AES. This technique can also be used to show the actual metal loadings of each catalyst. These are given in Table 5.7. It can be seen that the metal loadings vary significantly across the range of catalysts and is dependent on the Ce:Ti molar ratio. The higher the Ce content, the higher the metal loading. Au/CeO_2 has 1.72 wt% Au whereas Au/TiO_2 has just 0.09 wt% Au. The variations in metal loading can be rationalised by consideration of the nature of the metal surface in solution and the interaction of the Ce and Ti component with the Au hydroxyl species in solution. The loadings suggest that the Au species has a lower affinity for the titania surface than the ceria surface and so the loading is determined by the surface composition of the mixed metal oxide. This could be the result of several factors, such as the surface charge of each support at pH 8 as well as the number of nucleation sites present on the surface. Another factor to consider is the number of nucleation sites on the support surface. Oxygen vacancies have been reported to serve as nucleation sites for Au nanoparticles so this is also relevant.[33-35] In the $Ce_{0.1}Ti_{0.9}O_X$ and $Ce_{0.2}TiO_X$ catalysts, the composition of the support changes by a small amount whereas the gold loading almost doubles. This could be due to the creation of oxygen vacancies in the Ce-containing parts of the support.

N_2 physisorption

N_2 physisorption was used to measure how the surface area of the supports varied with Ce:Ti molar ratio. The data are shown in Table 5.7. There were significant differences in the CeTi oxides. The monometallic oxides have relatively low specific surface areas compared to the mixed metal oxides. The highest surface area was observed in the $Ce_{0.2}Ti_{0.8}O_X$ support, significantly larger than any of the other supports. The importance of a high surface area support is well known: Higher metal dispersions can be achieved and

particle agglomeration is less likely as each metal nanoparticle is situated further from one another. The origin of the high surface area could be the particle size of the supports. Wang and co-workers recently prepared and studied a series of Ce, Ti and Ce-Ti oxides for the combustion of 1,2-dichlorobenzene.[11] The surface area measurements were consistent with those in this work, whereby the mixed metal oxides exhibited higher surface areas than either CeO_2 or TiO_2. This effect was also reported by Song and co-workers.[53]

XRD

Figure 5.14 shows the XRD diffractograms of the $Ce_aTi_{1-a}O_x$ supports. The XRD pattern of CeO_2 is well studied and consists of several features. The most intense reflection occurs at 28.7 ^{o}, 33.2^o, 47.6^o and 56.5^o, which respectively correspond to the (111), (200), (220) and (311) planes of the fluorite-type cubic structure. These features decrease in intensity as Ti content increases, with $Ce_{0.8}Ti_{0.2}O_x$ and $Ce_{0.5}Ti_{0.5}O_x$ retaining a fluorite structure. $Ce_{0.2}Ti_{0.8}O_x$ and $Ce_{0.1}Ti_{0.9}O_x$ are amorphous. The TiO_2 sample has a characteristic pattern associated with the anatase phase of TiO_2.[7] This trend is very similar to that observed by Wang and co-workers for a similarly prepared series of $Ce_{0.5}Ti_{0.5}O_x$ supports. The lattice parameter of the cubic fluorite phase was calculated and is presented in Table 5.7. The lattice parameter is determined by a number of parameters, including the crystallite size and the molar ratio of the Ce and Ti. It also depends on the amount of Ce^{3+} in the sample.[54] Zhou *et al.* reported that single-phase solid solutions of Ce and Ti were formed when there was 80 and 90% Ce content and also noted that the lattice parameter did not significantly change from that of pure CeO_2. The materials exhibited enhanced redox properties.[55]

Using the Scherrer equation, the crystallite size of some of the $Ce_{0.5}Ti_{0.5}O_x$ supports was estimated from the (111) plane. This is shown in Table 5.7. The observed decrease in crystallite size is consistent with an increase in the surface area of the supports and the crystallite size trends of previous publications.[7, 11]

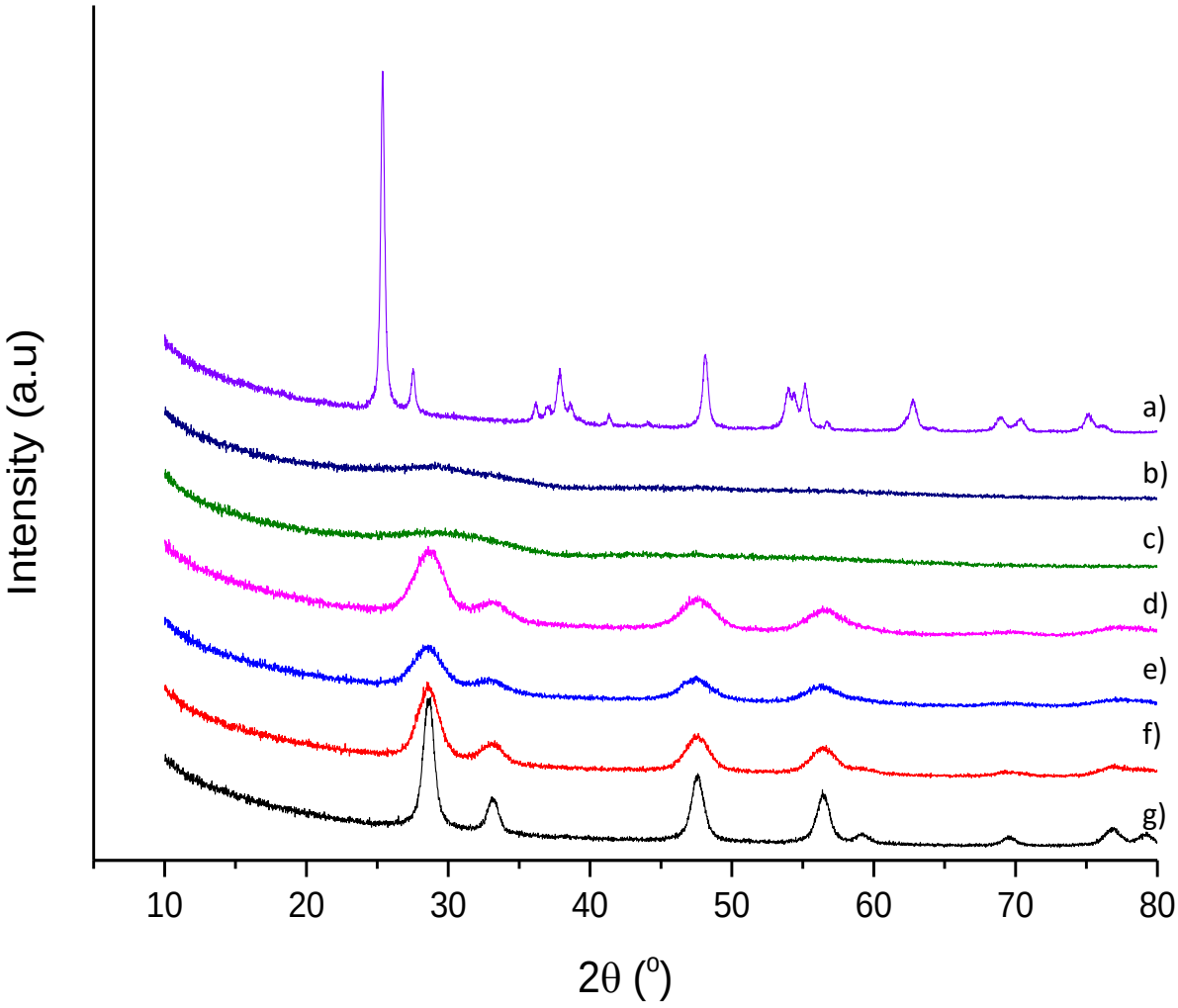

Figure 5.14 XRD diffractograms of $Ce_aTi_{1-a}O_x$ materials: a) TiO_2, b) $Ce0.1Ti_{0.9}O_X$, c) $Ce_{0.2}Ti_{0.8}O_X$, d) $Ce_{0.5}Ti_{0.5}O_X$, e) $Ce_{0.8}Ti_{0.2}O_X$, f) $Ce_{0.9}Ti_{0.1}O_X$ and g) CeO_2.

Table 5.7 Properties of the gold supported $Ce_aTi_{1-a}O_x$ catalysts

Sample	Wt % (MP-AES)	Specific surface area ($m^2\ g^{-1}$)	Crystallite size (Å)	Lattice parameter (Å)
CeO_2	1.72	62	123	5.390
$Ce_{0.9}Ti_{0.1}O_X$	1.70	106	51	5.396
$Ce_{0.8}Ti_{0.2}O_X$	1.39	168	39	5.396
$Ce_{0.5}Ti_{0.5}O_X$	1.30	143	42	5.398
$Ce_{0.2}Ti_{0.8}O_X$	1.08	300	amorphous	-
$Ce_{0.1}Ti_{0.9}O_X$	0.69	191	amorphous	-
TiO_2	0.09	13	145	6.071

Raman spectroscopy

Raman spectroscopy was utilised in order to supplement the analysis of the phases of the support as well as reveal information regarding the defect sites in the supports.[40] The data is presented in Figure 5.15 The main features observed were similar to that of $Ce_{0.5}Ti_{0.5}O_x$

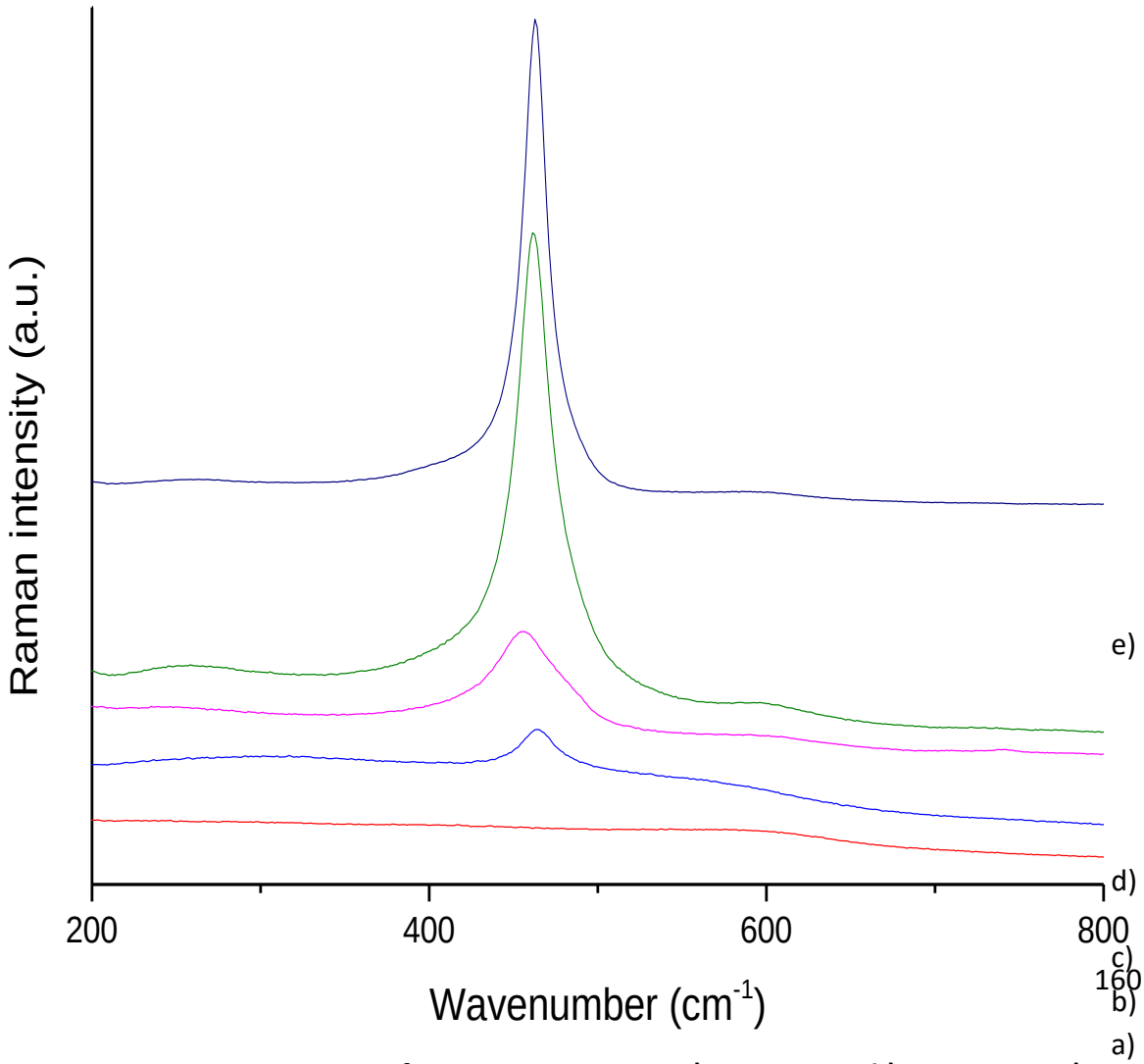

Figure 5.15 Raman spectra of $Ce_aTi_{1-a}O_x$ supports: a) $Ce_{0.2}Ti_{0.8}Ox$, b) $Ce_{0.5}Ti_{0.5}O_x$, c) $Ce_{0.8}Ti_{0.2}Ox$, d) $Ce_{0.9}Ti_{0.1}Ox$ and e) CeO_2.

when the Ce mol % was above 50. [40] The spectra featured the F_{2g} mode associated with CeO_2 at 460 cm^{-1} and the weak feature at 600 cm^{-1} associated with oxygen defects. The positions of the F_{2g} band vary across the range of $Ce_{0.5}Ti_{0.5}O_x$ samples.

The shift in the position of the F_{2g} band is most likely due to a number of factors. Herman *et al.* found that the size of a CeO_2 nanoparticle affected both the position of the band as well as the line shape. Smaller particles gave broader, more asymmetric bands at lower energies.[43] In addition to this, the intensity of the band has been shown to be proportional to the particle size of CeO_2[44]. The qualitative interpretation of this fits well with the XRD data: CeO_2 has the most intense Raman F_{2g} band, while the $Ce_{0.5}Ti_{0.5}O_x$ mixed metal oxides have much less intense bands. The weak band at 600 cm^{-1} was also examined in the same way as was done for the $CeMO_X$ catalysts in **Chapter 5.3.2.** This section also described the importance of oxygen vacancies in catalysts supports for the WGS reaction. The concentration of oxygen vacancies was estimated by measuring the ratio of the F_{2g} mode and the O_V mode at 600 cm^{-1}. The calculated ratio for the $Ce_{0.5}Ti_{0.5}O_x$ supports is shown in Figure 5.16. As Ti is introduced, there is a significant increase in the relative size of the shoulder at 600 cm^{-1} which was attributed to the formation of oxygen defects in the sample. $Ce_{0.5}Ti_{0.5}O_X$ exhibits the highest F_{2g}/O_V ratio of the samples examined.

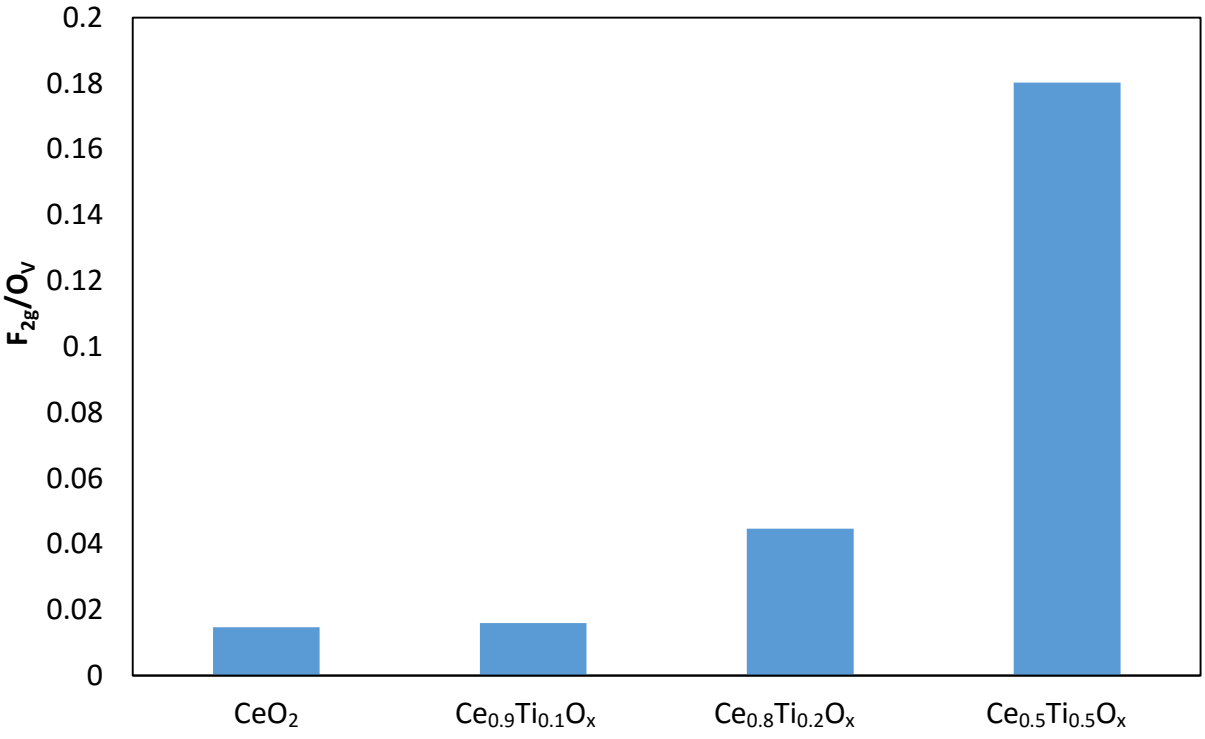

Figure 5.16 Quantification of oxygen vacancies on Ce-based oxides as determined from Raman spectroscopy

Samples of $Ce_{0.5}Ti_{0.5}O_x$ where there was more than 50 mol% Ti did not exhibit the F_{2g} band in their Raman spectrum and so it was not possible to calculate a ratio. Therefore it is unclear from the Raman data alone if there were high concentrations of defects in these samples. However, there is a clear shoulder in the O_v region which implies the presence of oxygen vacancies.

XPS

XPS was used to determine the surface composition of the oxides and to quantify the oxidation states of the constituent metals. The nature of the gold was analysed by examining the Au 4f signal. The peak fitting is shown in Figure 5.17. The number of species varies in each sample and the composition of the different Au species is shown in Table 5.8 below. The XP spectrum of the Au 4f region was analysed according to the standard procedure employed throughout this thesis. Au^0 was identified by a peak at 84 eV, a peak at 85 eV was due to $Au^{\delta+}$ (attributed to small gold nanoclusters) and a peak at 87 eV was due to Au^{3+}. For the Au/TiO_2 and $Au/Ce_{0.1}Ti_{0.9}O_X$ catalysts, no Au^{3+} was detected. In each of the catalysts the majority of the Au species was metallic Au, Au^0. In **Chapters 3** and **4** the concentration of $Au^{\delta+}$ was consistent with small gold nanoparticles. In **Chapter 4** a strong correlation between the concentration of $Au^{\delta+}$ and WGS activity was observed. In **Chapter 5.3.2** the importance of Au^{3+} was discussed in relation to previous reports that it is the precursor of well-dispersed nanoclusters.[24] The composition of the different gold species does not correlate well with the catalytic activity across the range of catalysts studied, suggesting that the properties of the support were highly important in producing an active WGS catalyst. Interestingly, the $Au/Ce_{0.9}Ti_{0.1}O_X$ catalyst contained large quantities of Au^{3+}, which would suggest that the gold is present in a highly dispersed form but the species associated with small gold nanoclusters had a significantly smaller concentration than other catalysts. In terms of WGS activity, it was less active than $Ce_{0.5}Ti_{0.5}O_X$ and more active than CeO_2 and followed the expected trend, illustrated in Figure 5.12.

Table 5.8 XPS analysis of the Au 4f spectrum for a range of $Au/Ce_aTi_{1-a}O_x$ catalysts

Sample	% concentration			Binding energy (eV)		
	Au^0	$Au^{\delta+}$	Au^{3+}	Au^0	$Au^{\delta+}$	Au^{3+}
Au/CeO_2	63.0	26.7	10.3	83.6	85.1	86.9
$Au/Ce_{0.9}Ti_{0.1}O_X$	68.3	10.7	21.0	84.3	85.7	86.8
$Au/Ce_{0.8}Ti_{0.2}O_X$	57.7	29.7	17.2	83.9	85.2	87.0
$Au/Ce_{0.5}Ti_{0.5}O_X$	58.0	24.9	17.2	84.1	85.2	86.9
$Au/Ce_{0.2}Ti_{0.8}O_X$	50.6	28.2	21.1	84.1	85.2	86.9
$Au/Ce_{0.1}Ti_{0.9}O_X$	75.1	24.9	-	84.2	85.5	-
Au/TiO_2	83.6	16.4	-	83.3	85.0	-

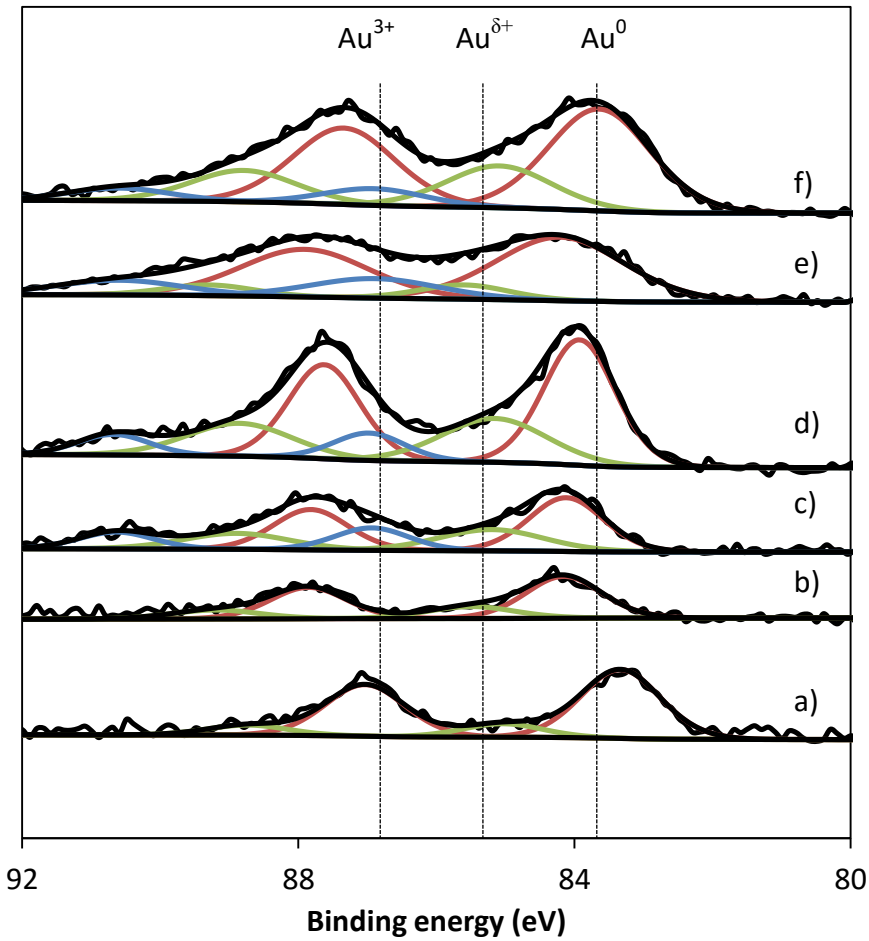

Figure 5.17 XPS analysis of the Au 4f spectra of $Au/Ce_aTi_{1-a}O_x$ catalysts: a) Au/TiO_2, b) $Au/Ce_{0.1}Ti_{0.9}O_X$, c) $Au/Ce_{0.2}Ti_{0.8}O_X$, d) $Au/Ce_{0.8}Ti_{0.2}O_X$, e) $Au/Ce_{0.9}Ti_{0.1}O_X$ and f) Au/CeO_2.

The Ce 3d spectrum was investigated to observe the relative population of Ce^{3+} and Ce^{4+} ions in the range of Ce-containing mixed metal oxides. Using the model proposed by Burroughs,[22] the Ce 3d region was deconvoluted into several peaks, described in full by Burroughs and in **Chapter 3**. Although the Ce^{3+} and Ce^{4+} surface concentration is presented below in Table 5.9, there is not a strong correlation between the Ce species and the Ce:Ti ratio. In fact there is very little variation at all across the range of $Ce_{0.5}Ti_{0.5}O_x$ materials.

One possible explanation for this is that under the experimental conditions, in particular exposure to the x-ray beam, reduction of the material occurs.[7] Based on the Raman spectroscopy that showed $Ce_{0.2}Ti_{0.8}O_X$ to have a very high level of oxygen defect sites, a high proportion of Ce^{3+} would be expected at the surface, and a low surface concentration of oxygen. The O content is consistent across the range of $Ce_{0.5}Ti_{0.5}O_x$ catalysts.

Table 5.9 XPS data for $Au/Ce_aTi_{1-a}O_x$ catalysts

Sample	Ce species (At %)		Surface elemental composition (At %)			Surface atomic ratio		Ti 2p (eV)
	Ce^{3+}	Ce^{4+}	Ce	Ti	O	Ce:Ti	M:O	
Au/CeO_2	39	61	28	0	71	-	0.4	-
$Au/Ce_{0.9}Ti_{0.1}O_X$	38	62	26	3	71	10.5	0.4	457.9
$Au/Ce_{0.8}Ti_{0.2}O_X$	39	61	22	5	72	4.6	0.4	458.1
$Au/Ce_{0.5}Ti_{0.5}O_X$	38	62	12	17	71	0.7	0.4	458.1
$Au/Ce_{0.2}Ti_{0.8}O_X$	38	62	14	15	70	0.9	0.4	458.1
$Au/Ce_{0.1}Ti_{0.9}O_X$	41	59	3	27	70	0.1	0.4	458.4
Au/TiO_2	-	-	-	30	70	-	0.4	458.5

The surface Au content is shown as a function of the total Au loading determined using MP-AES in Figure 5.18 (left) and approximates the trend observed in the MP-AES data: As Ti is introduced to the CeO_2, the Au content decreases. The dispersion of the Au can be indirectly measured by considering the relative quantity of “surface Au”, determined using XPS and “total Au”, determined using MP-AES.

When the Au mol% determined from XPS is divided by the Au loading from the MP-AES to give a ratio of “surface Au” to “total Au”, an interesting trend is observed. This is shown as

a function of Ce mol% in Figure 5.18 (right). The higher the ratio, the more Au was detected by XPS as a proportion of the total amount measured using MP-AES. The trend is clear: As Ce content increases, the metal dispersion increases. The $Au/Ce_{0.9}Ti_{0.1}O_X$ catalyst is a clear outlier and could indicate a large particle size of Au. In this sample, a relatively small amount of Au was detected compared to the quantity that was detected by MP-AES and so one explanation is that the Au particle size is large and XPS cannot probe deep enough into the sample to detect it. This was consistent with the low $Au^{\delta+}$ concentration in the sample. The assumption of this analysis is that the materials are not significantly porous. A porous material could support a considerable amount of gold that was inside the pores and potentially invisible to XPS. This could then explain why low Au content was detected in the XPS analysis. The general trend was surprising, because the most active catalysts for WGS (where Ce mol% = 20-50%) exhibited quite poor ratios of surface/total Au. This might suggest that the role of the support was particularly important in the range of $Au/Ce_{0.5}Ti_{0.5}O_x$ catalysts. In addition, the supports where Ce mol% =20-50% exhibited the highest surface areas measured which could imply a considerable degree of porosity and therefore significant quantities of the gold could be buried beneath the detection range of the XPS. Electron microscopy would be able measure the particle sizes and determine if the trends observed in Figure 5.18 are related to metal dispersion. Overall, the Au 4f XPS region showed large variations in the Au species present on the different catalysts. The most active catalysts featured high concentrations of non-metallic Au species, which was previously associated with well-dispersed, small Au particles. The high concentration of defect sites in the more active catalysts, as determined using Raman spectroscopy fits well with the XPS data, as it known that defect sites in CeO_2 can give rise to well dispersed Au.

The interaction of the Ti and the Ce was investigated by considering the position of the Ti peak. Shifts in the binding energy have previously been reported in mixed metal oxides of Ce and Ti.[11] Table 5.9 shows the binding energy of the Ti 2p signal and Figure 5.19 shows a plot of the line shapes for the corresponding spectra. The XP spectra of $Au/Ce_{0.9}Ti_{0.1}O_X$ and $Au/Ce_{0.8}Ti_{0.2}O_X$ were magnified by 10 and 5 times, respectively for clarity.

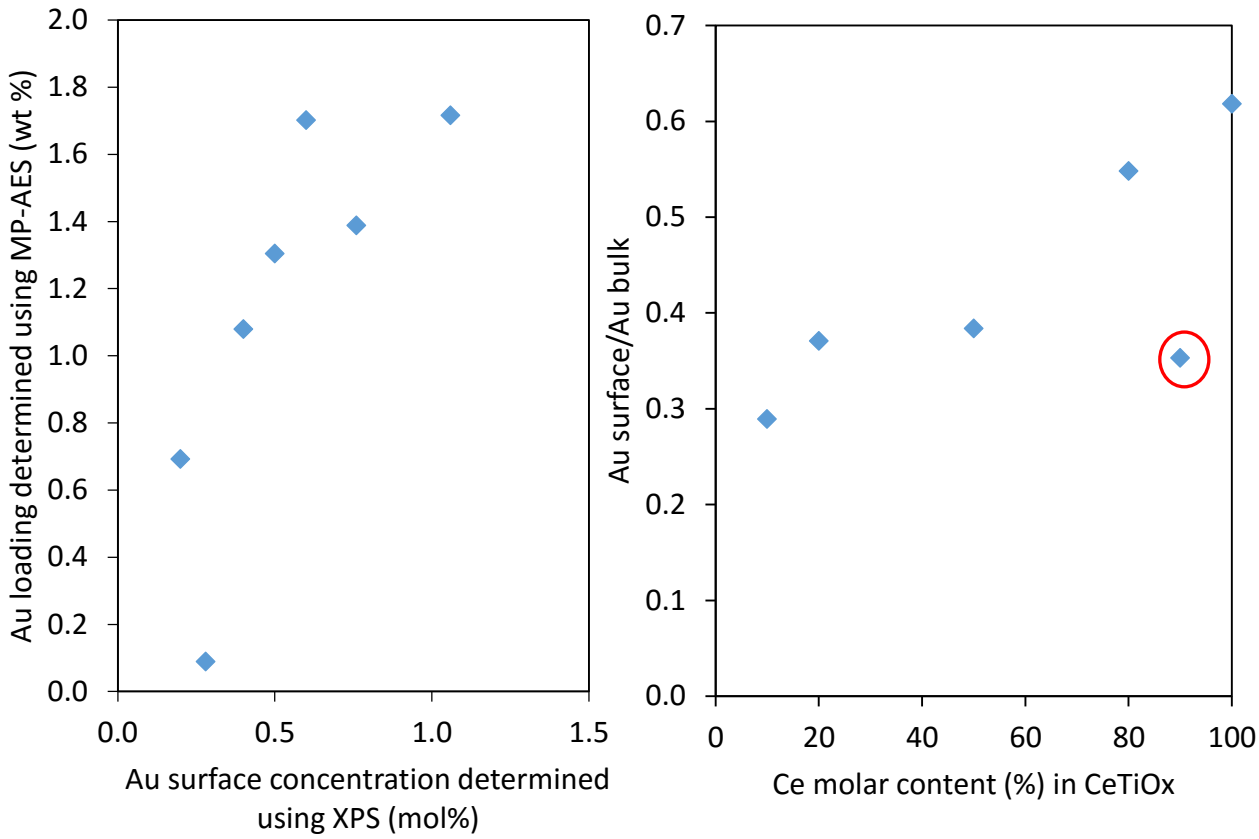

Figure 5.18 Left: The correlation between the total Au loading determined using MP-AES and the "surface" Au determined using XPS. Right: The surface Au:total Au ratio expressed as a function of Ce:Ti ratio

The Ti 2p region consists of two peaks: In the TiO_2 sample, the $2p_{3/2}$ feature is positioned at 458.5 eV which is due to Ti^{4+}. The split spin-orbit component is offset by 5.7 eV. The position of the $2p_{3/2}$ feature shifts according to the Ce:Ti ratio. This is illustrated in Figure 5.19 by the dashed line centred at 458.5 eV. The shifts in the binding energy were ascribed to the partial reduction of Ti^{4+} to Ti^{3+} by Song and co-workers[53] and Wang and co-workers.[11] However, this could also be due to the incorporation of Ti into the CeO_2 lattice.[7]

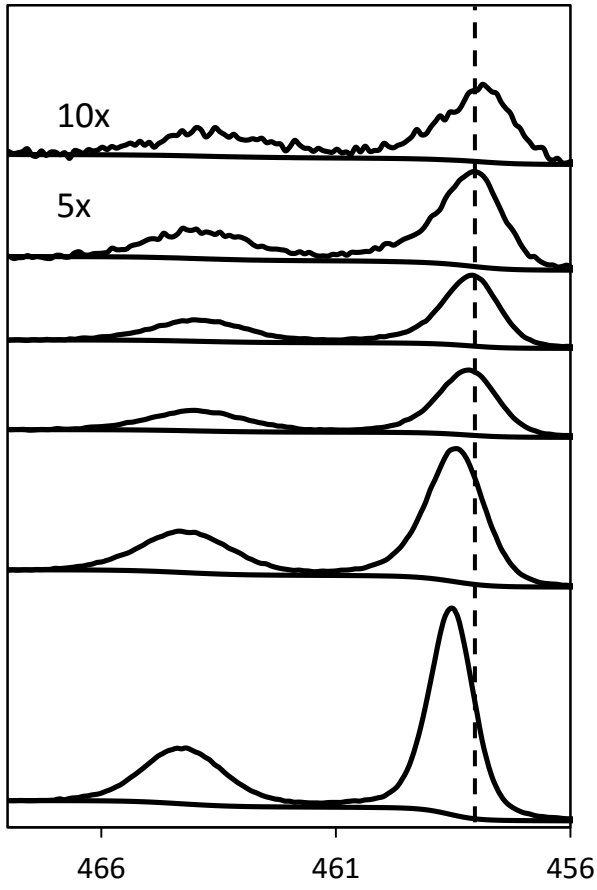

Figure 5.19 Ti 2p stack of $Au/Ce_aTi_{1-a}O_x$ catalysts. From bottom to top: Au/TiO_2, $Au/Ce_{0.1}Ti_{0.9}O_X$, $Au/Ce_{0.8}Ti_{0.2}O_X$, $Au/Ce_{0.5}Ti_{0.5}O_X$, $Au/Ce_{0.8}Ti_{0.2}O_X$ and $Au/Ce_{0.9}Ti_{0.1}O_X$.

SEM-EDX

The bulk elemental composition of the $Ce_{0.5}Ti_{0.5}O_x$ materials is presented in Table 5.10. The nominal molar ratio of the Ce and Ti is also shown. The measured values are in good agreement with the nominal values of the materials. Each material exhibited a high degree of homogeneity. This shows that Ce and Ti are well-dispersed within the material. It is instructive to compare the surface composition of the materials determined using XPS with the bulk composition determined using SEM-EDX. The surface and bulk compositions are similar for most of the $Ce_{0.5}Ti_{0.5}O_x$ materials with two exceptions. The $Ce_{0.5}Ti_{0.5}O_X$ and $Ce_{0.2}Ti_{0.8}O_X$ catalysts showed a higher than expected Ce:Ti surface ratio. The values were 0.7 and 0.9, respectively. $Ce_{0.2}Ti_{0.8}O_X$ in particular had the largest discrepancy as the surface Ce:Ti ratio was nearly three times higher than the nominal and bulk composition.

This is evidence of the surface enrichment of Ce in these two materials. Interestingly, these materials exhibited the highest catalytic activity of any of the $Au/Ce_{0.5}Ti_{0.5}O_x$ catalysts.

Table 5.10 EDX analysis of $CeMO_X$ supports showing the Ce:Ti molar ratio and the variation of the Ce:M molar ratio across different sites of the support expressed as a percentage of the average Ce:Ti ratio

Sample	Nominal Ce:Ti ratio	Ce:Ti molar ratio	Variation in Ce:Ti ratio (%)
CeO_2	-	-	-
$Ce_{0.9}Ti_{0.1}O_x$	9	10.2	0.9
$Ce_{0.8}Ti_{0.2}O_x$	4	4.8	3.3
$Ce_{0.5}Ti_{0.5}O_x$	1	0.94	5.1
$Ce_{0.2}Ti_{0.8}O_x$	0.25	0.23	1.0
$Ce_{0.1}Ti_{0.9}O_x$	0.11	0.11	0.7
TiO_2	-	-	-

5.5. Conclusions

In this chapter two strategies for stabilising the benchmark catalyst were attempted, with varying success: Sub-surface dopants and the substitution of Zr for Al or Ti.

Sub-surface dopants of Mo

The rationale behind this investigation was to implement the pioneering work done by Freund and co-workers in identifying the role of sub-surface dopants in affecting the properties of surface metal particles. It was demonstrated on CaO that sub-surface Mo can prevent 3-dimensional growth of a gold nanoparticle due to charge transfer from Mo to the surface.[4, 5, 56] $CeZrO_4$ was prepared using the sol-gel methodology and a Mo precursor was added to the reaction mixture. Several loadings were used and gold was subsequently deposited on the surface of the doped support. Characterisation by XPS revealed the presence of surface Mo in the majority of samples prepared and the WGS activity was shown to be significantly diminished as a result of Mo doping. The activity was correlated with surface Mo content as determined by XPS, and gave a clear trend showing the higher the Mo content, the lower the WGS activity. Furthermore, there was no improvement in the stability of the catalysts prepared. It is clear that the properties of the

support, the dopant and the metal nanoparticle must be carefully chosen in order to induce such an effect. Furthermore, the preparation of these materials requires a high degree of precision, perhaps too high for conventional preparation methods such as sol-gel to facilitate. It is also noteworthy that there are no reports that the original findings have been replicated in powder catalysts.

Substitution of Zr for Ti or Al

The effect of the support was probed by substituting Zr for Ti or Al to form a novel mixed metal oxide support upon which gold was supported. Comparative stability and activity studies showed that $Ce_{0.5}Ti_{0.5}O_x$ was more stable than $Au/CeZrO_4$ under the same reaction conditions. $Au/Ce_{0.5}Al_{0.5}O_x$ was the least stable catalyst. The activity of the $Au/CeZrO_4$ catalyst and $Au/Ce_{0.5}Ti_{0.5}O_x$ was very similar and both catalysts were more active than $Au/Ce_{0.5}Al_{0.5}O_x$. Subsequent characterisation was carried out to probe the surface and bulk properties of the $Au/CeMO_X$ catalysts. $Ce_{0.5}Ti_{0.5}O_x$ exhibited a high surface area compared to $CeZrO_4$ and the crystallite size determined using the Scherrer equation was in the range of 4.2 nm. H_2-TPR measurements showed that the material was very easily reduced and a high concentration of oxygen vacancies were found using Raman spectroscopy. EDX confirmed that the material was homogeneous in nature and the actual metal ratio was close to the nominal value.

On the other hand, the $Ce_{0.5}Al_{0.5}O_x$ was inhomogeneous in nature, with large variations between EDX measurements. In addition, the XRD showed that crystalline cerium hydroxyl carbonate was present, likely residual precursor that was not oxidised fully. The crystallite size was measured to be very large although the material did have a high surface area. H_2-TPR measurements showed poor hydrogen consumption which was likely to be due to the incomplete formation of the oxide. Raman spectroscopy showed the presence of the F_{2g} mode associated with CeO_2 and a similar concentration of oxygen vacancies to $CeZrO_4$ were measured. XPS analysis showed that there was a higher concentration of Au^{3+} in the $CeZrO_4$ and $Ce_{0.5}Ti_{0.5}O_x$ catalysts and this was hypothesised as being a precursor to well-dispersed nanoparticles of Au as previously reported.[24] It was concluded that a combination of a high surface area and a small particle size led to many surface defects

that could dissociate water and numerous nucleation sites that could anchor gold. This was thought to be the origin of the success of $Ce_{0.5}Ti_{0.5}O_x$ as a support.

Ceria-titania as a catalyst support for WGS

The enhanced stability of the $Au/Ce_{0.5}Ti_{0.5}O_x$ catalyst led to further work on this mixed metal oxide, whereby the effect of the Ce:Ti ratio was varied. A range of $Ce_{0.5}Ti_{0.5}O_x$ supports were prepared, including the monometallic oxides. After supporting gold on these materials, they were screened for WGS activity and stability. A strong synergistic relationship was observed in the supports whereby the monometallic supports (CeO_2 and TiO_2) produced less active catalysts but mixed metal oxide supports generally gave more active catalysts. $Au/Ce_{0.2}Ti_{0.8}O_X$ was the most active catalyst, converting 300 mol_{CO} h^{-1} mol_{metal}^{-1} compared to $Au/CeZrO_4$, which converted 263 mol_{CO} h^{-1} mol_{metal}^{-1}. In addition to this, $Ce_{0.2}Ti_{0.8}O_X$ displayed remarkable stability under WGS conditions. While the benchmark $Au/CeZrO_4$ catalyst retained 73% of its initial conversion after 16 h on-line, $Au/Ce_{0.2}Ti_{0.8}O_X$ retained 83% of its original activity. This is a significant difference.

The origin of this enhanced activity and stability was explored by carrying out extensive characterisation. The mixed metal oxides typically had a higher surface area which was consistent with smaller crystallite sizes determined using XRD. While the TiO_2 support showed reflections due to anatase in the XRD diffractogram, the Ce-containing supports exhibited a cubic fluorite-type structure similar to pure CeO_2. The exceptions to this were $Ce_{0.2}Ti_{0.8}O_X$ and $Ce_{0.1}Ti_{0.9}O_X$ which were amorphous. EDX measurements showed that the actual metal ratios were very close to the nominal ones, illustrating the ease with which the mixed metal oxides are formed. Raman spectroscopy was used to measure defect sites on the metal oxide supports and it was found that the higher the Ti content, the higher concentration of defect sites in the Ce-containing oxides. The $Ce_{0.2}Ti_{0.8}O_X$ sample did not exhibit a typical CeO_2 band and so a ratio could not be calculated, although the weak band associated with Ce^{3+} was present, implying the presence of oxygen defects. A high concentration of non-metallic Au was observed in the more active catalysts, perhaps suggesting differences in the metal dispersion.

Overall, the $Ce_{0.5}Ti_{0.5}O_x$ supports exhibited small crystallite sizes and high surface areas, in addition to high concentrations of defect sites. These attributes are important for catalyst supports in the WGS reaction for several reasons: The defect sites activate water and anchor gold. Defect sites were also found to result in strongly bound gold. In addition, the high surface area ensures large numbers of active sites can be formed per gram of support. However, to confirm the characterisation carried out in this investigation, high-resolution electron microscopy should be carried out. This would help clarify the origin of the stability enhancement seen in the $Ce_{0.5}Ti_{0.5}O_x$ supports.

5.6. References

1. F. Tao and Z. Ma, *Physical Chemistry Chemical Physics*, 2013, 15, 15260.

2. R. Burch, *Physical Chemistry Chemical Physics*, 2006, 8, 5483.

3. S. Prada, L. Giordano and G. Pacchioni, *Journal of Physical Chemistry C*, 2013, 117, 9943.

4. F. Stavale, X. Shao, N. Nilius, H.-J. Freund, S. Prada, L. Giordano and G. Pacchioni, *Journal of the American Chemical Society*, 2012, 134, 11380.

5. X. Shao, S. Prada, L. Giordano, G. Pacchioni, N. Nilius and H.-J. Freund, *Angewandte Chemie-International Edition*, 2011, 50, 11525.

6. *Catalysis by Ceria and Related Materials*, Imperial College Press, second edn., 2013.

7. S. Rico-Frances, E. O. Jardim, T. A. Wezendonk, F. Kapteijn, J. Gascon, A. Sepulveda-Escribano and E. V. Ramos-Fernandez, *Applied Catalysis B-Environmental*, 2016, 180, 169.

8. J. A. Rodriguez, R. Si, J. Evans, W. Xu, J. C. Hanson, J. Tao and Y. Zhu, *Catalysis Today*, 2015, 240, 229.

9. S. S. Kim, S. M. Lee, J. M. Won, H. J. Yang and S. C. Hong, *Chemical Engineering Journal*, 2015, 280, 433.

10. J. Xu, J. Harmer, G. Li, T. Chapman, P. Collier, S. Longworth and S. C. Tsang, *Chemical Communications*, 2010, 46, 1887.

11. W. Deng, Q. Dai, Y. Lao, B. Shi and X. Wang, *Applied Catalysis B-Environmental*, 2016, 181, 848.

12. J. B. Park, J. Graciani, J. Evans, D. Stacchiola, S. Ma, P. Liu, A. Nambu, J. Fernandez Sanz, J. Hrbek and J. A. Rodriguez, *Proceedings of the National Academy of Sciences of the United States of America*, 2009, 106, 4975.

13. D. Andreeva, I. Ivanov, L. Ilieva, J. W. Sobczak, G. Avdeev and T. Tabakova, *Applied Catalysis a-General*, 2007, 333, 153.

14. D. Andreeva, I. Ivanova, L. Ilieva and M. V. Abrashev, *Applied Catalysis a-General*, 2006, 302, 127.

15. E. Smolentseva, A. Simakov, S. Beloshapkin, M. Estrada, E. Vargas, V. Sobolev, R. Kenzhin and S. Fuentes, *Applied Catalysis B-Environmental*, 2012, 115, 117.

16. T. Seiyama, *New horizons in catalysis: Proceedings of the 7th International Congress on Catalysis, Tokyo, 30 June-4 July 1980 (Studies in surface science and catalysis)*, Elsevier, 2000.

17. D. Andreeva, I. Ivanov, L. Ilieva, J. W. Sobczak, G. Avdeev and K. Petrov, *Topics in Catalysis*, 2007, 44, 173.

18. D. Andreeva, I. Ivanov, L. Ilieva, M. V. Abrashev, R. Zanella, J. W. Sobczak, W. Lisowski, M. Kantcheva, G. Avdeev and K. Petrov, *Applied Catalysis a-General*, 2009, 357, 159.

19. T. R. Reina, S. Ivanova, M. A. Centeno and J. A. Odriozola, *Catalysis Today*, 2015, 253, 149.

20. F. Zhang, C. H. Chen, J. C. Hanson, R. D. Robinson, I. P. Herman and S. W. Chan, *Journal of the American Ceramic Society*, 2006, 89, 1028.

21. V. S. Escribano, E. F. Lopez, M. Panizza, C. Resini, J. M. G. Amores and G. Busca, *Solid State Sciences*, 2003, 5, 1369.

22. P. Burroughs, A. Hamnett, A. F. Orchard and G. Thornton, *Journal of the Chemical Society-Dalton Transactions*, 1976, 1686.

23. Q. Fu, S. Kudriavtseva, H. Saltsburg and M. Flytzani-Stephanopoulos, *Chemical Engineering Journal*, 2003, 93.

24. D. Tibiletti, A. Amieiro-Fonseca, R. Burch, Y. Chen, J. M. Fisher, A. Goguet, C. Hardacre, P. Hu and A. Thompsett, *Journal of Physical Chemistry B*, 2005, 109.

25. X. Wu, Q. Liang, D. Weng, J. Fan and R. Ran, *Catalysis Today*, 2007, 126, 430.

26. J. Manuel Lopez, A. L. Gilbank, T. Garcia, B. Solsona, S. Agouram and L. Torrente-Murciano, *Applied Catalysis B-Environmental*, 2015, 174, 403.

27. NIST X-ray Photoelectron Spectroscopy Database, http://srdata.nist.gov/xps/.

28. N. Radutoiu and C. M. Teodorescu, *Digest Journal of Nanomaterials and Biostructures*, 2013, 8, 1535.

29. J. C. Dupin, D. Gonbeau, P. Vinatier and A. Levasseur, *Physical Chemistry Chemical Physics*, 2000, 2, 1319.

30. S. Zhao, T. Luo and R. J. Gorte, *Journal of Catalysis*, 2004, 221, 413.

31. X. Wang, R. J. Gorte and J. P. Wagner, *Journal of Catalysis*, 2002, 212, 225.

32. A. Vazquez, T. Lopez, R. Gomez and X. Bokhimi, *Journal of Molecular Catalysis a-Chemical*, 2001, 167, 91.

33. R. Si and M. Flytzani-Stephanopoulos, *Angewandte Chemie-International Edition*, 2008, 47, 2884.

34. X. D. Zhou and W. Huebner, *Applied Physics Letters*, 2001, 79, 3512.

35. Q. Fu, W. L. Deng, H. Saltsburg and M. Flytzani-Stephanopoulos, *Applied Catalysis B-Environmental*, 2005, 56.

36. R. Pilasombat, H. Daly, A. Goguet, J. P. Breen, R. Burch, C. Hardacre and D. Thompsett, *Catalysis Today*, 2012, 180.

37. V. N. Morris, R. A. Farrell, A. M. Sexton and M. A. Morris, Univ Leeds, Leeds, ENGLAND, 2005.

38. V. Morris, P. Fleming, M. Conroy, J. D. Holmes and M. A. Morris, *Chemical Physics Letters*, 2012, 536, 109.

39. F. Zhang, S. W. Chan, J. E. Spanier, E. Apak, Q. Jin, R. D. Robinson and I. P. Herman, *Applied Physics Letters*, 2002, 80, 127.

40. O. H. Laguna, A. Perez, M. A. Centeno and J. A. Odriozola, *Applied Catalysis B-Environmental*, 2015, 176, 385.

41. I. Kosacki, T. Suzuki, H. U. Anderson and P. Colomban, *Solid State Ionics*, 2002, 149, 99.

42. T. Murota, T. Hasegawa, S. Aozasa, H. Matsui and M. Motoyama, *Journal of Alloys and Compounds*, 1993, 193, 298.

43. J. E. Spanier, R. D. Robinson, F. Zheng, S. W. Chan and I. P. Herman, *Physical Review B*, 2001, 64.

44. G. W. Graham, W. H. Weber, C. R. Peters and R. Usmen, *Journal of Catalysis*, 1991, 130, 310.

45. O. H. Laguna, F. R. Sarria, M. A. Centeno and J. A. Odriozola, *Journal of Catalysis*, 2010, 276, 360.

46. W. Y. Hernandez, M. A. Centeno, F. Romero-Sarria and J. A. Odriozola, *Journal of Physical Chemistry C*, 2009, 113, 5629.

47. Z.-Y. Pu, J.-Q. Lu, M.-F. Luo and Y.-L. Me, *Journal of Physical Chemistry C*, 2007, 111, 18695.

48. Y. Zhou, E. W. Peterson and J. Zhou, *Catalysis Today*, 2015, 240, 201.

49. D. Goodman, in *Dekker Encyclopedia of Nanoscience and Nanotechnology*, eds. C. Contescu and K. Putyera, CRC Press, Second edn., 2008, pp. 611-619.

50. M. Alifanti, B. Baps, N. Blangenois, J. Naud, P. Grange and B. Delmon, *Chemistry of Materials*, 2003, 15, 395.

51. G. Avgouropoulos and T. Ioannides, *Applied Catalysis B-Environmental*, 2006, 67, 1.

52. R. Burch, L. Gladden and S. Golunski, *Platinum Metals Review*, 2010, 54.

53. S. Watanabe, X. Ma and C. Song, *Journal of Physical Chemistry C*, 2009, 113, 14249.

54. L. Liu, Z. Yao, B. Liu and L. Dong, *Journal of Catalysis*, 2010, 275, 45.

55. G. Zhou, J. Hanson and R. J. Gorte, *Applied Catalysis a-General*, 2008, 335, 153.

56. X. Shao, N. Nilius and H.-J. Freund, *Physical Review B*, 2012, 85.

Chapter 6

Conclusions and future work

6.1. Conclusions and future work

The low-temperature WGS reaction is an extremely important process in upgrading H_2 streams in fuel cell technology. The discovery of a stable and active low temperature WGS catalyst would represent a significant step forward in realising the potential of the hydrogen economy. $Au/CeZrO_4$ is an extremely active catalyst that is susceptible to rapid deactivation under reaction conditions. Using state-of-the-art microscopy and XPS, the understanding of how this catalyst deactivates under reaction conditions has been improved. The electron microscopy data showed clear evidence of particle agglomeration and significant morphological changes to the supported Au nanoparticles, although evaluating the significance of the morphological changes in a statistically relevant way was not possible. To the best of our knowledge, this was the first microscopic study of its kind on gold catalysts for the WGS reaction where mixtures of gases that are relevant to fuel cell operation were used. In addition to the previous work in this area that showed particle de-wetting to play an important role,[1] it was concluded that enhancing the metal-support interaction was integral to achieving an active WGS catalyst. The significance of the support reduction was not established in this study – future work in this area should aim to achieve this. Studies involving careful pre-reduction of the catalyst would achieve this. Furthermore, it was observed that the rate of deactivation was highest in the first 6 h. Characterisation of a sample after this time would reveal whether other processes are relevant and show to what extent the Au particles have sintered after this time.

A series of $AuPd/CeZrO_4$ catalysts were prepared in order to establish how the introduction of a second metal affected the activity and stability of the final catalyst. It was found that the combination of Au and Pd yielded a catalyst with equivalent

stability and significantly lower activity than the monometallic gold catalyst. The WGS activity of the $Au_{44}Pd_{56}/CeZrO_4$ catalyst was less than ten times as active as the monometallic Au catalyst. This effect was characterised as *anti-synergy* because it was the opposite observation to many of the reports on AuPd bimetallic catalysts that observed a synergistic effect. This anti-synergy was investigated by utilising many characterisation tools to understand the properties of the catalyst.

H_2-TPR, CO-DRIFTS and XPS probe different aspects of a catalyst and are based on fundamentally different scientific principles. However, in this study complimentary information was extracted from each technique. This showed that using multiple techniques can greatly enhance the understanding of supported metal catalysts and give more weight to the findings of each technique.

HAADF STEM was used to gain quantitative information on the particle size of the gold nanoparticles and corroborated the H_2-TPR, CO-DRIFTS and XPS data. HAADF STEM is an expensive, time-consuming technique and this work has shown that very similar information can be obtained from much simpler characterisation techniques and the methods applied in this work could be used in the future as a quick and easy way to qualitatively compare metal particle sizes in similar supported metal catalysts.

HAADF STEM also revealed the presence of different particle morphologies. Further work to establish the importance of different morphologies could enhance the understanding of the active site. In addition, the nanostructure of the AuPd catalysts under reaction conditions was overlooked. The AuPd nanostructure has been shown to be dynamic under CO oxidation conditions due to the presence of CO and it is likely that the same is true for WGS. *In situ* studies should be undertaken in order to elucidate the nanostructure of the bimetallic catalysts. EXAFS, CO-DRIFTS or ETEM could prove powerful tools to achieve this. In addition, EDX measurements on the nanoparticles could indicate the position of Au and Pd atoms in the bimetallic particles.

The AuPd catalysts were also tested for their activity in the mechanistically similar CO oxidation and formic acid decomposition (FAD). Geoffrey Bond predicted that FAD could be used as a test reaction for WGS activity.[2] The observation that in each reaction the same catalyst activity was observed confirmed that Bond's hypothesis was correct. In addition, CO oxidation could also be used as a test reaction for WGS activity.

It was speculated that similar active sites i.e. small well-dispersed metal particles are needed in each reaction, but this was not demonstrated experimentally. While it was also hypothesised by Bond that FAD and WGS proceed through the same reaction intermediate, this was not investigated experimentally. The work carried out here should serve as an incentive to further explore the similarities between FAD, WGS and CO oxidation and could reveal common intermediates in the reaction mechanisms. *In situ* techniques such as CO-DRIFTS carried out carefully and quantitatively could help to identify such intermediates, as was reported by Meunier *et al.*[3] Furthermore, catalysts active for FAD and CO oxidation should be considered for their WGS activity.

The modification of the support consisted of two strategies. The first strategy involved using sub-surface dopants to stabilise the surface gold nanoparticles based on the pioneering work by Freund *et al.*[4] However, the doped supports were found to yield less active catalysts when the loading of Mo was above 0.1 wt%. XPS showed the presence of surface Mo and previous publications that showed Mo to be a poison to CeO_2 supported WGS catalysts.[5] In addition to this, the inclusion of Mo in the synthesis of the $CeZrO_4$ support led to large variations in the Ce:Zr molar ratios and this was also likely to affect the WGS activity. Overall, the addition of Mo to the synthesis of $CeZrO_4$ did not have the desired effect and proved to poison the catalyst. However, the prospect of controlling surface metal particles by using sub-surface dopants remains an appealing one. If this was successfully implemented it would have significant implications for the future design of supported metal catalysts. Future work should focus on first reproducing the work done on model surfaces on equivalent powder catalysts before introducing new components to the system, such as CeO_2, which would undoubtedly affect the charge transfer of Mo to the gold surface species. The characterisation carried out in this work revealed interactions between Au and Pd and electronic modification indicative of an alloy, but a full understanding of the catalyst nanostructure and morphology was not able to be achieved. Further characterisation on the dynamic nanostructure of the catalysts studied in this work under reaction conditions is needed to establish its importance. Recent work carried out by Gibson *et al.* showed that EXAFS could be used follow the restructuring of AuPd nanoparticles under CO oxidation conditions. This could be applied to WGS (and FAD) conditions to identify further similarities.[6]

The second strategy to develop a stable catalyst was more successful. It was shown that the substitution of Ti for Zr to produce $Ce_{0.5}Ti_{0.5}O_X$ resulted in a catalyst that was as active as and significantly more stable than the $Au/CeZrO_4$ catalyst. $Au/Ce_{0.5}Ti_{0.5}O_X$ catalyst still exhibited fairly rapid deactivation and would not be stable enough for commercial application, but the result was positive nonetheless. $Au/Ce_{0.5}Al_{0.5}O_X$ by contrast was less stable than $Au/CeZrO_4$ and less active. Characterisation of the three catalysts revealed significant differences. $Ce_{0.5}Ti_{0.5}O_X$ had a high specific surface area and a small crystallite size. It was also highly reducible and was observed to have a high concentration of surface O defects. The features that were responsible for its high stability were difficult to identify, due to the many parameters that varied between the samples, but the high surface area and high concentration of defect sites were thought to be important. These defect sites have been reported to strongly anchor gold nanoparticles, although this was not demonstrated experimentally. Future work should aim to replicate the microscopic study carried out on $Au/CeZrO_4$ on the $Au/Ce_{0.5}Ti_{0.5}O_X$ to compare the fresh and used samples. In addition, evidence of morphological changes could be examined. $Au/Ce_{0.5}Ti_{0.5}O_X$ featured a high concentration of non-metallic Au – combination of small gold nanoparticles and Au^{3+} which have been reported to be precursors to active sites and small gold nanoparticles, respectively.[1, 7] Therefore the $Ce_{0.5}Ti_{0.5}O_X$ could also facilitate a very high dispersion of gold. HAADF STEM would be able to confirm this. In addition, the doping of other metals with Ce would reveal whether other mixed metal oxides containing Ce could facilitate a similarly high concentration of defect sites and well dispersed gold.

$Ce_{0.5}Ti_{0.5}O_X$ was the subject of further investigation due to the high stability observed in the $Au/Ce_{0.5}Ti_{0.5}O_X$ catalyst. The Ce:Ti ratio was varied to produce several mixed metal oxides. It was shown that $Au/Ce_{0.2}Ti_{0.8}O_X$ achieved the highest activity and was as stable as $Au/Ce_{0.5}Ti_{0.5}O_X$. Characterisation showed that $Au/Ce_{0.2}Ti_{0.8}O_X$ had a very high surface area, although it was amorphous and quantification of oxygen vacancies from Raman spectroscopy was not possible. $Au/Ce_{0.2}Ti_{0.8}O_X$ was observed to a high concentration of non-metallic gold, indicating a large number of active gold species. The high concentration of these active gold species (Au^{3+} and $Au^{\delta+}$) was thought to be due to the high concentration of defect sites present on the surface.

Overall, the modification of the support resulted in a catalyst more active and stable than the Au/$CeZrO_4$ benchmark catalyst. The following properties were identified as being most important for producing an active gold catalyst:

- **Small crystallite size**. This promotes the formation of defect sites and enhances reducibility, which in turns facilitates the activation of water.
- **High specific surface area.** This can be achieved through ensuring small crystallite sizes. It allows gold to be well dispersed on the surface and minimises particle agglomeration.
- **High concentration of defect sites.** Oxygen defects are responsible for the activation of water in the WGS reaction. In addition, these defects serve as nucleation sites for gold and contribute to achieving a high dispersion of gold.
- **Sufficient redox properties.** Below 20 mol% Ce, it was found that the catalysts were not active for WGS. The reason for this was thought to be insufficient activation of water as a result of low levels of surface Ce content. Therefore it is important to ensure the support has sufficient levels of reducibility at the surface to facilitate the activation of water.

$Ce_{0.5}Ti_{0.5}O_X$ and $Ce_{0.2}Ti_{0.8}O_X$ exhibited all of these properties and the resultant catalysts were stable and very active in the WGS reaction.

The importance of each component was difficult to evaluate due to multiple variables changing between samples. Future work should aim to address this. One strategy would be to carry out different heat treatments on the same $Ce_{0.5}Ti_{0.5}O_X$ sample. This could induce changes to the surface area for example while retaining other factors such as the Ce:Ti molar ratio. Subsequent characterisation and catalyst testing could show different parameters to be more important than others.

6.2. References

1. A. Goguet, R. Burch, Y. Chen, C. Hardacre, P. Hu, R. W. Joyner, F. C. Meunier, B. S. Mun, A. Thompsett and D. Tibiletti, *Journal of Physical Chemistry C*, 2007, **111**.
2. G. Bond, *Gold Bulletin*, 2009, **42**, 337.
3. F. C. Meunier, D. Reid, A. Goguet, S. Shekhtman, C. Hardacre, R. Burch, W. Deng and M. Flytzani-Stephanopoulos, *Journal of Catalysis*, 2007, **247**, 277.
4. X. Shao, S. Prada, L. Giordano, G. Pacchioni, N. Nilius and H.-J. Freund, *Angewandte Chemie-International Edition*, 2011, **50**, 11525.
5. S. Zhao, T. Luo and R. J. Gorte, *Journal of Catalysis*, 2004, **221**, 413.
6. E. K. Gibson, A. M. Beale, C. R. A. Catlow, A. Chutia, D. Gianolio, A. Gould, A. Kroner, K. M. H. Mohammed, M. Perdjon, S. M. Rogers and P. P. Wells, *Chemistry of Materials*, 2015, **27**, 3714.
7. D. Tibiletti, A. Amieiro-Fonseca, R. Burch, Y. Chen, J. M. Fisher, A. Goguet, C. Hardacre, P. Hu and A. Thompsett, *Journal of Physical Chemistry B*, 2005, **109**.